UNIVERSITY OF SOUTHAMPTON

FACULTY OF ENGINEERING, SCIENCE AND MATHEMATICS

Optoelectronics Research Centre

Processing of ultra-short optical pulses for high bit-rate optical communications

by

Francesca Parmigiani

Thesis submitted for the degree of Doctor of Philosophy

December 2006

UNIVERSITY OF SOUTHAMPTON

ABSTRACT

FACULTY OF ENGINEERING, SCIENCE AND MATHEMATICS
OPTOELECTRONICS RESEARCH CENTRE

Doctor of Philosophy

Processing of ultra-short optical pulses for high bit-rate optical communications

by Francesca Parmigiani

In this thesis, the possibility of integrating linear pulse shapers into various all-optical signal processing devices for applications in high speed optical communication systems, to enhance the overall system performance, is investigated. The linear pulse shaping is performed using superstructured fibre Bragg gratings, which seem very promising passive devices for such application due to their compactness, easy integrability and compatibility with fibre based devices. At the same time, optical switching is facilitated by nonlinear effects in state of the art highly nonlinear fibres.

The generation and manipulation of waveforms with specific shapes also requires suitable techniques for their precise characterization. For this reason, optical sampling oscilloscope or linear and nonlinear frequency resolved optical gating techniques are presented in this thesis.

As a first example of all optical signal processing using pre-shaped pulses, the incident noisy data pulses are expanded into rectangular pulses at the input port of a nonlinear optical switch (nonlinear optical loop mirror). The flat top of the shaped pulses allows for the mitigation of any mistiming of the original signal across a time window defined by their width, simply by switching them with shorter clean clock pulses. By using a nonlinear switch with full regenerative properties as well, it is demonstrated that amplitude noise reduction as well as timing jitter reduction can be achieved in a single nonlinear switch.

In a different switch configuration, where cross-phase modulation is utilized in a single-pass configuration, retiming is obtained by preshaping clean control pulses into pulses with a parabolic shape. XPM induced by such pulses can provide linear frequency-shifting to shorter mistimed data pulses across a temporal window corresponding to the full width of the parabolic pulses. This frequency-shift is proportional to the relative pulse displacement from the control bit-slot centre. Propagation in a suitable length of a dispersive medium can then be used to correct for the mistiming. The parabolic pulse shape is also very interesting for nonlinear propagation in normal-dispersion fibres, since it can propagate at high peak powers without undergoing deleterious pulse distortion (avoiding wave-breaking effects). It is demonstrated that the nonlinearly broadened parabolic pulse spectrum is highly flat and coherent, with a high spectral density, as required for spectral slicing or pulse compression applications.

Finally, the use of Bismuth oxide highly nonlinear fibre is investigated in order to enhance the compactness and stability of the switching system. 2R-regeneration at 10- and 40-Gb/s is demonstrated using just 2 m of this fibre.

Contents

List of Figures

List of Tables

Declaration of Authorship

I, Francesca Parmigiani

declare that the thesis entitled:

Processing of ultra-short optical pulses for high bit-rate optical communications

and the work presented in the thesis are both my own, and have been generated by me as the result of my own original research. I confirm that:

- this work was done wholly or mainly while in candidature for a research degree at this University;
- where any part of this thesis has previously been submitted for a degree or any other qualification at this University or any other institution, this has been clearly stated;
- where I have consulted the published work of others, this is always clearly attributed;
- where I have quoted from the work of others, the source is always given. With the exception of such quotations, this thesis is entirely my own work;
- I have acknowledged all main sources of help;
- where the thesis is based on work done by myself jointly with others, I have made clear exactly what was done by others and what I have contributed myself;
- parts of this work have been published as: [See *List of Publications*].

Francesca Parmigiani

December 2006

Abbreviations

ASE	Amplified Spontaneous Emission
AWG	Arrayed Waveguide Grating
BER	Bit Error Rate
Bi-NLF	Bismuth Nonlinear Fibre
CR	Clock Recovery
CW	Continuous Wave
DCA	Digital Communications Analyzer
DCF	Dispersion Compensating Fibre
DDF	Dispersion Decreasing fibre
DFB	Distributed Feedback
DFG	Difference-Frequency Generation
DMF	Dispersion Managed Fibre
DPSK	Differential Phase Shift Keying
DQPSK	Differential Quadrature Phase Shift Keying
DSF	Dispersion Shifted Fibre
EAM	Electrical Absorber Modulator
EAM-FROG	Electrical Absorber Modulator Frequency-Resolved Optical Gating
EDFA	Erbium Doped Fibre Amplifier
EFRL	Erbium Fibre Ring Laser
ETDM	Electrical Time Division Multiplexing
FBG	Fibre Bragg Grating
FROG	Frequency-Resolved Optical Gating
FOM	Figure Of Merit
FWHM	Full Width at Half Maximum
FWM	Four Wave Mixing
GVD	Group Velocity Dispersion
HNLF	Highly Nonlinear Fibre
HP-EDFA	High Power Erbium Doped Fibre
IFWM	Intra Four Wave Mixing
ISI	Intersymbol Interference
IXPM	Intra Cross Phase Modulation
NLS	Nonlinear Schrödinger

NOLM	Nonlinear Optical Loop Mirror
NRZ	Non Return to Zero
O-E-O	Optical Electronic Optical
OCDMA	Optical Code Division Multiplexing Access
OFT	Optical Fourier Transform
OOK	On Off Keying
OSA	Optical Spectrum Analyzer
OTDM	Optical Time Division Multiplexing
PLL	Phase Locked Loop
PM	Polarization Maintaining
PMD	Polarization Mode Dispersion
PRBS	Pseudorandom bit Sequence
QPM	Quasi Phase Matched
RF	Radio Frequency
RMS	Root Mean Square
RZ	Return-to-Zero
SBS	Stimulated Brillouin Scattering
SCG	Supercontinuum Generation
SFG	Sum-Frequency Generation
SHG-FROG	Second Harmonic Generation Frequency-Resolved Optical Gating
SMF	Single Mode Fibre
SNR	Signal to Noise Ratio
SOA	Semiconductor Optical Amplifier
SPM	Self-Phase Modulation
SSFBG	Superstructured Fibre Bragg Grating
SSF	Split-Step Fourier
SRS	Stimulated Raman Scattering
TBP	Time Bandwidth Product
TDM	Time Division Multiplexing
TPA	Two Photon Absorption
WC	Wavelength Converter
WDM	Wavelength Division Multiplexing
XPM	Cross-Phase Modulation

Acknowledgements

A PhD, what an experience! I would definitely say what a tremendous life experience, where rewarding and painful times mixed together. Now that is over, I am very happy to pause and reflect on the many people who have supported me and helped my personal and professional growth throughout this unforgettable journey.

I wish to thank my supervisor, Professor David Richardson, for providing me the unique opportunity of working here at the ORC and for his constant support and encouragement throughout my PhD years. I really felt honoured to have been working with him; his ability of quickly catching up and understanding my work issues giving many times very useful advices and suggestions always impressed me.
I pay a special tribute to my co-supervisor Dr Periklis Petropoulos for his enormous supervision and guidance throughout all my research. Thanks for introducing me the telecommunication system lab and getting me started and following me with my project. I will always be grateful for your great support, patience, kindness and friendship you always offered me.
I would also like to take this opportunity to thank Dr Morten Ibsen for providing me all the unique superstructured fibre Bragg gratings described in this thesis as well as for the fruitful discussions on gratings and on many other different topics. I am also indebted to Dr Benn Thomsen for his lab support and Dr. Christophe Finot for his technical discussions on parabolic pulses. I would also like to thank Mr Kazunori Mukasa for providing me some of the HNLFs used in this thesis.
A big thank goes to the "telecom fellowship", with whom I have had the opportunity to work and become friend: even if it has been quite hard to work in this lab, I really appreciated your support and friendship. In particular, I would like to thank Paulo Almeida for his theoretical support, his help in many experiments described in this thesis as well as his assistance in my many Matlab issues, Michaël Roelens for helping me many times optimizing the gain switched lasers I used in my experiments and characterizing all my funny pulse shapes, Anoma McCoy and Chun Tian for having always a nice word for me, Symeon Asimakis for getting me involved in his 2R regeneration experiment using Bismuth fibre as well as providing me the photo of the Bismuth fibre reported in this thesis, Jerry Prawiharjo for showing me the potentiality of the FROG technique in PPLN waveguide devices and Nyuk Yoong Voo for explaining me how to glue gratings on stretching rigs without breaking them. I would also like to thank the new "telecom generation": Trina Ng and Lionel Provost.
My gratitude goes to Dr. Eleanor Tarbox for reading all my thesis, to Costa for helping me soft bounding and submitting my thesis and to all the ORC staff for helping me in many different ways during my stay at the ORC.

Finally a big thank to all my friends (from really all over the world!) that are not catalogued as group colleagues, but shared with me the daily ups and downs of a postgraduate student life. Your friendship and continuous support really helped me to make this possible. I decided not to list your names here, but to keep them tight in my heart. To all of you thank for making me feel at home in a foreign city.
Finally, I am eternally grateful to Paulo for his patience and for being supportive in the hardest times, to my parents, Elisa and Enzo, and the rest of my family, who have encouraged me to do my best through the years. You all filled my life with love, friendship and joy, when I needed more.

"If you would not be forgotten,
as soon as you are dead & rotten,
either write things worth reading,
or do things worth the writing."

-Benjamin Franklin-

To my grandfather, Alfio,
who is at last reunited
with the love of his life,
my grandmother.

Chapter 1

Introduction

The development of low loss [1], dispersion optimised transmission fibres [2] and the development of optical amplifiers, particularly the erbium doped fibre amplifier [3, 4], have revolutionized telecommunications, opening new opportunities for optical communication systems with ultra-high capacities and long-haul transmission distances. These achievements, in combination with the ever-growing demand for increased data capacity have forced the study of ever higher system capacities. This demand can potentially be met in a number of different ways, for example, by interleaving in time different channels all at the same wavelength (time domain multiplexing, TDM), or by using different channels transmitted along a single fibre at different wavelengths (wavelength division multiplexing, WDM).
Since their first introduction in the late 1980s, long-distance optical-fibre transmission systems have advanced from a transmission speed of 295.6 Mb/s in a single channel for the first transatlantic system, to greater than 1 Tb/s data capacity transmission in recent years using either single or multiple channels (see for example [5–8]).

As amplified transmission systems carry higher densities of data, interpulse interference due to both linear and nonlinear effects in the fibre start playing a more significant role, especially when transmission distances are long. These effects can degrade the quality of the signal and can result in errors in the detection of the data. The conventional way of restoring signal quality is to apply Optical-Electronic-Optical (O-E-O) conversion and to process the signal electrically. This, then, restricts the transmission rate per each channel to the processing speed of electronic circuits, and would definitely rule out any simultaneous processing of more than one channel. For these reasons and in order to fully exploit the inherent transmission capacity of the optical fibre within networks, the use of all-optical processing techniques is thus highly desirable.
Among the various optical regenerating devices, those based on optical fibres seem quite promising, especially after the achievement of significant advances in optical fibre technology in the recent years, most notably in the area of microstructured fibres. The main advantages of fibre based processing systems are that they are compatible with fibre

transmission systems and that their nonlinearity is characterized by a nearly instantaneous (fs) response time, making them very attractive for high speed signal processing (>160 Gb/s). The relatively weak nonlinearities of silica-based fibres typically requires high peak power levels and long fibre lengths (several hundreds of meters) for their manifestation. Recently, promising novel glasses with a higher nonlinearity than silica [9–11] have been developed, which have allowed the fabrication of fibres with a few orders of magnitude higher effective nonlinearity than standard single mode fibres, thereby enabling the implementation of meter-long nonlinear switches with improved performance in terms of stability and input power requirements. However, because of their relatively recent development compared to silica-based fibres, many issues remain to be addressed before such fibres can be seriously considered for use in real transmission systems.

In order to facilitate better control within optical switches and to improve the overall system functionality, it is possible to consider pre-conditioning the pulses (namely pulse shaping) within the various nonlinear optical switches. Indeed, the manipulation and control of the shape of short optical pulses constitutes an important field of research, motivated mainly by the recent developments in ultrafast optoelectronics. The capability of manipulating the temporal shape of an optical pulse relies on the ability to accurately control the precise amplitude and phase profile of its optical field. Such an operation is generally achieved by means of a pulse shaper that provides the desired spectral filtering operation (accurate control of its spectral content). The shaping and the manipulation of optical pulses is conventionally achieved using liquid crystal spatial light modulators [12, 13], or arrayed-waveguide gratings (AWGs) [14].
More recently, the use of fibre Bragg gratings (FBGs), as passive devices for optical pulse shaping, was demonstrated to be very promising due to their compactness, easy integrability and compatibility with fibre based devices (see for example [15, 16]).
Although a large variety of FBG-based devices have been fabricated and used for many applications in fibre optics communication systems, such as dispersion compensation in long-haul fibre networks and wavelength multiplexing in WDM systems, to name but two, the demonstration of their use for coherent pulse manipulation and control to obtain various shapes which would be very difficult to achieve otherwise, is relatively recent. This was possible due to the recent advances in the FBG writing technology, which have made it possible to fabricate complex grating structures (the so called superstructured fibre Bragg gratings, SSFBGs) with precise control of both the gratings amplitude and phase response profiles [17–20]).

The work described in this thesis focuses on the enhancement of various nonlinear fibre-based devices for all optical signal processing applications. For this purpose, I have looked at the possibility of integrating SSFBG pulse shapers into various all-optical signal processing devices for applications in high speed optical communication systems to improve the overall system performance. The work focuses on the demonstration of powerful techniques for the re-timing and reshaping of ultra-short pulses in proof-of-

principle experiments. According to the particular nonlinear switch configuration used, the optimal pulse shape is determined and the corresponding enhancement of the overall system, compared to conventional shapes, is demonstrated.
10 Gb/s single wavelength signals are usually considered in most of the demonstrations; however all of the schemes presented can be easily scaled to higher repetition rates, as well as to WDM systems in order to increase the overall transmission capacity.

The thesis is organized as follows. The initial Chapters present some theoretical background, along with some techniques to assess the quality of short pulses. Subsequent Chapters report the progress and achievements that I have made in the telecommunication systems laboratory of the Optoelectronics Research Centre towards the improvement of the overall system performance using SSFBGs together with fibre based nonlinear devices.

Outline

Chapter 2 contains the general background needed to understand the work developed in this thesis. The main signal distortions in short pulse systems operating at high bit-rate are discussed and the basic principle of Optical Regeneration is described. Two regenerator schemes are briefly analyzed. The first one is based on self-phase modulation (SPM) and subsequent offset filtering; the second one is based on cross-phase modulation (XPM) in a nonlinear optical loop mirror (NOLM). Because I supported most of the experiments by simulations using the Split Step Fourier (SSF) method, this method has also been explained. Finally an introduction to SSFBGs is given, with an emphasis on their design, which I carried out personally, and their fabrication, which was carried out by Dr Morten Ibsen.

One of the main points of the work reported herein is the reshaping of ultra-short optical pulses into different pulse shapes, such as rectangular pulses or parabolic pulses. The precise shape of these pulses is absolutely critical for the implementation of the system applications and for a complete understanding of the results obtained. Direct detection techniques using fast photodetectors are inadequate for such applications and optical correlation methods give very little information when the pulse under test has a quite complicated shape, such as the pulses used in this thesis. In Chapter 3, an optical sampling oscilloscope technique, with a temporal resolution of $\sim$2 ps, has been investigated to assess different pulse shapes obtained after reflection by SSFBGs. The accuracy of this technique was tested against a commercial Second Harmonic Generation Frequency-Resolved Optical Gating (SHG-FROG) device and an Electrical Absorber Modulator Frequency-Resolved Optical Gating (EAM-FROG) device, implemented in the laboratory by Dr M. Roelens and Dr B. Thomsen. A 20 ps rectangular pulse shape, obtained using an SSFBG, is chosen for comparison and a good agreement between the

three different techniques is shown.

The first example of all optical signal processing using preshaped pulses is presented in Chapter 4. The technique relies upon expanding the incident noisy data pulses into 20 ps rectangular pulses using a SSFBG at the input port of a nonlinear optical switch, which is a NOLM in the particular case described here. These broadened pulses are then used to switch a well-conditioned and well-defined local clock signal. The flat top of the rectangular pulses plays an important role in enhancing the timing jitter tolerance of the system. In particular, it ensures that the switch is transparent to the mistiming of the original signal that otherwise would manifest itself as a severe amplitude noise at the output of the switch. The clock signal, which was chosen properly so that its pulse width is comparable to that of the noisy signal and the walk-off between them inside the NOLM is negligible, ensures that the noisy signal is retimed, whilst retaining its original pulse width and maintaining its original wavelength. The amount of timing jitter that can be compensated for is determined by the width of the reshaped pulse, which can be readily adjusted to fit the specific jitter characteristic of a given transmission system, and cannot exceed the repetition rate of the incoming data signal. A reduction in the standard deviation of the pulse timing jitter, by more than a factor of 4, has been demonstrated using this technique.

In a second configuration shaping was applied to the control (rather than the signal) pulses of the nonlinear switch. In this way the regenerative properties of the NOLM could be properly exploited, as described in Chapter 5. The S-shaped switching characteristic of the NOLM and the square switching window provide the pulse amplitude- and timing-noise reduction respectively. A reduction in the standard deviation of the pulse timing jitter, by a factor of 3, has been demonstrated using linear pulse reshaping and all-optical switching. A Q-factor improvement from 5.9 to 8 was measured in the worst condition of $\sim$11 ps induced timing jitter. An improvement in the receiver sensitivity of more than 2.3 dB was achieved after the switch in the case of $\sim$5.5 ps induced timing jitter, demonstrating the amplitude noise reduction performed in the NOLM.

Chapter 6 demonstrates a different technique for correct retiming of short optical pulses. The principle behind this scheme relies on converting temporal jitter into wavelength (frequency) jitter and then using an appropriate level of dispersion to provide temporal compensation. This frequency-shift of the mistimed pulses is provided by XPM in a highly nonlinear fibre (HNLF) using an intense control pulse at a well defined clock rate. Because the induced frequency chirp is proportional to the derivative of the control pulse shape, to ensure a one-to-one linear mapping of timing to frequency jitter, the control pulse should have a parabolic intensity profile. In this demonstration, the control pulses are shaped via the SSFBG into $\sim$10 ps parabolic pulses. The profile of these pulses ensures that the chirp on the switched pulses is linear over a wide range (almost the whole of the 10 ps full width at half maximum (FWHM) of the pulse), so that it can be removed by linear propagation in a subsequent fibre that provides dispersion of general

opposing chirp. A wavelength shift of up to ∼0.5 nm is numerically and experimentally demonstrated, while a retiming window of ±5 ps is demonstrated. The cancellation of up to 4 ps rms timing jitter is demonstrated in a system experiment.

The same parabolic pulse source is used to demonstrate the merits of parabolic pulses for other ultrafast all-optical processing applications in Chapter 7. Indeed, these parabolic pulses are exploited to generate ultra-flat SPM broadened spectra in a normal dispersion HNLF. This pulse shape has been numerically and experimentally demonstrated to provide better performance in terms of the extent of SPM-based spectral broadening and flatness relative to the use of conventional secant hyperbolic (sech) pulses. Indeed, it is shown that most of the pulse energy remains within the 3 dB spectral bandwidth, ensuring minimum overall loss for spectral slicing applications and thereby maximum spectral density. The flat spectrum and the optimized spectral density are attractive for spectrally sliced source applications. 38 sliced channels have been demonstrated and their characterizations confirm the good noise performance of the system.
Pulses of such a broad bandwidth are potentially useful for pulse compression as well. A compression factor of more than 30 relative to the initial parabolic pulse is demonstrated, highlighting the quality of the linear chirp generated in the HNLF.

All the aforementioned experiments have used silica based HNLFs. Although these fibres are very well optimized in terms of low loss and dispersion, the relatively low nonlinearity of silica requires long corresponding fibre lengths. The implementation of more compact nonlinear devices represents a very challenging and promising topic. Bismuth-Oxide glasses exhibit effective nonlinearities per unit length which are some orders of magnitude higher than standard single mode fibres, allowing for a drastic reduction in the length requirements of fibre-based nonlinear devices and enabling the implementation of meter-long nonlinear switches with improved performance in terms of stability and input power requirements.
Chapter 8 reports the use of a 2-m-long Bismuth Oxide fibre with an ultra-high nonlinearity of ∼1100 $W^{-1}km^{-1}$ in a simple 2R regeneration experiment based on self phase modulation and offset filtering at repetition rates of 10 Gbit/s and 40 Gbit/s. The fibre was properly spliced to SMF with losses of ∼3 dB per splice. Numerical simulations and experimental results confirm the suitability of this kind of fibre for 2R regeneration. The regenerator benefits from the strong normal dispersion of the Bismuth nonlinear fibre (Bi-NLF) in addition to its high nonlinearity. The performance of the regenerator was tested with heavily degraded input signals and evaluated using both eye diagram and Bit Error Rate (BER) measurements. The regenerated pulses were characterized using SHG-FROG. Even in such a short piece of fibre, and at power levels which are readily achieved using commercial amplifiers, an improvement in the receiver sensitivity of ∼5.0 dB at 10 Gb/s and >2 dB at 40 Gb/s was achieved.

The thesis concludes with Chapter 9, where I summarise the results and discuss the directions for future work.

Chapter 2

Background

2.1 Introduction

The scope of this Chapter is to provide sufficient background information for the understanding of the subsequent Chapters.
A brief introduction to the main origin of system distortions and to the basic principle of Optical Regeneration in short pulse, high bit-rate communication systems is described. All the experiments proposed in this thesis are applications of nonlinear phenomena in optical fibres and exploit the ability of shaping sech pulses into pulses with different kinds of temporal profile using SSFBGs. For these reasons, a brief overview of the nonlinear applications, developed here, is provided and a basic equation, the so-called nonlinear Schrödinger (NLS) equation, which describes the propagation of a generic pulse in an optical fibre, is introduced. Because most of the experiments are followed by numerical results, the standard split-step Fourier method, used for solving the NLS equation, is explained.
Finally, the linear relation that exists between the spatial modulation of the refractive index in a fibre Bragg grating and its temporal response is described. Indeed, the considerable progress in FBG fabrication techniques allows the possibility of using such structures for novel pulse shaping applications, which, in principle, can be of "any" desired form. The limits of their design are discussed and a brief description on the SSFBG writing technique used to fabricate the gratings I employed within my research, is presented for completeness.

2.2 Signal Distortions in Communication Systems

This section briefly investigates the propagation distortions of return to zero (RZ) pulse shapes. There are actually many different sources responsible for pulse degradations.

A distinction can be made between distortions causing energy fluctuations (amplitude jitter) and pulse position fluctuations (timing jitter). Because these degradations can become a particular problem within long haul, high bit-rate transmission [21, 22], it is important to understand the limits that they impose on the system.
First of all, attenuation of the signal, as it propagates along the fibre, is the first limitation in the transmission distance. The invention and deployment of in-line Erbium Doped Fibre Amplifiers (EDFAs) has largely simplified loss compensation of transmission systems, even though this amplification is always accompanied by the generation of amplified spontaneous emission (ASE) noise, which might give rise to other distortions as discussed below.
Furthermore, in an optical transmission system, the pulses, which represent the bits of information, can spread out, due to the chromatic dispersion of the fibre, which may lead to overlapping of adjacent pulses (Intersymbol Interference (ISI)). Indeed, when an electromagnetic wave propagates in a generic dielectric medium, its propagation velocity depends on its optical frequency ω, so that different spectral components associated with the pulse travel at different speeds.
If the dispersion is only of the first order (i.e. dispersion changes linearly with ω), though, the degradation can be compensated for using, for example, a dispersion compensating fibre (DCF) with a length and dispersion design such that the dispersion of the transmission fibre is negligible.
Long-haul transmission links experience performance degradations due to ASE-noise from optical amplifiers along the line. Indeed, in transoceanic systems, over 100 amplifiers are cascaded, which add noise onto the signal stream. This ASE noise induces energy fluctuations on the pulse leading to amplitude noise. When soliton systems are concerned, the ASE noise induces as well fluctuations of the relative carrier frequency position ($\delta\omega$) of the propagated pulses, known as the Gordon-Haus effect [23]. This leads, in the presence of dispersion in the transmission line, to arbitrary changes in the group velocity of the propagating pulses which in turn translates to random timing jitter ($< \delta t >$) of the pulses ($< \delta t > \propto \beta_2 \delta\omega L$, where β_2 is the group-velocity dispersion parameter and L is the length of the transmission line).
Nonlinear pulse-to-pulse interaction is another limiting factor in high-bit-rate transmission systems [24, 25]. Nonlinearities due to the Kerr effect denote the phenomenon that the refractive index of an optical fibre, as within any material, varies not only according to the frequency, but also to the electric field intensity of the optical signal passing through the fibre as well. So these kinds of effects, among neighbouring bits, can also distort and jitter signals when the dispersion of the transmission system causes significant intersymbol interference. Then the combined effects of ISI and pulse chirp lead to timing fluctuations due to Intrachannel Cross Phase Modulation (IXPM) [26] and result in significant amplitude fluctuations as well as the creation of "ghost" pulses at the centre of the zeros due to Intrachannel Four Wave Mixing (IFWM) [26, 27].
Polarization Mode Dispersion (PMD) is becoming another leading source of signal degra-

dation as systems move to higher bit rates (>40 Gb/s). In fact, the small, randomly varying birefringence of standard telecommunication fibres tends to depolarize optical signals and randomize their phase. This phase variation broadens an input optical pulse as it propagates through the fibre, leading to severe ISI due to the spreading of part of the pulse energy beyond the allocated bit slot [28] ($< \delta t_{PMD} > \propto D_p\sqrt{L}$, where D_p is the PMD parameter and depends on the particular distribution of the randomly varying birefringence along the transmission line). New fibres have improved the PMD parameter down to 0.02 ps $km^{-1/2}$ [2].
Another nonlinear effect is Stimulated Raman Scattering (SRS), which is an interaction between the propagating signal and the vibrations of the molecules in the fibre [29]. This causes the frequency of the light to be downshifted and results in the transfer of power from one optical field to another, attenuating in this way the initial signal. Stimulated Brillouin Scattering (SBS), which is an interaction between the signal and the sound waves in the fibre [29], is another nonlinear effect that can lead to distortion and excess attenuation of the optical signal. This effect causes frequency conversion too and backward scattering of the signal beam.
A different kind of contribution to the interactions between different short pulses in optical fibres is the acoustic effect due to the electrostrictive mechanism, when long propagation distances are considered [30]. In the presence of this effect the non-linear refractive index of the fibre is the sum of the Kerr effect, with a response time of the order of femtoseconds, and of the electrostrictive effect, with a response time of nanoseconds. The second effect, in fact, can explain the pulse interaction at large temporal intervals at propagation over great distances.
When more than one channel is launched in the transmission line, i.e. in a WDM system, all these distortion effects still hold for all the different channels (see for example [31]). Moreover, pulses at different wavelengths will propagate at different velocities and collide with each other causing severe interchannel interference, crosstalk and distortion due to the same optical nonlinearities.
All of these effects can contribute to the deterioration of the performances of the system, leading to errors. Preserving a high contrast between '1' and '0' powers and keeping amplitude and time fluctuations at low levels are mandatory to achieve high transmission quality, as measured through BER or Q-factors, which will be introduced in Chapter 4.

2.3 Basic principles of an optical Regenerator in optical communication systems

The accumulation of impairments in the optical signals in all-optical high capacity networks, due to both long-haul transmission with in-line EDFAs and signal processing at network nodes creates the need for signal quality restoration procedures, as discussed in the previous paragraph. Regeneration is therefore essential to reduce timing and am-

plitude jitter, which in many instances effectively limits the transmission distance of a system and severely compromises the performance of optical switches and demultiplexers.

Two approaches can be considered for regeneration. The first, known as Optical-Electronic-Optical regeneration, relies on segmenting the system into independent trunks and uses Optical-Electronic (O-E) conversion by means of a photodiode followed by Electronic-Optical (E-O) conversion through a laser and modulator in order to return the signal back into the optical domain. Nowadays, the operating frequencies of individual transistors have reached the terahertz regime [32] and photodiodes have been greatly improved, through the use of sophisticated structures, to provide both a large bandwidth (up to 160 Gbit/s operation) and high output powers [33]. Thanks to the performance of such components, the full range of functional electronic devices required for high speed optoelectronic application is drastically improving. Fully electronic circuitry for all critical 40 Gb/s processing functions is already commercially available [34]. Transmission systems based on Electrical Time Division Multiplexing (ETDM) operating above 80 Gb/s have also recently been reported [35, 36]. In 2006, an integrated 100 Gb/s ETDM receiver was employed in a transmission experiment over 480 km Dispersion Managed Fibre (DMF) [37]. However, the enormous traffic growth that has been observed over the last few years leads to a drastic increase in the demand for broadband networks and higher transmission rates.

The second approach is to implement in-line all-optical signal regeneration. It performs the same signal-restoring functions as the O-E-O solution and offers ultra-high speed operation much beyond 100s of GHz without any restrictions imposed by the bandwidth of the electrical components.

In this thesis, different all-optical signal processing devices have been proposed as promising schemes for signal regeneration, exploiting the recent advances in optical fibre technology, most notably in the area of nonlinear fibres and superstructured fibre Bragg gratings for the manipulation and shaping of ultrashort pulses. The results described in this thesis demonstrate the potential new opportunities of the combination of these two technologies within future high speed communication systems.

In general, a complete regeneration system involves three basic signal-processing functions, namely re-ampli-fication, re-shaping and re-timing, hence the generic acronym '3R' [21] (see Fig. 2.1). Many of the techniques described in this thesis apply to 3R regeneration, whereas others perform re-shaping and re-amplification only (usually termed as 2R). The basic block diagram of the full 3R system is shown in Figure 2.2. In these regenerators, a Clock Recovery (CR) module has to be incorporated to facilitate the retiming function. Part of the signal is extracted in order to recover a clock signal synchronized to the input data, while the remnant is fed into the decision block, for re-shaping and re-timing. The clock signal drives the optical pulse source to generate a high-quality optical pulse stream at the frequency of the incident data. This stream is used as a decision control in the decision gate to assess if the incoming bits represent $0s$

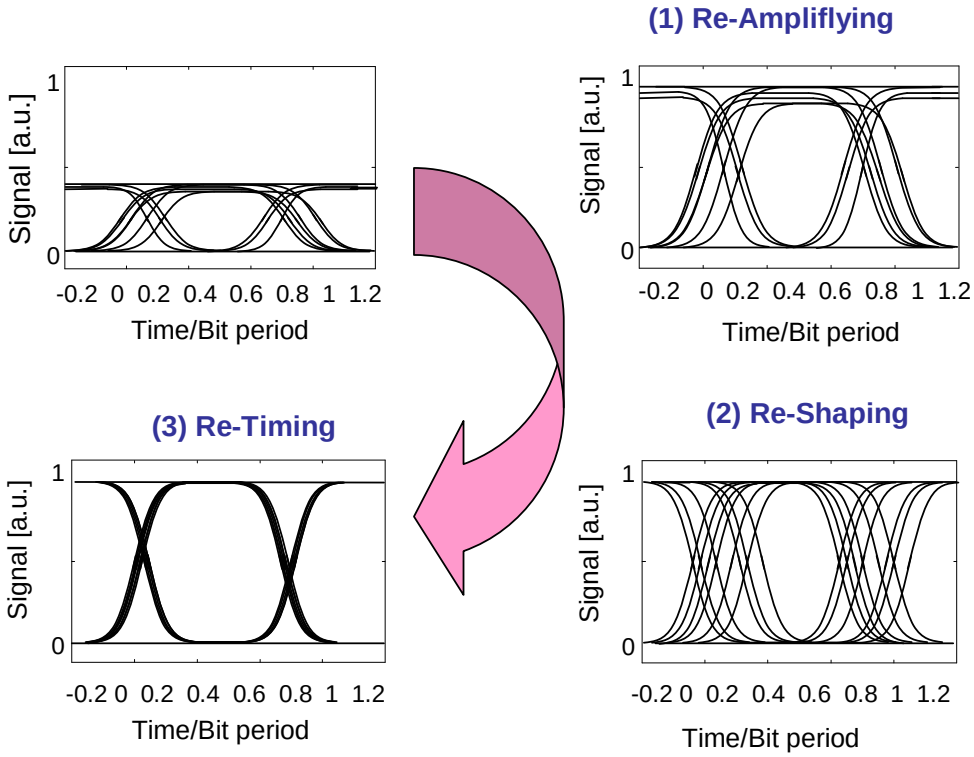

FIGURE 2.1: Principle of 3R regeneration, as applied to NRZ signals: (1) Re-amplifying, (2) Re-shaping and (3) Re-timing (taken from [21]).

or $1s$.

Many different approaches for clock recovery have been reported in the literature. Employing a phase-locked loop (PLL) is the typical technique used (see for example [38]). Furthermore, the development of ultrafast optical phase comparators based on, for example, Four Wave Mixing (FWM) [39] or XPM [40] in semiconductor optical amplifiers (SOAs) or based on bidirectionally operated electro-absorption modulators (EAMs) at 160 Gb/s [41, 42] and 320 Gb/s [43] have also been reported.

It should be noted that the development of CR techniques was beyond the scope of this project. Also, to simplify the experiments, which have been carried out in the course of this work, clock recovery has not been incorporated into the system, as would normally be required to synchronize the clock and data pulses in any real-world implementation of a synchronous 3R regenerator. Note that in my experiment, to ensure synchronization between the various signals, a common clock was used to drive the corresponding sources.

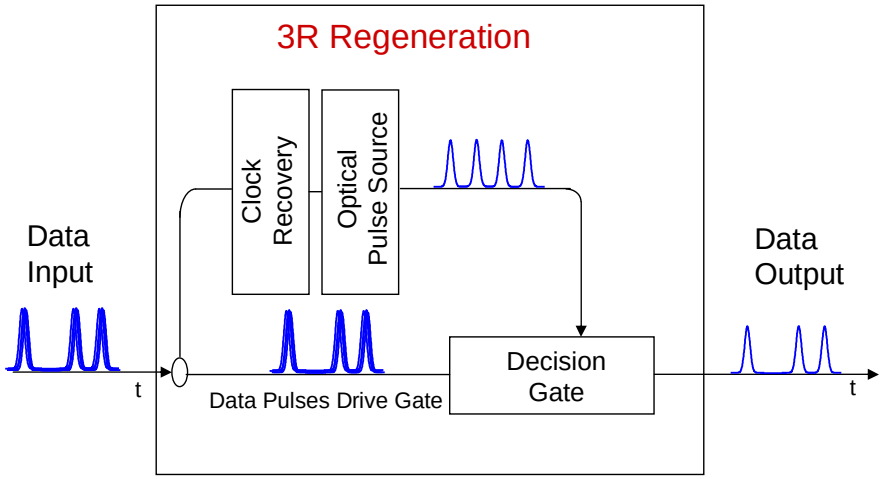

FIGURE 2.2: Generic layout of a typical 3R regenerator (adapted from [21]).

2.4 Applications of nonlinear phenomena for all optical Regeneration

All linear and nonlinear effects can be both harmful and beneficial depending on the circumstances applications. For example, on one hand, optical fibres for transmission cables need to have low nonlinearity to suppress waveform distortion, as already discussed, while, on the other hand, the optical fibres for signal processing are required to have high nonlinearity to realize effective nonlinear functionalities. SPM, XPM or FWM effects can limit the performance of a generic WDM system, but, at the same time, they can be used for applications such as 2R-regeneration in Mamyshev-type schemes, 3R-regeneration in NOLMs and so on.
The same is true of chromatic dispersion, which, according to the application to be developed, can be seen as an impairment or not.
In this Section, two different fibre based optical regenerator schemes are presented, the first one based on SPM, the second on XPM, both in HNLFs.

2.4.1 Self-Phase Modulation and offset filtering

Among the various fibre based optical regenerator schemes, the scheme relying on spectral broadening in HNLF and subsequent offset-filtering is considered particularly advantageous, since it combines a very good noise reduction performance with stability and robustness [44]. This scheme is commonly referred to as a Mamyshev regenerator. A general schematic of this approach is shown in Fig 2.3.a. Pulses at a central wavelength λ_c are amplified by a high power EDFA (HP-EDFA) and launched into a HNLF. The spectrum of the pulses is broadened after propagation through the fibre due to SPM. Indeed, a generic signal, E(t), induces, as it propagates along a fibre of length L,

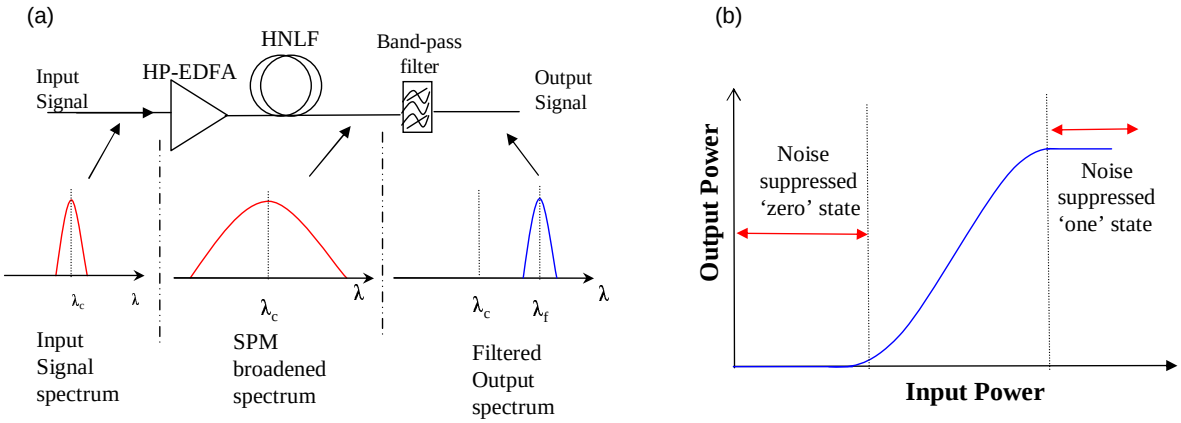

FIGURE 2.3: SPM-based 2R-Regenerator basic scheme.

intensity dependent modulation on the refractive index, and hence modulation on the optical phase:

$$\Delta\phi_{SPM} = \frac{2\pi n_2 |E(t)|^2 L_{eff}}{\lambda}, \tag{2.1}$$

where n_2 is the nonlinear coefficient and L_{eff} is the effective length, which is defined as:

$$L_{eff} = \frac{[1 - exp(-\alpha L)]}{\alpha}, \tag{2.2}$$

where α accounts for the fibre losses.

The SPM-induced spectral broadening is a consequence of the time dependence of $\Delta\phi_{SPM}$. Indeed, a temporal change in the phase implies that the instantaneous optical frequency varies across the pulse from its central value (frequency chirping), so that new frequency components are generated.

Noise suppression is favoured if the SPM-broadened pulse spectrum has a flat-top, which dictates the use of HNLF with normal dispersion [45]. The operation of the regenerator is based on the use of a narrow band optical filter with a central wavelength detuned relative to the central wavelength of the signal as a decision gate. Pulses with sufficient peak power levels (ones) generate substantial spectral broadening due to SPM and can pass through the filter. On the other hand, noisy zero signals (spaces) are unable to produce significant spectral broadening and therefore these are largely rejected by the filter. In general, the filter bandwidth is determined by the requirement that the width of the pulses coming out of the regenerator should have the same width as the initial signal pulses. By proper selection of the filter offset, the launched power, the fibre length and its dispersion characteristics, the 2R regenerator can exhibit a nonlinear transfer function as shown in Fig 2.3.b.

In Chapter 8, this scheme, using just 2 m of Bi-NLF, is implemented to demonstrate an improvement of the receiver sensitivity of more than 5 dB at a repetition rate of 10 Gb/s and 2 dB at a repetition rate of 40 Gb/s.

Finally, a comment related to the energy efficiency (i.e. output versus input energy ratio

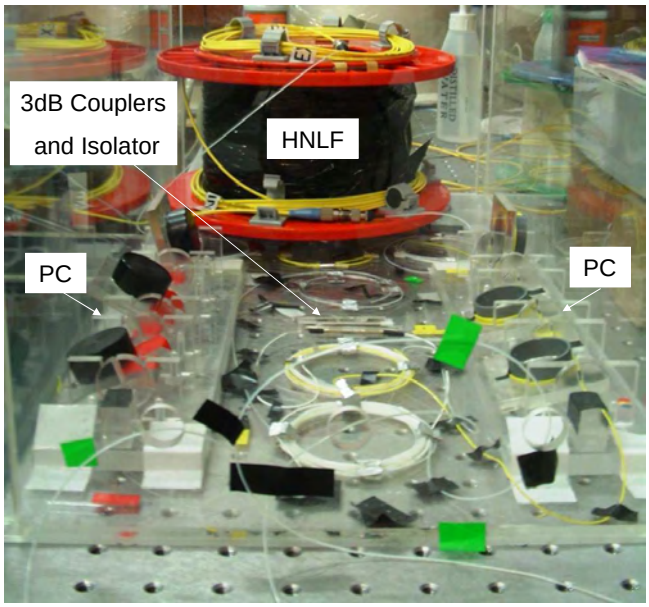

FIGURE 2.4: Photograph of the NOLM device, widely used in this thesis. PC: Polarization Controller.

of the "ones") of this Mamyshev-type regenerators is required. By its nature, the scheme is known to exhibit poor efficiency. More quantitative values of its loss will be given in Chapter 8. Qualitatively, the higher the filter offset, the broader the signal spectrum has to be, and the lower this efficiency becomes.

2.4.2 Nonlinear Optical loop mirrors

A nonlinear optical loop mirror is an attractive interferometric scheme for ultra-fast switches (Fig. 2.5). For this fibre-based device, the phase shift is induced through the Kerr effect in an optical fibre. Two different configurations of NOLMs are possible; in the first one, an external syncronized clock signal, co-propagating with the signal to be regenerated in one of the two arms of the loop, induces a phase shift on the propagating signal through XPM (I will be calling this type an active NOLM in the rest of this thesis). In the second configuration, the loop is unbalanced by amplifying or attenuating only one of the two signals propagating along the NOLM, so that SPM in the HNLF occurs only for the signal component with more peak power (I will be calling this type a passive NOLM in the rest of this thesis). A complete discussion of both configurations is provided below.

An active NOLM consists of a fibre coupler with two output ports joined through a length of nonlinear fibre thereby forming a loop. Fig. 2.4 shows the NOLM device, which I have built for all the experiments involving NOLMs, while Fig. 2.5 shows the corresponding schematic. The input signal ($E_{s1}(\lambda_1)$) enters onto port 1 of the coupler and is split into two counter-propagating pulses ($E_3(\lambda_1)$ and $E_4(\lambda_1)$) which, under linear propagation, acquire identical linear phase shifts (θ) as they traverse the loop. The optical path

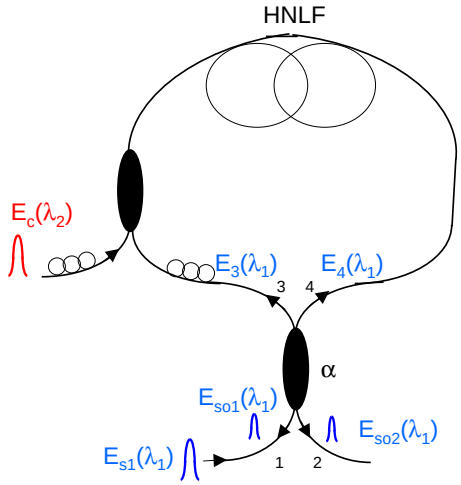

FIGURE 2.5: Sketch of a generic active NOLM.

length is precisely the same for both pulses, since they propagate along the same path but in opposite directions. These pulses then interfere constructively at the coupler and exit back through the input port (port 1). So, in the linear regime, the device works as a mirror. The loop can be unbalanced by introducing a control pulse ($E_c(\lambda_2)$) that co-propagates with one of the two signals, nonlinearly shifting its phase (providing the signals under test have the same polarization state):

$$\Delta\phi_{NL} = 2\frac{2\pi n_2 |E_c(\lambda_2)|^2 L_{eff}}{\lambda}. \tag{2.3}$$

This time, when the two signal pulses interfere at the coupler, some portion of the input signal will appear at port 4 of the coupler (transmission port of the NOLM) [46].
The equations relating the input and output signals of the coupler are:

$$E_3 = \alpha^{\frac{1}{2}} E_{s1} + i(1-\alpha)^{\frac{1}{2}} E_{s2}, \tag{2.4}$$
$$E_4 = i(1-\alpha)^{\frac{1}{2}} E_{s1} + \alpha^{\frac{1}{2}} E_{s2}, \tag{2.5}$$

where α is the power-coupling ratio and, since a single input signal is considered coming from only port 1, $E_{s2} = 0$. After the two signals propagate along the loop, they will acquire a phase shift given by:

$$E_3 = \alpha^{\frac{1}{2}} E_{s1} exp[i(\Delta\phi_{NL} + \theta)], \tag{2.6}$$
$$E_4 = i(1-\alpha)^{\frac{1}{2}} E_{s1} exp(i\theta). \tag{2.7}$$

Note that the phase dependence of the counter-propagating signal E_4 on the mean power of the control signal has been neglected for simplicity. This approximation is valid if the average power is much smaller than the peak power. In the experiments described here, the control pulses are usually in the range of ∼2-20 ps all at the repetition rate

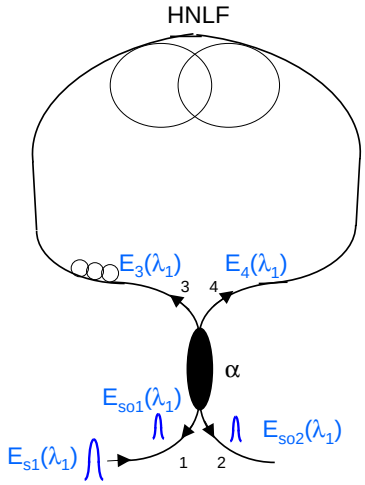

FIGURE 2.6: Sketch of a generic passive NOLM.

of 10 Gb/s, so that this simplification holds. To calculate the outputs, E_{so1} and E_{so2}, Eqs. 2.4 and 2.5 are used, where E_{s1} and E_{s2} are now replaced by E_3 and E_4, respectively, to obtain the following expression for the output at port 1 (reflected signal) and at port 2 (transmitted signal):

$$E_{so1} = i\frac{E_{s1}}{2}exp(i\theta)[exp(i\Delta\phi_{NL}) + 1], \tag{2.8}$$

$$E_{so2} = \frac{E_{s1}}{2}exp(i\theta)[exp(i\Delta\phi_{NL}) - 1], \tag{2.9}$$

when a 50-50 coupler is considered, i. e. α=0.5.
These Equations can be rewritten in terms of output powers:

$$P_{so1} = \frac{P_{s1}}{2}[1 + cos(\Delta\phi_{NL})], \tag{2.10}$$

$$P_{so2} = \frac{P_{s1}}{2}[1 - cos(\Delta\phi_{NL})], \tag{2.11}$$

where $P_{si} = |E_{si}|^2$ with i = o1, o2, 1.
In turn, the phase modulation is converted into a variation of the signal intensity at the output, making it possible to switch the signal via the control. Eq. 2.3 shows that by injecting the appropriate control pulse intensity into the loop, a nonlinear phase shift of π is possible to achieve so that the transmitted signal switches to the maximum ($P_{so2} = P_{s1}$), while the reflected signal switches to the minimum ($P_{so1} = 0$).

Similar equations can be derived in the case of a passive NOLM, in which only one optical signal is considered, as discussed above, see Fig. 2.6. In this case, the effect of propagation will no longer be identical along the two arms of the loop if $\alpha \neq \frac{1}{2}$. The corresponding nonlinear phase shifts acquired by the two propagating signals are

proportional to their intensities (SPM effect) along the HNLF and are given by:

$$\Delta\phi_{NL1} = \frac{2\pi n_2 \alpha |E_{s1}(\lambda_1)|^2 L_{eff}}{\lambda} = \alpha\Delta\phi, \tag{2.12}$$

$$\Delta\phi_{NL2} = \frac{2\pi n_2 (1-\alpha) |E_{s1}(\lambda_1)|^2 L_{eff}}{\lambda} = (1-\alpha)\Delta\phi, \tag{2.13}$$

where $\Delta\phi$ is defined as:

$$\Delta\phi = \frac{2\pi n_2 |E_{s1}(\lambda_1)|^2 L_{eff}}{\lambda}. \tag{2.14}$$

The final expressions of the two outputs can be calculated in terms of power as follows:

$$P_{so1} = P_{s1}[2\alpha(1-\alpha)[1+cos((1-2\alpha)\Delta\phi)], \tag{2.15}$$

$$P_{so2} = P_{s1}[1-2\alpha(1-\alpha)[1+cos((1-2\alpha)\Delta\phi)]. \tag{2.16}$$

As can be seen, if $\alpha = \frac{1}{2}$, the signal goes all through port 1 ($P_{so1} = P_{s1}$ and $P_{so2} = 0$) and the loop operates as a mirror. If $\alpha \neq \frac{1}{2}$, these equations show that maximum power emerges from port 2 (maximum transmission) whenever the argument of the cosine function is an odd multiple of π, i.e.:

$$\Delta\phi = m\frac{\pi}{1-2\alpha}. \tag{2.17}$$

for m odd.
For example, in the passive NOLM implemented in this project, a 70:30 coupler was chosen [47].

The key advantage of these kinds of device lies in the near instantaneous (fs) response of the Kerr nonlinearity, making it very attractive for ultra-high bit-rate operation ($\geq$ 160 $Gbit/s$). Furthermore, a NOLM can act as a 3R regenerator [48]: accumulation of background noise, amplitude fluctuations and jitter can be cancelled through switching of a "clean" optical clock by the noisy signal.
On the negative side of realizing optical switching using optical fibres, major limitations come from environmental instability, a strong polarization dependence and reduced integrability, arising from the requirement of relatively long (km) fibre lengths. However, polarization maintaining (PM) fibres towards the implementation of polarization-insensitive NOLMs and HNLF towards the implementation of very compact nonlinear fibres are currently hot topics in fibre technology research.
Furthermore,in two wavelength NOLMs, as signal pulses become shorter at higher repetition rates, the walk-off [29] between the data pulse and the clock pulse due to the group-velocity dispersion limits the achievable nonlinear phase-shift. Indeed, the interaction between two optical pulses of wavelengths λ_1 and λ_2 respectively ceases to occur when the faster moving pulse completely walks through the slower moving pulse. Then, the pulses, which were overlapping at the beginning of the fibre, will be separated after

some distance, so that the efficiency of the switch is lower. This feature is governed by the walk-off parameter d_{12} defined as:

$$d_{12} = v_g^{-1}(\lambda_1) - v_g^{-1}(\lambda_2), \tag{2.18}$$

where $v_g(\lambda_i)$ is the group velocity at the wavelength λ_i. The walk-off time is thus defined as the product of the walk-off parameter and the length of the fibre, L, where the two signals propagate. This walk-off time can be easily rewritten as a function of the zero-dispersion wavelength of the fibre, λ_0, and the dispersion slope of the fibre, S, when this can be assumed to be constant, as follows:

$$\tau_{12} = SL\frac{\Delta\lambda^2}{2} + SL(\lambda_2 - \lambda_0)\Delta\lambda, \tag{2.19}$$

where $\Delta\lambda = \lambda_1 - \lambda_2$.

From Eq. 2.19, it is clear that if the walk-off effect needs to be suppressed, one could either choose an appropriate fibre with low dispersion slope or operate the two signals symmetrically about λ_0. Current state of the art HNLFs enable very low dispersion slopes. In [2] Takahashi et al. reported the characteristics of some newly manufactured HNLFs. It is shown that HNLFs with a dispersion @ 1550 nm as low as 0.005 $ps\ nm^{-1}km^{-1}$ can be achieved with a dispersion slope of 0.0013 $ps\ nm^{-2}km^{-1}$ (maintaining a nonlinear coefficient value as high as 20.5 $W^{-1}km^{-1}$). The dispersion slope of typical standard single mode fibres is $\sim$0.08 $ps\ nm^{-2}km^{-1}$.

In the experiments developed in this thesis, the HNLF widely used has a dispersion slope of 0.03 $ps\ nm^{-2}km^{-1}$ (see Tab. 3.1), which for the signal and control wavelengths always considered produces a negligible walk-off.

A comment related to the energy efficiency of the NOLM regenerator scheme is required. Similar to the Mamyshev-type scheme, it is known to exhibit poor efficiency. While a quantitative discussion of the loss will be given later on in the Chapter where the scheme will be discussed, a qualitative discussion is presented here.

Firstly, the power associated with the control signal, required to achieve a π-phase shift in the NOLM, is rejected since it is subsequently filtered out at the output port of the NOLM. Secondly, the particular NOLM, which I built and then used in all my experiments (Fig. 2.4), gives additional losses due to the 3 dB couplers that were used in the loop. Referring to Fig. 2.5, apart from the 3 dB coupler used to split the signal into two identical counter-propagating replicas which does not result in losses for an appropriate nonlinear phase shift, I included a second one to couple the signal and the control together. Furthermore, a third 3 dB coupler was included inside the loop, symmetrically about the HNLF, to ensure a perfect mirror, so that the on/off extinction ratio of the NOLM would be maximized, when the control signal was off.

2.5 Generalized nonlinear Schrödinger equation

The propagation of a generic optical field can be described by starting from the evolution of its electric and magnetic fields in a fibre (Maxwell's equations). Without attempting to describe any of its derivation, which has been widely studied and documented in several books over the years (see, for example [29]), I present the main elements of the analysis and notation used below, as this will be used in the following Sections.
Assuming that the fundamental mode of the electric field is linearly polarized in the x or y direction, while z is the propagation direction, the electric field E′(x,y,z,t) can be written as:

$$E'(x,y,z,t) = \frac{1}{2}\{E(x,y,z,t)exp[i(\beta_0 z - \omega_0 t)] + c.c.\} \tag{2.20}$$

where E(x,y,z,t) is the envelope of the waveform, which is a slowly varying function of time t, β_0 is the propagation constant and ω_0 is the carrier frequency. This approximation will always be valid for the pulses used in this work, which have an envelope duration definitely higher than the period of a cycle ($2\pi/\omega_0$) of their carrier (ω_0). For instance, considering a carrier of 1550 nm, which corresponds to a carrier frequency of 193 THz, a pulse of 1 ps is composed of more than 200 cycles.
For a single mode fibre, using the method of separation of variables, it is possible to separate the longitudinal and temporal evolution of the electric field, A(z,t), from the transverse evolution, F(x,y):

$$E(x,y,z,t) = F(x,y)A(z,t). \tag{2.21}$$

F(x,y) corresponds to the modal distribution of the fundamental fibre mode, often approximated by a Gaussian distribution, while A(z,t) is the slowly varying pulse envelope, which, under the influence of both linear and non-linear effects, is described by the nonlinear Schrödinger equation, which can be expressed as follows (see [29] for the steps that lead from Maxwell's equations to the NLS equation):

$$\frac{\partial A}{\partial z} + \frac{\alpha}{2}A + i\frac{\beta_2}{2}\frac{\partial^2 A}{\partial t^2} - \frac{\beta_3}{6}\frac{\partial^3 A}{\partial t^3} = i\gamma|A|^2 A, \tag{2.22}$$

Eq. 2.22, as shown here, includes the effects of loss (α), second- and third- order dispersion (β_2 and β_3) and Kerr nonlinearities (γ), which are the most relevant contributions in the work described here. It is useful to relate β_2 to the dispersion parameter D, which is commonly used in fibre optics literature, as follows:

$$D = -\frac{2\pi c}{\lambda^2}\beta_2. \tag{2.23}$$

The NLS equation can be analytically solved only in some particular cases, so a numerical approach is therefore often necessary. A robust method that has been used extensively to solve this pulse propagation problem is the SSF method, which is presented in the

following Section and which makes it possible to precisely know the evolution of a generic signal. This numerical tool is very important for the best comprehension of the physical phenomena affecting a pulse during its propagation.

2.5.1 Split Step Fourier Method

In the general case, the NLS equation is not a solvable differential equation. It is thus essential to turn to a numerical approach. The SSF method is the most common one [29]. The results presented in this thesis will all be calculated using this method. Its principle consists in solving the propagation of the pulse over an extremely small distance h, for which the linear and nonlinear effects can be considered to be independent of each other. It is useful to rewrite Eq. 2.22 in the form:

$$\frac{\partial A}{\partial z} = (\widehat{D} + \widehat{N})A, \tag{2.24}$$

where $\widehat{D}$ is the differential operator, which describes the dispersion and the attenuation in a linear medium and $\widehat{N}$ is the nonlinear operator, which describes the nonlinear effects in the fibre. These operators are given by:

$$\widehat{D} = -\frac{\alpha}{2} - i\frac{\beta_2}{2}\frac{\partial^2}{\partial t^2} + \frac{\beta_3}{6}\frac{\partial^3}{\partial t^3}, \tag{2.25}$$

$$\widehat{N} = i\gamma|A|^2. \tag{2.26}$$

In Eq. 2.26 nonlinear effects, such as Self-Steepening and Raman scattering, are not included, since they are considered negligible in the work developed here.
The formally exact solution of Eq. 2.24 is given by:

$$A(z+h,t) = exp[h(\widehat{D} + \widehat{N})]A(z,t). \tag{2.27}$$

An approximate solution of Eq. 2.27 can be obtained by assuming that the linear and nonlinear effects can be considered independent over the distance h, so that Eq. 2.27 can be rewritten as:

$$A(z+h,t) \approx exp(h\widehat{D})exp(h\widehat{N})A(z,t). \tag{2.28}$$

In this way the propagation along h is carried out in two steps. In the first step, only the nonlinear operator $\widehat{N}$ acts ($\widehat{D} = 0$) in Eq 2.28. The problem can then be easily solved in the time domain after an interval h:

$$B(z,t) \approx exp(h\widehat{N})A(z,t). \tag{2.29}$$

In the second step, only the linear operator $\widehat{D}$ acts ($\widehat{N} = 0$) in Eq 2.28. The problem can then be solved in the spectral domain:

$$\widetilde{B}(z+h,\omega) \approx exp(h\widetilde{\widehat{D}}(i\omega))\widetilde{B}(z,\omega), \tag{2.30}$$

where $\widetilde{B}(z,\omega)$ is the Fourier transform of B(z,t) and $\widetilde{\widehat{D}}(i\omega)$ is the Fourier transform of the linear operator, $\widehat{D}$. In particular, $\widetilde{\widehat{D}}$ is obtained by replacing the differential operator ∂/∂ t by iω in the frequency domain. After making this kind of substitution, the evaluation of Eq 2.30 is straightforward. Finally, it is possible to go back to the time domain by simply carrying out the inverse Fourier transform:

$$exp(h\widehat{D})B(z,t) = F^{-1}(exp(h\widetilde{\widehat{D}}(i\omega))\widetilde{B}(z,\omega)). \tag{2.31}$$

By iterating these two steps a large number of times, the electric field evolution along a generic fibre can be obtained.

To improve the accuracy of the method a slightly different procedure can be carried out. The main difference compared to the previous case is that the effect of the nonlinearity is included in the middle of the distance segment rather than at the segment boundary, i.e. the optical pulse propagates over $\frac{h}{2}$ where only the dispersive effects are considered, then the effects of nonlinearity are included at the middle of the segment ($\frac{h}{2}$) and finally the dispersive effect are included in the last $\frac{h}{2}$ of the segment. A schematic illustration of this SSF method principle is depicted in Fig. 2.7.
Mathematically [29]:

$$A(z+h,t) \approx exp(\frac{h}{2}\widehat{D})exp(\int_{z}^{z+h}\widehat{N}(z')dz') \cdot exp(\frac{h}{2}\widehat{D})A(z,t). \tag{2.32}$$

In my simulations, I consider this second procedure, where the integral is approximated by h$\widehat{N}(z)$, which holds if the step size, h, is small enough. For this reason the optimum value of h has to be chosen carefully. In my simulation, h is a defined fraction (i.e. typically a 1-2%) of the minimum value between the actual length of the fibre under test, L, which is under test, the nonlinear length (L_{NL}) and the dispersion length (L_D), defined as:

$$L_{NL} = \frac{1}{\gamma P_0}, \qquad L_D = \frac{T_0^2}{|\beta_2|}, \tag{2.33}$$

where P_0 is the peak power of the initial signal and T_0^2 is the full width at 1/e of the maximum. L_D and L_{NL} denote the distance where the linear effects and nonlinear effects respectively start becoming important.

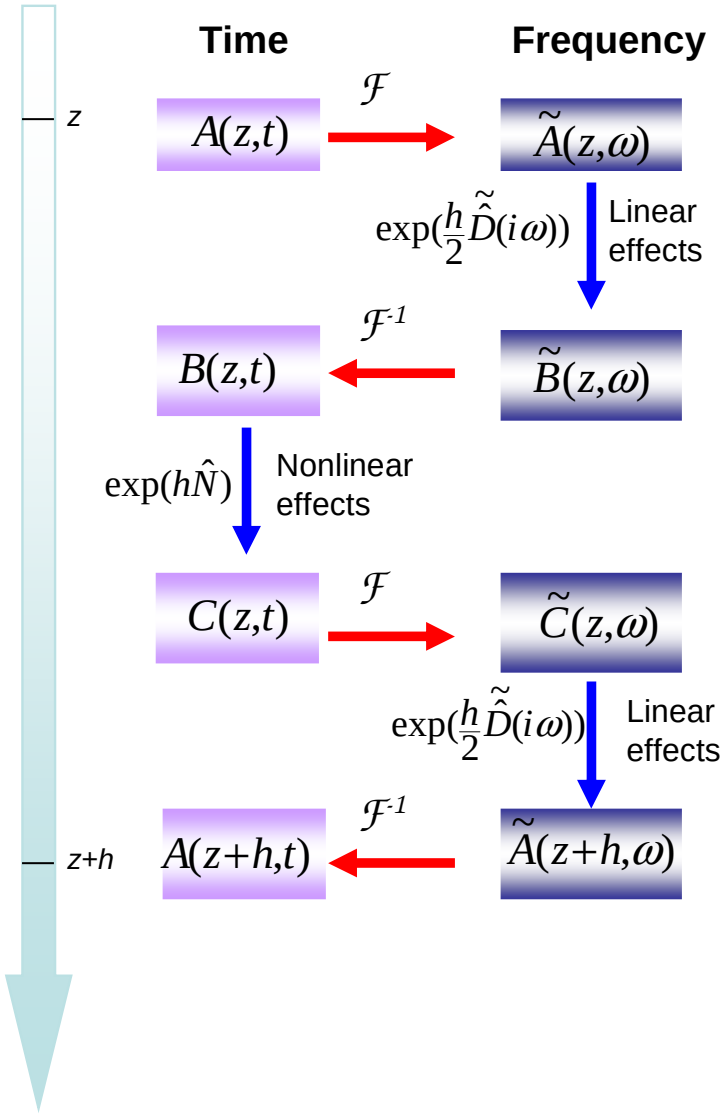

FIGURE 2.7: Schematic illustration of the SSF method principle.

2.6 Introduction to superstructured fibre Bragg gratings

Recent advances in the area of ultra-fast optics demand new techniques for the precise control and manipulation of the shape of optical pulses. In order to "synthesize" a particular optical pulse form, one needs to be able to reliably define the amplitude and phase profile of the optical field. The general approach is to generate pulses with a well-defined pulse form and then to pass the pulses through some pulse-shaping element with an appropriately designed transfer function to rephase and reshape the incident spectrum so as to obtain the desired output optical field.

The considerable progress in the fabrication techniques of fibre Bragg gratings allows the possibility of using such structures for novel pulse shaping applications. Indeed, the fine control of grating characteristics has allowed the fabrication of very complicated designs, the so-called SuperStructured fibre Bragg gratings. The term SSFBG generally

refers to a fibre Bragg grating whose refractive index profile is not uniform in amplitude and/or phase along its length [17]. In other words, it can be defined as a standard fibre grating, i.e. a grating with a rapidly varying refractive index modulation of uniform amplitude and pitch, onto which a slowly varying refractive index modulation has been applied along its length. It can be readily proven that the impulse response of a weakly reflecting SSFBG (reflectivity less than ∼20 %) follows the same form as the slowly varying, superstructure refractive index profile, see for example [49] as a reference.
SSFBGs are a powerful and flexible technology, having all the benefits of a fully fiberised system, such as compactness, ready integration into a fibre system and minimal coupling losses.
In general FBGs are commonly used in telecommunication systems for familiar applications such as add-drop filtering of dense WDM channels and dispersion compensation [50, 51], just to name but a few. More recently, with the development of SSFBGs, several applications that make use of this technique have successfully been explored, ranging from encoding/decoding within coherent Optical Code Division Multiplexing Access (OCDMA) systems [18], to pulse repetition rate multiplication [19].
In this project, I concern myself with two demanding shaping applications and their use in processing of optical signals. The first one relates to the reshaping of short pulses of a few ps duration into rectangular pulses [17, 52] - such shaping is difficult to perform by other means. These pulse forms can be very useful for applications that require a rectangular window for nonlinear optical switching such as jitter tolerant optical demultiplexing of short data pulses [52] or retiming techniques, as will be discussed in this thesis.
The second application relates to shaping into parabolic pulses. This is the first time that a linear technique is employed to generate this pulse form. Furthermore, the significance of these pulses for pulse retiming and for the generation of broad and smooth optical spectra is demonstrated later on in the corresponding Chapter.

2.6.1 Design of SSFBGs

The SSFBG technique has often been developed using weakly written FBGs, i.e. FBGs in which the relative changes of the refractive index are small enough to allow the incident light to penetrate the full grating length without significant attenuation. In this weak grating limit, it is possible, in the first approximation, to design a SSFBG to synthesize a pulse of a given desired shape on reflection using Fourier analysis, provided that the characteristics of the pulses incident upon the grating are known. Indeed, in this limit, the two following observations hold; the wave vector response $F(\kappa)$ can be shown to be given simply by the Fourier transform of the spatial refractive index modulation profile, A(x), used to write the grating [53]:

$$F(\kappa) = \frac{1}{2\pi} \int_{-\infty}^{+\infty} A(x) e^{i\kappa x} dx, \tag{2.34}$$

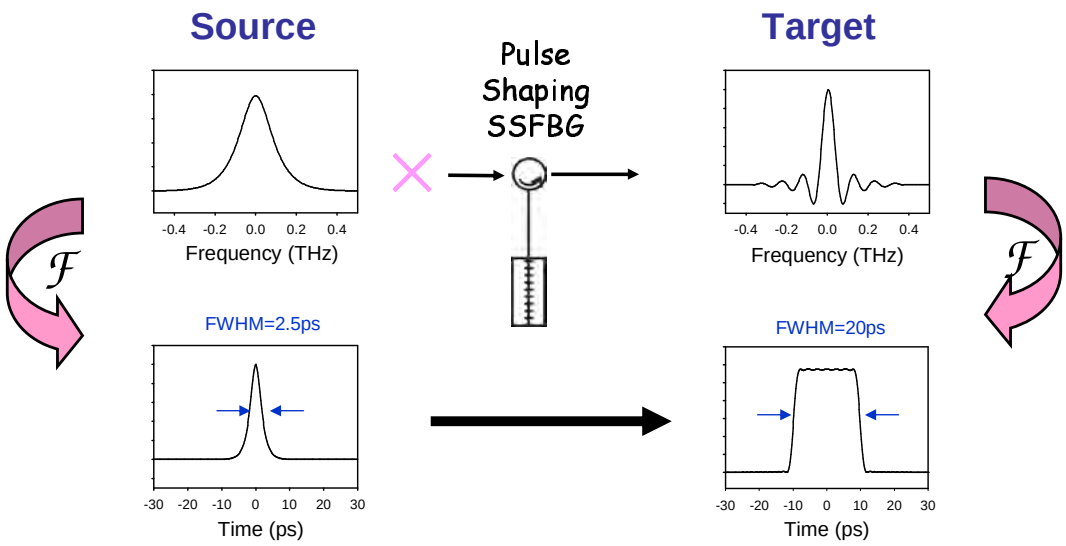

FIGURE 2.8: Simulation graphs of the electric field representation of the input 2.5-ps sech pulses (left graphs) and the output 20 ps square pulses (right graphs) in the time and frequency domain, respectively.

where κ is the wave vector that is proportional to the optical frequency, ω.
The second observation is that the impulse response of the fibre grating, h(t), is given by the inverse Fourier transform of its frequency response $H(\omega)$:

$$h(t) = \int_{-\infty}^{+\infty} H(\omega) e^{-i\omega t} d\omega, \tag{2.35}$$

From the equations above, it follows that h(t) of a weak grating, has the same temporal profile as its A(x). For example, in the instance that the grating has an amplitude modulation only (grating phase is uniform), its impulse response follows precisely its spatial amplitude modulation profile. Obviously, an appropriate conversion between the temporal and the spatial domain would be required ($t = \frac{2nx}{c}$, where n is the refractive index of the fibre core and c is the speed of light).

Fig. 2.8 depicts the basic principle of SSFBG based pulse synthesis. The SSFBG acts as a linear filter: the reflected signal, $Y(\omega)$, is the product of the incident signal, $X(\omega)$ and $H(\omega)$ in the frequency domain:

$$Y(\omega) = X(\omega)H(\omega) \tag{2.36}$$

or, in the temporal domain, the temporal shape, obtained after reflection via the SSFBG, is given by the convolution between the input pulse, x(t) and the impulse response of the grating i.e.:

$$y(t) = x(t) * h(t), \tag{2.37}$$

where x(t) and y(t) are the corresponding inverse Fourier transforms of $X(\omega)$ and $Y(\omega)$, respectively. In the particular case depicted in Fig. 2.8, a temporal shape of a 20 ps rectangular pulse was targeted (see Chapters 4 and 5 for the application of such a tem-

poral shape), starting from a ∼2.5 ps sech pulse. Therefore, the initial pulse needs to be filtered via the SSFBG such that the representation of the electric field of the reflected signal in the frequency domain is a sinc-function (Fourier transform of a rectangular shape) consisting of lobes of alternative phase, separated by ∼50 GHz from each other. The requirement for full penetration of the signal to the FBG structure limits the strength of the grating itself, resulting in significant loss on reflection. An additional energy loss is incurred as a result of the spectral filtering of the input spectrum which can be appreciable if the incident pulses are much shorter than the grating's impulse response. For example, the 20 ps rectangular grating (reflectivity <10%), used in the experiments reported in Chapters 4 and 5, has a overall measured loss of 25 dB, while the parabolic grating (reflectivity <20%), for which applications will be discussed in Chapter 6 and 7, has a measured loss of 12 dB. In general, this is not a big issue in terms of signal-to-noise ratio degradation. For example BER measurements at 10 Gb/s were performed employing rectangular pulses and show that error free operation could be achieved with only a slight power penalty of less than 0.5 dB relative to the back-to-back measurements at 10^{-11} [17].
However, recent research has shown that the grating strength limits can be overcome by using advanced design algorithms known as inverse scattering techniques to design the superstructure function [54] rather than the simple Fourier analysis used in this thesis.

2.6.2 Fabrication of SSFBGs

The implementation of complicated grating structures requires precise control over the imposed amplitude and phase of the modulated refractive index of the grating. The fabrication of the FBG's reported in this thesis was made possible by the continuous grating writing technique, which adopts plane by plane grating writing technique.

Fig. 2.9 shows the continuous grating writing apparatus. This technique is properly described in [55]. The main advantage of this technique is that the photosensitive fibre is mounted on a computer-controlled translation stage, which is used to move the fibre relative to the fixed phase mask. Indeed, by placing the fibre in the interference pattern which consists of regions of high and low UV intensity generated by the phase mask, a grating will be formed with a period given by the periodicity of the interference pattern. The fibre-waveguide is then translated continuously at a constant velocity along the axis perpendicular to the interference fringes, with a sub-nanometre precision provided by an interferometer. The UV exposure on the fibre occurs always under the same part of the phase mask, while any amplitude or phase modulation are imposed by reducing the incident UV flux or dephasing the fibre relative to the phase mask. Thus, any errors introduced during the writing process, or imperfections in the phase mask, are averaged out since the fibre is exposed to different parts of the phase mask many times during the writing process.
All the gratings used in this thesis were written by Dr. Morten Ibsen at the Optoelec-

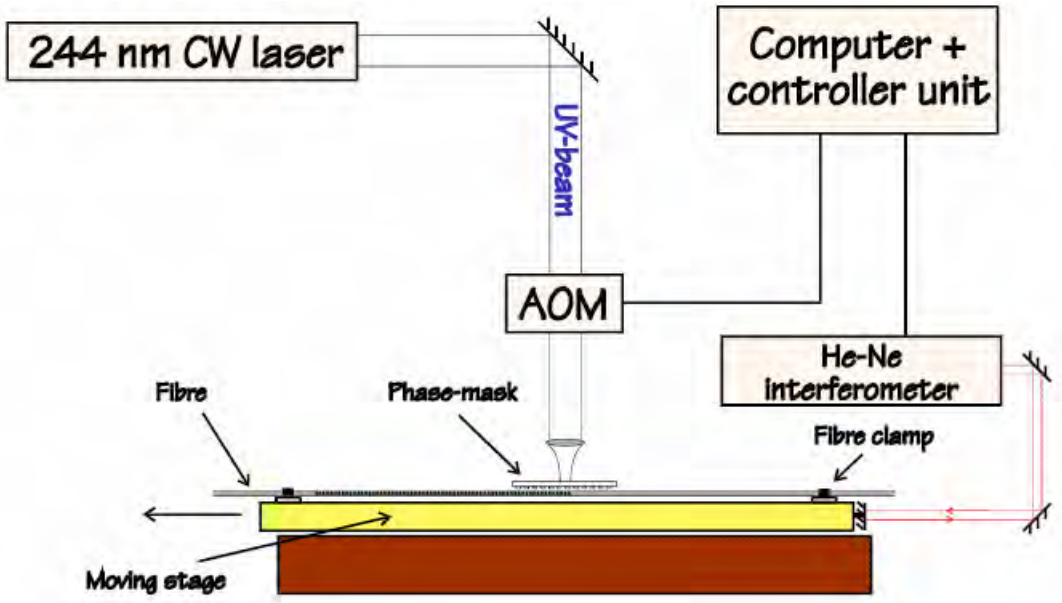

FIGURE 2.9: Continuous writing technique set-up.

tronics Research Centre.

2.7 Conclusion

This Chapter gives a theoretical overview of the main topics that need to be known to allow a detailed understanding of the thesis.
An introduction of the basic principle of optical regeneration in optical communication systems is given, and the origin of the main distortion impairments are explained.
Applications of nonlinear phenomena, such as SPM and XPM, are described for nonlinear optical processing, namely the Mamyshev-type 2R-regenerator and NOLM. Furthermore, for an understanding of the linear and nonlinear phenomena in optical fibres, it is necessary to consider the basic equation that governs the propagation of optical pulses in fibres, the NLS equation is introduced and the SSF method is described, as a numerical method widely used to solve the NLS equation.
An equally important topic in this thesis is the linear shaping of arbitrary signal pulses into different kinds of shapes, such as rectangular and parabolic pulses, via SSFBGs, which are demonstrated to be suitable for versatile operation in optical processing. The capability of implementing structures, the realization of which requires precise control over their amplitude and phase properties, has been briefly discussed and demonstrated.

Chapter 3

Assessment of the quality of short pulses shaped using SSFBGs

3.1 Introduction

The main emphasis in this work is given on the improvement in performance of optical processing systems provided by the inclusion of precise pulse shapers. Linear pulse reshaping is performed using SSFBG, as discussed in the previous Chapter. A detailed knowledge of the precise shape of these pulses is absolutely critical for the implementation of the system applications and for a complete understanding of the results obtained, as will be discussed in the following Chapters. These pulse shaping applications require the generation of precise and complicated pulse structures and so direct diagnostic tools with picosecond to femtosecond time resolution are needed for accurately assessing the exact pulse shapes.
In general, direct detection techniques using fast photodetectors are inadequate for such applications. The bandwidths required are far higher than those available with current state-of-the-art technology, distorting the measurement of the temporal intensity profile of the high speed optical communication pulses. An important additional limitation is that photodetectors respond to the intensity of the pulse, so their output contains no information about the phase of the incident radiation.

Most ultrashort optical measurements are performed with optical correlation methods and of these, the second order intensity autocorrelation is the most often used. This technique essentially measures the autocorrelation intensity of the signal and is achieved by interfering two replicas of the signal with an accurately defined relative time delay between the two. This method provides a reasonable estimate of the pulse width down to a few femtoseconds, but gives very little information on the detailed pulse shape. A given autocorrelation profile can be realized by more than one intensity profile, so that it does not uniquely identify the pulse profile. Furthermore, the autocorrelation trace

does not provide any information on the phase or chirp of the pulse. For this reason, autocorrelation measurements are usually accompanied by measurements of the optical spectrum, and the combination of the two can be used to gain a better appreciation of the shape and the amount of chirp on the pulses.

The optical sampling oscilloscope technique is a good candidate to measure directly the intensity profile in the temporal domain [56]. The signal to assess is combined with a very short sampling pulse at a different repetition rate (much lower than that of the signal) in a nonlinear medium. In the following Section, a FWM effect between the signal and the sampling pulse will be discussed as an example of nonlinear interaction. The FWM components generated represent a sample from the signal, and their energy is proportional to the power of the signal at that position of temporal overlap with the probe. Using a low bandwidth photodetector, the temporal profile of the signal intensity can be displayed on an electrical sampling oscilloscope. This technique has long been considered as an effective means for reliably viewing the direct temporal shape of fast waveforms [57] and has now been demonstrated to have sufficient resolution to satisfy a variety of applications including the measurement of eye-diagrams within ultra-high bit rate communication systems [58]. However, the resolution of this technique is limited, among other factors, by the duration of the sampling pulse. For the assessment of the pulse quality of the SSFBG shaped pulses, discussed in this thesis, such a technique is quite well suited because of their relatively long duration (∼10-20 ps), even if it does not give any information about the phase of the signal.

Another interesting technique, called frequency-resolved optical gating, has been widely used to determine the full electric field [59–61]. It can measure the pulse shape and offers the additional advantage of providing information on how the optical phase and the frequency chirp varies across the pulse. The signal is gated, through a nonlinear interaction, by another optical pulse, which is usually a replica of it with a relative time delay. This produces a cross- or auto-correlation signal which instead of being measured in time directly, is then dispersed and recorded by a spectrometer. From this two-dimensional time-frequency spectrogram of the pulse, the time-dependent intensity and phase profiles can be reconstructed using iterative Fourier-transform algorithm techniques [62]. Further details about this technique are discussed in Section 3.3.

In bulk configurations, though, the sensitivity of the FROG device is limited by diffraction, which imposes a trade-off between the beam cross section and the interaction length. Guided-wave configurations can overcome this constraint and improve the efficiency by as much as two orders of magnitude [63]. In this direction, the implementation of the FROG technique in a Quasi Phase Matched (QPM) $LiNbO_3$ waveguide was first demonstrated in [63]. In that demonstration, the spectrally resolved cross correlation of two unknown pulses was measured using Sum-Frequency Generation (SFG) in a QPM $LiNbO_3$ device. Obviously, as the interaction length is increased, the acceptance bandwidth of the nonlinear interaction decreases, hence limiting the temporal resolution.

Therefore, a trade-off between sensitivity and temporal resolution needs to be established. A novel configuration based on cascaded second-order nonlinear interactions is demonstrated in [64, 65]. More details regarding the experimental implementation will be discussed in Section 3.4.

Finally, an extremely sensitive characterization technique has been demonstrated recently in a linear device [66]. Indeed, Dorrer and Kang demonstrated the linear characterization of optical pulses using a fast intensity modulator as a gate, instead of using a nonlinear optical interaction. A spectrogram of the pulse is constructed by means of measuring the spectrum of the gated pulse as a function of the delay between the pulse and the gate. From this time-frequency representation, it is possible to extract complete information about the pulse and the gate. More details can be found in Section 3.5.

In this chapter, a brief overview of all these kinds of techniques to characterize optical pulses, all of which used in further Chapters, is presented together with some results of novel pulse characterizations. Furthermore, a comparison of the results of some of those techniques is given for the 20 ps rectangular shaped pulse case, showing a good agreement between them.

3.2 Real time measurements using an Optical Sampling Oscilloscope

Optical sampling oscilloscopes are very well suited to the assessment of pulse quality in SSFBG pulse shaping applications. In this section, I demonstrate direct and high-resolution measurements of the response of the pulse shaping SSFBGs in real time, using this technique.
So far, the most advanced sampling techniques, with a temporal resolution that is primarily limited by the width of the sampling pulses, are based on the nonlinear interaction of the optical signal and the sampling pulses. The sampling pulses are generally generated using a separate source and typically the nonlinear interaction is SFG in crystals [67] or FWM in semiconductor optical amplifiers [68] or in optical fibre [57, 58]. The optical sampling measurement described herein is based on FWM when the two signals overlap in a highly nonlinear fibre, caused by the third-order nonlinear susceptibility [29]. FWM occurs when two phase-matched optical signals having different optical frequencies are injected into the fibre.
Fig. 3.1 depicts a schematic illustration of how the sampling signal at frequency f_S can slowly "scan" through the signal at frequency f_m and how the optical sampling technique works. The relationship between the two frequencies can be defined as follows:

$$f_S = f_m + \Delta f. \tag{3.1}$$

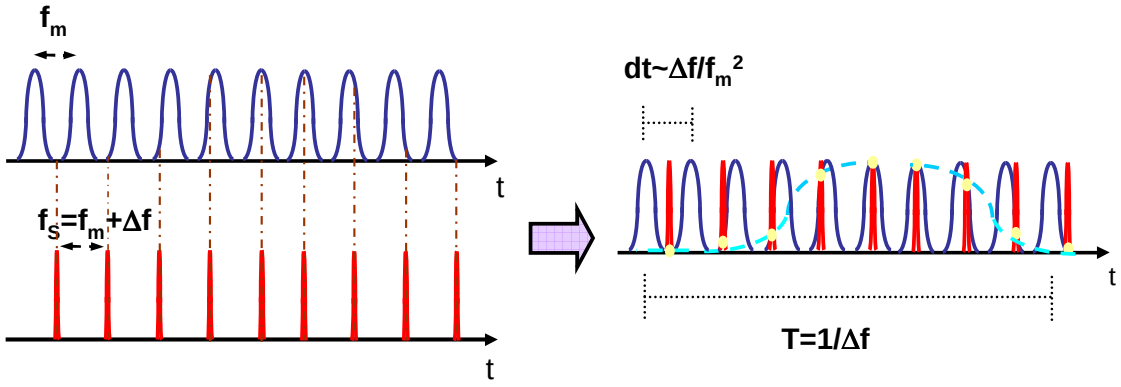

FIGURE 3.1: Sketch of the operation principle of an optical sampling oscilloscope.

If there is an integer relationship between f_m and f_S, then the same part of the signal would be sampled each time. If the sampling pulse is slightly unsynchronized with the signal and $\Delta f \ll f_m$, the sampling pulse can "walk" slowly through the signal. This means that the FWM component appears as a comb of sampling pulses which are amplitude modulated by the signal being measured, but at a much reduced time scale (see right plot in Fig. 3.1). Indeed, the optical power of the generated FWM signal is proportional to the power of the signal at the position of the temporal overlap with the sampling pulses. The signal can then be detected by a slow photodiode and displayed on an electrical sampling oscilloscope triggered at the frequency Δf.
The sampling frequency is typically [58]:

$$f_S = \frac{f_m + \Delta f}{M} \tag{3.2}$$

where M is an integer with a value around 100 and $\Delta f/M$ is usually of the order of hundreds of kHz. In the particular case presented herein, Δf is 30 MHz and M is 1. Even if this is a quite high value compared to typical implementations, it is still very slow compared to the photodetector used. Furthermore, using such a value of Δf, a conventional electrical filter with a -3 dB bandwidth of ~2.95 GHz could be employed to separate the sampling and signal frequencies after the mixer, see the set-up in Fig. 3.2.

I developed the optical sampling system shown in Fig. 3.2. Two Erbium Fibre Ring Lasers (EFRLs) operating at ~10 GHz were used as the signal and the sampling sources. The operating wavelengths for the signal EFRL and the sampling EFRL were 1557.6 nm and 1551.0 nm respectively. The signal source was a regeneratively and harmonically mode-locked EFRL, which incorporated an optical PLL to lock the repetition frequency to an exact multiple of the resonant frequency of the cavity. The Radio Frequency (RF) signal produced at the output of the PLL was also used as a reference to produce the drive signal for the sampling EFRL. The sampling EFRL was capable of operating at any given drive frequency by actively adjusting the exact length of its cavity, via another optical PLL. The repetition rate of the sampling EFRL was set at a frequency, which

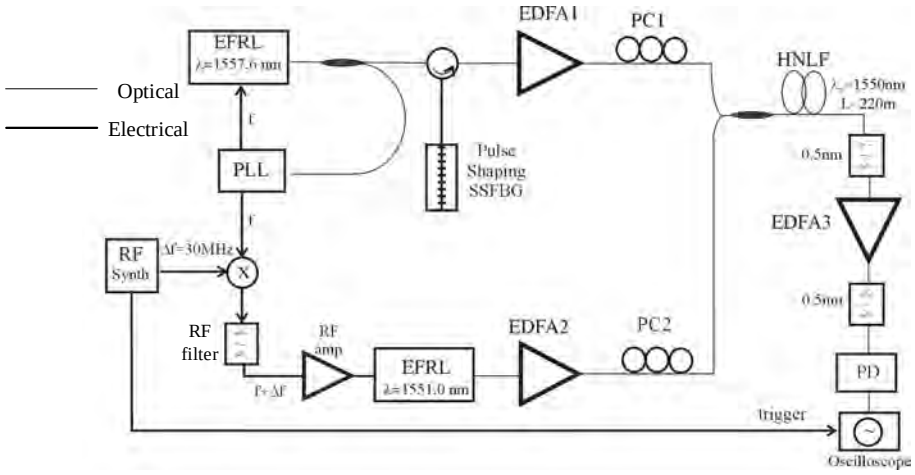

FIGURE 3.2: Experimental Set-up. PC: polarization controller. PD: photo-detector.

Dispersion @1550nm ($ps\ nm^{-1}km^{-1}$)	Dispersion Slope ($ps\ nm^{-2}km^{-1}$)	Length (km)	Loss ($dB\ km^{-1}$)	Effective Nonlinearity ($W^{-1}km^{-1}$)
0	0.03	0.22	0.53	20

TABLE 3.1: Fibres' parameters

was 30 MHz offset (Δf) from the frequency of the signal EFRL, as discussed above.

The signal pulses were 2.5 ps wide and, after being shaped through the SSFBG, were combined with the sampling pulses through a 3 dB coupler. The sampling was achieved by generating FWM due to the fibre's third-order nonlinear susceptibility when the sampling and the signal pulses overlap. The parameters of the HNLF used are reported in Tab. 3.1. Care was taken to ensure that the peak powers of both the sampling and signal waveforms remained sufficiently low to ensure that no distortion of the two signals took place within the HNLF due to SPM [29]. An example of the spectrum obtained after the nonlinear interaction of the signal with the sampling pulses in the HNLF is given in Fig. 3.3. The generated Four-Wave Mixing product was filtered using 0.5 nm filters and used to sample the data because the strength of the FWM product is proportional to the signal strength. The sampled data was detected using a 2.95 GHz detector. The detected output was monitored on a sampling oscilloscope, triggered at 30 MHz from the RF frequency synthesizer, resulting in a sampling step, dt, of 0.3 ps:

$$dt \simeq \frac{\Delta f}{f_m^2} \tag{3.3}$$

Note that an even lower bandwidth detector than the one used here would be sufficient to detect the sampled data. As explained above, the output of the FWM component consists of narrow spikes that are amplitude modulated by the data signal but at a much reduced time scale. This signal is subsequently detected with a slow receiver which detects only the envelope of the sampled signal. In this example, the fundamental

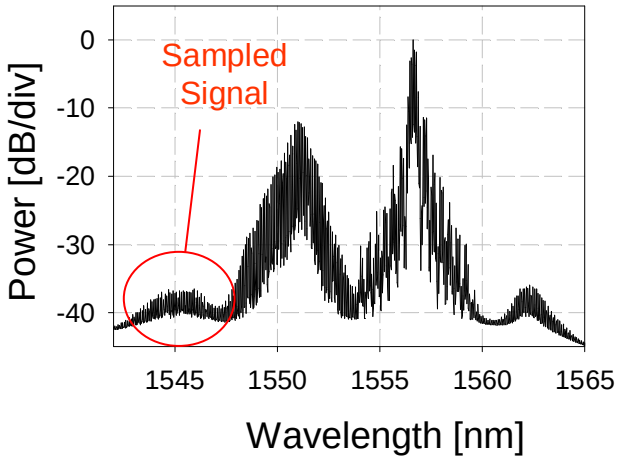

FIGURE 3.3: Optical spectrum after the HNLF; the signal in this instance is the 20ps square pulses.

f_m rate of the sampling is altered by Δf so that the reduced time scale (t_{red}), compared to the real one (t) becomes:

$$t_{red} = t * \frac{f_m}{\Delta f} \tag{3.4}$$

For the example in our case, where $f_m = 10\ GHz$ and $\Delta f = 30\ MHz$, a 1 ps pulse time scale translates into a 0.3 ns sampled signal time scale.

The temporal resolution of the current system was limited by the ~2 ps pulse width of the sampling EFRL source. Generally, the resolution of this technique will also depend on the fibre dispersion which causes a walk-off between data and sampling pulses and on the timing jitter of the sampling source. In this experiment, the walk-off time of two pulses at the wavelengths of the two EFRLs co-propagating through the HNLF was ~15 fs, much less than the resolution of the system defined by the pulsewidth, while the sampling source timing jitter was ~200 fs.

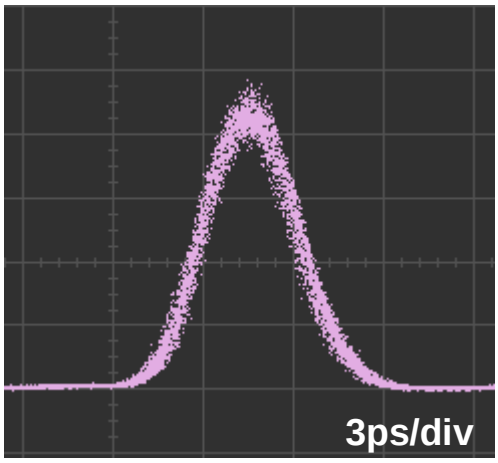

FIGURE 3.4: A trace of the signal EFRL pulses obtained using the optical sampling oscilloscope.

Fig. 3.4 shows a scope trace obtained by direct sampling of the signal pulses, and reveals that traces with very good noise characteristics can be obtained. The temporal resolution of the system was estimated to be ~ 2.2 ps by comparing the observed pulsewidth of $\sim$3 ps, see Fig. 3.4, with the estimated pulsewidth of $\sim$2 ps obtained from an autocorrelation trace ($\tau_{res} = \sqrt{3^2 - 2^2} = \sqrt{5}\ ps$). The optical sampling oscilloscope technique also confirms the levels of timing jitter present in the EFRLs, which has been used in all the experiments described in this thesis. The timing jitter of the trace shown in Fig. 3.4 was measured on the digital communications analyzer (DCA) using the histogram technique (to be described in more detail in Sec. 4.4). This measurement gave a root mean square (rms) standard deviation (much higher than the rms of the DCA itself), which corresponds to a real value of $\sim 300\ fs$, according to Eq. 3.4. Assuming that the timing jitter of the two sources has similar and uncorrelated characteristics, an rms timing jitter of $\frac{300}{\sqrt{2}}\ fs \simeq 200\ fs$ was estimated. This number is in agreement with independently conducted measurements.

The pulses of the signal EFRL were then shaped into 20 ps square pulses, using the SSFBG described in [17], before being combined with the sampling pulses. The measured optical spectrum of 20 ps square pulses (a), together with the corresponding autocorrelation trace (b), are plotted in Fig. 3.5. The SSFBG spectral response was such that the reflected signal exhibited well-defined sinc-like features in the frequency domain, see Fig. 3.5 a, and hence had a square shape in the time domain (triangular shape according to the autocorrelation trace). This is clearly demonstrated in Fig. 3.6, where it is seen that the short soliton pulses are shaped into 20 ps square pulses at a repetition rate of 10 GHz. The pulses have a good flat top section and sharp trailing and leading edges. These pulses were subsequently used to implement the retiming and reshaping techniques at a repetition rate of 10 Gbit/s, and this work is described in Chapters 4 and 5.

Shorter square windows will be required for applications at higher repetition rates. Sim-

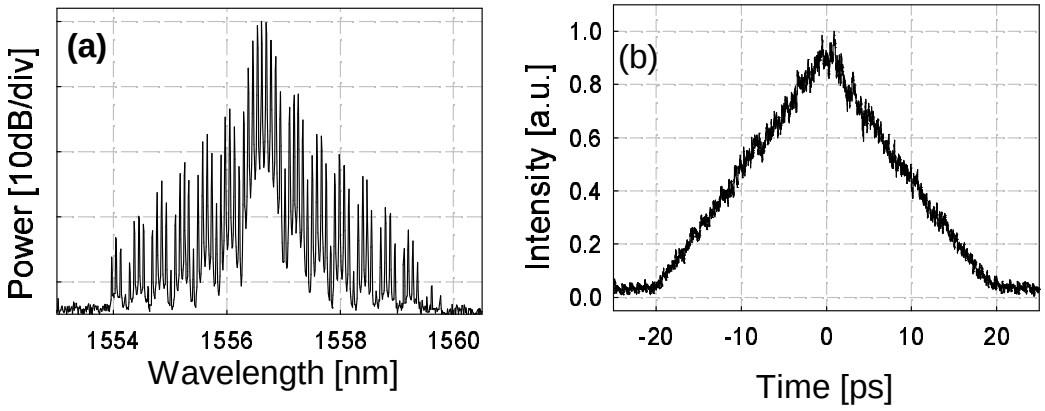

FIGURE 3.5: Optical spectrum of the 20 ps square pulses at a central wavelength of 1556.8 *nm* and a repetition rate of 10 GHz(a) and corresponding autocorrelation profile(b).

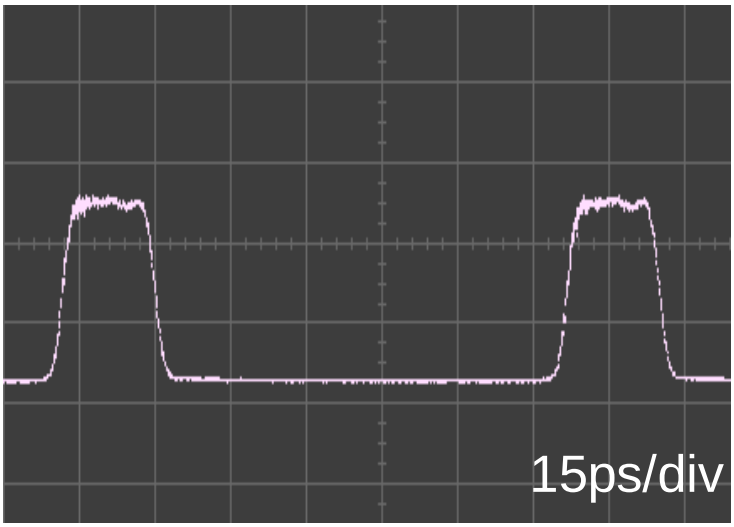

FIGURE 3.6: Optical sampling oscilloscope trace of the 20 ps square pulses.

ilar designs, which incorporate broader spectral features, have already been employed to demonstrate the generation of 10 ps square pulses [52]. An optical sampling oscilloscope trace of these pulses is shown in Fig. 3.7. It should also be noted that this SSFBG was designed to operate with 1.7 ps input soliton pulses, slightly narrower than the pulses provided by the EFRL. The pulses thus have slightly more rounded features at the edges than for the ideal case that the grating was designed for. Nevertheless, clean, flat-topped 10 ps pulses at 10 GHz were resolved.

Although not relevant to the work reported herein, provision of the optical sampling oscilloscope enabled the examination of another pulse shaping SSFBG that was previously developed within my group, i.e. a pulse multiplication SSFBG. In this case the individual characteristics of the pulses are maintained and the repetition rate of the stream itself is altered by sampling appropriate spectral features in the pulse spectrum [19]. The

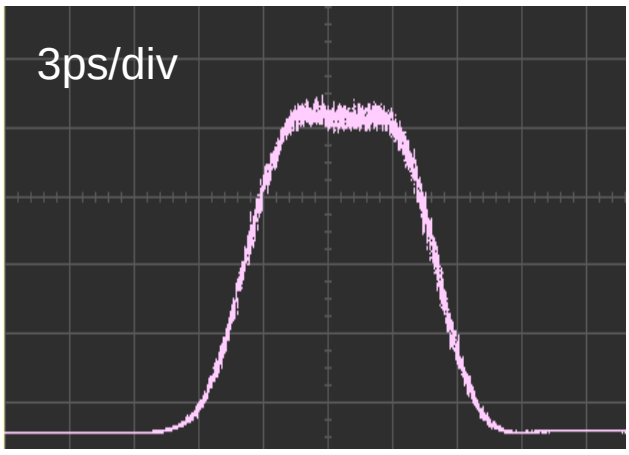

FIGURE 3.7: Optical sampling oscilloscope trace of the 10 ps square pulses.

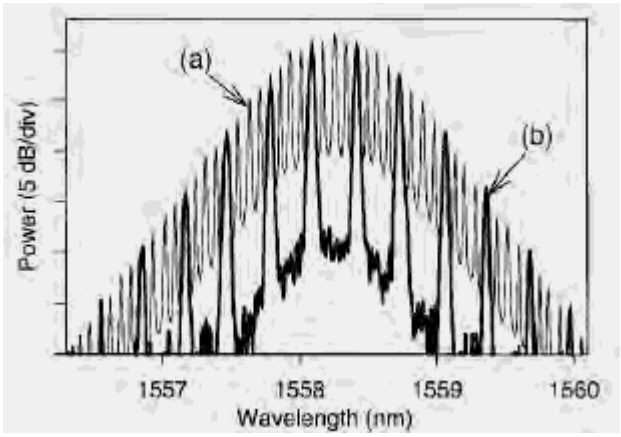

FIGURE 3.8: Optical spectra of (a) the 10 GHz input pulses and (b) the 40 GHz output pulses (taken from [19]).

reshaping can be performed by a filter that selectively filters out certain spectral lines of the periodic signal, thereby changing the pulse periodicity, while the phase coherence of the remaining spectral lines is retained. Pulse multiplication, for example from 10 GHz to 40 GHz, relies on aligning the SSFBG channels to the periodic 10 GHz spectral lines of the source: one in every four spectral lines is reflected, resulting in pulse multiplication by a factor of four in the time domain. The spectrum and the autocorrelation trace of the shaped pulses are shown in Fig. 3.8 and Fig. 3.9 respectively, where they are compared to the original pulses (these measurements are taken from [19]). From the comparison, the filtering action of this FBG is evident: three out of every four spectral lines have been filtered out, down to the $\sim -18\ dB$ level relative to the remaining 40 GHz components.

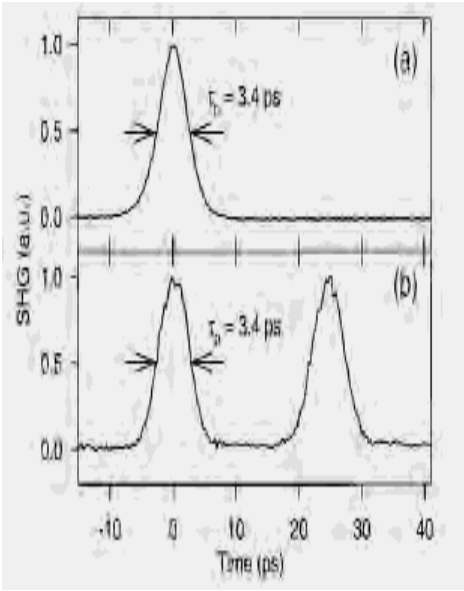

FIGURE 3.9: Autocorrelation traces of (a) the 10 GHz input pulses and (b) the 40 GHz output pulses (taken from [19]).

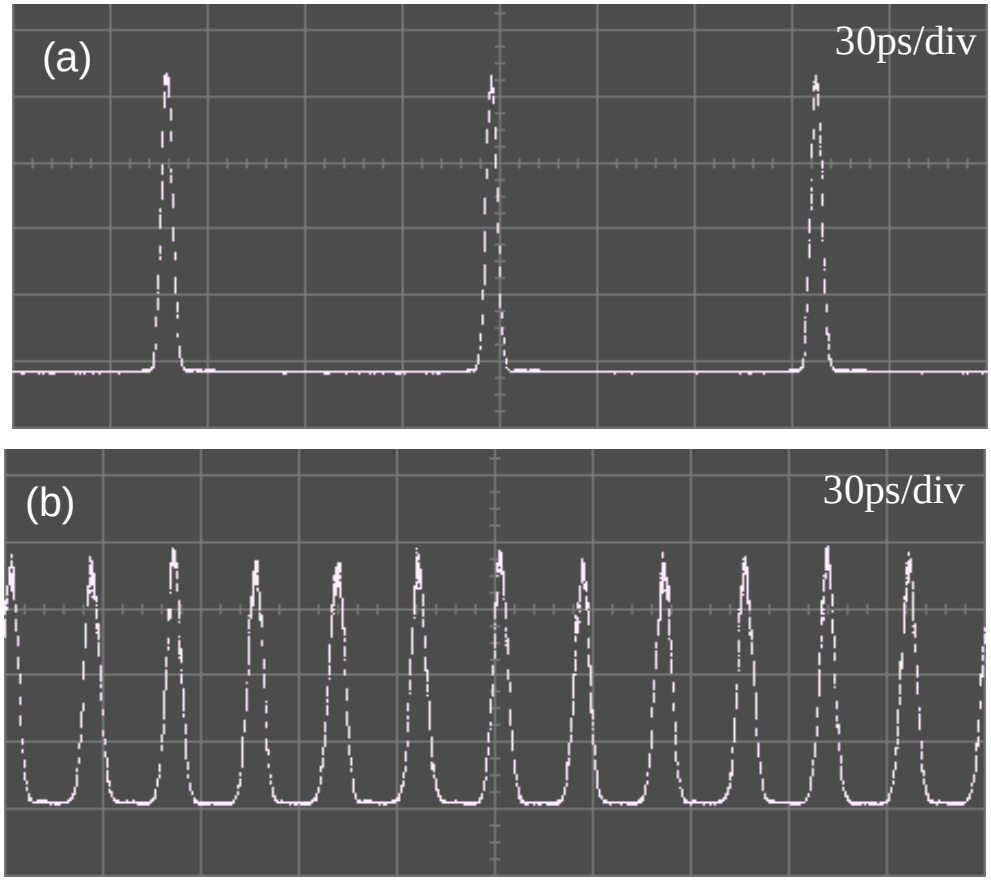

FIGURE 3.10: Optical sampling oscilloscope trace of the original 10 GHz pulses (a) and the 40 GHz pulses (b).

The corresponding optical sampling oscilloscope trace I took is shown in Fig. 3.10.b, and should be compared to the original 10 GHz trace, see Fig. 3.10.a. Thanks to the long period of the sampling process of our system, the individual traces of adjacent pulses can be resolved correctly, allowing for an assessment of the uniformity of the constituent pulses. Extremely good uniformity of amplitude is achieved, with an amplitude fluctuation of $\sim 3\%$. Using the traces of adjacent pulses it was also possible to confirm that the pulses were pedestal-free with a reasonably good inter-pulse extinction of 15 dB.

3.3 Frequency Resolved Optical Gating

FROG based on the nonlinear interaction in a second harmonic generating crystal between two replicas of the same pulse under test is nowadays among the most frequently used characterization techniques used in the area of pulsed laser research.
In principle, the FROG technique consists of two parts: a physical measurement to acquire a spectrogram, and the use of an algorithm to retrieve the intensity and phase of the measured pulses from the spectrogram. In general, the SH intensity spectrum of a pulse E(t) after gating with a function G(t) is measured as a function of the delay τ

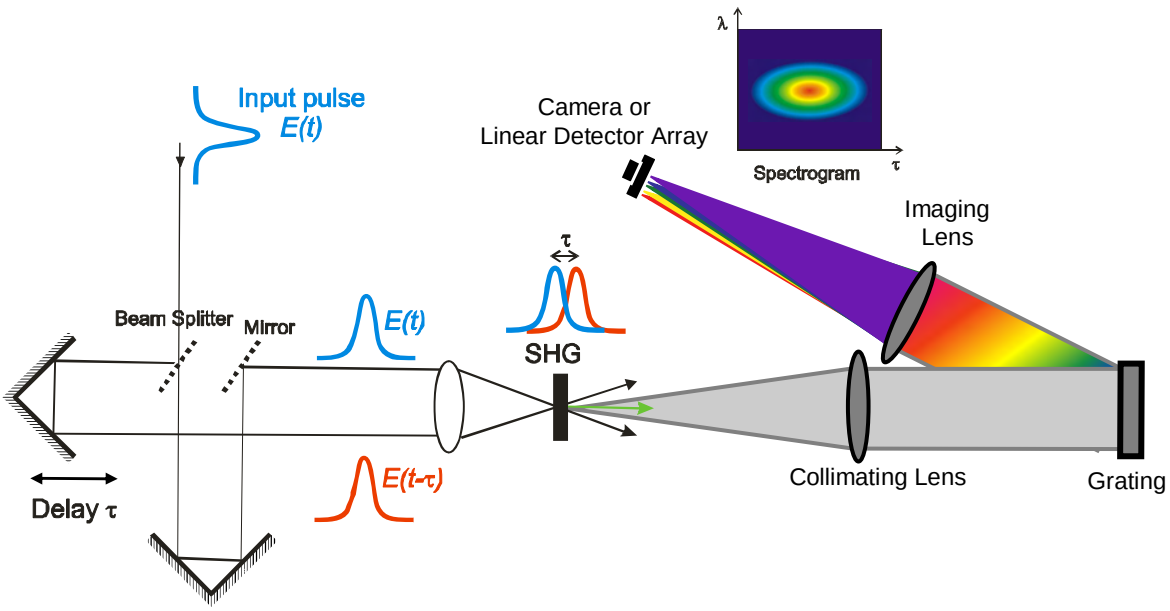

FIGURE 3.11: Sketch of the operation principle of a FROG (adapted from [69]).

between the gate and the pulse under test. The experimental trace is thus represented by:

$$S(\tau,\omega) = \mid \int E(t)G(t-\tau)exp(i\omega t)dt \mid^2 . \tag{3.5}$$

In the case when the gate is a simple replica of the pulse under test, $G(t-\tau)$ becomes $E(t-\tau)$. A retrieval algorithm is then used, which attempts to find a pulse shape that would have exactly the same spectrogram as that measured.
A schematic showing this principle is depicted in Fig. 3.11.

The two-dimensional FROG trace is a time symmetric function (E(t) and E(-t) functions have the same spectrogram), leading to an inherent ambiguity in the direction of time. The FROG apparatus, commercially available in the lab, is a *Southern Photonics* HR100 Pulse Analyser and is specified to have a temporal resolution of 15 fs. This apparatus has been used for several characterizations of pulses within this thesis. Unfortunately, the alignment between the two pulses has to be adjusted very carefully if maximum efficiency in the crystal needs to be reached, and seems to be wavelength dependent for the particular apparatus used. This limited us on the characterizations of very short pulses (broadband spectrum) as we will see for a specific example in Chapter 7.

Fig. 3.12 shows an example of SHG-FROG characterization. In particular, the results of a ∼2 ps sech pulse generated from an EFRL at the operating wavelength of 1542 nm, which is used as the initial signal in many experiments reported herein, are shown. Fig. 3.12.a and Fig. 3.12.b depict the measured and reconstructed spectrograms respectively. The spectrogram itself is a highly intuitive display of the waveform under test as a function of time and frequency, so it is already possible to derive some imformation simply by looking at its shape. As expected, the spectrogram is a symmetric function of

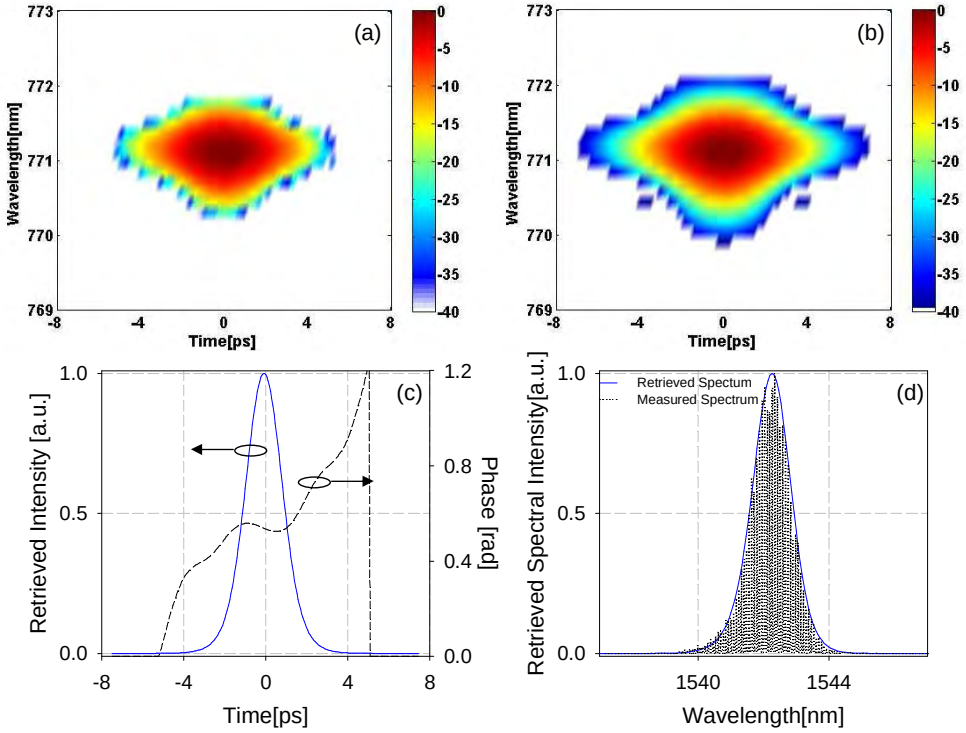

FIGURE 3.12: SHG-FROG results for 2 ps sech pulses. Measured (a) and Reconstructed (b) spectrograms, retrieved temporal intensity and chirp (c), and the retrieved spectral intensity and chirp compared to the independent measured spectrum (d).

the time. Furthermore, because the pulse to be measured is gated with itself, the time range of the spectrogram is roughly double the full pulse duration. On the other hand, its symmetry along the frequency axis depends on the real symmetry of the pulses in this domain. Furthermore, the broader the plot along this axis the more chirped the pulses, as can be qualitatively estimated from general spectral traces.

For this particular measurement, the retrieved pulse yields a minimum FROG error (rms error between the experimental and retrieved traces) of $\sim$0.2%, which implies a very good extimation of the pulse under test. Fig. 3.12.c displays the corresponding retrieved pulse intensity and phase in the temporal domain, while Fig. 3.12.d shows the corresponding measured and retrieved spectral intensities. As can be seen, the temporal phase has a fairly linear profile across the pulse, implying chirp-free pulses, as expected directly after the laser source.

3.4 FROG in Periodically Poled Lithium Niobate waveguide devices

The use of waveguide devices in a FROG configuration has shown to provide efficiency enhancement over bulk materials [63]. Dr Jerry Prawiharjo and Dr Katia Gallo developed a novel FROG configuration based on cascaded ($\chi^{(2)} : \chi^{(2)}$) SHG and Difference-

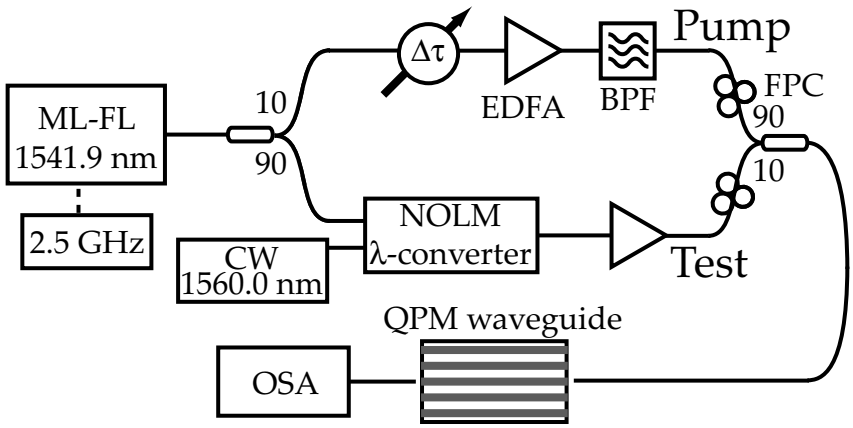

FIGURE 3.13: Cascaded SHG:DFG FROG experimental set-up in Periodically Poled Lithium Niobate waveguide device.

Frequency Generation (DFG) interactions in a uniform QPM waveguide. In particular they analysed, theoretically and numerically, such configurations [64]. I helped in the experimental realization of the proposed configuration. The experimental results are reported herein, but no pulses shaped with the SSFBG are analysed with this method because the QPM PPLN was not available at the time of those measurements.

The experimental set-up is shown in Fig. 3.13. A 2.5 GHz stream of picosecond pulses from the EFRL, operating at 1541.9 nm, was split into two signals via a 90:10 coupler. The first path, which contains 10% of the power, was amplified by an EDFA to generate the pump pulse and filtered by a filter with a 5 nm FWHM bandwidth. A motorised variable optical delay line was included in this path. The remaining 90% of the pulse train was used to generate the test pulse. The pulse train was used as the control of a NOLM configuration, with the signal being a Continuous Wavelength (CW) laser diode operating at 1560 nm. The resulting signal was then amplified by a variable gain amplifier. The characteristics of the HNLF inside the loop are described in Tab. 3.1. Afterward, 90% of the pump pulse power and 10% of the test pulse power were combined, resulting in an average power (energy) of 0.2 mW (80 fJ), respectively, before being launched into the waveguide. Note that due to the polarization sensitivity of the nonlinear interactions in the $LiNbO_3$ waveguides, the polarizations of the pump and test pulses were independently controlled by polarization controllers. The waveguide was fibre coupled at both the input and the output, with a total fibre-to-fibre throughput loss of $\sim$ -11.5 dB. This loss was estimated to be due to uncoated end faces ($\sim$ -1.7 dB), intrinsic propagation loss ($\sim$ -2.6 dB), and fibre-waveguide mode mismatch ($\sim$ -7.2 dB). These figures could be significantly improved by waveguide optimization and tapering of the input-output waveguides.

The spectra at the output of the waveguides were measured by an Optical Spectrum Analyzer (OSA) and are shown in Fig. 3.14, where the distinct spectra of the test, the pump and the generated output pulses can be seen at the waveguide output at zero time delay τ=0. The coherent peak in the test pulse spectrum is a residual CW component

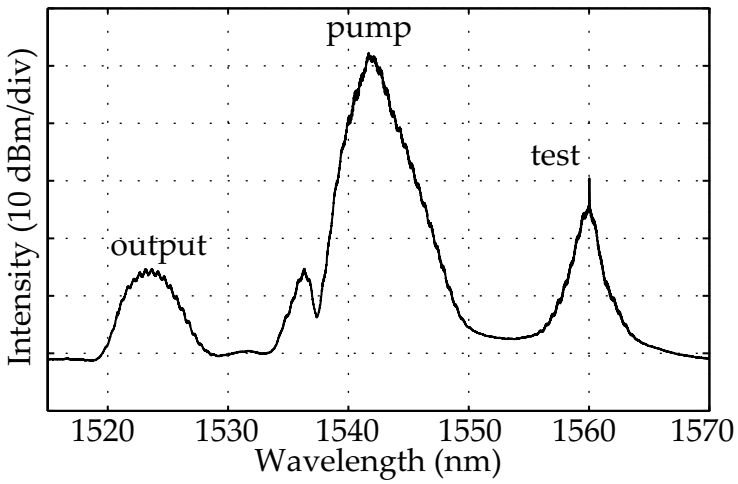

FIGURE 3.14: Measured Spectra at the output of the waveguide. The test pulse average power is 0.2 mW. The generated output pulse is shown st zero delay ($\tau = 0$).

from the nonlinear optical loop mirror, which, because of is low power, relative to the peak pump power of the pulses, provides little contribution towards the nonlinear interactions, and consequently no corresponding CW component is observed in the spectrum of the retrieved pulses. The power-dependent side lobe structure on the shorter wavelength side of the pump pulse spectrum is an indication of SHG cascading self-phase modulation. However, this does not affect the FROG measurement.
Fig. 3.15.a shows the measured spectrogram for the test pulses, while Fig. 3.15.b shows the retrieved spectrogram. The relative root mean square error between measured and retrieved spectrograms was 0.9%.

Fig. 3.16.a shows the intensity (black solid trace) and chirp (dashed black trace) of the test pulses as retrieved from the spectrogram in Fig. 3.15. Fig. 3.16.b plots the measured (solid line) autocorrelation trace of the test pulses with the numerical (circles) trace, generated from the retrieved test temporal profile, showing very good agreement between the two. Similarly, the measured (solid line) and the retrieved (circles) spectra in Fig. 3.16.b show an excellent agreement (over a 30 dB range). The temporal FWHM of the retrieved pulse is 2.1 ps, while its spectral FWHM is 0.18 THz (1.5 nm), yielding a Time Bandwidth Product (TBP) of 0.39.

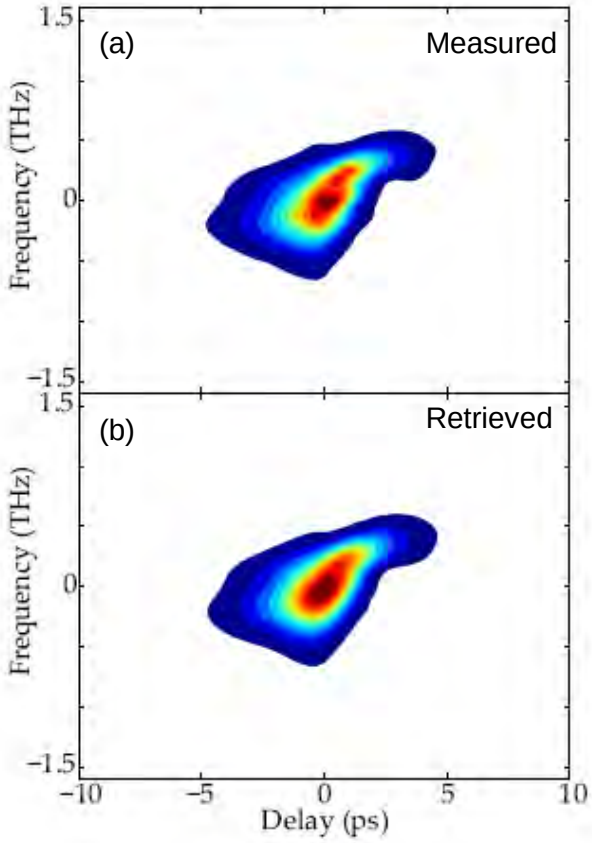

FIGURE 3.15: Measured (a) and Reconstructed (b) spectrograms of retrieved test pulses with an average power of 0.2 mW.

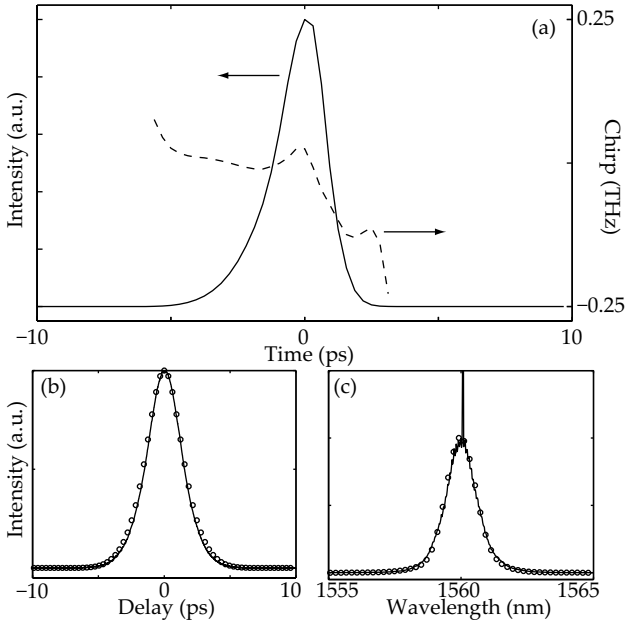

FIGURE 3.16: a) Retrieved temporal intensity and corresponding chirp of the test pulse. b) Measured and numerical autocorrelation traces from the retrieved test pulse. c) Measured and numerical spectra of the test pulse. In all cases the retrieved test pulse has an average power of 0.2 mW.

3.5 Frequency Resolved Electro-Absorption Gating

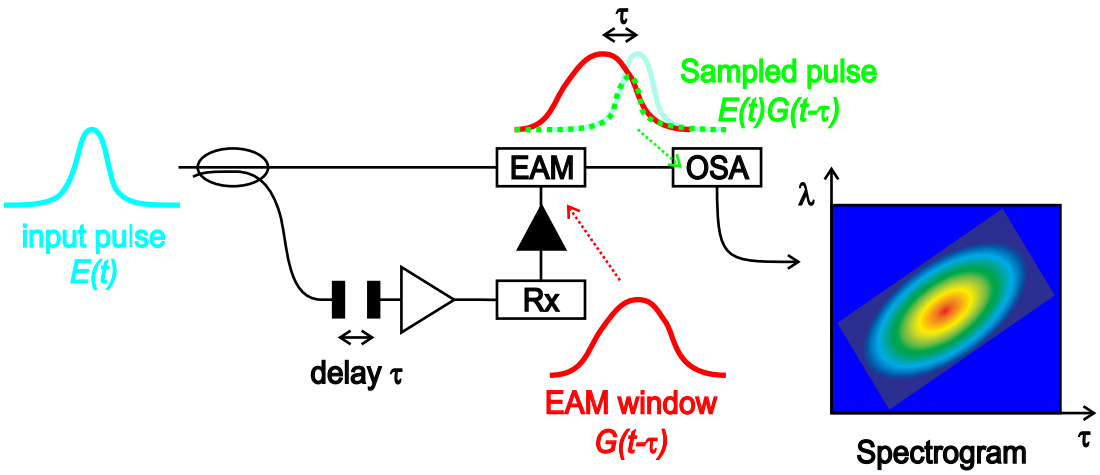

FIGURE 3.17: Sketch of the operation principle of an EAM-FROG.

In [66], it was demonstrated that it was possible to replace the nonlinear optical interaction by implementing the gating with a temporal intensity modulator. This method is quite interesting because it is extremely sensitive, since it relies on a linear process, and it can be implemented using devices designed for optical telecommunications.
In the lab, Dr Michaël Roelens and Dr Benn Thomsen developed this technique, incorporating an EAM into the system. For this reason, this pulse characterization method is called EAM-FROG. Fig. 3.17 shows the basic schematic of the set-up, implemented by them, which is now regularly used in the lab. The input pulse under test is split into two replicas, one is the probe signal (E(t)) that then passes through the EAM. The other one, which is the gate signal, is delayed by a motorized variable time delay, $G(t-\tau)$, and used to drive the EAM. The gated signal is then spectrally resolved by an OSA, the resulting signal can thus be expressed by Eq. 3.5. The choice of directly converting part of the signal into an electrical signal, which is used to drive the modulator, makes the system self-referenced and allows shorter electrical pulses to be created than the sinusoidal signals available from an RF signal generator synchronized to the probe.
Fig. 3.18 shows an example of EAM-FROG characterization. In particular, the same ∼2 ps sech pulse, generated from an EFRL at the operating wavelength of 1542 nm, is shown. Fig. 3.18.a and Fig. 3.18.b depict the measured and reconstructed spectrograms respectively. As can be seen, they look very different from the FROG ones. First at all, they are not a symmetric function of the time and they extend over a broader temporal range. This is because in this case the gate function is given by the optical transmission window of the EAM that is ∼10-16 ps long. The rms error in the temporal intensity arising from the mismatch between the retrieved spectrum and the measured spectrum for these pulses is 0.27%. The main difference between the two graphs is due to the setting of the noise floor of the measured trace, which is higher than the corresponding retrieved one.

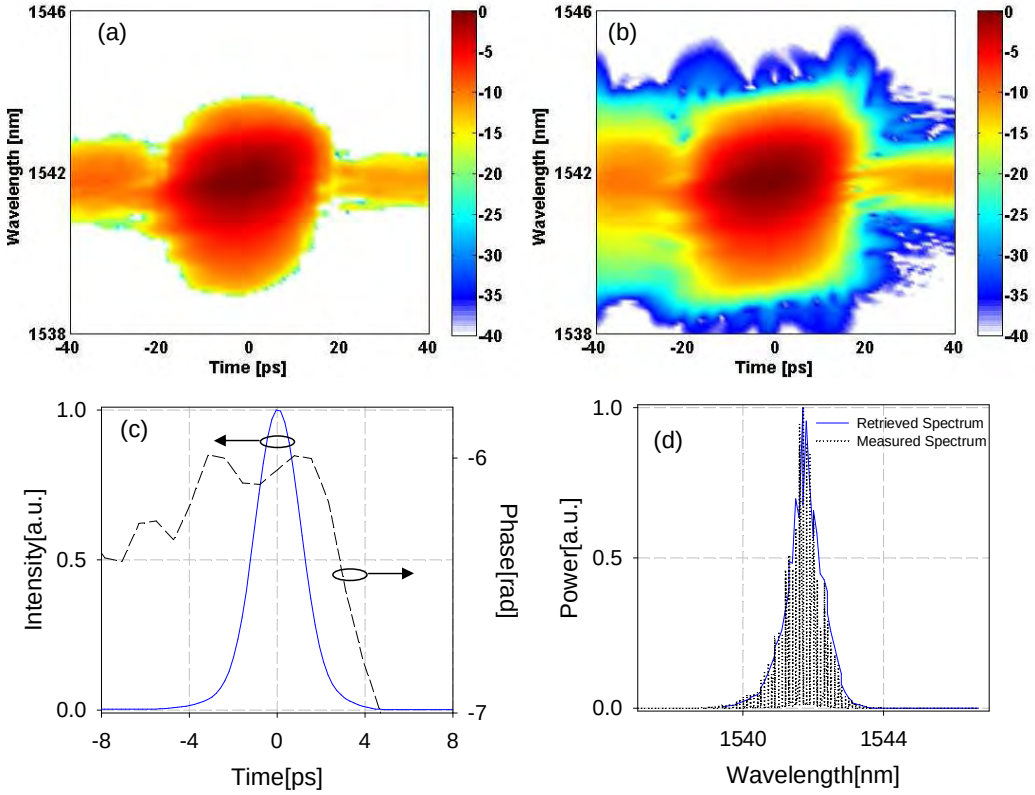

FIGURE 3.18: Spectrogram of 2 ps sec-hyperbolic generated from an harmonically mode-locked EFRL using the EAM FROG technique. Measured (a) and Reconstructed (b) spectrograms, retrieved temporal intensity and chirp (c), and the retrieved spectral intensity and chirp compared to the independent measured spectrum (d).

Fig. 3.18.c displays the corresponding retrieved pulse intensity and phase in the temporal domain, while Fig. 3.18.d shows the corresponding measured and retrieved spectral intensities.

3.6 Comparisons of various pulse measuring techniques

As already underlined, the precise shape of the shaped pulses affects directly the performance of the schemes implemented in this thesis. For example, a non flat top of the rectangular pulses after the SSFBG will be translated directly into amplitude noise at the output of the re-timing and reshaping system, in the techniques described in Chapters 4 and 5. It is hence necessary to have an accurate measurement of the pulse shapes. The next question that arises is how well matched is the picture obtained with the different measuring techniques to the actual waveform. For this reason, the optical sampling oscilloscope trace is compared against the SHG-FROG and EAM-FROG techniques.

The measured (a) and reconstructed (b) SHG-FROG spectrograms of the 20 ps rectangular pulses are shown in Fig. 3.19. The relative error between the measured and retrieved spectrograms was less than 0.34%, which is a fair value of convergence. The

measured (a) and reconstructed (b) EAM-FROG spectrograms of the 20 ps rectangular pulses are shown in Fig. 3.20. In this case the relative rms error was ∼0.17%. As can be noticed, because the EAM-FROG is a linear process compared to the SHG-FROG (lower power levels required), its corresponding measured spectrogram shows more spectral sidelobes compared to the one measured with the other technique. Their corresponding retrieved temporal intensities are plotted in Fig. 3.21 against the optical sampling trace, evaluated in Section 3.2, while the corresponding spectra are shown in Fig. 3.22. While the SHG-FROG and the optical sampling traces were taken at the same time, the EAM-FROG trace was measured at a different time. To ensure that the pulse forms were similar, the central wavelength of the signal was chosen so that similar spectral profiles were obtained in all the cases. However, this made it very difficult to reproduce exactly the same pulse shape. Indeed even a slight detuning of the pulse compared to the central wavelength of the grating can affect the detailed shape of the rectangular pulse itself. This might explain the difference of the profiles at the top of the rectangular pulse. However, excellent agreement between the EAM-retrieved and the optical sampling trace, at the edges of the pulse, is achieved. Comparing the reconstructed spectrum of the EAM-FROG (blue trace) with the measured one (black

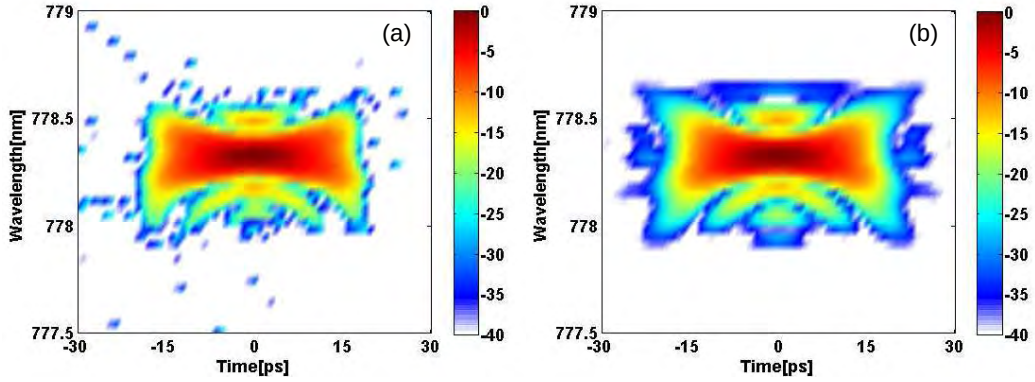

FIGURE 3.19: SHG-FROG results for the 20 ps rectangular pulses. Measured (a) and Reconstructed (b) spectrograms.

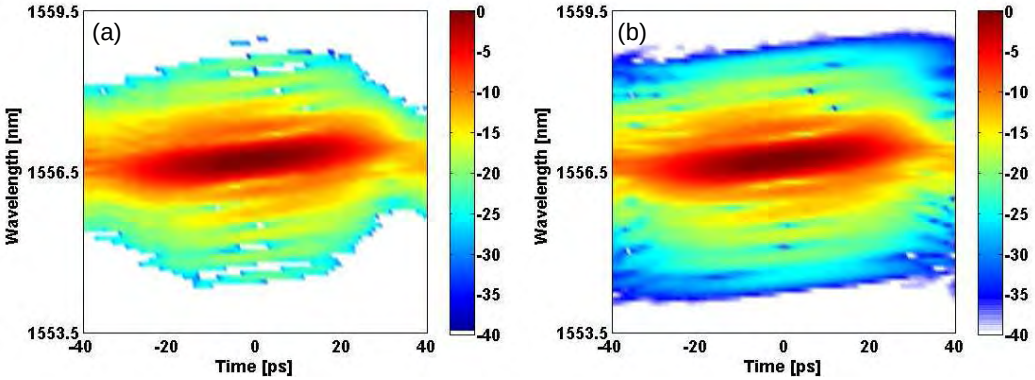

FIGURE 3.20: EAM-FROG results for the 20 ps rectangular pulses. Measured (a) and Reconstructed (b) spectrograms.

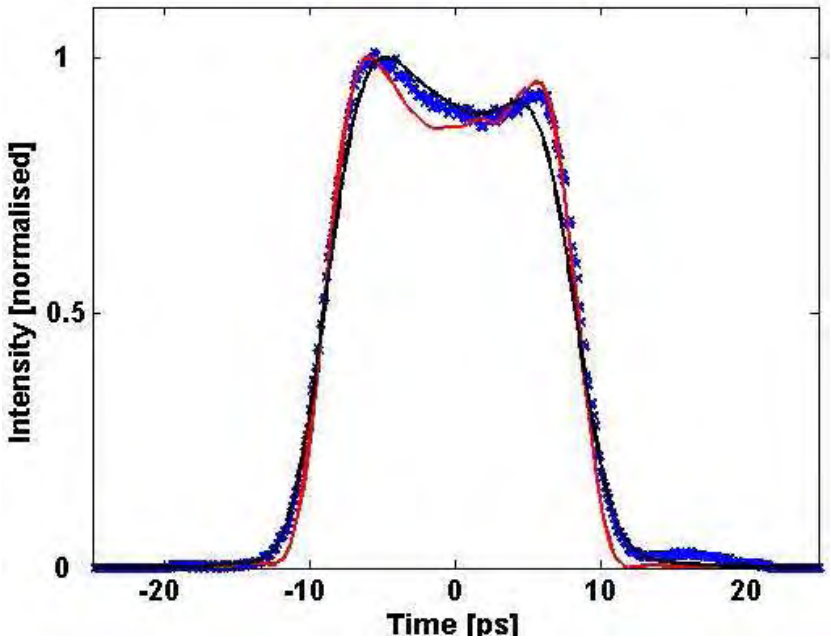

FIGURE 3.21: Intensity traces for the 20 ps rectangular pulses, measured in the following different ways: optical sampling (blue), SHG-FROG (red)and EAM-FROG (black).

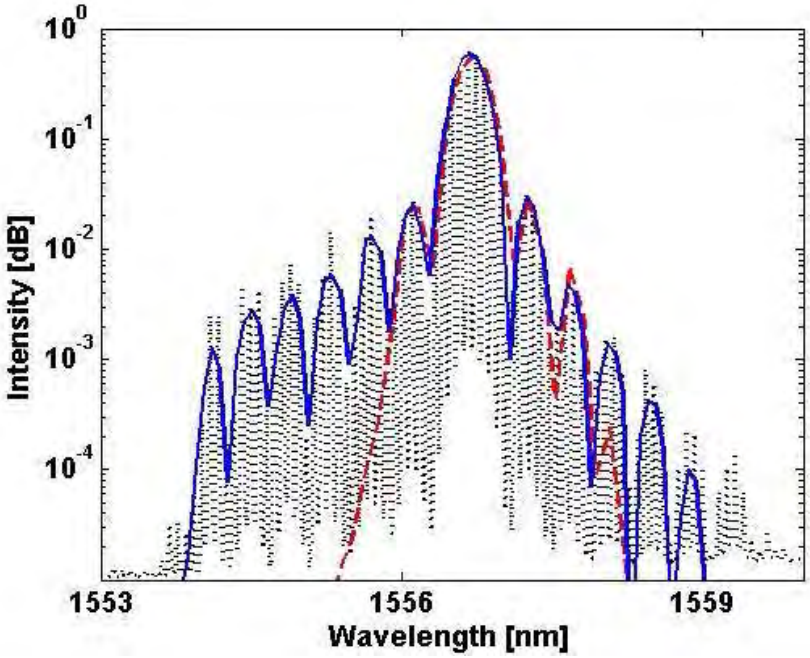

FIGURE 3.22: Spectral Intensity traces for the 20 ps rectangular pulses, measured in the following different ways: optical spectrum analyzer (dotted black), SHG-FROG (red) and EAM-FROG (blue).

dotted trace), see Fig. 3.22, it can be seen that the EAM-FROG is able to reproduce nearly all the sidelobes that the grating covers, implying a dynamic range as high as $\sim 40\ dB$, as discussed above.

On the other hand, in Fig. 3.22 it is also very clear that the reconstructed spectrum

originated from the SHG-FROG (red trace) cannot resolve more than two sidelobes, due to the much lower dynamic range ($\sim$ 15 dB). In this way, the information that can be retrieved from the spectrogram might not be enough to properly reconstruct the pulse, especially for the finer temporal details. This can explain why the SHG-FROG reconstructed temporal intensity shows a slightly different profile compared to the other traces.
However, all things considered, there is a good agreement between the three profiles. Indeed, all traces show some variation on the amplitude of the top part of the pulses. The relative ripple depth at the top of the square pulses, defined as the ratio of the difference between the highest and lowest intensity points of the ripple at the maximum intensity of the pulse, is less than 14% for all the cases.

3.7 Conclusion

In this Chapter, different techniques to measure ultrafast optical pulses are discussed. Direct detection techniques using fast photodetectors are inadequate for such applications and optical autocorrelation methods give very little information when the pulse under test has a quite complicated shape, such as the ones used in this thesis.
The optical sampling oscilloscope technique has been used to assess different pulse shapes obtained after reflection by SSFBGs. The temporal resolution of this technique is $\sim$ 2 ps, mainly limited by the sampling pulsewidth. The direct measurements obtained with the optical sampling oscilloscope were compared against a commercial SHG-FROG device and a EAM-FROG device, implemented in the lab. The rectangular pulse is chosen for comparison and its characterization shows a good agreement between the three different techniques. Finally, the SHG-FROG technique in a QPM $LiNbO_3$ device is discussed.

Chapter 4

Retiming technique using rectangular pulses shaped in an SSFBG

4.1 Introduction

As pointed out in 2.2, the effects of amplifier noise accumulation, fibre nonlinearities and fibre dispersion can cause energy fluctuations and pulse position fluctuations on the transmitted optical signals. The degradation due to timing jitter can become a particular problem within long-haul, high bit-rate transmission systems. Indeed the interaction of the individual data pulses with amplified spontaneous emission accumulated in the system can lead to arbitrary changes in the group velocity of the propagating pulses. These group velocity changes translate to random timing jitter of the pulses as a result of the transmission line dispersion. Such timing jitter can severely compromise the performance of optical switches and demultiplexers, and effectively limit the transmission distance of the system, especially at high date rates ($> 40\ Gb/s$) [21]. All-optical regeneration techniques, capable of operating at speeds beyond the limits of electronic processing devices, are therefore of great relevance to future high bit-rate long-haul communication networks.

The impact of timing jitter in long-haul Non Return to Zero (NRZ) systems is less severe than in case of Return to Zero (RZ) ones. This can be easily explained because of the wider temporal width and flatter top of the NRZ format compared to the RZ one. Indeed if we want to perform an optical switch with another ultra-short pulse, a NRZ pulse will be more insensitive to possible temporal misalignment of the signal. For this reason, rectangular-like pulse forms can be very useful for applications that involve nonlinear optical switching of short data pulses. The benefit of using this kind of pulse has been previously demonstrated in a timing-jitter-tolerant demultiplexing scheme operat-

ing at repetition rates of up to 80Gb/s [52, 70]. This scheme used shaped rectangular pulses as the control signal to a nonlinear demuxing switch based on a nonlinear optical loop mirror. The corresponding broad switching window (relative to the pulses to be demultiplexed) relaxed the tolerance on the relative timing between the data and the clock, although it is to be appreciated that the original jitter itself was not eliminated and was passed on to the demultiplexed signal. In this Chapter the concept is extended and the shaping function is applied to the data itself, rather than to the control signal, before feeding it into the NOLM. This allows the elimination of the timing jitter introduced in short pulse transmission systems, provided that a clean clock signal is available. The technique relies upon switching the reshaped rectangular pulses with a synchronous optical clock signal. The required linear pulse reshaping is performed using a Superstructured Fibre Bragg Grating, as already discussed in Section 2.6. Note that this reshaping mechanism is reasonably robust and not particularly sensitive to the input pulse shape, wavelength misalignment, and grating imperfections (see [17]). Furthermore, this scheme can be used in conjunction with a common reshaping regenerator with a nonlinear characteristic similar to that of an ideal hard limiter in order to avoid the transfer of any amplitude noise from the original signal to the regenerated signal. How this can be implemented in a single NOLM switch will be discussed in Chapter 5. A similar technique for generating a rectangular switching window at the input of an optical regenerator was developed in [71] in a 160 Gb/s transmission experiment. In that scheme the pulse shaper was based on obtaining controllable pulse broadening in a Hi-Bi fibre due to polarization mode walk-off. However, the polarization sensitivity of this approach is likely to represent a practical limiting factor for its application within a real system. Also, the width of the rectangular pulse cannot be arbitrarily chosen if a flattened-top signal is desired. In [72], a rectangular switching window was obtained in a NOLM by making use of the walk-off generated between the co-propagating control and signal pulses in the fibre incorporated in the loop. This scheme however compromises the efficiency of the switch and makes the operation of the system strongly wavelength dependent.

This Chapter opens by explaining the basic principle of the pure re-timing technique used; then it explains how timing jitter was measured and artificially induced in the system and, finally, it describes the experiment and the results achieved.

4.2 Retiming technique: Basic principle

The basic idea behind the re-timing scheme is shown in Fig. 4.1. The figure shows schematically what is happening in an all-optical switching stage in the instance that no re-timing technique (a), or a rectangular-switching-window re-timing technique (b), is applied to the signal. As can be seen in case (a), large timing jitter of the signal pulses results in a significant pulse amplitude noise at the output of the switch when the signal

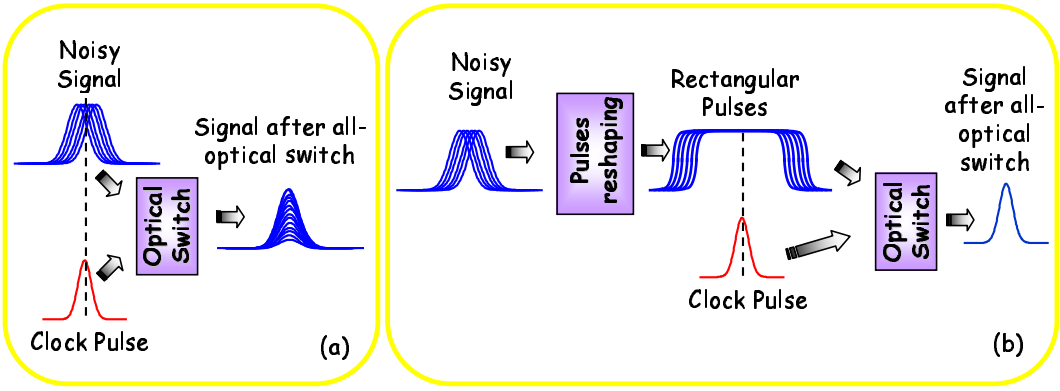

FIGURE 4.1: Principle of the Re-timing technique as applied to RZ signals: Switching without (a), and with (b), use of shaped rectangular pulses.

is switched by a short optical pulse. The re-timing technique, case (b), relies on the incorporation of an intermediate stage within which each data pulse is reshaped into a rectangular pulse in the time domain expanding each data pulse prior to being injected into the switch. The maximum tolerable amount of timing jitter that it is possible to suppress is defined by the width of the rectangular pulse and cannot be bigger than the allowed temporal bit misplacement for the system, i.e. the duration allocated to each data bit. This width can be readily adjusted to fit the specific jitter characteristic of a given transmission system. It has already been demonstrated that SSFBG technology is suitable for generating temporal features as short as 3.1 ps [73], a number which by no means represents the ultimate limit of the technology. The combination of rectangular pulses, having such a short pulse width, with nonlinear optical switches that exploit the ultrafast Kerr effect in optical fibres (fs response times) should allow the regeneration of signals with bit rates as high as 320 Gb/s.

In a subsequent step, this signal is switched by a clean short-pulse clock signal, which is temporally aligned at the nominal centre of the rectangular data pulses. The clock signal ensures that the output signal is retimed and that it maintains the original pulse width. In this way, even if the optical switching window is very short, the flat-topped signal generated by the SSFBG ensures that the switch is insensitive to any mistiming of the original signal.

4.3 Timing jitter measurements

It is very important to generate controllable and quantifiable optical timing jitter in order to be able to characterize the performance of the retiming system. Two different approaches can be used to characterize the random pulse to pulse timing fluctuation. The first one measures the integrated noise of the power spectrum of the signal under investigation around the RF harmonics [74]. Such power spectra are readily obtained by launching the signal onto a suitably fast photodetector and by measuring the output

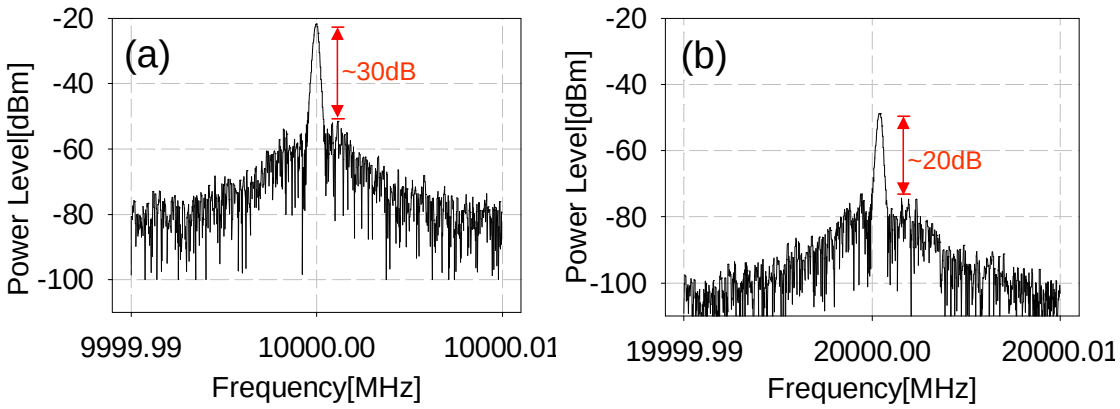

FIGURE 4.2: Example of RF spectral measurements for 10 GHz and 20 GHz respectively. ResBW=300 Hz, Span=20 kHz, SWP=1.3 s, VidBW=10 kHz.

with an electrical spectrum analyzer.

The output intensity profile of a idealized perfect signal can be expressed as a pulse train of identical pulses spaced by the bit period. On the other hand, real signals exhibit a certain amount of random fluctuations that add to the noise-free idealized signal. If the random variations of the time interval between successive pulses in the train are assumed to be small compared to the bit period of the idealized train, it can be shown that it is possible to distinguish between two different noise contributions in the frequency domain: one related to the amplitude jitter, and the other to the timing jitter [74]. In particular, this timing jitter term increases with the increasing order of the frequency components (higher harmonics), while the amplitude noise is constant for all harmonics. This fact permits the two different types of noise to be distinguished by analyzing the noise bands that exist at different harmonics.

Unfortunately, in my experiments, the measured electrical power spectrum was restricted by the bandwidth limitations imposed by either the photodetector or the spectrum analyzer. At the time of the experiments reported here, the available units were a spectrum analyzer with a frequency range from 100 Hz to 33 GHz and a photodetector with a -3 dB bandwidth of less than 7.5 GHz, a value which is even lower than the first harmonic, 10 GHz, of the assessed signal. Fig. 4.2.a and Fig. 4.2.b show an example of the measured power spectra around the first and second harmonics, 10 GHz and 20 GHz respectively. Because of the limited bandwidth of the photodetector, the value of the 20 GHz harmonic is significantly lower compared to the 10 GHz one. Normally, this measurement would require a comparison of the power spectra around several harmonics of the signal. Therefore, it has not been possible to take precise noise measurements using this technique.

The second approach, which is the one used in this thesis, uses a high speed sampling oscilloscope to directly measure temporal histograms at the FWHM point on the leading edge of the pulses. Fig. 4.3 shows an example of how the temporal histograms are taken. As can be seen, the histogram provides the value of several important parameters, such

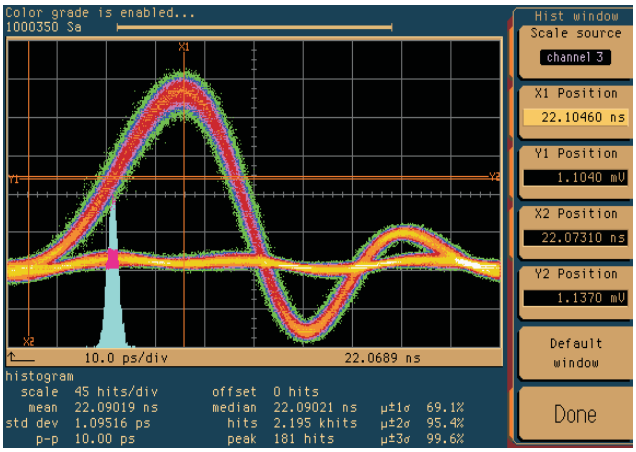

FIGURE 4.3: Example of a histogram trace taken with the oscilloscope.

as the mean, μ, that is the most prevalent value, the standard deviation, σ, that gives information on how spread the values are, and the peak-to-peak value that gives the range of the histogram. Additional statistics on the number of hits falling within $\mu \pm \sigma$, $\mu \pm 2\sigma$, and $\mu \pm 3\sigma$ give an idea of how close the histogram is to a Gaussian shape. Obviously the timing jitter of the instrument itself has to be considered when evaluating the overall timing jitter measurement obtained with this technique. In particular the timing jitter standard rms deviation in the instrument ($\sigma_{instrument}$) can be assumed to have a normal distribution. Then, the rms deviation of the signal, σ_{signal}, relates to the rms deviation measured by the oscilloscope, $\sigma_{measured}$, as:

$$\sigma_{measured} = \sqrt{\sigma_{signal}^2 + \sigma_{instrument}^2} \tag{4.1}$$

in the case that the measuring jitter has also a normal distribution. Here the $\sigma_{instrument}$ is equal to $\sim 0.8\ ps$. However in some of the experiments several different RF signal generators had to be synchronized so that the rms deviation of the instrument, due to the non-optimum synchronization of the trigger signal fed into the oscilloscope, would increase $\sigma_{instrument}$ up to $\sim 1\ ps$, as for the example shown in Fig. 4.3.

4.4 Artificial introduction of Timing jitter

As I already pointed out, this is a proof-of-principle experiment and the performance of the retimer was not assessed in a transmission experiment. As a lab demonstration, timing jitter had to be artificially introduced into the system. To do that a linearly chirped FBG was used with a bandwidth which was broad enough to encompass the full spectrum of the pulses. Its reflectivity and group delay are shown in Fig. 4.4. The FBG was mounted on a stretching rig, which allowed the tension applied to the grating to be periodically modulated, and thus to modulate the physical position from which the pulses were reflected from within the grating. Indeed, as soon as tension is

applied to the grating, its reflectivity and group delay drift slightly in wavelength, see Fig. 4.5. A pulse at a particular wavelength within the FBG passband is now reflected at a different point along the grating and therefore the overall distance it travels, or the time required to go through the FBG will change. A continuous modulation of the FBG tension will translate into (deterministic) timing jitter at the output of the system. In this experiment, a sinusoidal modulation at a frequency of 500 Hz was used, which was determined by the bandwidth of the piezo-electric stretching stage. A photograph of the stretching rig I built is shown in Fig. 4.6, where a visible Helium Neon source was used to highlight the position of the fibre on the piezo-electric stage. Because the reflected pulses acquired a chirp, after reflection from the FBG, an additional chirped fibre grating or a length of fibre was required to produce unchirped pulses. In this experiment the chirp introduced by the grating was 10 ps/nm, so a 90 m-long DCF had to be used to remove the chirp ($D_{DCF} \simeq -107\ ps/nm/km$).

As can be seen from Fig. 4.4, the spectral response of the chirped grating, used to introduce jitter in the system, does not have an ideal rectangular shape with a linear phase. When some tension is applied on the FBG, its central wavelength shifts by up to ∼1.4 nm, see Fig. 4.5. The transmitted signal, with a sech optical spectrum profile centered at 1556.8 nm and a FWHM of 1.2 nm, sees a different reflectivity and phase of the FBG according to the tension applied and this might cause some distortion. Obviously, in a real system, timing jitter is expected to result from the propagation of the signal along the amplified and dispersive system, so no spectral distortion is expected.

To calculate the total timing jitter of the pulse, the fluctuations of the timing jitter, introduced by the pulse source itself, have to be added to the artificial timing jitter induced. In particular the total timing jitter is the convolution of the induced timing jitter and the timing jitter of the source itself. Fig. 4.7 shows a simulation of total jitter distribution for a pulse source with an inherent rms jitter of 0.2 ps, which is the timing jitter of the mode-locked laser used in the experiment, as estimated in Sec. 3.2. For an

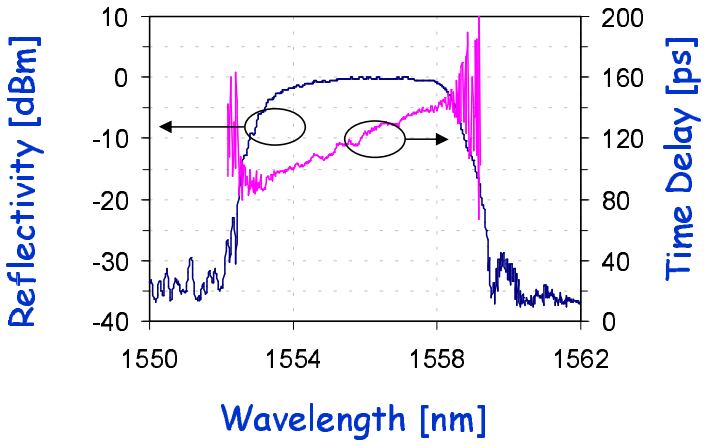

FIGURE 4.4: Reflectivity and group delay profiles of the linearly chirped fibre Bragg grating used to introduce timing jitter in the system.

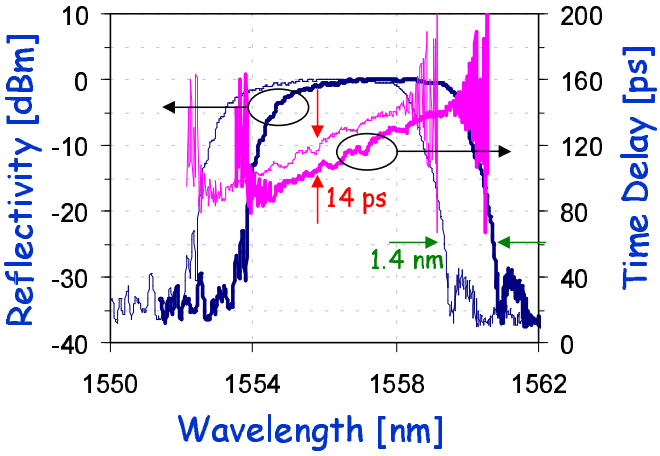

FIGURE 4.5: Comparison of Reflectivity and group delay profiles of the linearly chirped fibre Bragg grating with (darker solid lines) and without tension applied (lighter solid lines).

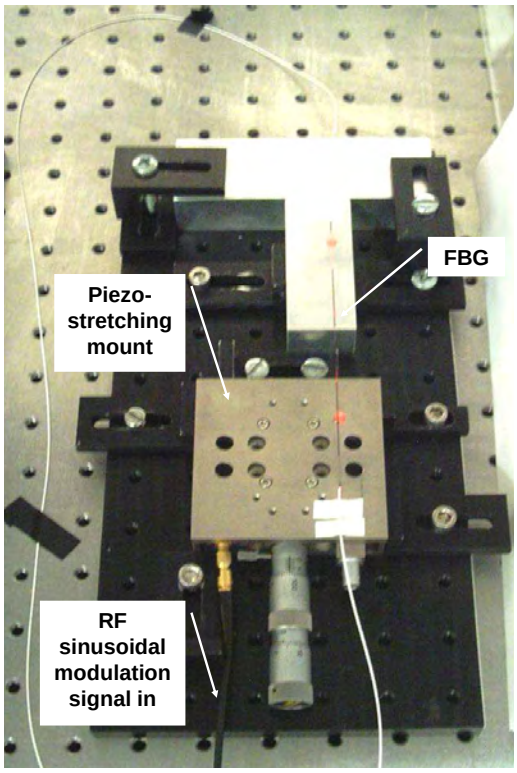

FIGURE 4.6: Photo of the grating mounting to generate timing jitter. (For illustrative purposes, a red-light source has been used to illuminate the fibre.)

induced timing jitter equal to ∼8.8 ps, the peak-to-peak timing jitter is ∼10 ps (rms is ∼3.1 ps), as shown in Fig. 4.7. Note that the induced timing jitter (8.8 ps in this case) is a figure directly deduced by the peak-to-peak value of the sinusoidal modulation applied to the FBG stretcher. As can be seen, the probability of finding the pulse at a particular delay from the ideal case of no added jitter is double peaked, as expected

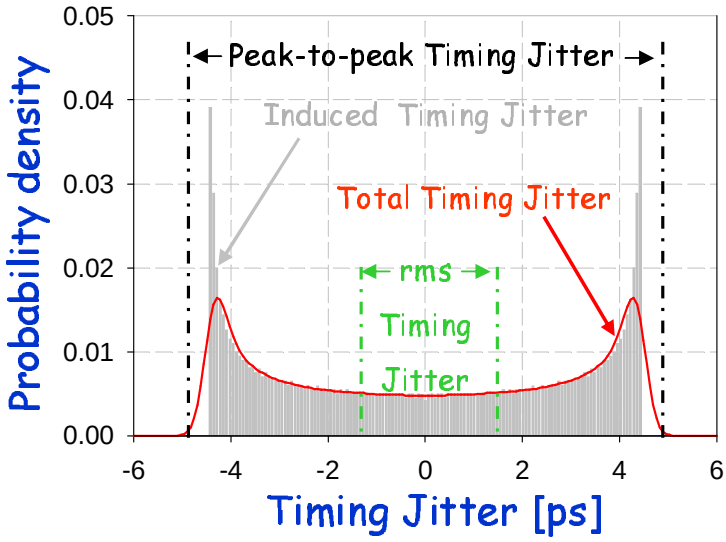

FIGURE 4.7: Simulated jitter distribution of a pulse for an induced timing jitter of ~8.8 ps with an inherent rms jitter of 0.2 ps.

from the sinusoidal modulation of the laser clock frequency. Fig. 4.8 clarifies this last point, where the linear (red trace) and sinusoidal (blue trace) frequency modulations are compared. When linear modulation is considered, there is a one to one relation between the modulation of the laser clock frequency and the induced timing jitter. However, when sinusoidal modulation is used, for small values of frequency modulation the one to one mapping still holds, while for larger values, corresponding to the peak of the sine profile, a fixed range of frequency modulation corresponds to a much smaller range of induced timing jitter, increasing the probability of those specific values of timing jitter.

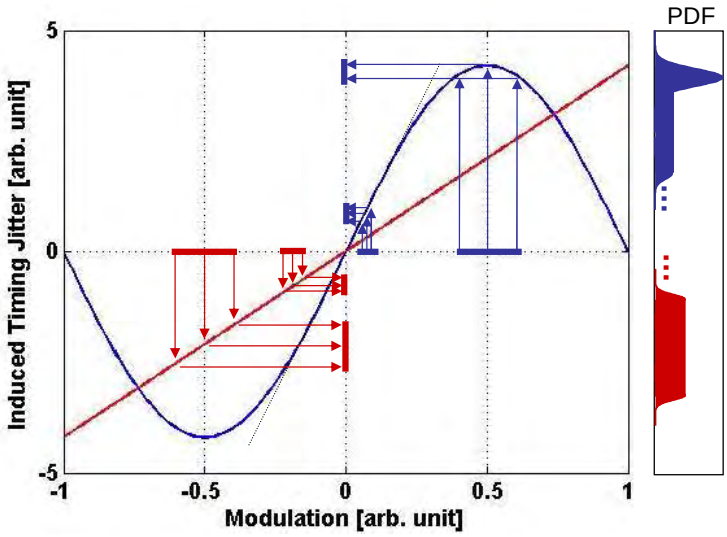

FIGURE 4.8: Sketch of how different frequency modulation profiles can change the induced timing jitter profiles. Inset: Sketch of the timing jitter probability distribution function (PDF).

4.5 Experimental Set-up

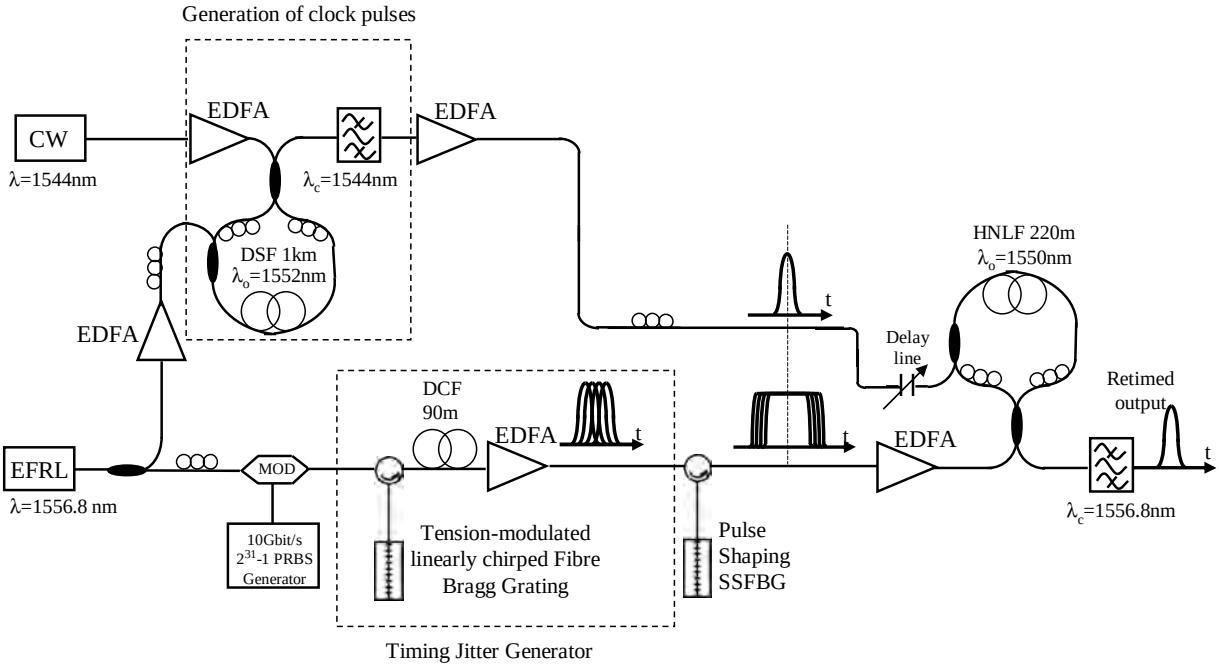

FIGURE 4.9: Experimental Set-up. MOD: modulator.

The set-up used to implement the optical retiming system, is shown in Fig. 4.9. As mentioned before, the re-timing technique relies on broadening each data pulse in the time domain, by reshaping it into a rectangular pulse whose duration defines the maximum tolerable amount of timing jitter that can be compensated. In a following step, the data are switched by a short-pulse clock signal within a NOLM.

Pulses from a 2.5 ps 10 GHz actively mode locked erbium fibre ring laser, operating at 1556.8 nm, were first split using a coupler into two separate channels. The first one was modulated by a $2^{31} - 1$ pseudorandom bit sequence (PRBS), using a lithium niobate modulator, and then coupled onto the linearly chirped FBG, by means of an optical circulator, in order to introduce timing jitter. This FBG was mounted on a piezoelectric stage driven by a RF signal generator at a frequency modulation of 500 Hz. An example of the spectrum (a) and the autocorrelation (b) traces of the signal is shown in Fig. 4.10 when no timing jitter was induced. The signal was then coupled onto the reshaping SSFBG by means of a second optical circulator in order to shape the pulse. The SSFBG, which produces rectangular pulses with a full width of ∼20 ps from 2.5 ps sech pulses, was described in Section 2.6. In Chapter 3 spectral traces of the signal after reflecting off the grating are given together with attempts to characterize its temporal shape (see Fig. 3.21 and Fig. 3.22). The shaped data pulses were then used as the input signal for a NOLM at an average power of ∼16 dBm. The nonlinear element in the NOLM was a HNLF, whose parameters are reported in Tab. 3.1.

The other component of the stream split-off from the laser was first amplified and then fed to the control port of another NOLM, employed as a wavelength converter (WC).

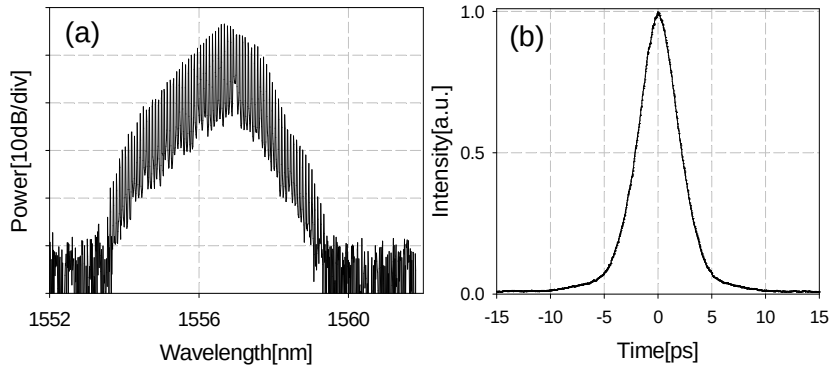

FIGURE 4.10: Optical spectrum of the sec-hyperbolic after being coupled onto a linearly chirped grating (a) and corresponding autocorrelation profile (b). The autocorrelation trace has a FWHM of 4.3 ps (corresponding to a pulse FWHM of ∼2.5 ps if sech-pulses are considered).

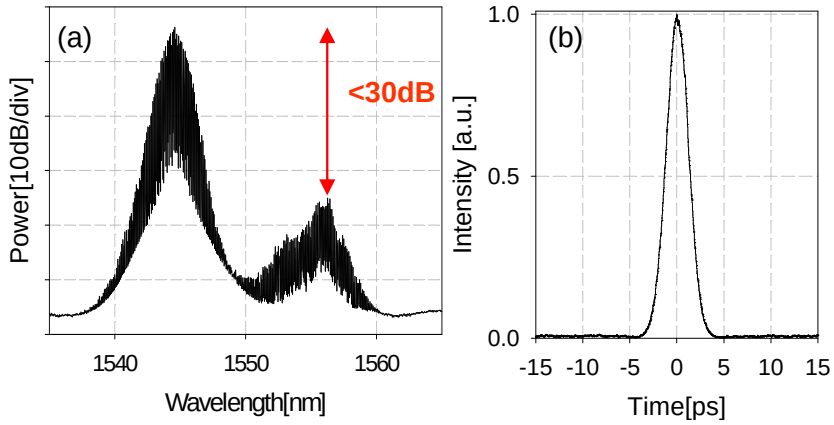

FIGURE 4.11: Optical spectrum of signal after the WC-NOLM (a) and the corresponding autocorrelation trace (b): the autocorrelation trace has a FWHM of 2.8 ps.

The WC-NOLM incorporated a 1 km long Dispersion Shifted Fibre (DSF) with a zero-dispersion wavelength at 1552 nm. The nonlinear switch allowed us to modulate the output of a CW DFB laser operating at 1544 nm using the 1556.8 nm control pulses. By appropriately setting the polarization of light within the WC-NOLM, and filtering out the 1556.8 nm control pulses at the loop output, a 10 GHz train of high-quality 2 ps pulses at 1544 nm was generated. The spectrum and autocorrelation traces are shown in Fig. 4.11. Finally the pulses, at an average power of ∼15 dBm, were used to feed the control port of the second NOLM as shown in Fig. 4.9. Fig. 4.12 shows the spectrum of the signal at the very end of the system when the control pulse was switched off, case (a), and on, case (b), respectively. As can be seen, the shape of the spectrum from a sinc-function (rectangular shape in time domain) becomes Gaussian-like, as well as more powerful, when the signal is properly switched by the control pulses. Fig. 4.12.c shows the corresponding autocorrelation profile, when the signal is then filtered out by a broad-band filter.

Importantly for this demonstration, the control train and the signal train of this NOLM were synchronized at two different wavelengths. In this way the data were switched back

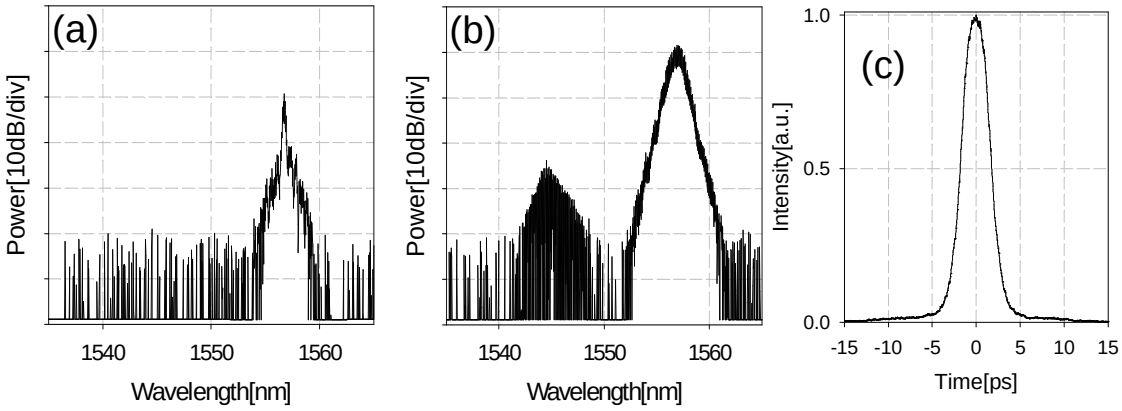

FIGURE 4.12: Optical spectrum of signal after the second NOLM when the control pulse was respectively off (a) and on (b). c) Corresponding autocorrelation trace: the autocorrelation trace has a FWHM of 3.6 ps.

to their original pulsewidth by a short pulse clock signal and retimed. The clock signal has to be temporally aligned at the nominal centre of the rectangular data. This was achieved by using a tunable free-space delay line at the control signal.
In the next section I present some results in order to examine and evaluate the performance of the switch, with and without the pulse shape grating.

4.6 Results and discussion

In order to evaluate the performance of the system eye-diagrams, timing jitter and amplitude noise distribution as well as BER measurements were carried out.
Fig. 4.13 shows some eye-diagrams at various positions and settings of the system: the top-row shows the initial data at the input of the system, the middle-row shows the output of the switch when no reshaping has been applied to the pulses and finally the bottom-row shows the output of the system when the re-timing technique has been applied. In order to give a complete evaluation, these cases for three different settings of the system are examined, i.e. for three different values of the induced timing jitter. Starting from the left hand side the eye-diagrams show the case where no timing jitter is induced, then the case where ∼5.1 ps timing jitter was induced (corresponding to a rms and peak-to-peak values of the jitter distribution of 2.8 ps and 12 ps respectively) and finally one of the most extreme cases of timing jitter, where ∼11.9 ps timing jitter was introduced in the system (corresponding to a rms and peak-to-peak values of the jitter distribution of 4.5 ps and 17 ps respectively). This last case was considered in order to provide a significant test of the re-timing system.

The eye diagrams of Fig. 4.13.a and Fig. 4.13.c, in the case when no timing jitter was applied to the data pulses, demonstrate that the re-timing system does not in itself introduce significant additional noise to the signal. Next, the quality of the output signal for the case when timing jitter was deliberately applied to the incident data pulses is

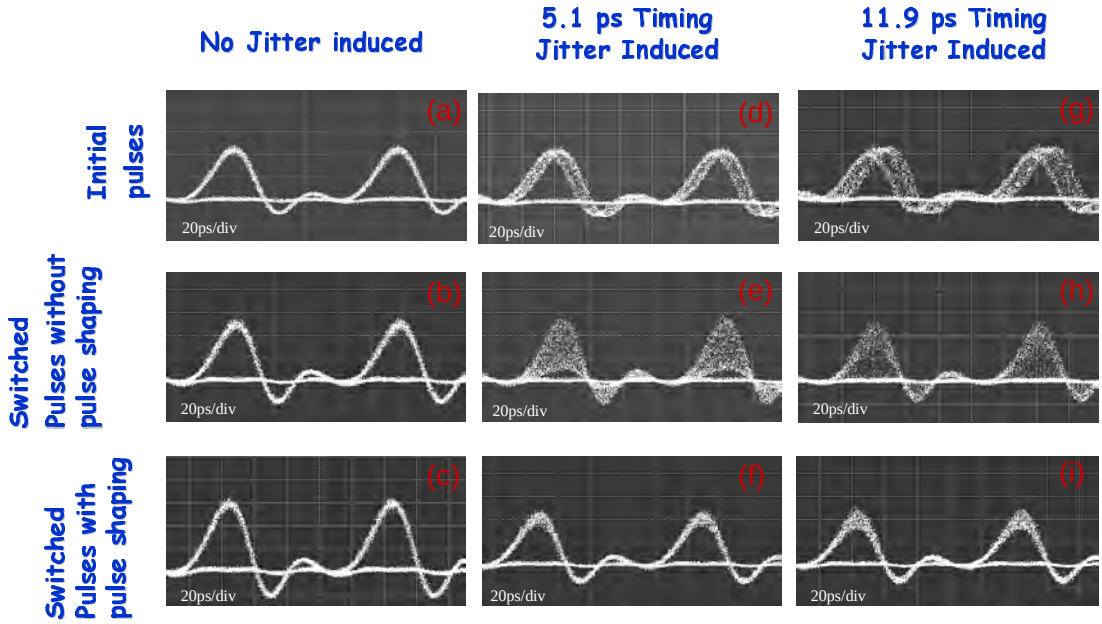

FIGURE 4.13: Eye diagram at various positions and settings of the system. Top-row (a, d, g): at the input of the system. Middle-row (b, e, h): at the output of the switch when no reshaping has been applied to the pulses. Bottom-row(c, f, i): at the output of the system when the re-timing technique has been applied. Horizontal Scale: 20 ps/div. Scope bandwidth: 20 GHz.

examined. In these cases, as can be seen in Fig. 4.13.e and Fig. 4.13.h, the large timing jitter of the signal pulses results in a significant pulse amplitude noise and a complete closure of the eye for both cases. However when pulse reshaping is applied, Fig. 4.13.f and Fig. 4.13.i, the timing jitter is eliminated and open eye diagrams are again obtained. An open eye is obtained also for the most extreme case of timing jitter, albeit with a slight increase in amplitude noise. This increase of amplitude noise was linked to the non-uniformity of the rectangular pulse-shape and to the spectral distortion of the signal during the introduction of timing jitter. Note that the non-uniformity (non flat-top) is related to the specific SSFBG we used to create a rectangular pulse and, in the real system, the timing jitter is already present in the pulses, so no spectral distortion due to the timing jitter generator would be introduced. Fig. 4.14 explains how the non flat-topped signal introduces amplitude noise at the output of the switch: because of the timing jitter, the arrival time is different for different pulses, so the switching will be at different positions along the rectangular shape. In this way, the amplitude of the switched signal will be described by the same rectangular-top fluctuation of $\varepsilon \sim 0.14$.

Fig. 4.15.a and Fig. 4.15.b present timing jitter distributions for the same three different cases of timing jitter induced both before and after the re-timing system respectively, measured as described in Sec. 4.3. As can be seen the jitter distributions for the pulses at the input of the system are double peaked, as expected from the sinusoidal modulation of the tension applied on the chirped grating, see Fig. 4.7 and Fig. 4.8. Fig. 4.15.b shows that the timing jitter of the retimed pulses in both cases approaches that of the original

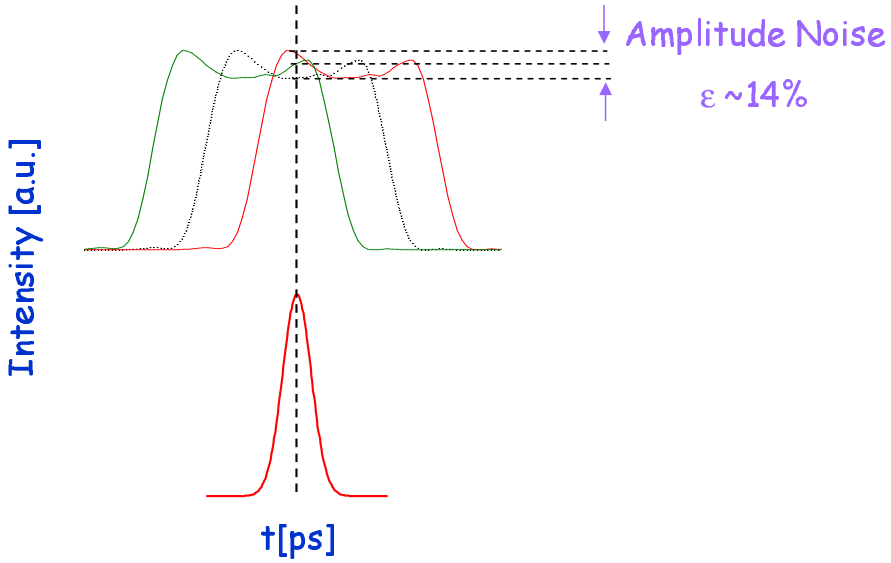

FIGURE 4.14: Sketch of how the non-uniformity of the square pulses can introduce amplitude noise.

seed laser.

Fig. 4.15.c shows the standard deviation of the timing jitter both before and after the re-timing system as a function of the induced timing jitter. The rms jitter values of the

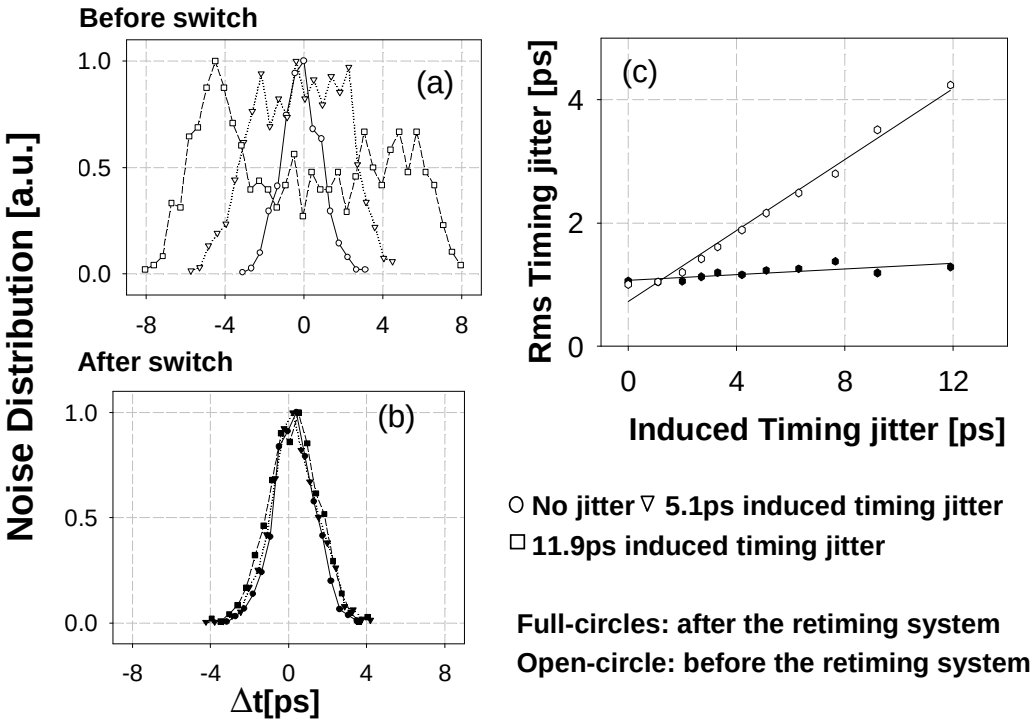

FIGURE 4.15: Noise Distributions for 3 different cases of timing jitter before (a) and after (b) the retiming system. (c) Timing jitter standard deviation versus induced timing jitter characteristic before (open-circles) and after (full-circles) the retiming system.

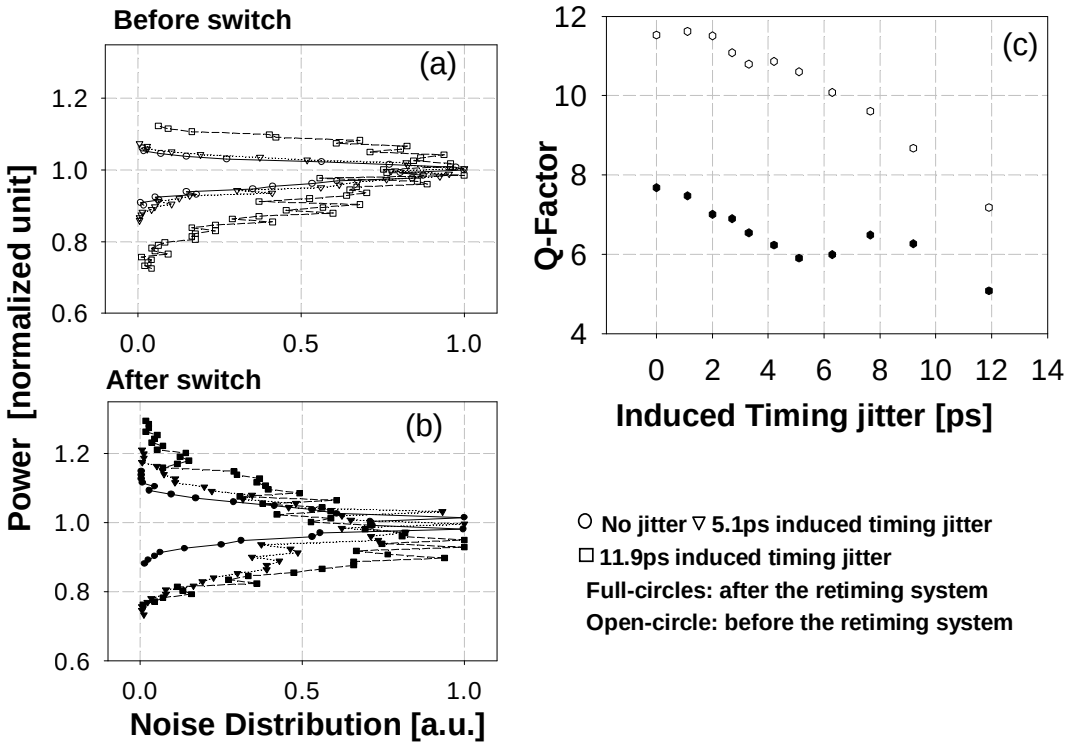

FIGURE 4.16: Noise Distributions for 3 different cases of amplitude jitter before (a) and after (b) the retiming system. (c) Q-factor versus induced timing jitter characteristic before (open-circles) and after (full-circles) the retiming system.

pulses before the retiming scheme increase linearly with the induced timing jitter. On the other hand, these values remain fairly constant for all values of induced timing jitter after the retiming system. Note that the level of 1 ps of rms timing jitter corresponds to the noise limit of the DCA used for the measurements.

Histogram data on pulse amplitude noise (as measured at the pulse centre) were also examined for the same three cases shown in Fig. 4.13. The corresponding distributions are plotted in Fig. 4.16.a and Fig. 4.16.b. The increase of the amplitude distribution for the initial pulses is only an artefact of the technique used to measure it. Indeed, when increasing the timing jitter it becomes very hard to distinguish between timing and amplitude jitter, see for example Fig. 4.13.g. For the unjittered case the amplitude noise of the retimed pulses is similar to that of the initial pulses, however for the jittered cases an increased amplitude noise is observed (the relative rms standard deviation goes from ~ 0.04 for the unjittered case to ~ 0.12 for the most extreme induced timing jitter), as previously discussed.

These data were used to calculate the Q-factor values of the eye diagrams.

Briefly, the Q-factor is the signal-to-noise-ratio (SNR) at the decision circuit in voltage or current units, and is typically expressed by the following formula [75]:

$$Q = \frac{|\mu_1 - \mu_0|}{\sigma_1 + \sigma_0} \tag{4.2}$$

where $\mu_{1,0}$ is the mean value of the marks/spaces rail, and $\sigma_{1,0}$ is the corresponding standard deviation. If the noise distributions of the "zeros" and "ones" can be approximated to Gaussian distributions and are equiprobable, it is possible to relate the measurement of the Q-factor with the bit-error-rate (BER) of the system that corresponds to the number of errors over the number of bits transmitted during the duration of the measurement, as follows:

$$BER = \frac{1}{2} erfc[\frac{Q}{\sqrt{2}}] \approx \frac{1}{\sqrt{2\pi}} \frac{e^{\frac{-Q^2}{2}}}{Q} \tag{4.3}$$

where erfc is the complementary error function. As already discussed, in all the experiments proposed in this thesis, the noise was introduced artificially and was described by a doubled-peak rather than a normal distribution. For this reason, it is not possible to relate directly Q-factor and BER values and Eq. 4.3 does not hold. For a complete characterization of the system Q-factor and BER measurements have to be performed independently. However, even though Q-factor values are not as meaningful as in the system with normal distribution, their evolution before and after the re-timing scheme can give an idea of the performance of the scheme itself.

Fig. 4.16.c shows the corresponding Q-factor values of the eye diagrams as a function of the induced timing jitter. A degradation of the Q-factor, even before the retiming system, is noticeable from the curve; this can be attributed to the "mark" level appearing thicker at the pulse centre due to the added timing jitter, as already discussed. The corresponding Q-factor curve for the pulses after the retiming system shows some degradation in the signal in terms of amplitude noise, even though all the Q-values are around 6, which would correspond to error-free operation of the system under normal noise distribution conditions.

Nevertheless, in this system, the idea is to incorporate an amplitude regeneration stage in order to overcome the increased amplitude noise and reduce the amplitude jitter of the transmitted signal, as will be discussed in the next Chapter.

Finally BER measurements were made versus the induced timing jitter, in order to assess the performance with and without switching, as is shown in Fig. 4.17, for three different positions along the system. These measurements were taken for a constant input power of -21 dBm at the receiver, which corresponded to a back-to-back BER measurement of 10^{-10}. As can be seen, pulse re-timing and a low BER can be achieved as long as the timing jitter is less than the duration of the rectangular pulses. As soon as the induced timing jitter exceeds the duration of the rectangular pulse, the BER characteristic has the same shape as the one when no reshaping has been applied. The BER curve for the signal at the input of the system almost overlaps the one for the pulses at the output of the re-timing system, meaning that no degradation is introduced by the system. It is noticeable that the BER curve of the signal, at the input port of the system, does not show appreciable degradation with increasing induced timing jitter. This is clearly understandable because of the nature of the detector used to take BER measurements.

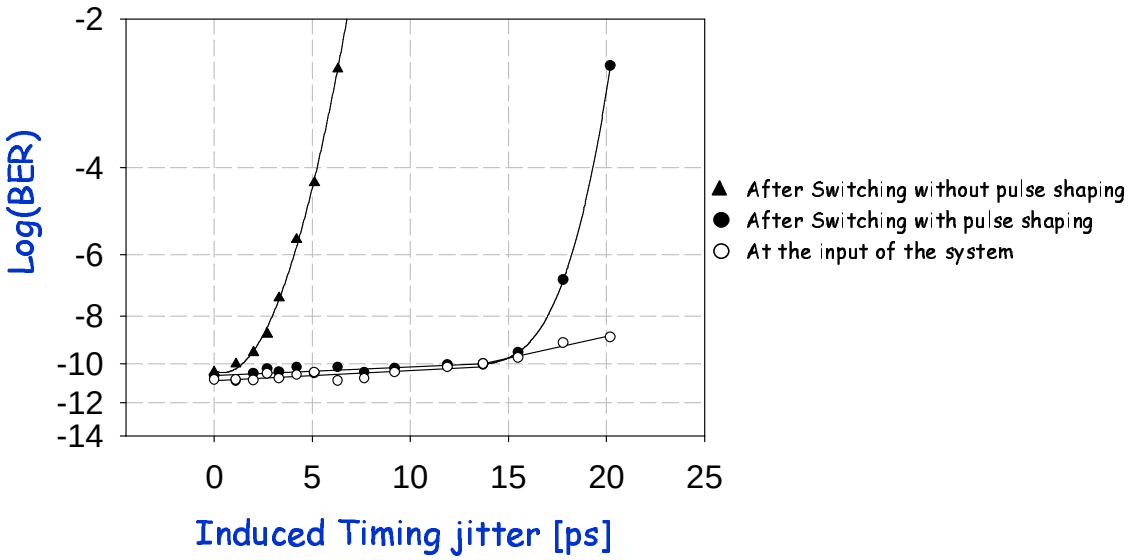

FIGURE 4.17: Bit-error rate measurements versus induced timing jitter characteristic before (open-circles) and after the re-timing system with (full-circles) and without (full-triangular) pulse shaping.

In the re-timing technique timing jitter was drastically reduced, but some amplitude noise was introduced. The particular detector used in the bit error rate tester has a longer detection window than the amount of timing jitter introduced to the pulses, and thus in itself is more sensitive to amplitude noise than timing jitter noise.

Finally, some comments related to the losses of the grating and the NOLM itself are required. Regarding the first point, as discussed in Section 2.6, the SSFBG was designed in the weak limit conditions so that the Fourier design limit was satisfied. In particular, the overall loss was about 25 dBm, making it necessary to use two standard amplifiers to keep the SNR constant. However, it has to be appreciated that the grating acted as a filter removing the out of band ASE noise of the amplifiers and, furthermore, that the BER measurements performed showed that error free operation was readily achieved down to the 10^{-11} level, with only a slight (<0.5 dB) power penalty relative to back-to-back measurements [17].

Regarding the loss of the NOLM, the average optical input power at the signal port is 16 dBm, while at the output port, after the filter, the power is about $\sim$ -2 dBm. This implies an overall loss of 18 dBm, which is due to the 50:50 couplers in the NOLM (see Section 2.4.2 for further details), to the insertion losses of the filter used and the finite extinction ratio of the NOLM itself.

4.7 Conclusion

In this chapter I have demonstrated, in a simple proof-of-principle experiment, a powerful technique for the re-timing of short optical pulses. The technique relies on linear

pulse reshaping performed using an SSFBG, and subsequent optical switching with synchronous optical clock pulses. The amount of jitter that can be compensated for is determined by the width of the reshaped pulses and this can be readily adjusted at the SSFBG design stage to fit the specific jitter characteristics of a given transmission system.

All the measurements described needed quite a long time to acquire the data, implying that the system was stable enough to allow all those measurements. However, system stability, based on fibre devices of a length of hundreds of meters is always a critical issue, due to temperature fluctuations, as discussed in Section 2.4.2. Recently, promising new highly nonlinear fibres have been developed, such as bismuth highly nonlinear fibres, allowing for a drastic reduction in the length requirements of fibre based nonlinear devices [76] and enabling the implementation of meter-long nonlinear switches with improved performance in terms of stability and input power requirements. The application of this type of fibre will be discussed in Chapter 8.

Although the results achieved indicate that timing jitter was eliminated to a great extent, the fact that the Q-values of the eye diagrams degraded after the switch indicates that this re-timing technique has to incorporate an amplitude (re-shaping) regeneration stage within the system. The performance of the system that includes an amplitude regenerator is discussed in the next Chapter.

Chapter 5

Retiming and Reshaping technique using rectangular pulses shaped in an SSFBG

5.1 Introduction

In the experiment described in the previous Chapter, the noisy data were re-shaped using a SSFBG, before being fed into the signal port of a nonlinear switch (a NOLM), which was controlled by a clean clock signal. This gave not only a timing jitter tolerant operation of the switch but also enabled retiming of the data pulses at the switch output and, in addition, there was the benefit of maintaining the wavelength of the data signal. However any amplitude noise that was present on the original signal would be passed on at the output of the switch, which might limit its practical application. Also, the Q-factor measurements showed that imperfections in the shaping of the SSFBG degraded the quality of the signal. In this Chapter this previous work is extended to obtain pulse reshaping/amplitude noise reduction as well as retiming of the data pulses, using the regenerative properties of a NOLM. The technique still relies upon converting the incident data pulses into rectangular pulses at the NOLM input and using these broadened pulses to switch a well-conditioned and well-defined local clock signal. However, the S-shaped switching characteristic of the NOLM is now exploited to provide amplitude noise reduction, as discussed in Sec. 2.4.2.

This Chapter opens by explaining how amplitude and timing jitter were artificially induced in the system, and then explains the basic principles of the re-shaping techniques used. Finally, it describes two different modifications for the same kind of experiment and the corresponding results achieved.

5.2 Artificial introduction of Timing jitter and amplitude noise

In order to study the regenerative property of this system, timing jitter and amplitude noise were artificially introduced to the data pulses.
In contrast to the previous experiment, two independent, but synchronized laser sources operating at two different wavelengths, one for the clock and the other for the data signal were now available. In this way it was possible to introduce timing jitter directly onto the source that generated the data pulses. The operation of the particular EFRL used is controlled by a PLL circuit, which compares the frequency of the laser cavity to the frequency of the reference input clock from an external RF synthesizer. The difference in these two frequencies generates an error signal which is used to drive a piezoelectric transducer that stretches or contracts a length of fibre wound around it within the laser cavity. I introduced timing jitter on the pulses generated inside the laser cavity, by frequency modulating the RF drive signal of the EFRL with a 4 kHz tone. I had found that this frequency was lower than the response time of the PLL, thus allowing it to follow the changes in applied RF frequency. If the modulation frequency was too high, the PLL would not see these frequency changes, the cavity length would remain unchanged and no temporal pulse fluctuations would be introduced on the output signal of the laser. The pulse quality though would be likely degraded.
The amount of induced timing jitter could be varied by varying the amplitude of the frequency modulation applied to the 10 GHz laser drive signal. Note that, in accordance with the previous Chapter, "induced timing jitter" implies the amount of pulse period fluctuation as defined by the amplitude of the frequency modulating noise signal (Fig. 4.7). Obviously, the inherent timing jitter of the pulse source itself has to be considered, in addition to the induced timing jitter, to calculate the corresponding total timing jitter.
The amount of induced amplitude jitter could be varied by degrading the extinction ratio between the marks and spaces of the data, facilitated by choosing a non-optimum bias voltage for the operation of the lithium niobate data modulator. In a similar scheme, [77] has also used an externally driven $LiNbO_3$ modulator to artificially induce amplitude noise to the signal. Using this technique, the "zero" level was more distorted than the "one" level. This operation point was chosen due to the non-ideal flat-top of the rectangular signal, which would introduce already some noise on the "one" level. If the same amount of amplitude noise on the zero and on the one levels needs to be compensated for, a different reshaping regenerator has to be considered. In Chapter 8, a different technique to suppress amplitude noise is described, and, as will be discussed there, a better nonlinear characteristic function can be obtained, so that the technique is more robust for the compensation of amplitude noise.

5.3 Re-shaping technique: Basic principle

In-line all-optical signal regenerators are likely to play an important role in future large-scale photonic networks, by significantly extending the transmission lengths. The most widely used method to realize signal regeneration in high bit-rate transmission systems is to transfer the information from the incoming data signal to a locally generated "clean" clock pulse. In order to avoid the transfer of amplitude fluctuations from the initial signal to the output signal, the regenerator should have a nonlinear characteristic similar to an ideal hard limiter. It is known that a suitably biased NOLM has such a nonlinear transfer characteristic and is able to reduce the noise both on the zeros and the marks of the switched signal, provided that the peak power of the incoming pulses is high enough to induce a π nonlinear phase shift over the length of the fibre inside the loop [46]. In order to use the regenerative (reshaping) properties of the NOLM in our experiments, the noisy and pre-shaped data signal should be properly amplified and used as the control signal to the switch. It should be noted at this point that, because of the long duration of the shaped pulses, the average power required to achieve a π nonlinear phase shift in the NOLM was much higher than in the case described in the previous Chapter where short pulses were used. I have, therefore, studied two different modifications of the experimental set-up described in Chapter 4 (one of which avoids the use of a high-power amplifier and another which uses one) and assessed both of them in terms of their regenerative properties.

In the first configuration, the retiming and reshaping (reduction of amplitude fluctuations) functions are performed in two separate steps. Because the control data does not have enough power to achieve the π-phase shift, a single NOLM would not be enough to achieve re-shaping of the signal and a second passive NOLM stage is cascaded to the previous set-up, see Fig. 5.1.a. This NOLM is constructed from a 70:30 coupler and 6.6 km of DSF with a zero-dispersion wavelength of 1541 nm and a nonlinearity coefficient, γ, of 1.55 $W^{-1}km^{-1}$. Its purpose is solely to perform 2R regeneration of the data pulses. A complete discussion to establish the optimum NOLM design as a function of coupling ratio, dispersion and length can be found in [47]. The transfer functions of the passive NOLM for the two wavelengths of the data and the clock signal were considered. The data signal wavelength was 1556.8 nm as dictated by the operating wavelength of the SSFBG. The operating wavelength of the clock was then chosen to give minimum walk-off in the first (active) NOLM. For the specific HNLF, used in this NOLM, the optimum wavelength is 1544.5 nm. Fig. 5.2 shows the two curves for 1544.5 nm (blue line) and 1556.8 nm (red line) respectively. As can be seen from a comparison between the two nonlinear functions, the NOLM operates better at the wavelength of 1544.5 nm. In order to feed a signal at 1544.5 nm into the passive NOLM, the noisy data signal has to be used as the control signal to the active NOLM. This configuration is chosen, even though it is not the ideal case for the active NOLM, because amplitude noise on the "one" level associated with the data signal would be amplified by the nonlinear charac-

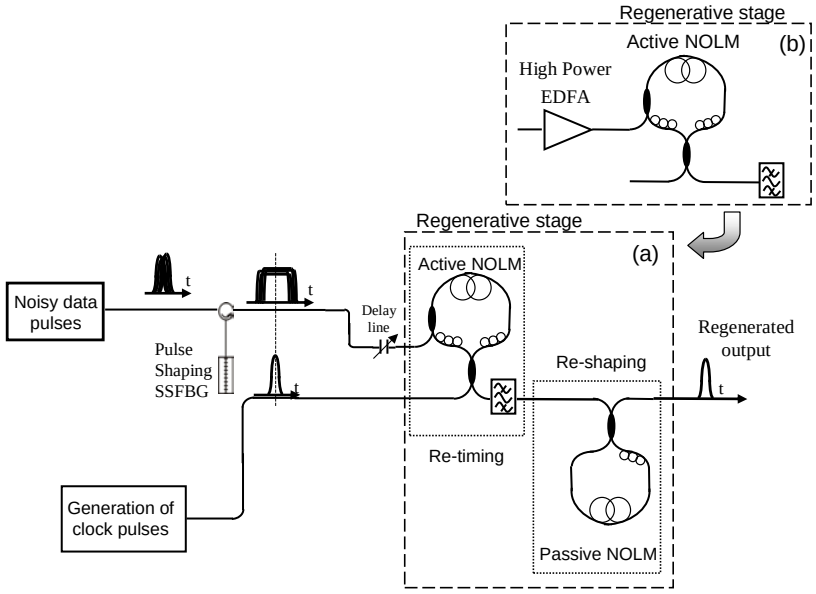

FIGURE 5.1: Sketches of two different regeneration stages.

teristic function for the particular values of peak powers used, as will be discussed later on in this Chapter.

The second configuration is shown in Fig. 5.1.b. The experimental set-up is essentially the same as before; however, because of the use of a high power amplifier, only one, active NOLM is considered. In fact, in this configuration, the NOLM acts as a simultaneous re-timing and re-shaping stage. Therefore the demands in average powers are higher relative to what has been used in Chapter 4, in order to ensure that a π nonlinear phase shift is achieved in the presence of the longer control pulses. In more detail, in the experimental configuration of the previous Chapter, the control pulses were $T_{FWHM} = 2\ ps$ solitons

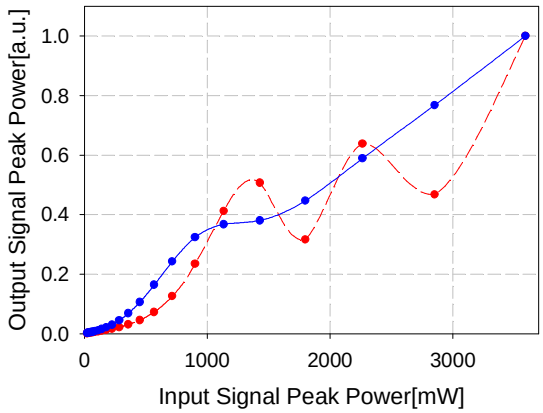

FIGURE 5.2: Nonlinear transfer characteristics of the passive NOLM at two different wavelengths: 1544.5 nm(blue line) and 1556.8 nm(red line). The NOLM was made from a 70:30 coupler and 6.6 km of DSF with a nonlinear parameter of $\sim$1.55 $W^{-1}km^{-1}$ and a zero-dispersion wavelength at 1541 nm.

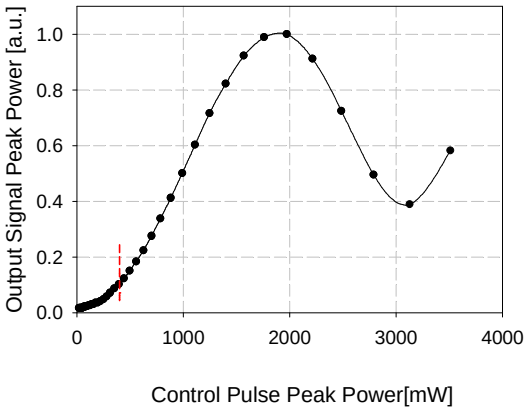

FIGURE 5.3: Nonlinear transfer characteristic of the NOLM. The NOLM consisted of 220 m of Highly Nonlinear Fibre (HNLF) with a nonlinear parameter of $\sim 20\ W^{-1}km^{-1}$ and a zero-dispersion wavelength at 1550 nm

and the bit period was $T_{bit} = \frac{1}{10\ GHz} = 100\ ps$. Then the average power, P_{ave}, required to achieve a certain peak power, P_{pk}, was:

$$P_{ave} = \frac{1.13 T_{FWHM}}{T_{bit}} P_{pk}, \tag{5.1}$$

if sech pulses are considered. When square data pulses with $T'_{FWHM} = 20\ ps$ are considered as the control signal to the switch (current experimental configuration), then the corresponding average power, P'_{ave}, is:

$$P'_{ave} = \frac{T'_{FWHM}}{T'_{bit}} P_{pk}, \tag{5.2}$$

where $T'_{bit} = 2T_{bit}$ on average, if we consider an equal density of ones and zeros in the 10 Gb/s data signal. In order to achieve the same peak power in both cases, i.e. to achieve a π phase shift, P'_{ave} should thus be 6.5 dB higher than P_{ave}. According to the transfer characteristic of this NOLM, see Fig. 5.3, the shaped data pulses should be amplified up to $\sim$23 dBm before being fed to the control port. This value is much higher than the typical saturated output power of a commercial telecommunications EDFA (typical values range between 15 and 18 dBm), but can be achieved using cladding pumped amplifier technology. In the configuration with two NOLMs, this requirement for a high power amplifier was alleviated since the active NOLM acted as a re-timing stage only, but it is to be appreciated that the fact that the π phase shift point of the active NOLM was not reached, made the task of the second NOLM even more demanding. This will become more evident in the following Section.

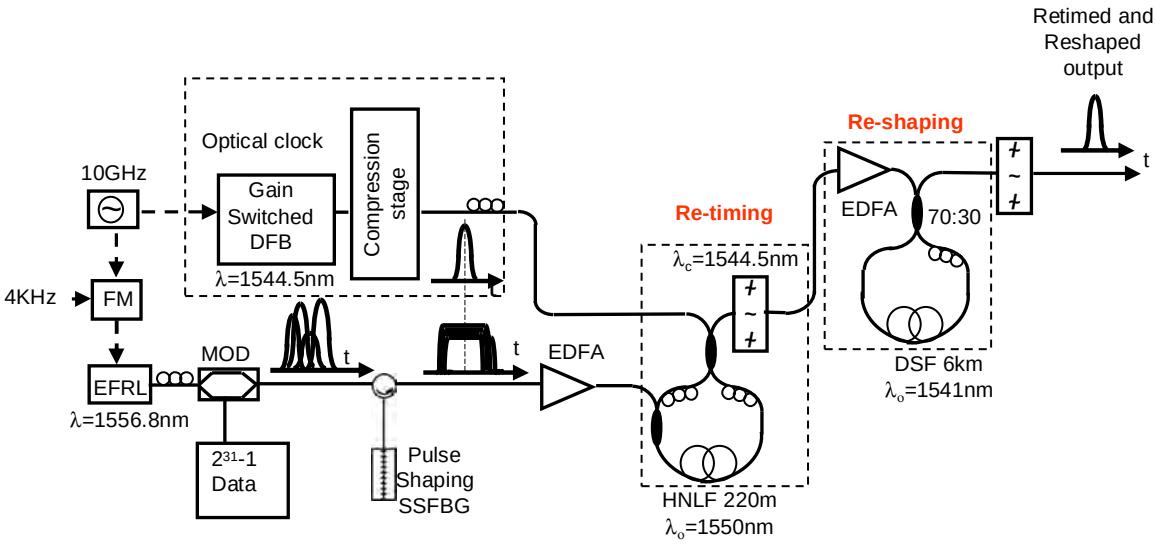

FIGURE 5.4: Experimental set-up and principle of the retiming and reshaping operation

5.4 Regeneration System: First configuration

5.4.1 Experimental Set-up

The detailed experimental set-up of the reshaping-retiming scheme, employing two NOLM stages, is shown in Fig. 5.4. As described in the previous Chapter, a 10 GHz actively mode-locked EFRL was used as the data source to generate ∼2.5 ps sech pulses at the operating wavelength of 1556.8 nm. The pulses were modulated to provide a $2^{31} - 1$ PRBS and were then fed onto the pulse-shaping SSFBG (via a circulator) to convert the 2.5 ps sech into 20 ps rectangular pulses. Compared to the set-up of Fig. 4.9, these pulses, after being amplified by a conventional telecom amplifier, were launched into the control port of the NOLM rather than the signal port. The average power of the control signal was ∼16 dBm, which was not sufficient to ensure that the desired π phase shift point was reached and a separate regenerative stage was indispensable, as already described in the previous Section. The nonlinear medium in the NOLM consisted of 220 m of HNLF, whose parameters are described in Tab. 3.1.

The input signal to the NOLM (clock signal) was provided by a gain-switched DFB laser, which operated at 1544.5 nm and was driven by a 10 GHz RF signal synchronized to the laser oscillator. The pulses of the gain-switched distributed feedback (DFB) laser were compressed down to ∼2 ps using a 125 m length of DCF followed by a nonlinear compression stage comprising an EDFA, 490 m of a HNLF (λ_o=1573 nm, Slope=+0.029 ps/nm^2/km) and ∼27 m of SMF. The signal power was ∼12.8 dBm. These pulses were characterized using the SHG-FROG technique, see Fig. 5.5. Fig. 5.5.a shows the retrieved intensity profile and the corresponding chirp. As can be seen, some residual chirp was still present on the pulse, so that the minimum temporal width was

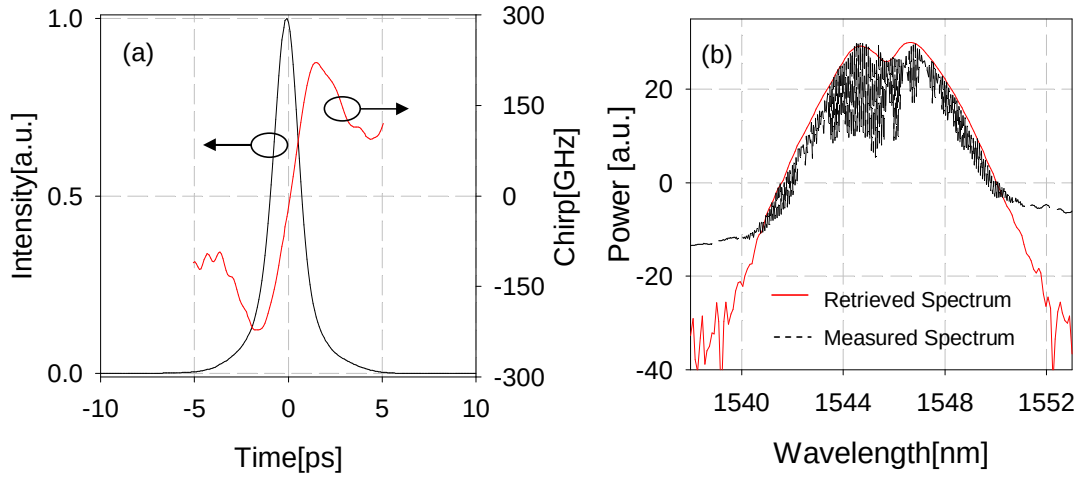

FIGURE 5.5: a) Intensity and chirp profile of the pulse at the signal port of the first NOLM, measured using SHG-FROG technique. b) Measured (black trace) and retrieved (red) optical spectrum of the pulses.

reached inside the HNLF, in the active NOLM. Fig. 5.5.b compares the measured optical spectrum of the pulses with the retrieved spectrum of a single pulse. The SHG-FROG gives a temporal FWHM of the pulse of ∼1.7 ps and a TBP of ∼0.68.
Spectral traces of the data signal, after the active NOLM, are shown in Fig. 5.6.a, for the cases when the control signal is properly switching the signal (red trace) or not (black trace) respectively. As indicated in the Figure, a SNR of ∼18 dB is obtained. The signal was then filtered out, see Fig. 5.6.b, before being amplified up to ∼12 dBm and fed onto the second NOLM for reshaping. The corresponding spectrum is shown in Fig. 5.7.a. The signal was then filtered with a narrow-band filter (spectral FWHM∼0.5) to remove nonlinear spectral components originating in the DSF. The spectrum and the corresponding autocorrelation traces at the very end of the system are shown in Fig. 5.7.b and Fig. 5.7.c. The autocorrelation trace FWHM is ∼6.6 ps, mainly determined by the

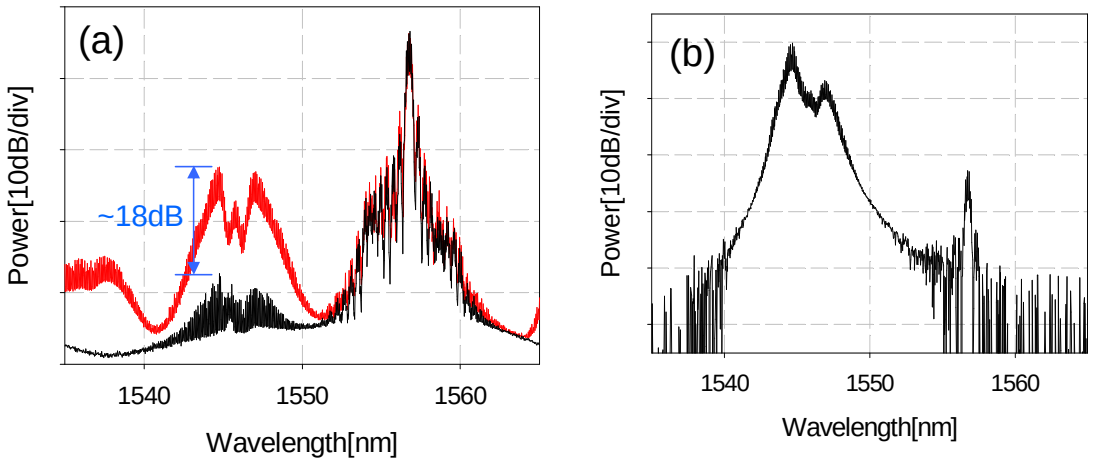

FIGURE 5.6: Spectra of the data signal after the active NOLM when the control signal was properly switching the signal data or not, respectively (a), and after filtering (b).

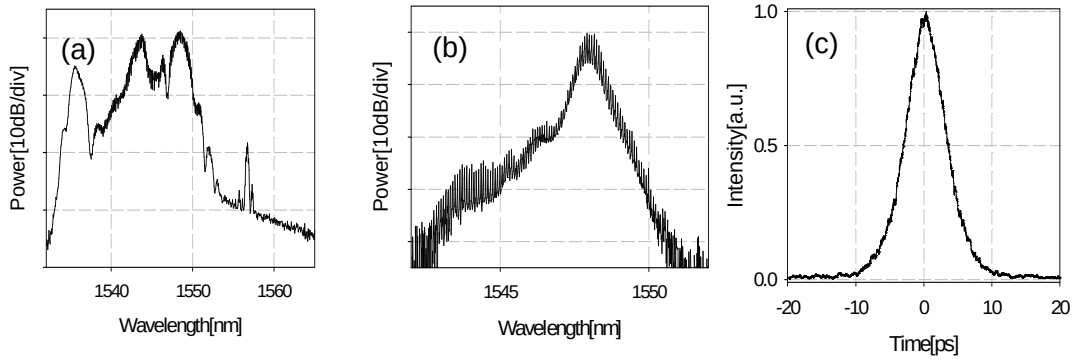

FIGURE 5.7: a) Spectrum of the signal after the second NOLM. Spectrum (b) and corresponding autocorrelation trace (c) of the data signal at the very end of the set-up.

narrow-band filter used.

5.4.2 Results and discussion

In order to evaluate the performance of the system, eye diagrams, timing jitter and amplitude noise distributions were measured and BER curves recorded. For the measurements, a constant amount of amplitude noise was applied on the data pulses, degrading their Q-factor from 17.5 to ~ 5, and a variable amount of induced timing jitter, ranging from $\sim$0.8 ps up to $\sim$12 ps. In Fig. 5.8 eye diagrams of the initial data signal are shown for increasing induced timing jitter, while the amplitude jitter induced is kept constant. First, I assessed how the non-optimum working condition of the first NOLM affects the overall performance of the system. Fig. 5.9 shows eye diagrams after the first NOLM for some of the cases of noise applied to the data pulses. As predicted in the previous Section, any amplitude noise already present in the system is magnified. Indeed, with an input control power of $\sim$ 16 dBm (peak power of $\sim$400 mW if 20 ps square pulses are considered), which corresponds to the maximum output power of the EDFA used, the data signal itself sits on the very sharp slope of the characteristic function of the NOLM, highlighted by the red short dashed line in Fig. 5.3. This extra induced amplitude noise makes the re-shaping process of the second NOLM more challenging. It follows that reaching the π phase shift operation point is critical to optimize the system, implying the use of a higher power amplifier before the control port of the active NOLM, as I will discuss in Sec. 5.5. However, the overall system performance was still assessed to test if the re-shaping process could compensate for such an amount of extra noise.

Fig. 5.10 shows the eye diagrams of the data at the output of the regenerative system for the same settings of noise as in Fig. 5.8. As can be seen, timing jitter is eliminated from the data pulses and amplitude noise is very much reduced even in the most extreme case of timing jitter.

In Fig. 5.11, the standard deviation of the timing jitter is presented, both before and after the re-timing and re-shaping system, as the induced timing jitter increases. These

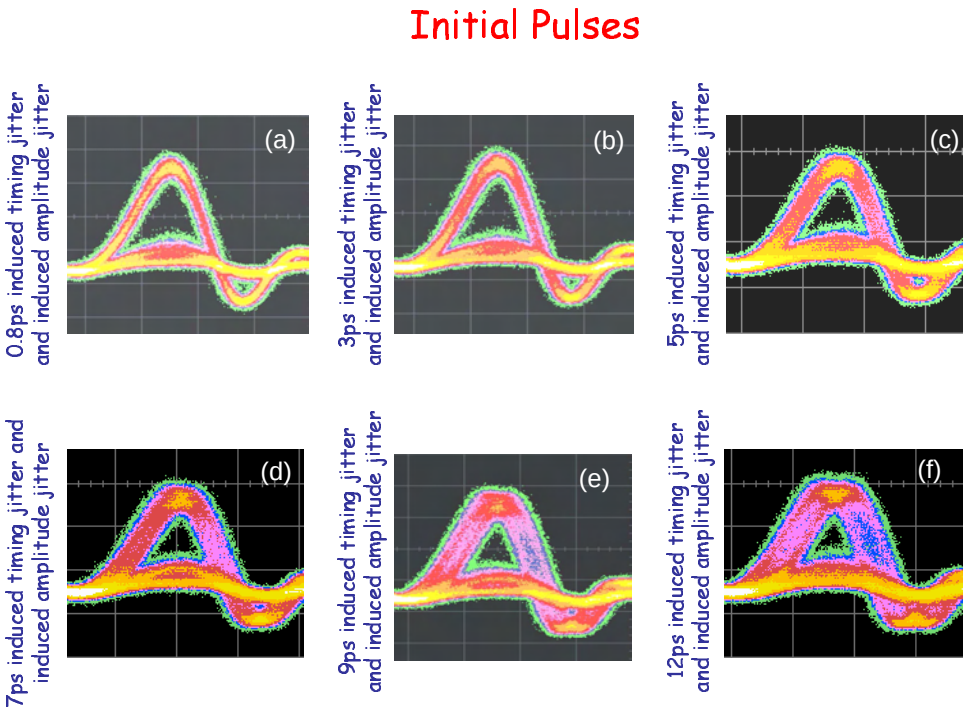

FIGURE 5.8: Eye diagrams at the input of the system at various noise settings. The amount of amplitude noise introduced on the pulses is kept constant for all the measurements (degradation of the Q-factor from ∼12 to ∼5), while the timing jitter noise is increased. Top-row: ∼0.8 ps induced timing jitter (a), ∼3 ps induced timing jitter (b) and ∼5 ps timing jitter (c). Bottom-row: ∼7 ps induced timing jitter (d), ∼9 ps induced timing jitter (e) and ∼12 ps timing jitter (f). Horizontal Scale: 20 ps/div. Scope bandwidth: 20 GHz.

values were measured from histograms, taken at the FWHM point on the leading edge of the data eye diagrams. As can be seen, while the rms values of the timing jitter increase linearly for the pulses before the re-timing system, they remain fairly constant approaching the original value of the clock signal (∼0.9 ps as measured with the same technique) after the re-timing system. The histogram data on pulse amplitude noise (as measured at the pulse centre) were also examined for various noise settings of the system. These data were then used to calculate the Q-factor values of the eye diagrams, which are shown in Fig. 5.12. The Q-factor improved by almost a factor of 2 in all cases. For the worst case that we examined (timing jitter of ∼ 12 ps) the Q-factor increased from ∼ 4.5 to ∼ 9.

Finally BER measurements, with respect to the receiver input power, were made for the data pulses before and after the system, see Fig. 5.13. In order to evaluate the performance of the system, first the switched signal was examined for the case that no timing or amplitude jitter was applied to the data pulses. The BER curves in these conditions demonstrate that the retiming and reshaping system, in itself, introduced a slight power penalty of ∼ 1 dB, even for the condition of no added noise, relative to the back-to-back. This is understandable because of the long fibres used in the system without the use of separate clock extraction at the receiver, and because of the many

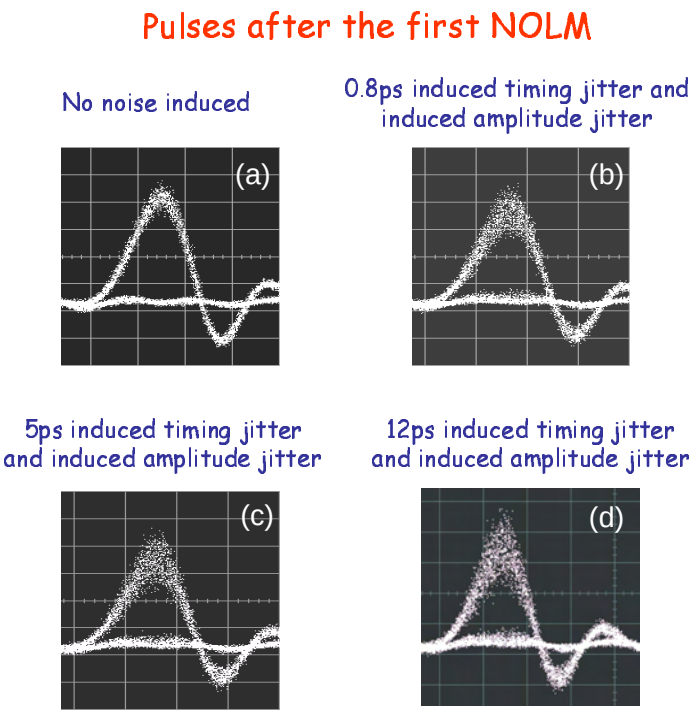

FIGURE 5.9: Eye-diagrams after the first NOLM and the 1544.5 nm filter for various noise settings of the system. The amount of amplitude noise introduced on the pulses is kept constant for all the measurements (degradation of the Q-factor from ∼12 to ∼5), while the timing jitter noise is increased. Top-row: no- noise induced (a) and ∼0.8 ps induced timing jitter (b). Bottom-row: ∼5 ps induced timing jitter (c) and ∼12 ps induced timing jitter (d). Horizontal Scale: 20 ps/div. Scope bandwidth: 20 GHz.

amplifiers in between the two measuring points. Next, the quality of the input and output signal was examined when the noise was deliberately applied to the incident data pulses. It is worth noting that the BER curves of the input signal do not show any degradation with increasing timing jitter. This is because of the particular receiver used in the bit error rate measurements, which has a longer detection window than the amount of timing jitter introduced to the pulses, as already analyzed in the previous Chapter (see discussion on Fig. 4.17). Error free operation was achieved after the switch, demonstrating the amplitude noise reduction provided by the passive NOLM and the timing jitter reduction provided by the square switching window. Unfortunately, due to the long fibre used and the temperature fluctuations in the room, the system was not very stable during the measurements, making them very difficult to take, so just a few cases were assessed.

However, the curves show some error floor for all cases of induced timing and amplitude jitter due to residual noise at the output of the system. This could also be noticed from the eye diagrams of Fig. 5.10. The second NOLM is able to compensate for most of the noise despite the extra amplitude noise added after the first NOLM but some amplitude noise still remains on the data signal, penalizing the system in terms of BER performance.

In conclusion, even though this configuration allows the use of conventional telecom

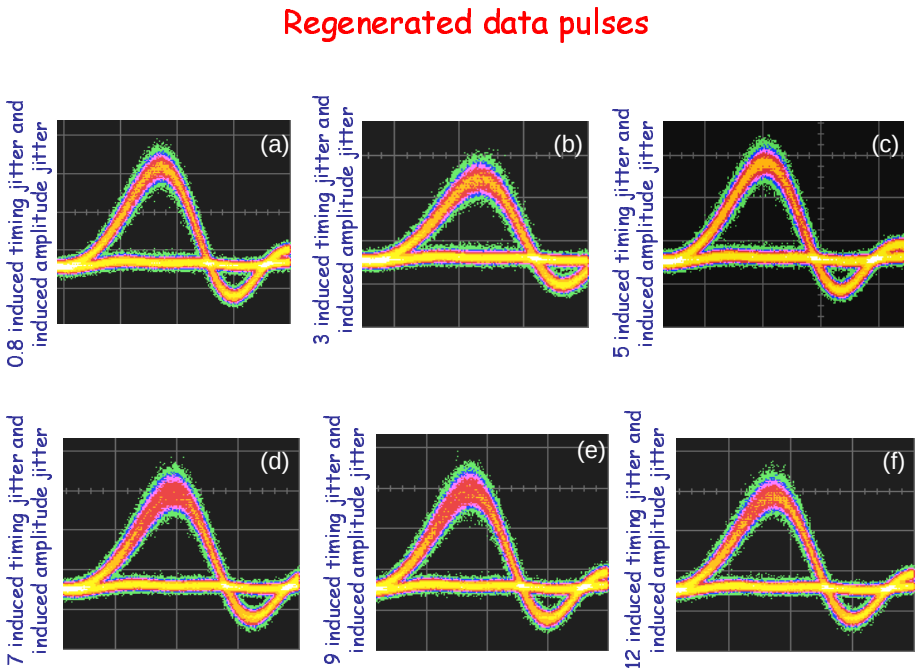

FIGURE 5.10: Eye diagrams at the output of the system for various noise settings. The amount of amplitude noise introduced on the pulses is kept constant for all the measurements (degradation of the Q-factor from ∼12 to ∼5), while the timing jitter noise is increased. Top-row: ∼0.8 ps induced timing jitter (a), ∼3 ps induced timing jitter (b) and ∼5 ps timing jitter (c). Bottom-row: ∼7 ps induced timing jitter (d), ∼9 ps induced timing jitter (e) and ∼12 ps timing jitter (f). Horizontal Scale: 20 ps/div. Scope bandwidth: 20 GHz.

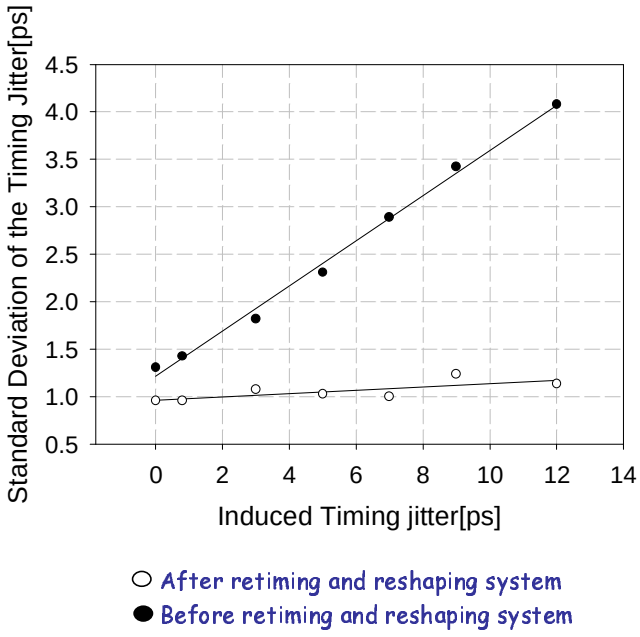

FIGURE 5.11: Timing jitter standard deviations versus induced timing jitter characteristic before (full-circles) and after (open-circles) the re-timing and re-shaping system.

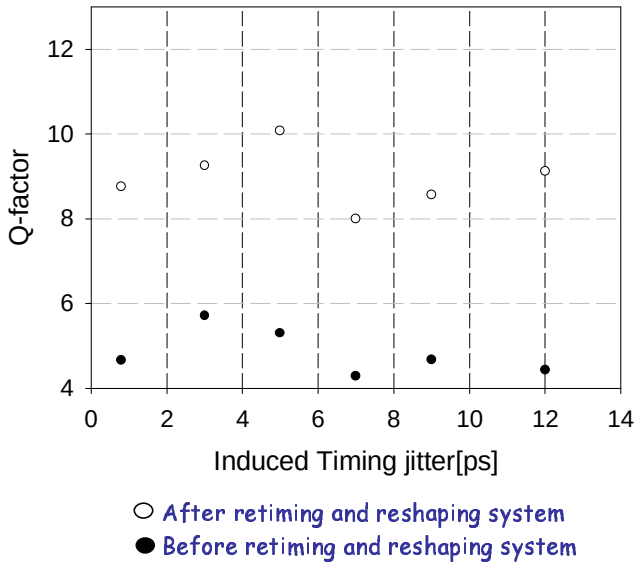

FIGURE 5.12: Q-factor values versus induced timing jitter before (full-circles) and after (open-circles) the re-timing and re-shaping system.

amplifiers, a good regenerator should not introduce extra amplitude noise to the data signal due to a non-optimum operation of one of the stages. This led me to investigate the second configuration, utilizing a high power amplifier.

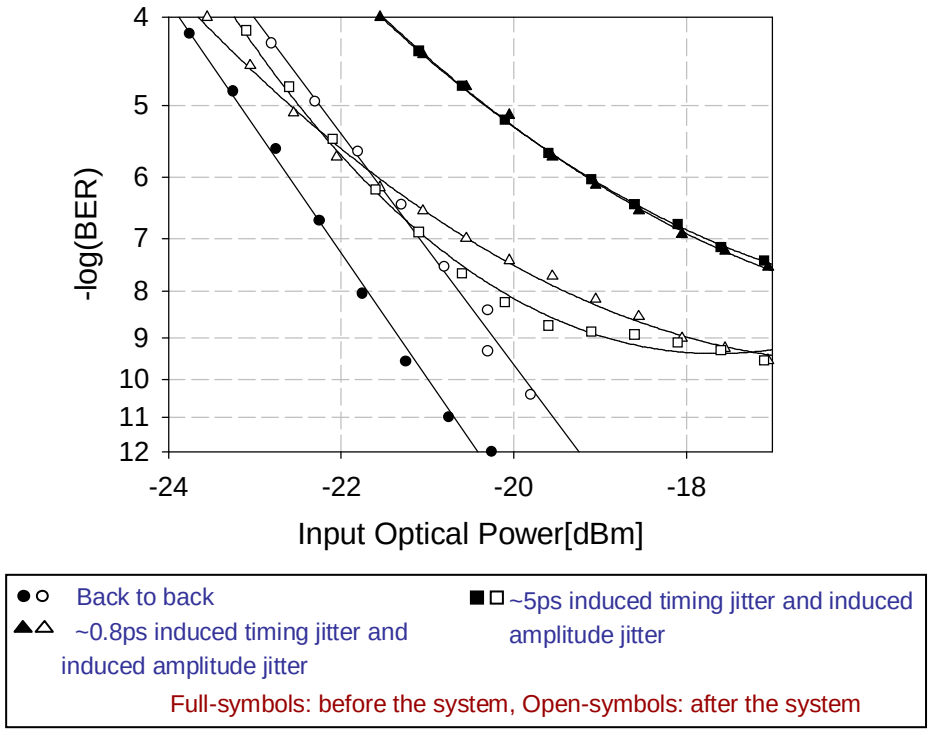

FIGURE 5.13: BER curves before (full-symbols) and after (open-symbols) the re-timing and re-shaping system.

5.5 Regeneration System: Second configuration

5.5.1 Experimental Set-up

Since the regenerative properties of the system used in the previous configuration were not completely optimized, it was changed slightly in order to exploit properly the non-linear characteristic function of the first NOLM (Fig. 5.14). In particular, replacing the EDFA before the control port of the first NOLM with a HP-EDFA, it was possible to launch an average power of ∼23 dBm to the NOLM, enough to reach the value required to achieve a π nonlinear phase shift over the length of the fibre inside the loop. In this way, pulse amplitude noise reduction was obtained as well as retiming of the data pulses in a single step. A broad-band filter of ∼5 nm, following the HP-EDFA, was also introduced to reduce the ASE noise into the NOLM. Fig. 5.15.a shows the spectrum directly

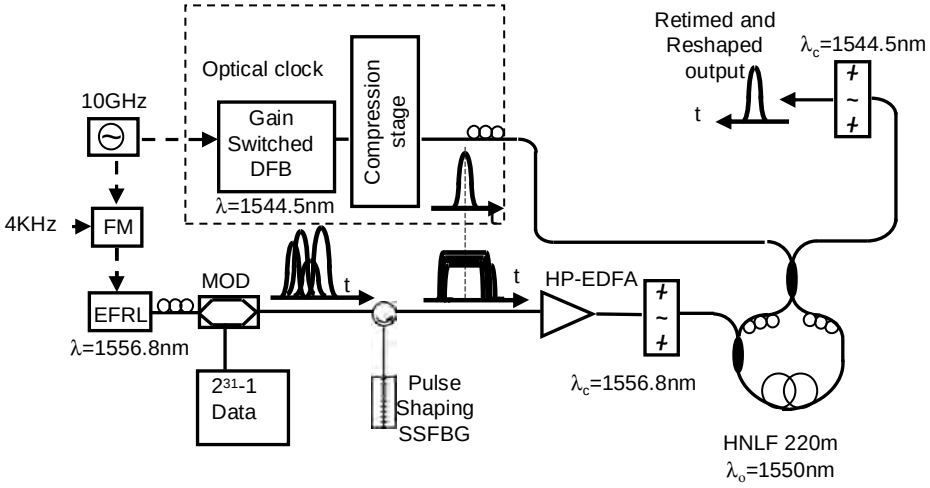

FIGURE 5.14: Experimental set-up and principle of the retiming and reshaping operation.

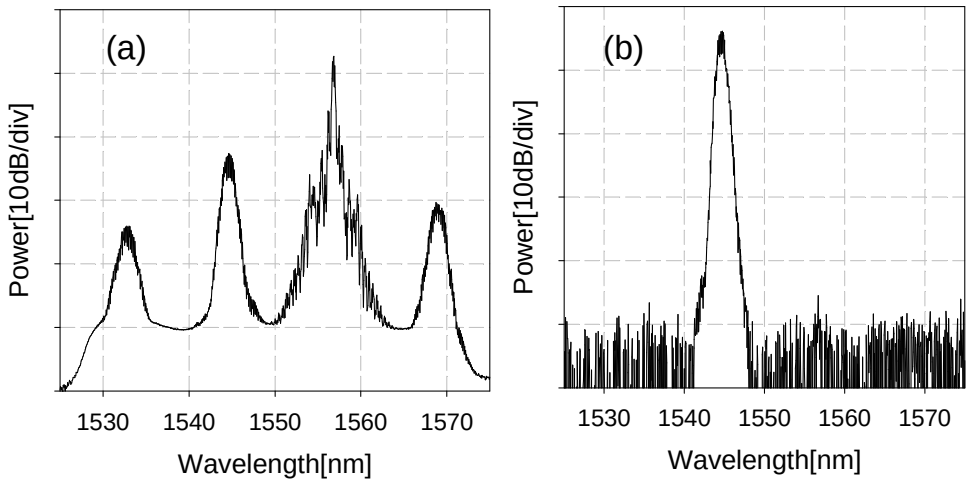

FIGURE 5.15: Spectrum after the NOLM (a) and after the 3 nm filter.

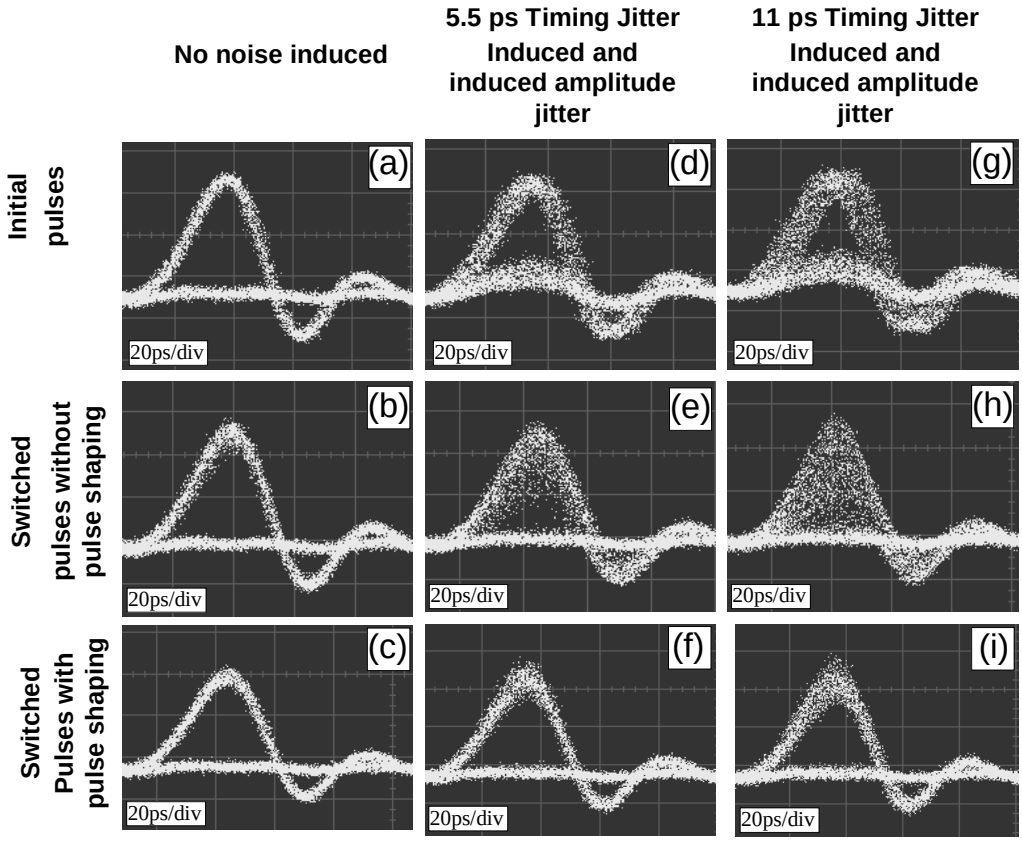

FIGURE 5.16: Eye diagrams at various positions and settings of the system. Top-row(a, d, g): at the input of the system. Bottom-row(c, f, i): at the output of the system when the re-timing technique has been applied. Middle-row(b, e, h): at the output of the switch when no reshaping has been applied to the pulses. Time Scale: 20 ps/div. Scope bandwidth: 20 GHz.

after the NOLM. The figure shows that because of the low dispersion of the HNLF in the NOLM, strong FWM components appear at the output of the switch. Fig. 5.15.b shows the filtered signal spectrum after the 3 nm filter, highlighting a good SNR of the signal at the output of the system.

5.5.2 Results and discussion

In order to evaluate the performance of the system I repeated similar measurements to those previously described in Chapter 4 and Section 5.4.2. The system performance was assessed for the case when timing jitter was added together with amplitude noise onto the data. For the measurements a constant amount of amplitude noise was applied, degrading the Q-factor of the data eye diagram from 17.5 to 7.4, and the data were taken for five different values of induced timing jitter ranging from ∼0.8 ps up to ∼11 ps, which represents an extreme value of induced timing jitter and a significant test of the system. Eye diagrams for three different induced timing jitter settings in the system are shown in Fig. 5.16. Fig. 5.16.a and 5.16.c corresponding to the data signal at the input and the output of the system respectively for the case when no noise is induced, demonstrating

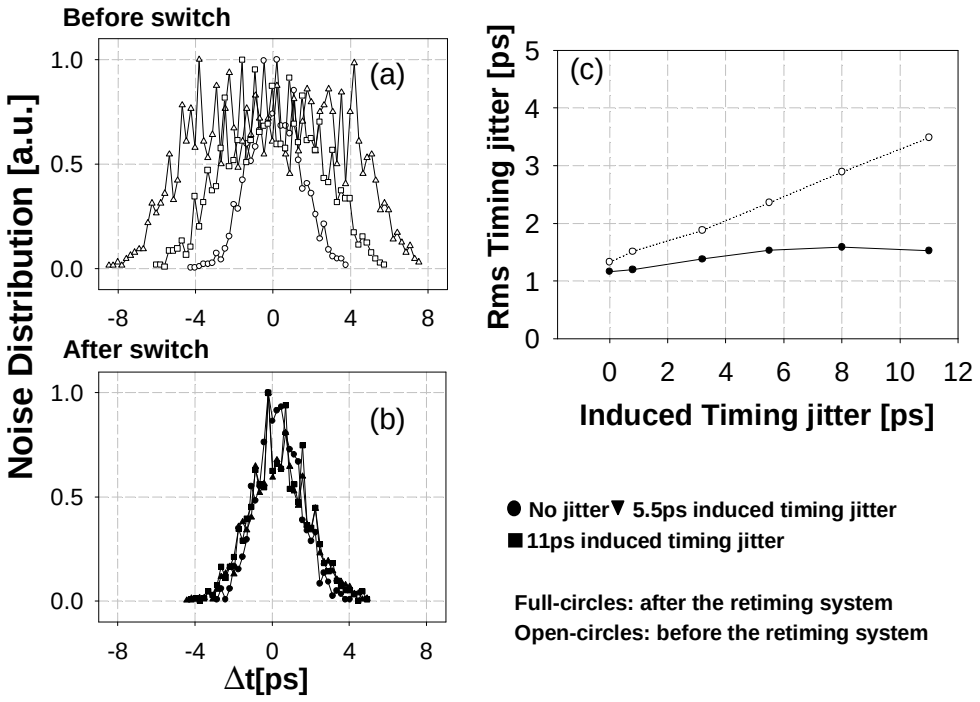

FIGURE 5.17: Distributions for 3 different cases of timing jitter before (a) and after (b) the retiming system. (c) Timing jitter standard deviations versus induced timing jitter characteristic before (open-circle) and after (full-circle) the re-timing and re-shaping system.

that the retiming and reshaping system does not, in itself, introduce any additional noise to the signal. Fig. 5.16.d to 5.16.i demonstrate that after the inclusion of the pulse shaping SSFBG, the timing jitter is eliminated at the output of the system and open eyes are obtained for both cases of induced timing jitter. When pulse shaping is not applied, there is a severe degradation in the quality of the eye diagrams (Fig. 5.16.e and Fig. 5.16.h) which is evident even for relatively small values of timing jitter. To illustrate this point more clearly histogram analysis on the eye diagrams was performed. The results are summarized in Fig. 5.17 and 5.18. In Fig. 5.17.a and Fig. 5.17.b the timing jitter distributions are presented for the three cases considered in Fig. 5.16, before and after the system. As expected from the sinusoidal modulation applied to the RF laser drive signal, the jitter distributions for the pulses at the input of the system are double peaked (see Fig. 4.7 and Fig. 4.8 for further details). Fig. 5.17.b shows that the timing jitter of the retimed pulses in both cases approaches that of the original clock laser pulses. A graph of the standard deviation of the timing jitter before and after the system, as a function of different values of induced timing jitter, is shown in Fig. 5.17.c. As expected from previous discussions, the pulses at the output of the switch are retimed and the timing jitter for all cases approaches the resolution limit of the DCA.

Histogram data on pulse amplitude noise (as measured at the pulse centre) were also examined for the same three cases shown in Fig. 5.16. The corresponding distributions are plotted in Fig. 5.18.a and Fig. 5.18.b. These data were used to calculate the Q-factor values of the eye diagrams (see Fig. 5.18.c). For the unjittered case the amplitude noise

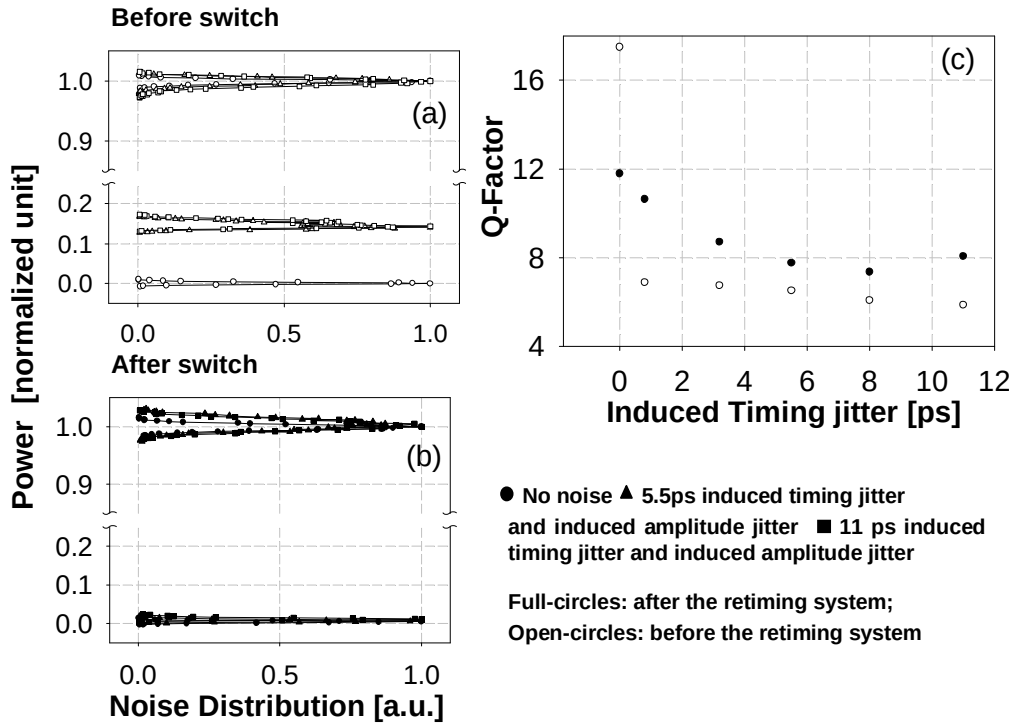

FIGURE 5.18: Distributions for 3 different cases of amplitude jitter before (a) and after (b) the retiming system. (c) Q-factor values versus induced timing jitter before (open-circle) and after (full-circle) the re-timing and re-shaping system.

of the retimed pulses is similar to that of the initial pulses, however when amplitude noise is induced together with different values of timing jitter, an improvement at the output of the system is achieved. Note that the origin of the third level in Fig. 5.18.a can be explained considering Fig. 5.16. When some amplitude noise is induced the standard deviation of the "zero" level increases and its mean value becomes larger than zero (appearance of ghost pulses in Fig. 5.16.d and Fig. 5.16.g and corresponding appearance of the third level in Fig. 5.18.a).

The intensity histograms of Fig. 5.18.b demonstrate that the amplitude noise associated with the 'zero bits' is drastically reduced, as intuitively suggested by the flat region of the nonlinear transfer characteristic for low input power values, see Fig. 5.3. The amplitude noise on the marks remains roughly constant for low values of induced timing jitter owing to the reshaping capabilities of this NOLM configuration. However, on increasing the induced timing jitter some additional amplitude noise appears on the marks. As discussed in Sec. 4.6, this increase is associated with the non-uniformity of the rectangular pulse-shape. Furthermore, some of this noise could be attributed to slight distortions of the rectangular pulses caused by self-phase modulation experienced during propagation in the HNLF due to such high input powers. Spectral traces of the 20 ps rectangular data pulses after the HNLF, in the absence of an input signal to the NOLM, are shown in Fig. 5.19 for different power levels. In particular the black line corresponds to an average power of ∼6 dBm, the red one to ∼16 dBm and the blue one to ∼23 dBm, i.e. the power level used in the system experiments. As can be seen, the

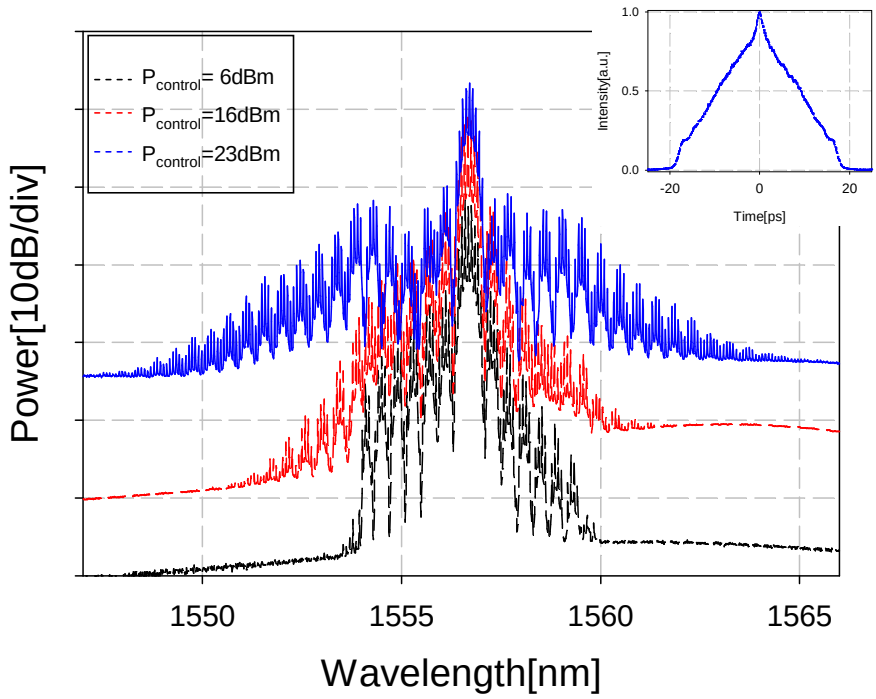

FIGURE 5.19: Measured spectral traces at different average powers (∼6 dBm (black line), ∼16 dBm (red line), ∼23 dBm (blue line)) of the rectangular data pulses after the HNLF. Inset Figure: Corresponding measured autocorrelation traces for ∼23 dBm.

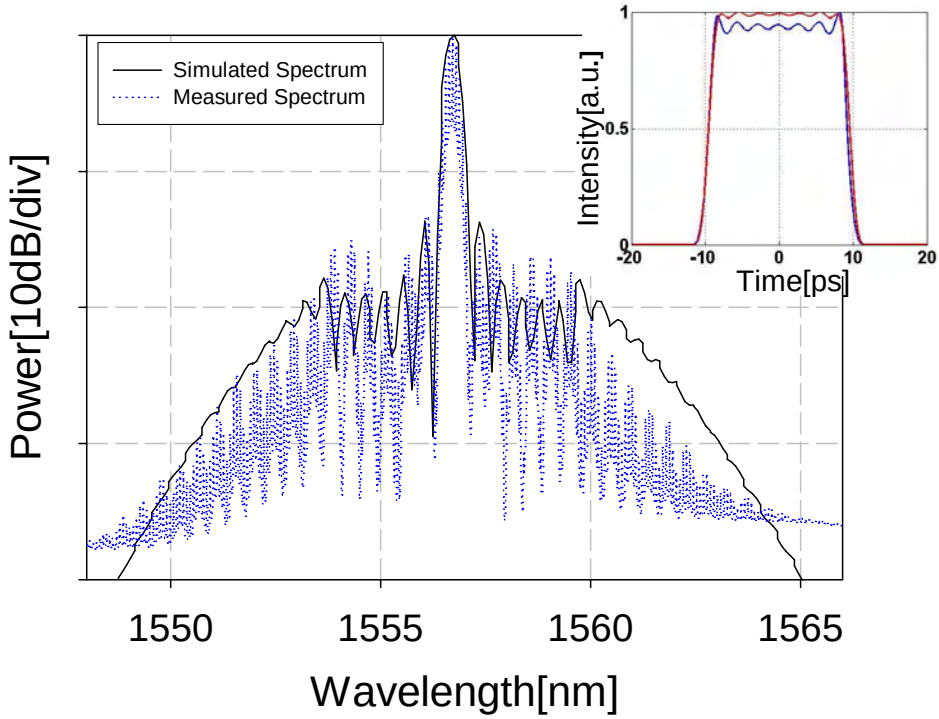

FIGURE 5.20: Simulated(black trace) and measured optical spectrum of the rectangular data pulses after the HNLF for the same broadening (Average Power ∼23 dBm). Inset Figure: Corresponding simulated intensity traces before (red line) and after (blue line) the HNLF.

spectral broadening of the rectangular pulses becomes significant at average input power levels approaching ∼23 dBm. To understand the consequences of this effect better, I have numerically simulated the SPM broadening of ideal rectangular pulses during propagation in the HNLF, using the Split Step Fourier method. Fig. 5.20 compares the simulated (black trace) and measured (blue trace) spectra for the rectangular pulses for similar input powers; while the inset of the same Figure shows the corresponding simulated intensity trace before (red trace) and after (blue trace) the HNLF. As can be observed, the ripples on the top of the pulse are amplified especially close to their edges resulting from SPM effects. Because the employed rectangular pulses have already a non-flat top, see Fig. 3.6, this effect will be even more pronounced. The increased distortion close to the edges of the shaped pulses explains the slightly different slopes on the experimental autocorrelation trace, shown in the inset of Fig. 5.19, measured after the HNLF for an average input power of ∼23 dBm.
Finally, as can be seen from Fig. 5.19, the noise floor increases by more than ∼20 dB due to the presence of the high power amplifier. Taking into account the fact that the spectrum of the clock signal sits ∼15 dB down compared to the peak power of the data spectrum, see Fig. 5.15.a, it is possible that the degraded SNR could be another source of noise in the regenerated data signal.

BER measurements of the system are presented in Fig. 5.21. First the system was

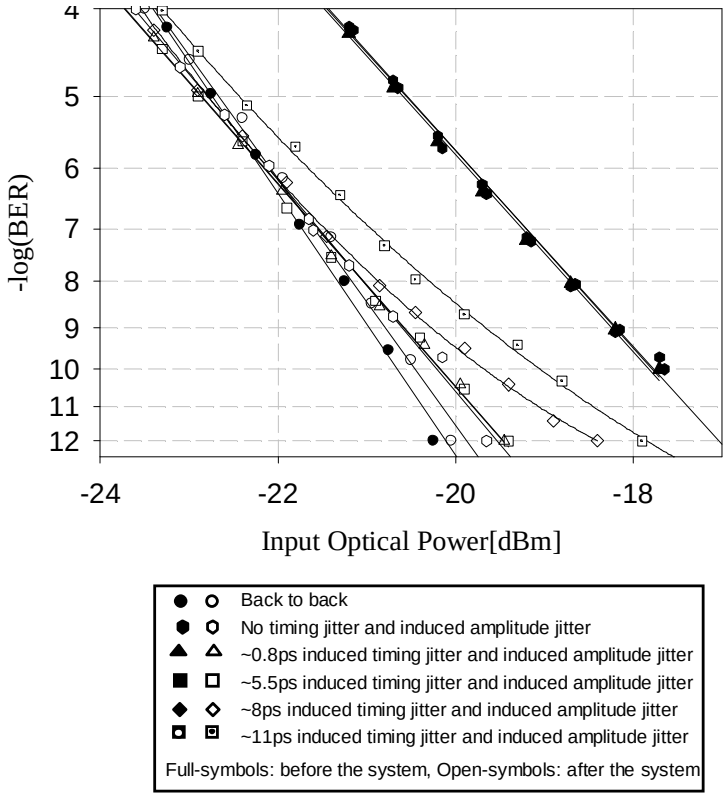

FIGURE 5.21: BER curves at various positions and settings of the system, before (full-symbols) and after (open-symbols) the re-timing and re-shaping system.

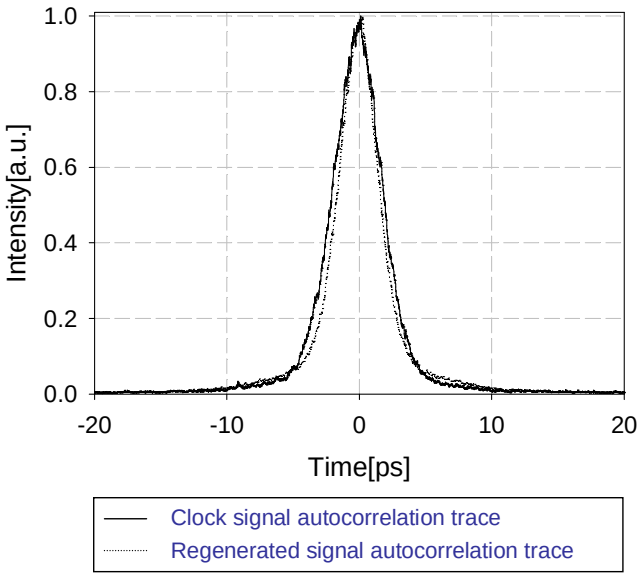

FIGURE 5.22: Autocorrelation profiles of the clock signal and of the switched signal. Both traces were taken using 16 times averaging.

characterized for the case when no noise was added, and the results confirmed that there was no power penalty relative to the back-to-back case. Next, the case where only amplitude noise was deliberately applied to the incident data pulses was considered. An improvement in the receiver sensitivity of more than 2.3 dB was achieved after the switch, demonstrating the amplitude noise reduction provided by the NOLM. Once again, it is worth noting that the BER curves are insensitive to timing jitter, due to the low-pass action of the electronic receiver. Hence, for the same amplitude noise setting, the BER curves of the input signal overlapped for all cases of induced timing jitter that were examined. As long as the induced timing jitter values remained lower than ∼5.5 ps the BER curves at the output of the reshaping - retiming system still overlapped with the back-to-back curve. For more extreme cases, a small power penalty in the BER curves (∼1 dB for ∼11 ps induced timing jitter) was observed, as previously discussed. Nevertheless, for all cases there was a clear improvement in the BER performance of the signal after the introduction of the reshaping - retiming system.

Finally, Fig. 5.22 compares the autocorrelation traces of the clock signal before being launched to the NOLM and that of the switched signal after the 3 nm filter. As can be seen they overlap reasonably well and the FWHM of the switched signal autocorrelation trace is ∼ 3.5 ps.

5.6 Conclusion

This Chapter presents a modification to the set-up described in Chapter 4 that makes use of the regenerative properties of the NOLM configuration in order to obtain reshaping/amplitude noise reduction, as well as retiming of the data pulses. In particular,

I used the combination of rectangular-pulse SSFBG and NOLM to temporally expand and flatten the noisy data pulses prior to switching them with clean clock pulses. The linear reshaping function of the SSFBG is responsible for eliminating any mistiming of the pulses at the switch output, as already discussed in the previous Chapter, while, by using the nonlinear switch based on NOLMs, it is possible to equalize the pulse amplitudes of the switched output signal.

In order to fully analyze the performance of the scheme, two different configurations are considered. Even if they present similar behaviour in terms of output timing jitter reduction, they have very different performance in terms of amplitude noise reduction.

In the first approach, two cascaded NOLMs (one active and the other passive) are implemented. While this allows the use of only commercially available amplifiers, it makes the system more complex and unstable due to temperature fluctuations and the long fibre lengths used. Furthermore, its performance was more susceptible to any amplitude noise on the original data because of the failure to achieve the π nonlinear phase shift over the length of the fibre inside the first NOLM (the signal power at the output of the EDFA before entering the first NOLM saturated at $\sim$16 dBm). Not only the amplitude noise would still remain after the first NOLM, but it would be amplified, making the task of the second NOLM even more challenging and penalizing the system in terms of Q-factor and BER performance.

In the second configuration, a single active NOLM is implemented, using a high power amplifier. This makes the configuration simpler and more robust to any amplitude noise on the original data, since no additional noise is introduced within the regenerator itself. Even if the high powers of the pulses results in slight deformations of the square pulses, the overall system performance shows more that 1 dB improvement in the receiver sensitivity for all the cases considered. A Q-factor improvement from 6 to 8 was obtained for the most extreme case of timing jitter induced.

Although the operating principle of the technique was developed at 10 Gb/s, it is envisaged that this scheme will be useful in ultra-high bit rate communications, as discussed in the previous Chapter.

Chapter 6

Retiming technique using parabolic pulses shaped in SSFBGs

6.1 Introduction

As widely emphasized in this thesis, in optical transmission, when a data pulse train is transmitted through fibres the pulse waveform can be severely distorted by perturbations including high-order chromatic dispersion, PMD and noise induced by amplifiers. These factors limit the transmission quality.
In Chapter 4, a retiming technique, based on expanding the data pulses in the time domain into rectangular pulses and then switching them with a synchronous optical clock signal aligned to the nominal center of the rectangular pulse using a nonlinear element was presented. Though its robustness was demonstrated, the technique might potentially suffer from pulse distortions affecting the signal to be shaped. Therefore, a technique where the shaping is done on the control signal, of which the pulse shape and wavelength can be accurately controlled, is preferred.

Recently, Nakazawa et al. investigated the use of the temporal Optical Fourier Transform (OFT) technique to mitigate all linear distortions after transmission [78]. The scheme relies on the fact that when a pulse is transmitted along the fibre, then in the presence of pure linear distortions, the time-domain waveform is greatly distorted, while the spectral profile remains unchanged. Because it is the temporal pulse amplitude and not the spectrum that determines the data decision at the receiver terminal, the degree, to which the waveform is distorted in the time domain, usually plays a more important role compared to the transmitted spectrum. So, if the spectrum of the signal pulse is maintained along the transmission line and the spectral shape somehow projected into the time domain before being assessed, ideal undistorted transmission can be realized.

Furthermore, if the transmitted pulses present the same shapes in both domain, e. g. Gaussian or sech envelopes, a complete reconstruction of the initial undistorted pulse can be achieved, as soon as they are Fourier transformed.

Temporal OFT is not a new concept. Back in 1983, Jannson analysed the conditions for obtaining the Fourier transformation of temporal signals in optics, exploiting the analogy between the spatial problem of diffraction through lenses and the temporal problem of dispersion [79]. This duality has led to the conclusion that an element that provides quadratic phase modulation in time is the analog of a thin lens in space that is why the technique is known as a "time lens". Jannson showed that a real time optical Fourier transformer was realizable by using temporally linearly chirped pulses and propagating them in a dispersive medium. Following these studies, in 1994 Kolner presented and derived the expressions for the time-domain analog of an imaging system by preceding and following a quadratic phase modulation ("time lens") with a suitable dispersive element, which allows scaling in time the waveform, while maintaining the overall shape of the envelope [80]. A careful choice of the time lens and the dispersive media can thus yield pulse magnification or compression.
Since then, there have been many very interesting reports on the use of a time lens in both Fourier Transform and imaging configurations for network signal processing [78, 81–87]. The properties of this time lens have been applied for compensation of polarization mode dispersion [82], removal of timing jitter [83, 84] and the elimination of higher order dispersion [85, 86]. In the first cases, the physical explanation of the time lens shows that each component of the linearly chirped pulse, generated by a parabolic phase medium, travels at a different speed owing to Group Velocity Dispersion (GVD) in the subsequent fibre. As a result, a pulse distorted by timing jitter or PMD can be restored to its original position and any distortion removed. Regarding higher order dispersion pulse distortion, since it is a linear effect, the spectrum is unchanged so that its Fourier transform in the time domain will give an undistorted pulse. A novel optical signal transmission system, which is highly tolerant to the dispersion of the transmission fibre, was proposed in [87], using this concept.

Applying a controllable linear chirp to an input pulse, has previously been achieved (1) by using an electro-optics phase modulator synchronously driven at the data repetition rate (see for example [82–84, 86]), (2) by optically switching the data pulses with synchronous, linearly chirped pulses with a rectangular temporal intensity profile [88, 89], or (3) by phase modulation in an optical fibre [90]. The speed of the first scheme is limited by the electrical bandwidth of the modulator/drive electronics and by the fact that the phase modulation profile is sinusoidal and can only be approximated to a parabolic shape only within a small region of the period. Furthermore, the maximum induced chirp on the signal is restricted by the V_π and the amount of voltage that can be applied on commercial phase modulators [91]. The second scheme has the disadvantage of environmental sensitivity due to the interferometric nature of the nonlinear optical

loop mirror used for switching. The third scheme has the disadvantage of producing a nonlinear chirp across the pulse if Gaussian- or sech-like pulses are considered as input data signals, as will be seen in the following Section.
In this Chapter, an ultrafast all-optical phase modulation technique will be described to alleviate all of these restrictions and drastically reduce the timing jitter induced in short pulse transmission systems. The scheme is based on the well-known frequency shifting effect of XPM in a HNLF [92] and [93] and incorporates a parabolic pulse shaper. In [94] the retiming of signal pulses by orthogonally polarized control pulses co-propagating in an anomalously dispersive polarization maintaining fibre is demonstrated using sech pulses. However, to obtain a linear relation between time and frequency shift, the intensity envelope of the control pulses has to be parabolic. For this reason in my experiments, the control pulses are shaped into unchirped parabolic pulses using pulse shaping in a SSFBG.

This Chapter opens by explaining the basic principle of the re-timing technique used and then explains how the parabolic pulses were generated and characterized. Finally, the experimental set-up and the complete characterization of the system, which is supported both by experimental data and numerical analysis, are presented.

6.2 Retiming technique: Basic principle

A common approach to the treatment of timing jitter is to map the temporal misplacement associated with a given bit from the nominal bit slot center onto a linear frequency chirp [84, 88]. The frequency-chirped bits can then be retimed by propagating them in a length of optical fibre, or by reflection from a fibre Bragg grating, with suitably matched net-dispersion. In this way, the positional fluctuations can be reduced at the expense of the carrier frequency jitter. Such a process leads to improvement of the timing signal, since the optical bandwidth of the detectors is large enough to be insensitive to frequency jitter.
The scheme proposed herein is based on XPM in a HNLF and utilizes the time derivative effect of XPM-induced spectral broadening to induce chirp onto the data pulses.
Considering a transform limited data signal, which has a Gaussian pulse shape, its profile can be written as:

$$A(T) = \sqrt{P_0} exp(-\frac{T^2}{2T_0^2}), \tag{6.1}$$

where T_0 is the full width at 1/e of the maximum and P_0 is the corresponding signal peak power. This data signal is assumed to co-propagate with a control signal with electric field profile $B(T)$, which has an initial relative time delay ΔT compared to the signal A(T).
Note that, in this theoretical analysis, I consider only one data pulse and one control pulse, so I have decided to use the initial position of the data pulse as a reference (see

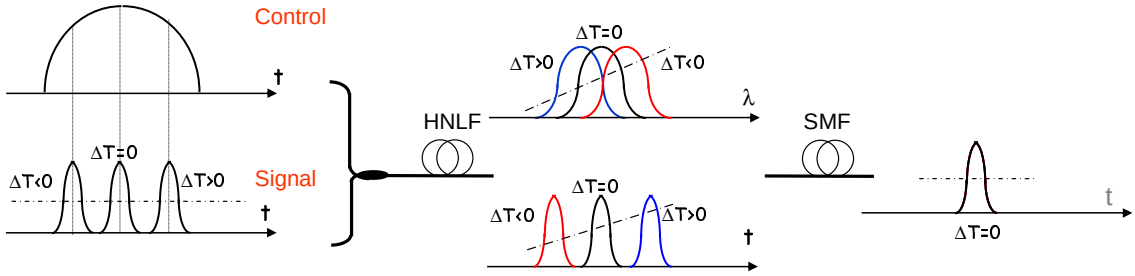

FIGURE 6.1: Sketch of the principle of the Re-timing technique based on XPM in a HNLF.

Fig. 6.3). In this way the analysis of the main effects of the control signal on the data pulse are more explicit and easy to follow.
The description of the phase, $\phi(T)$, induced by the control pulse on the signal via XPM can be mathematically described by [29]:

$$\phi(T) = 2\gamma P_{o,par} L_{eff} |B(T - \Delta T)|^2, \tag{6.2}$$

where γ is the nonlinear coefficient of the fibre, $P_{o,par}$ is the control peak power, $B(T)$ is the normalized slow varying amplitude of the control pulse envelope and L_{eff} is the effective length of the fibre, already defined in Eq. 2.2.
Consequently, the XPM frequency shift induced on the signal, $\delta\omega_{sig}(T)$, is given by:

$$\delta\omega_{sig}(T) = -\frac{\partial\phi}{\partial T} = -2\gamma P_{o,par} L_{eff} \frac{\partial |B(T - \Delta T)|^2}{\partial T}. \tag{6.3}$$

In these formulas, the dispersive walk-off between the signal and control pulses is neglected and the control pulse is assumed to maintain its temporal intensity profile while propagating along the HNLF. These conditions can easily be met with state-of-the-art HNLFs. For example, in the experiment described below, the control/signal pulse walk-off is less than 0.1 ps, and the control pulses experience a small normal dispersion which minimizes any temporal pulse distortion arising from the high power levels.
Eq. 6.3 shows that a XPM modulated signal acquires a chirp, which depends on the slope of the control pulse (see Fig. 6.1). Signal pulses which overlap with the leading (trailing) edge of the control pulses experience a red (blue) frequency shift in their spectrum due to XPM. By contrast, when the signal pulses are aligned to the peak of the pump pulses the mean optical frequency remains unchanged. Consequently, the group velocity of the individual XPM modulated data bits after the HNLF will depend on the amount of induced frequency shift: signal pulses that get red (blue) frequency shifted will require a longer (shorter) time to propagate through a fibre with anomalous dispersion. One can then use this group velocity variation between mistimed pulses, in order to cancel the initial temporal misalignment ΔT on a bit-by-bit basis, e.g. by propagating the XPM modulated signal through an appropriate length of SMF, see Fig. 6.1.
It is quite straightforward to prove that in order to obtain a linear relation between

$\delta\omega(T)$ and ΔT, the intensity envelope of the control pulses should have a parabolic shape. The electric field profile of a parabolic pulse, which has an initial time delay, ΔT, compared to the data signal centre, can be written as:

$$U(T-\Delta T)=\sqrt{P_{o,par}}\ B(T-\Delta T)=\sqrt{P_{o,par}(1-\frac{(T-\Delta T)^2}{T_{o,par}^2})} \tag{6.4}$$

where $T_{o,par}\sqrt{2}$ is the temporal full width at half maximum. In this case, ignoring the constant-phase term, the induced nonlinear phase on a co-propagating monochromatic signal (ignoring any walk-off effects) becomes:

$$\phi(T)=-2\gamma P_{o,par}L_{eff}\frac{(T-\Delta T)^2}{T_{o,par}^2}, \tag{6.5}$$

and the change in the optical frequency is then a linear function of the time and the time delay:

$$\delta\omega_{XPM}(T)=4\gamma P_{o,par}L_{eff}\frac{T-\Delta T}{T_{o,par}^2}. \tag{6.6}$$

If more conventional pulse forms (e.g. Gaussian or sech pulses) are to be used as control signals instead, then Eq. 6.5 or Eq. 6.6 would be accurate only for a small region close to the center of the pulse (less than half the FWHM of the data pulse). This is clearly demonstrated in Fig. 6.2, where different control pulse shapes and the corresponding intensity time derivatives are compared. Note that the time derivatives are proportional to the wavelength shift that can be induced by the control signal on the signal via XPM. As can be seen, only the parabolic shape ensures a linear chirp across its total width (see red trace). Gaussian (green trace) and sech pulse shapes (blue trace) with the same FWHM do not exhibit exactly linear slopes and anyway they do not extend across the whole pulse width.

Fig. 6.2.a also emphasizes the fact that parabolic pulses have sharper tails than the other

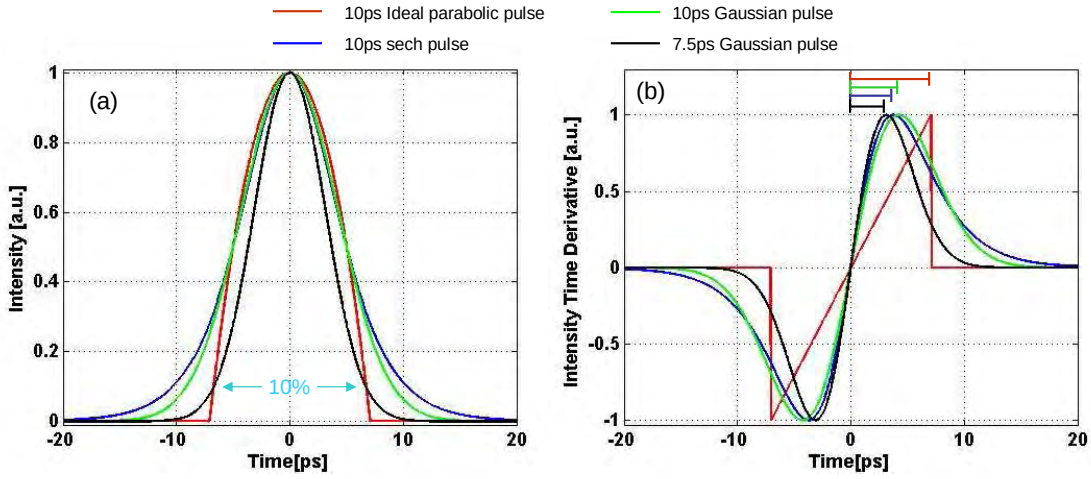

FIGURE 6.2: Comparison of different intensity shapes (a) and their corresponding intensity derivative shapes (b).

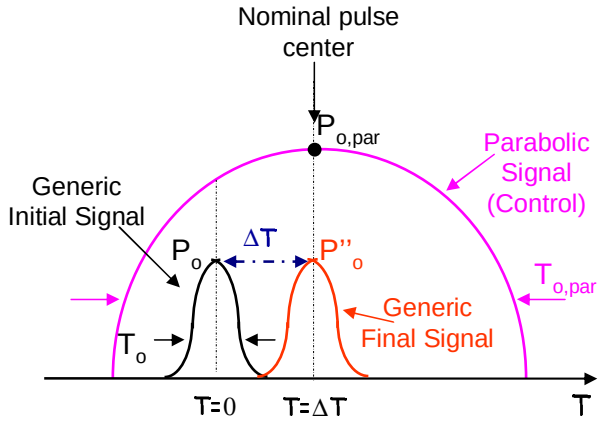

FIGURE 6.3: Schematic of the relative positions of the Gaussian and the parabolic signals.

two types of pulse shape. This is very interesting for high repetition rate transmission where intersymbol interference can become an issue. For this reason, the 10 ps parabolic pulse is also compared with a Gaussian pulse of ∼7.5 ps FWHM, which has the same full width at 10% of the intensity maximum. In this last case, see black traces, the linear slope of the parabolic pulse extends more than two times compared to the sech case.

Fig. 6.3 shows a schematic of the initial relative positions of the data (black profile) and control parabolic (pink profile) signals, in which the main parameters are highlighted. As already pointed out in the beginning of this Section, because the centre of reference is considered to be the initial position of the data pulse, the parabolic signal has a time delay ΔT relative to this signal. This implies that the final signal (red profile) is properly retimed if it has the same relative time delay ΔT as the control signal.

Taking into account the XPM contribution induced in the HNLF, the incident electric field, A', of the data signal given by Eq. 6.1 can be rewritten as:

$$A'(T) = \sqrt{P_0} exp(-\frac{1+iC}{2}\frac{T^2}{T_0^2}) exp(\frac{iCT\Delta T}{T_0^2}) exp(-\frac{iC\Delta T^2}{2T_0^2}), \tag{6.7}$$

where $C = -4\gamma P_{o,par} L_{eff} T_0^2 / T_{0,par}^2$.
The first term in Eq. 6.7 is a standard linearly chirped Gaussian pulse, the second term describes a linear phase ramp, which indicates a center frequency shift of the pulse equal to:

$$\Delta\omega = -\frac{C\Delta T}{T_0^2}, \tag{6.8}$$

and the last term is only a constant-phase term. As can be noted, the XPM in a HNLF (time lens) gives each signal pulse a frequency shift that is proportional to its temporal jitter displacement. Obviously, if the time delay between the control and the signal pulses is nil ($\Delta T = 0$), the mean optical frequency remains unchanged.
As discussed above, the XPM signal can then be propagated through an appropriate

length of SMF to remove the offset in time ΔT (i. e. to retime the signal). Specifically, the time shift, T_s, caused by the centre frequency shift as the pulses propagate through the fibre can be written as:

$$T_s = \beta_2 \Delta\omega z = -\beta_2 (C\frac{\Delta T}{T_0^2})z = -sgn(\beta_2)C\Delta T\frac{z}{L_D}, \tag{6.9}$$

where L_D id the dispersion length, defined in Eq. 2.33. To eliminate timing jitter, the induced time shift has to compensate for this, i.e.:

$$T_s = -\Delta T = -sgn(\beta_2)C\Delta T\frac{z}{L_D}. \tag{6.10}$$

This condition imposes a precise value for the length of the SMF required to retime the signal, which is:

$$z = sgn(\beta_2)\frac{L_D}{C}. \tag{6.11}$$

Note that according to how the values of C and β_2 are chosen for this derivation, their product is always positive.

To calculate the electric field after propagating through such a fibre (A"), the standard Fourier transform method can be used and the final result is [95]:

$$A''(T-\Delta T) = \sqrt{P_o}\sqrt{\frac{C}{i}}\ exp\ [\frac{iC}{T_0^2}(T-\Delta T)]\ exp\ [\frac{iC(T-\Delta T)^2}{2T_0^2}]\ exp\ [-\frac{C^2(T-\Delta T)^2}{2T_0^2}]. \tag{6.12}$$

Eq. 6.12 shows that the peak of the output signal is now exactly at the position of the control peak $(T-\Delta T)$, implying that timing jitter is accurately removed (see red trace in Fig. 6.3). The first two terms in Eq. 6.12 are jitter-dependent phase shift contributions, which can be simply ignored in an OOK system, where only the pulse intensity is detected. Furthermore, it is interesting to note that if $\mid C \mid$>1, the time lens will also provide some degree of pulse compression, while if $\mid C \mid$=1, the final pulse shape becomes exactly the same as the input one. This means that, according to the system application required, a careful choice of the induced XPM is required.

In the case of a sech data pulse shape, it is not easy to calculate an analytic expression for the final electric field after the retiming scheme, however similar behaviour to the Gaussian shape is expected.

Finally, note that later on in the Chapter, when the numerical and experimental results are discussed, I change the reference system to agree with the control signal. This choice is due to the fact that in the real experiment the control pulses have the same centre position, while the data pulses have a variable delay, so a variable initial position.

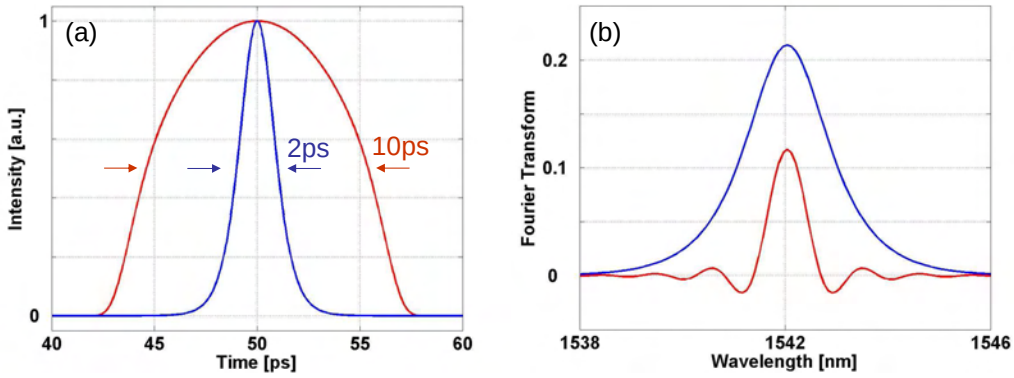

FIGURE 6.4: a) Intensity of the initial pulse and of the reflected signal via the SSFBG. b) Fourier transform of the corresponding pulses.

6.3 Parabolic Pulse Generation and its characterization

As mathematically derived in the previous Section, to obtain a linear relation between the instantaneous frequency chirp induced by XPM and the time, the intensity envelope of the control pulses should have a parabolic shape. To date, parabolic pulses have been generated in many different ways, for example, under certain conditions within normally dispersive optical fibre amplifiers (both in rare-earth doped amplifiers [96, 97] and in Raman amplifiers [98]) by exploiting the interplay between gain, nonlinearity and dispersion, however this makes for a complex system. Parabolic pulse generation is also possible in a passive manner, by using normally dispersive dispersion decreasing fibres [99]. For my experiments, I used pulse shaping in a SSFBG to generate unchirped parabolic control pulses. Thus, parabolic pulses are generated in a passive, linear and highly stable manner within a few centimeters of SSFBG, making the system very compact. The operation of the SSFBG is similar to that in the previous Chapters for shaping into rectangular pulses: the grating applies precise spectral filtering to the amplitude and phase of short laser pulses, such that upon reflection the spectrum of the signal acquires the complex spectral envelope corresponding to the required parabolic pulse form, see Section 2.6 for further details.

I designed the parabolic pulse shaper as follows. Fig. 6.4.a shows the starting 2 ps sech pulse (blue trace), together with the target parabolic pulse (red trace). The parabolic envelope (FWHM of ∼10 ps) was apodized by a 5th order super-Gaussian profile, which was used to smoothen the pulse edges and reduce their spectral extent. In Fig. 6.4.b, the electric fields of the initial pulse and of the reflected signal are plotted in the wavelength domain (blue and red trace respectively). Note that the electric fields of these signals are plotted in the Figure, rather than their intensities, in order to highlight the π phase shifts between the different lobes in the parabolic pulse case. The same Figure also shows how the initial spectrum has to be shaped (filtered out) via the SSFBG so that the representation of the electric field of the reflected signal in the frequency domain corresponds to the red trace.

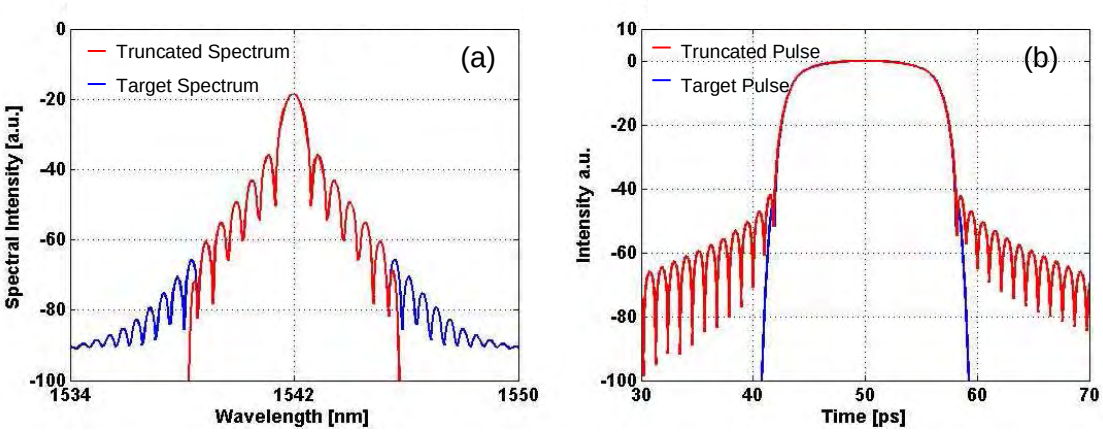

FIGURE 6.5: Comparison between the target and truncated pulse in the temporal (a) and wavelength (b) domain.

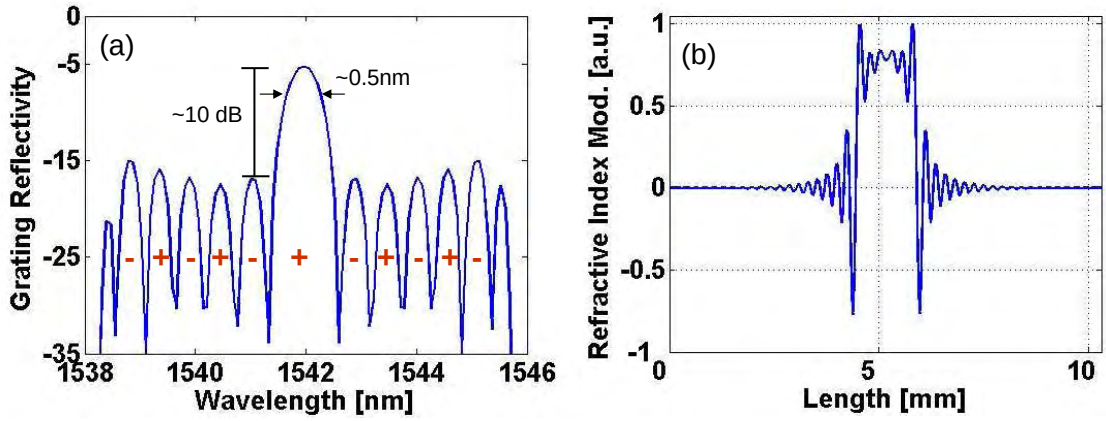

FIGURE 6.6: a) Calculated spectral response of the SSFBG's performing pulse shaping of sech pulses into parabolic pulses and (b) the corresponding refractive index modulation profile.

The blue trace in Fig. 6.5.a shows the spectral intensity of the "target" parabolic pulse spectrum plotted on a logarithmic scale. The spectrum extends to infinity and this would correspond to a very high temporal resolution. Indeed, the temporal resolution is proportional to the inverse of the total frequency bandwidth, which would require very fast changes in the superstructure profile of the grating. For this reason, the spectrum needs to be truncated (red trace in Fig. 6.5.a) and Fig. 6.5.b shows the corresponding intensity profile in the time domain of the target and truncated pulses. The two curves only differ for values 40 dB below their peak values, demonstrating that the truncation function lightly affects the parabolic shape. Finally, Fig. 6.6.a shows the simulated spectral response of the apodised SSFBG for parabolic pulse generation. 11 spectral lobes were accommodated within a ∼7 nm bandwidth to obtain a close approximation to a parabolic shape pulse in the time domain. The +/- signs in each lobe stand for a 0 or a π phase shift in the phase of the designed grating, as already discussed above. The corresponding refractive index modulation profile of the grating, required to achieve such response, is shown in Fig. 6.6.b and highlights the precision required within the

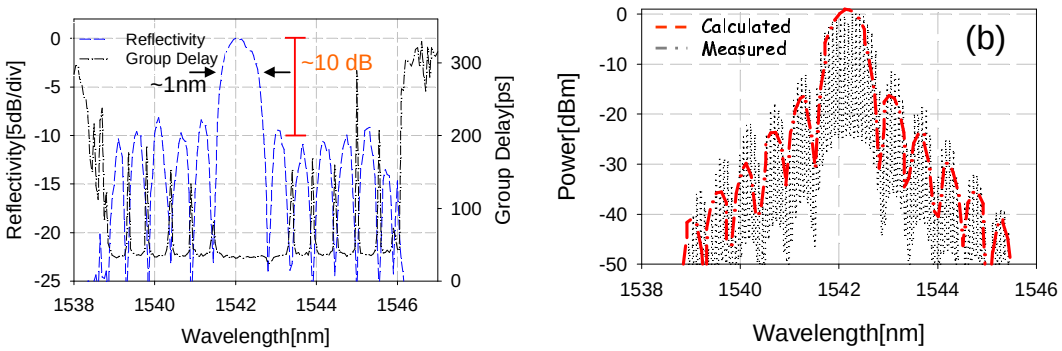

FIGURE 6.7: a) Measured spectral response of the parabolic pulse shape SSFBG: reflectivity (blue trace) and corresponding group delay (black trace). b) Measured (red trace) and calculated (black trace) optical spectrum of the signal reflected off the SSFBG.

grating writing process.

The measured reflectivity of the grating is plotted in Fig. 6.7.a together with its corresponding group delay. While the extinction ratio between the main lobe and the side lobes is ∼10 dB as expected from the numerical simulations and the π phase shifts at the boundary of each lobe are very clear, the main lobe bandwidth is ∼2 times broader than the expected one (see Fig. 6.6.a). However, by using slightly broader initial pulses in the experiment (from ∼1.4 nm corresponding to 2 ps pulses to ∼1.1 nm corresponding to 2.5 ps), which correspond to a narrower spectrum compared to those specified in Fig. 6.4.a, it is possible to improve the -3dB bandwidth of the final shaped pulses. Indeed, Fig. 6.7.b compares the measured optical spectrum of the pulses reflected off the SSFBG (gray dash-dot trace) with the spectrum of a single parabolic pulse, showing a fair agreement between the two. The quality of the shaped pulses was assessed using the SHG-FROG technique, see Fig. 6.8. In particular, Fig. 6.8.a and Fig. 6.8.b show the measured and retrieved spectrograms of the parabolic pulse plotted on a logarithmic scale to highlight the spectral side lobes. Fig. 6.8.c shows the comparison between the retrieved spectrum (black solid line) and the direct spectral measurement (gray dash-dot line). Good agrement is obtained within the resolution of our SHG-FROG system. Fig. 6.8.d shows the temporal profile of the shaped pulses as characterized by the SHG-FROG and the calculated time derivative of the intensity profile, which is shown to be fairly linear across the central 10 ps region of the pulse. Even if some pedestal is visible from the reconstructed temporal intensity, it will not cause particular problems for the induced timing jitter values used in my experiments. However, as I will discuss in the next Chapter, this pedestal will be an issue when investigating the nonlinear propagation of these pulses along a HNLF. In that case, a more critical analysis will be carried out to identify what can be done to the grating to amend the discrepancy between the designed and the measured reflectivity profile and to improve the final pulse shape.

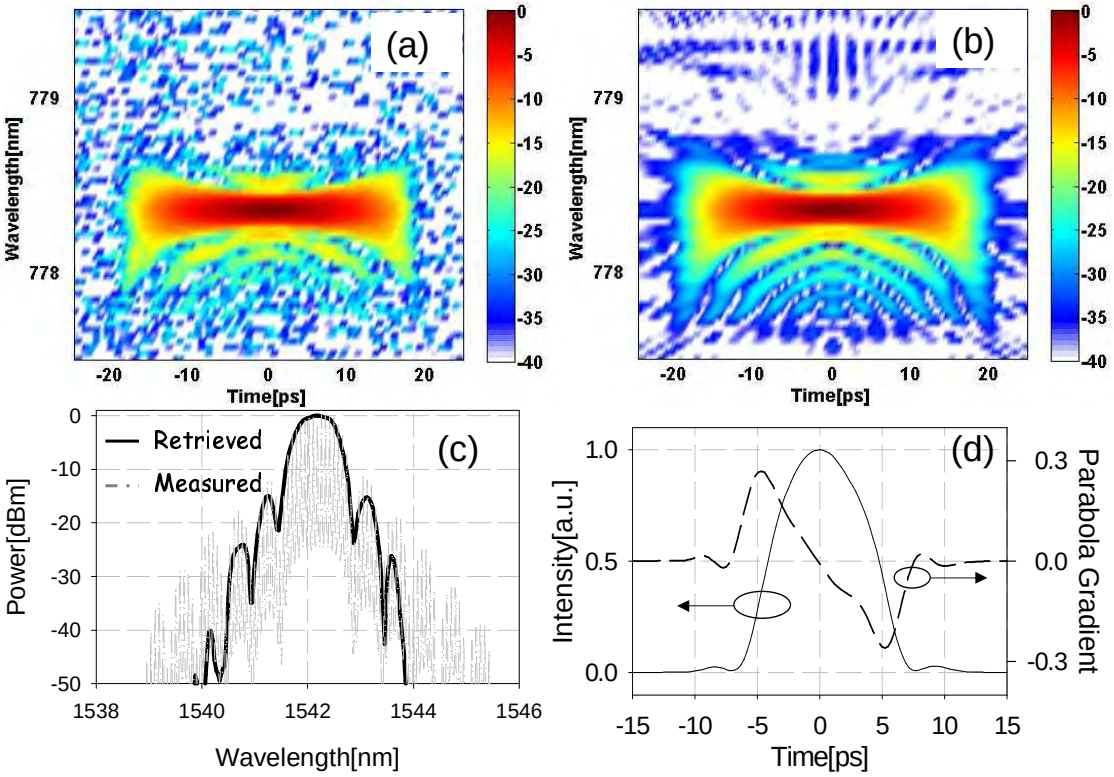

FIGURE 6.8: Spectrograms: Measured (a) and reconstructed (b). c) Measured (grey dash-dot line) and SHG-FROG retrieved (black solid line) spectra of the parabolic pulses. d) Intensity of the parabolic pulses measured using SHG-FROG and its corresponding gradient.

6.4 Experimental Re-timing Set-up

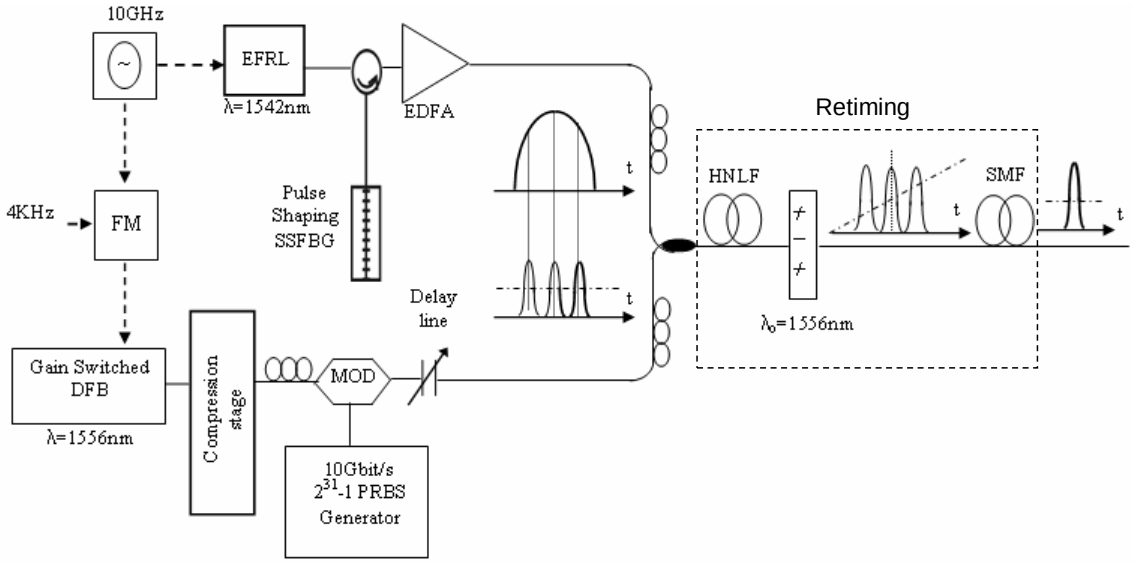

FIGURE 6.9: Experimental set-up of the re-timing system using parabolic pulses as control signal.

The experimental set-up for the implementation of the retiming system is shown in Fig. 6.9. The same mode-locked EFRL to that used in the previous system experiments, this time operating at 1542 nm, was used to generate ∼2.5 ps sech pulses at a repetition rate of 10 GHz. These pulses were used as the input to the parabolic pulse shaper formed by a SSFBG, as described in Sec. 6.3. The data source, operating at 1556nm, was a gain-switched DFB laser, synchronized to the EFRL. Timing jitter was artificially introduced on the data pulses by frequency modulating the 10 GHz RF drive signal to the laser with a 4 kHz tone, as discussed in Section 5.2. The pulses of the gain-switched DFB were compressed down to ∼2 ps using a fibre-based compressor, see Section 5.4 for further details, and then modulated by a $2^{31}-1$ PRBS using a lithium niobate modulator and fed into 220 m of a HNLF via the 10% port of a 90-10 coupler. The characteristics of the HNLF are reported in Tab. 3.1. The parabolic pulses were amplified and coupled to the HNLF via the 90% port of the coupler, and served as the control signal for the XPM process. An optical delay line was used to temporally overlap the two signals. The average power of the control signal was ∼21 dBm and the power of the data signal was kept quite low, ∼3 dBm, to avoid any SPM, which might otherwise induce additional chirp on the data pulses. An example of the spectrum after the HNLF is presented in Fig. 6.10.a. The signal then passed through a 5 nm wide optical filter which filtered out the control without affecting the data spectrum, and was launched onto an appropriate length of SMF (500 m) which removed the chirp and retimed the pulses. Fig. 6.10.b shows the spectrum of the data signal before and after the filter to confirm that very little information is lost during the filtering.

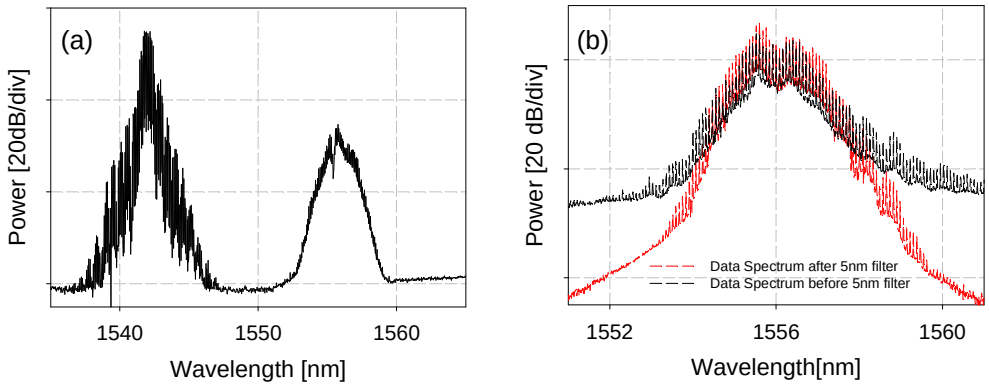

FIGURE 6.10: a) Spectrum of the signals after the HNLF. b) Spectrum of the signal before (black trace) and after (red trace) the 5 nm filter when the signal pulses are aligned to the middle of the parabolic pulses ($\Delta T = 0$).

6.5 Results and discussion

To have a better feeling of the effect of the data pulsewidth on the system performance and to better examine and understand the overall retiming system, as well as the maximum total amount of induced timing jitter that could be applied, I modelled the propagation of the signals in the HNLF and SMF using the nonlinear Schrödinger equation (see Section 2.5.1 for further details on the implementation of the standard split-step Fourier method).

The first point to be resolved was the tolerance levels of the system with respect to the data signal pulsewidth. It is obvious that the shorter the pulsewidth, the better the performance will be. However, it is important to study how the duration of the data pulses can affect the performance of the retiming system.

At the time of the experiment, a gain switched DFB laser was employed as the data signal. Straight after the DCF (linear compression), the pulsewidth was about 5 ps, while after nonlinear compression ~2 ps pulses could be easily achieved. So 2 and 5 ps sech pulses were modelled as the data signal with the same peak power value of 88 mW (a low value is chosen in order to minimize any SPM effects). The control signal was modelled as designed for the experiment, i.e. ~10 ps parabolic pulse superimposed with a 5^{th} order super-Gaussian.

Fig. 6.11.a and Fig. 6.11.b show the position of the initial data pulses (blue pulses), before the time compensator, relative to the control pulse (red pulse) centre, which has been chosen as absolute reference ($\Delta T = 0$). The maximum amount of delay was set to $\Delta T = \pm 5\ ps$, corresponding to the FWHM of the parabolic pulses and the step considered was 0.5 ps. Clean sech shapes are obtained in both cases of data pulsewidths, when the data sit close to the middle of the parabolic pulses. However, when the relative offset increases, then part of the pulses sit outside the parabolic shape and this is even more critical for broader data pulses. This means that there will be a nonlinear chirp across these pulses that will translate into distortion on the pulse shapes themselves.

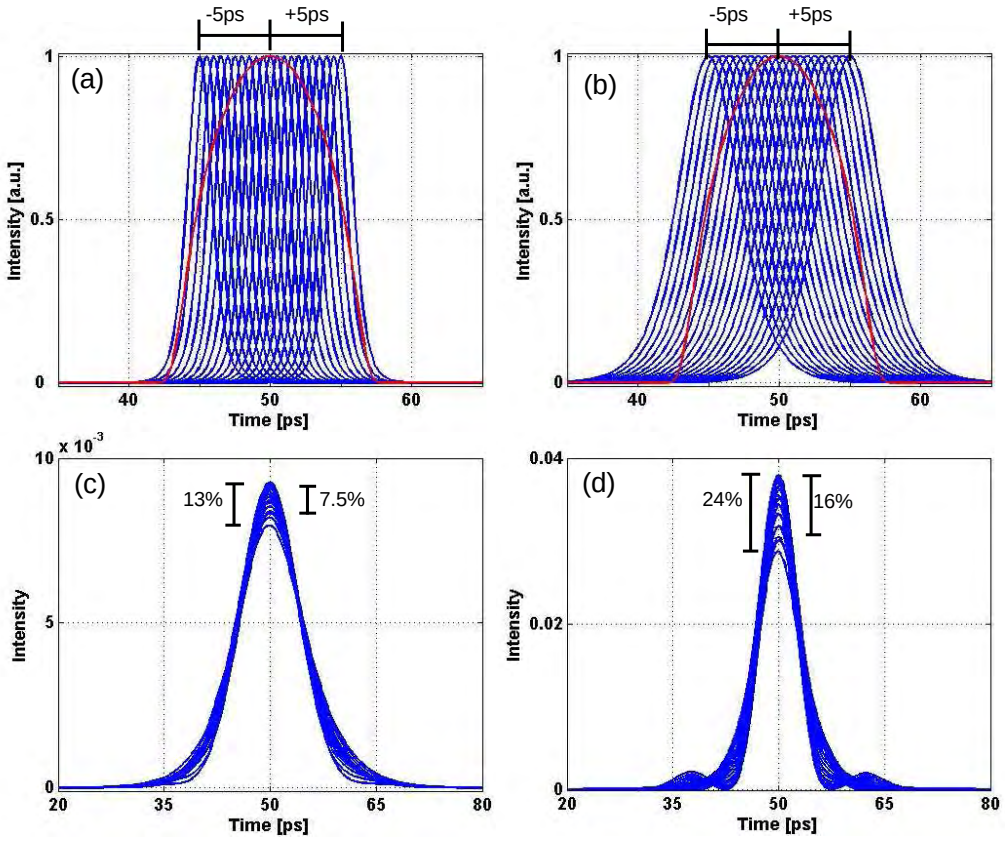

FIGURE 6.11: Data and control signals before the simulated retiming scheme for 2 ps (a) and 5 ps (b) sech pulses. Corresponding pulses at the output of the system (c) and (d).

Because each pulse will have the same energy after the propagation through the HNLF, the distortion will cause some fluctuations in the peak power, introducing some amplitude noise.

Indeed, Fig. 6.11.c and Fig. 6.11.d show the final pulses at the output of the simulated retiming system. When 2 ps initial pulses are considered, the retiming is clearly achieved and the pulses broaden up to ∼10 ps because of the dispersive medium (few hundred meters of SMF). Some amplitude noise fluctuations, due to distortions, are evident as previously discussed. In particular, peak amplitude fluctuations of ∼13% are obtained for a maximum delay of $\Delta T_{max} = \pm 5\ ps$, and only ∼7.5% if a maximum delay of $\Delta T_{max} = \pm 4\ ps$ is considered. When 5 ps initial pulses are propagated, the situation becomes more critical. Retiming is still achieved, but highly distorted pulses with significant pedestal and amplitude noise (∼24% for $\Delta T_{max} = \pm 5\ ps$ and ∼16% for $\Delta T_{max} = \pm 4\ ps$) are obtained.

From these preliminary studies, it is clear that the data signal should be as narrow as possible, compared to the control signal, to avoid distortion on the signal. On the other hand, the 2 ps initial pulses result in broader final pulses than the 5 ps initial pulses. This is clearly understood in terms of Fourier transforms as discussed in the introduction of this Chapter. The shorter the pulse is in the time domain and broader it is in the

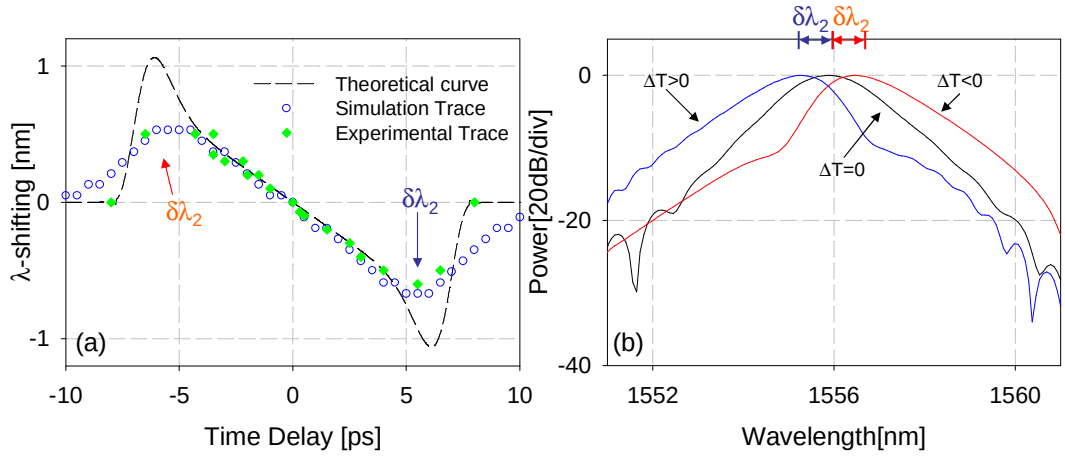

FIGURE 6.12: a) Analytical, numerical and experimental curves of the wavelength shift versus time delay between the control and data signals. b) Numerical XPM data spectra for different cases of overlap.

frequency domain. At the end of the retiming system, the signal is the Fourier transform of the initial one, so that shorter pulses broaden up more than the corresponding broader pulses. However, this broadening can be avoided. For example, the initial pulse that needs to be retimed can be carefully pre-chirped so that the final pulsewidth is comparable to the input width one [84]. Obviously, though this would imply a broader pulse when it interacts with the control pulse in the HNLF. Alternatively, a higher control peak power, which corresponds to a higher induced XPM frequency shift, can be used, so that a shorter length of SMF can be used. In Section 6.2, it was already pointed out that in order to keep the same initial pulse shape, a careful choice of the control peak power (proportional to the parameter C) was required, see Eq. 6.12.

To test the linearity of the XPM chirping scheme, the shift of the central wavelength of the data signal was first simulated as a function of their temporal misplacement, ΔT, relative to the centre of the parabolic pulses. The simulated trace is shown in Fig. 6.12.a (blue circles). The XPM-induced wavelength shift is found to vary linearly with the delay ΔT, closely following the trend anticipated from my design, obtained by calculating the instantaneous frequency shift from Eq. 6.3 (see dashed curved in the same Figure). The divergence of the theoretically calculated slope from a straight line close to the edges of the control pulses is due to the super-Gaussian profile superimposed upon the ideal parabolic shape. The figure also highlights that the simulated trace does not follow the monochromatic signal trend when the data pulses sit close to the edges of the parabolic pulse wings. This is because of the finite width of the spectrum of the data pulses, which gives rise to distortion at these extreme cases of input time delays. This is illustrated in Fig. 6.12.b, which shows some simulated examples of spectral traces of the data signal, just after the HNLF. In particular, a blue shifted- (Δ T>0), un-shifted- (ΔT=0) and a red shifted-spectrum (ΔT<0) are shown.

Next the signal after the SMF was examined. In particular, the temporal difference

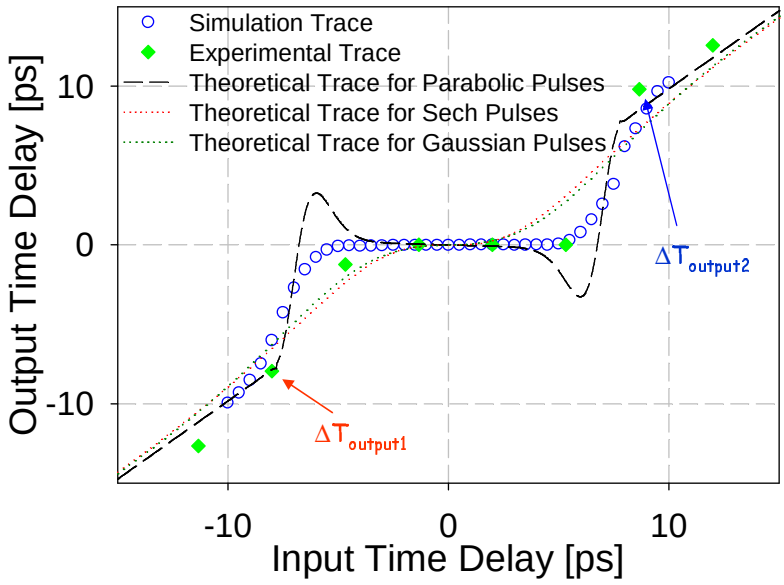

FIGURE 6.13: Relative time delay of the data pulses at the output of the system for various control pulse shapes as a function of the initial time delay between control and data pulses.

between the center of the control pulse and the data pulse was studied as a function of the relative mistiming of the pulses at the system input. In Fig. 6.13 the results are plotted together with the theoretical curve, which is obtained by considering only XPM-induced frequency shifting in the HNLF and linear propagation in the SMF. For reference, the Figure also shows the predicted performance of Gaussian and sech pulses of the same FWHM (10 ps) as control signals, highlighting the importance of the use of a parabolic shape in achieving a broad retiming window (+/-5ps retiming window for parabolic pulses).

For the characterization of the performance of the experimental set-up, I performed the same kinds of measurements that were previously simulated. The results from the experiments are compared against the simulation results in Fig. 6.12.a and Fig. 6.13. In Fig. 6.12.a, the measured XPM-induced wavelength shift (diamond points) is plotted against both the theoretical and simulated results, previously discussed, showing a very good agreement between the two. In Fig. 6.14 I show some experimentally obtained examples of spectral traces of the data signal, showing one of the most extreme cases of blue shifted- ($\Delta T>0$), un-shifted- ($\Delta T=0$) and red shifted-spectrum ($\Delta T<0$), used to derive some of the previous points in Fig. 6.12.b. Note that these measurements were taken before the SMF, but the same results would have also been obtained after the SMF, since linear propagation through a dispersive medium does not affect the intensity of the spectral components.

Next, the signal after the SMF was examined in the experiment. The control signal was not completely filtered out, so that this could be used as a temporal reference point. By adjusting the optical delay line, the combined autocorrelation of the control and data

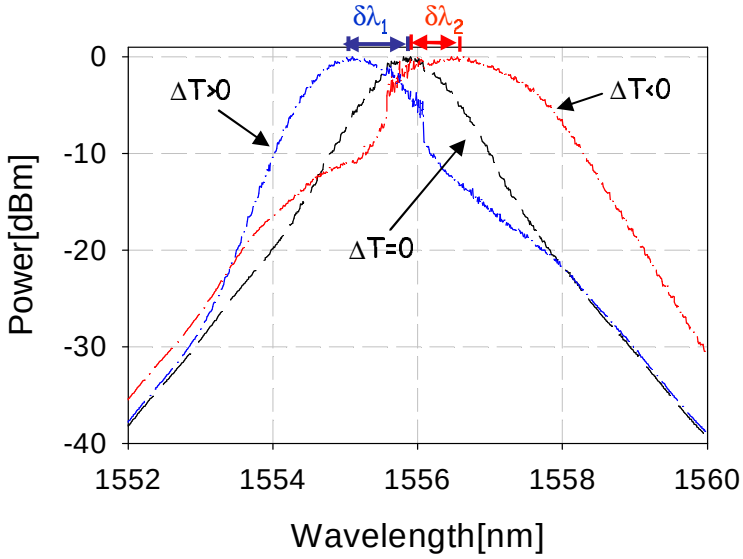

FIGURE 6.14: Experimental XPM data spectra for different cases of overlap.

signals at the output of the SMF was measured for various values of ΔT, and from that the information on the relative mistiming of the pulses was extracted (diamond points in Fig. 6.13). Once more, the measurement is in good agreement with the theoretical and numerical curve. Examples of three cases of different arrival times of the data pulses, relative to the parabolic control pulses cross-correlation trace, are shown in Fig 6.15. It is worth noting that because of the difference in the group velocity between the control and data wavelengths inside the SMF, the two signals do not overlap in the case of ΔT=0 at the output of the system. From Fig. 6.15, it can be noted that the autocorrelation pulsewidth in the case of ΔT=0 is slightly narrower compared to the other two cases. This can be explained, considering Fig. 6.11, where it is shown that by increasing ΔT, a

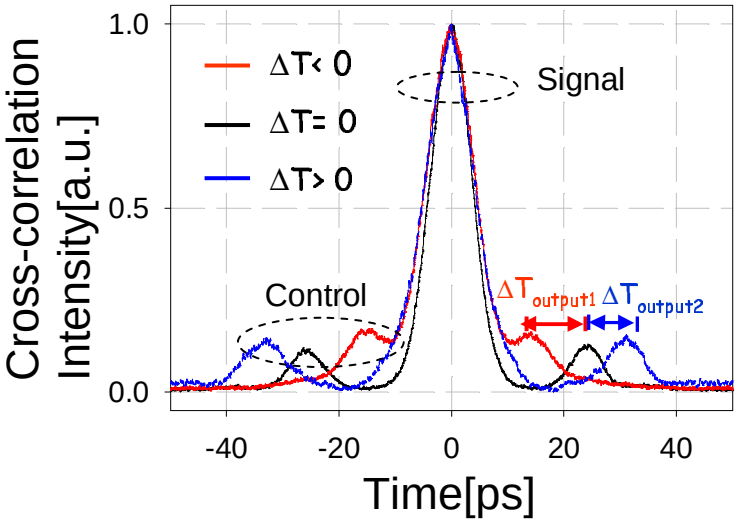

FIGURE 6.15: Cross-correlation traces of three cases of different arrival time of the data pulses relative to the parabolic control pulses.

greater portion of the pulses sit outside the parabolic shape, meaning that these pulses will get more distorted. In particular, the pulse broadens to the detriment of the peak power and the corresponding autocorrelation pulse width increases.

The performance of the retiming system was evaluated for several values of deterministic timing jitter, deliberately applied to the initial data pulses. The eye diagrams at the input and output of the system were observed on a DCA, and the timing jitter measured by means of the intensity distribution histograms at the FWHM point (taken on the trailing edge of the pulses), as already discussed (see Section 4.3). These measurements are summarized in Fig 6.16 and Fig 6.17. It is possible to suppress the timing jitter by as much as ∼4 ps (rms value) in the incoming data stream, corresponding to a peak-to-peak (p-p) value of ∼18.2 ps. Above this value, the probability of finding the pulse outside the retiming window increases drastically. Fig 6.16 shows some examples of eye diagrams at the input and output of the retiming system, obtained for incoming signals with an rms timing jitter of ∼1.8 ps (p-p of ∼10.4 ps), ∼2.9 ps (p-p of ∼15.3 ps) and ∼3.5 ps (p-p of ∼16.4 ps) respectively. The corresponding timing jitter histograms of these pulses are plotted in Fig 6.17.a and Fig 6.17.b. The jitter of the pulses at the output of the retiming system was measured to be ∼1 ps (rms value) for all the cases examined, see Fig 6.17.c, which corresponds to the resolution limit of the DCA used for my measurements. Note that, similar to other retiming schemes that rely on the conversion of timing jitter to a wavelength jitter, an additional switching stage would be

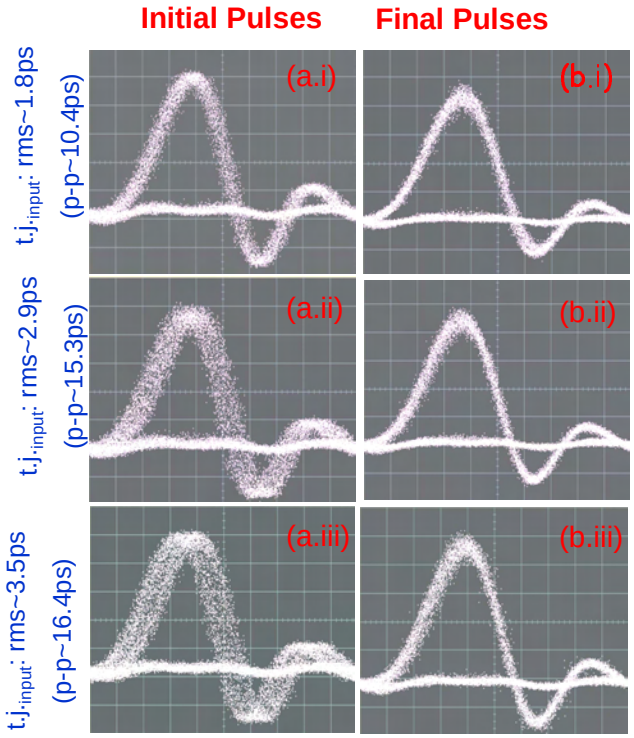

FIGURE 6.16: Eye diagrams before (a.i-iii) and after (b.i-iii) the retiming scheme for three different values of induced timing jitter. Time scale: 10 ps/div. Scope bandwidth: 20 GHz.

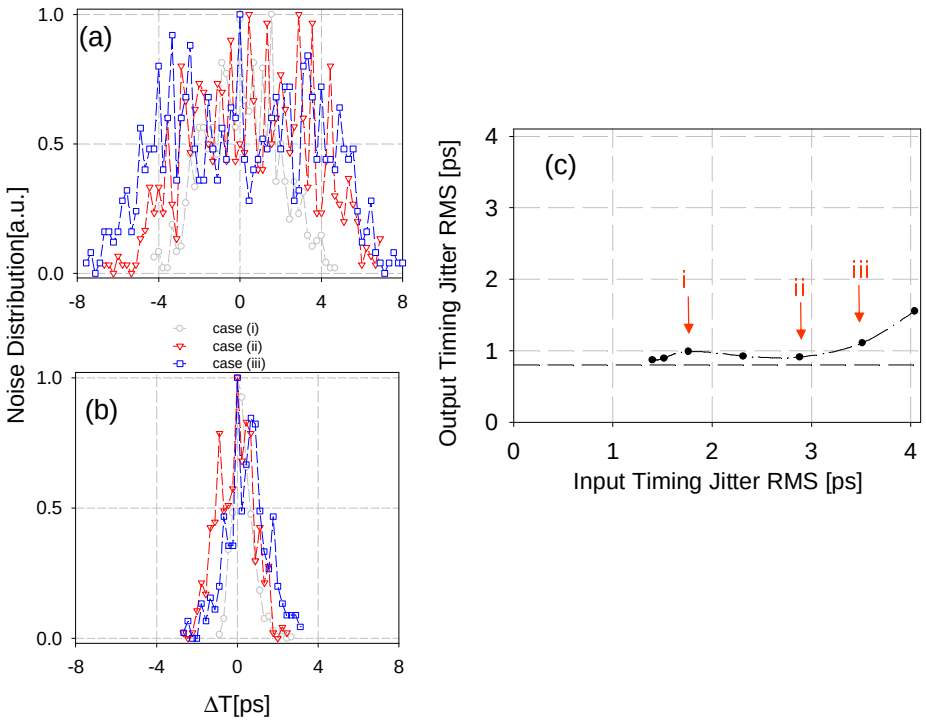

FIGURE 6.17: Noise distributions for 3 different cases of timing jitter before (a) and after (b) the retiming scheme. (c) Output versus input rms timing jitter of the data signal.

needed to be included at the output of the system, in order to transmit the pulses further.

6.6 Conclusion

In conclusion, the application of SSFBG-based linear pulse shaping to parabolic pulse generation and the use of such pulses for the retiming of short optical pulses was numerically and experimentally demonstrated. The retiming technique relies on frequency-chirping mistimed pulses using XPM in a HNLF pumped by parabolic clock pulses. The profile of these pulses ensures that the chirp on the switched pulses is linear over a wide range, so that it can be removed by linear propagation in an appropriate length of SMF. If more conventional control profiles, such as Gaussian or sech, are to be used, the approximation of the XPM-induced phase to a linear curve would be accurate only for a small region close to the centre of the pulse, as clearly demonstrated in this Chapter. The importance of using broad data parabolic pulses relative to the data pulses to reduce distortion of the pulses is also shown.

The quality of the FBG used to shape the initial pulses into parabolic pulses is also discussed, highlighting that the discrepancy between the designed and measured grating reflectivity gives rise to parabolic pulses with some pedestal. However this will become an issue when the nonlinear propagation of such pulses is investigated (see next Chapter),

while it is not causing any problem for the retiming scheme proposed in this Chapter. Considering ∼10 ps parabolic pulses as the control signal, a wavelength shift of up to ∼0.5 nm is numerically predicted and experimentally verified, while a retiming window of ±5 ps is demonstrated. Furthermore, the cancellation of up to 4 ps rms timing jitter is demonstrated in a system experiment.

The average power of the control pulses was ∼21 dBm, requiring ∼500 m of SMF to retime the data signal. Due to the length of the dispersive medium considered, the final pulse width was broader than the initial one. However, this is not a limiting issue and different approaches can be carried out to solve it. For example, by carefully choosing the peak power of the control pulse, so that the chirp value (C) is one, it is possible to have a final pulse width that equals the initial one. In the particular experiment discussed here, this would have required a control average power of ∼26 dBm.

The sharp tails of the shaped pulses facilitate scalability of the scheme to far higher repetition rates. For the case examined in this Chapter, data signals up to 80 Gb/s could be considered directly. However, because of the fs response of the nonlinear effects in optical fibre, even higher repetition rates can be envisaged, if shorter parabolic pulses are implemented as the control signal. Obviously, higher bit rate would require higher average power level of the control signal.

Finally, this technique is directly applicable to the simultaneous retiming of several synchronized WDM channels.

Chapter 7

Nonlinear propagation of parabolic pulses shaped in an SSFBG

7.1 Introduction

Recent progress in high quality supercontinuum generation (SCG) techniques in optical fibres has enabled a wide range of applications including optical coherence tomography [100], frequency metrology [101] and dense wavelength multiplexed optical communication systems based on spectral slicing [102]. For some of these applications, optimising the spectral density for a given pump power whilst maintaining a flat spectral profile is critical, whereas for others maintaining a high degree of coherence across the pulse is a primary concern.

Broad spectra can be generated in both dispersion regimes by launching short pulses in HNLFs. Anomalous dispersion fibres can provide the highest broadening factors [103] resulting from the complex interplay between various non-linear effects e.g. SPM, four wave mixing and soliton self-frequency shift. In normally dispersive fibres, the combination of dispersion and self-phase modulation has the advantage of allowing the generation of flatter spectra [102]. However, the main limits to spectral pulse quality in this regime is the spectral ripple that arises from SPM of the sech-shaped pulses, typically generated by most short pulse lasers, and the effects of wave-breaking which may lead to a significant change in the temporal pulse shape and to a severe transfer of energy into the wings of the spectrum. Such effects can in principle be avoided by using a parabolic temporal intensity profile [104]. SPM induces a perfectly linear chirp to such a pulse shape, so that parabolic pulses remain parabolic during their propagation in HNLFs, resulting in spectrally flat, highly-coherent pulses. However, it remains a key issue as to how to reliably generate parabolic pulses in the first instance. As discussed in the previous

Chapter, various techniques to generate such parabolic pulses have been demonstrated, especially in the field of optical amplifiers, see for example [96–98]. However, it has been shown in this thesis, see Sec 6.3, that parabolic pulses can be passively generated using superstructured fibre Bragg grating with typical lengths of few centimetres. The SSFBG applies precise spectral filtering to the amplitude and phase of short laser pulses, so that upon reflection the spectrum of the signal acquires the features that correspond to the required pulse form.
In this Chapter, the results of numerical and experimental studies of SPM-induced spectral broadening of these shaped parabolic pulses are reported in a normally-dispersive, silica-based HNLF. Results in terms of the extent of spectral broadening, the proportion of energy stored within the 3dB bandwidth, and the reduction of spectral ripple relative to the case of conventional sech shaped pulses, are presented for both cases. It is found that the initial pulse form, as well as any residual pedestal associated with the pulse, play important roles for the subsequent evolution of the pulse in the HNLF.
Further, the demonstration of the benefits that this simple parabolic pulse reshaping technique can provide for spectral slicing source applications at telecommunications wavelengths, and how the smooth chirp profile of the output pulse spectrum can be exploited for pulse compression, are demonstrated.

This Chapter opens with the description of the experimental set-up used to study the SPM-induced spectral broadening of different kinds of pulse shapes and pulse widths. A complete characterization of the results achieved are presented, which are supported both by numerical and experimental data and, finally, two different applications are reported to exploit the flat spectrum and the optimised spectral density.

7.2 Experimental Set-up

I studied the SPM-induced spectral broadening performance of different pulse-shapes and pulse-widths using the experimental set-up shown in Fig. 7.1. The transmitter was based on the EFRL used in the previous experiments. However, this time the optical signal was gated down by the modulator to produce a 5 GHz train of ∼2 ps pulses at a wavelength of 1542 nm. In this way, a higher peak signal power level could be reached, thus allowing a broader spectrum at the end of the system. These pulses were then used as the input to the 10 ps parabolic pulse shaper formed by a SSFBG. The grating implemented for this demonstration is the same as used in the previous Chapter. The corresponding profiles of the shaped pulses in the time and frequency domain, as characterized by the SHG-FROG, are shown in Fig. 6.8.c and Fig. 6.8.d. The performance of these pulses was compared with that of nearly transform-limited sech pulses with a FWHM of either ∼2 ps, obtained directly from the laser source, or 10 ps, obtained after filtering the 2 ps pulses with a narrow band filter (Fig. 7.1). Fig. 7.2.a and Fig. 7.2.b show the profiles of the 2 ps (red traces) and 10 ps (green traces) pulses,

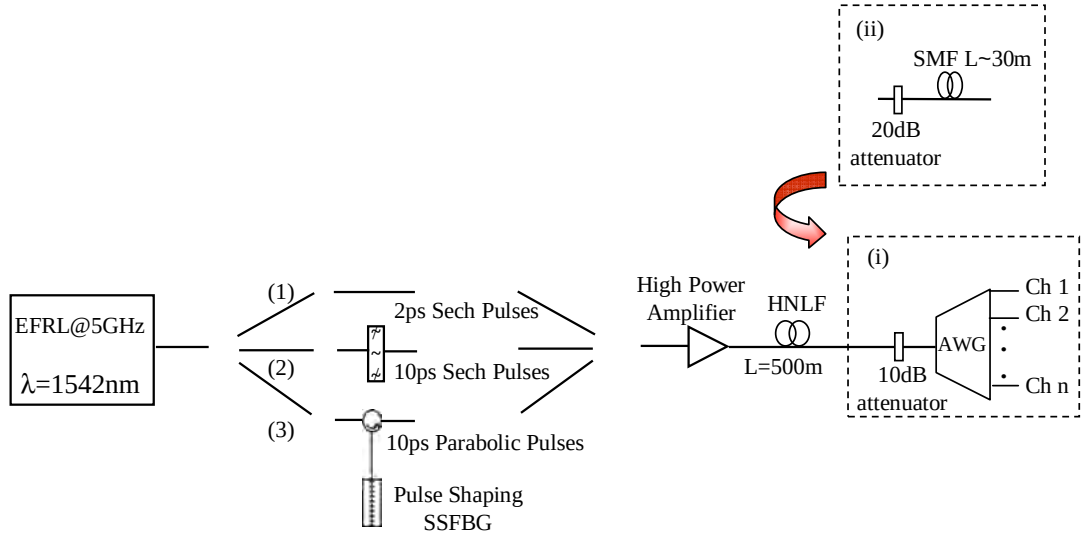

FIGURE 7.1: Experimental Set-up.

Dispersion @1550nm ($ps\ nm^{-1}km^{-1}$)	Dispersion Slope ($ps\ nm^{-2}km^{-1}$)	Length (km)	Loss ($dB\ km^{-1}$)	Effective Nonlinearity ($W^{-1}km^{-1}$)
-0.87	-0.0006	0.5	1	19

TABLE 7.1: Fibres' parameters

in the wavelength and time domain, obtained by an OSA and a commercial SHG-FROG system respectively. Each of these pulse forms were then amplified and fed into 500 m of HNLF, whose parameters are reported in Tab. 7.1. The pulses were then passed through either an arrayed waveguide grating or ∼30 m of SMF depending on the end-application needs.

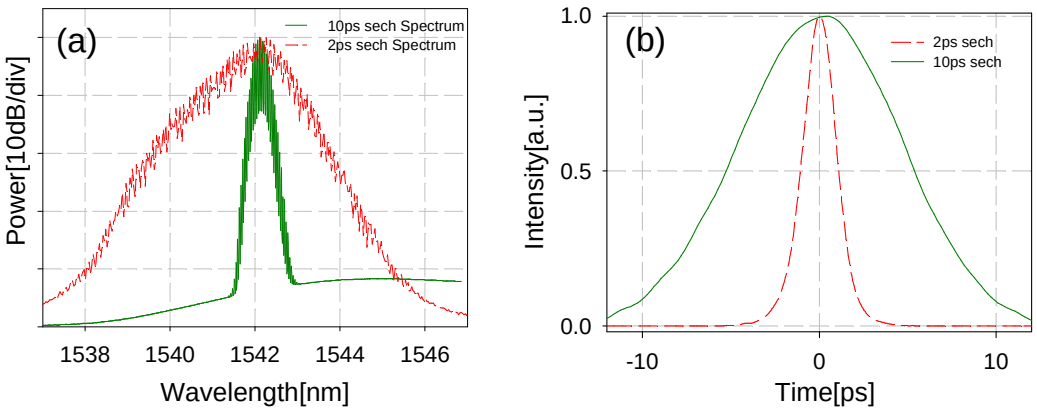

FIGURE 7.2: Spectral (a) and temporal (b) intensity profiles of the 2 ps and 10 ps sech pulses using SHG-FROG.

7.3 SPM broadening results and discussion

Prior to performing any experiments, the propagation of the different waveforms in the HNLF were simulated using the standard split-step Fourier method (see Section 2.5.1 for further detail on the method) in order to examine the dependence of the spectral broadening on the initial pulse properties (shape and energy). In particular, 2 ps and 10 ps idealized sech pulses as well as 10 ps ideal apodized parabolic pulse were considered, as initial pulses. The different cases are compared for the same initial pulse energy, in terms of the 3 dB spectral bandwidth at the HNLF output, and the ratio between the energy within the 3 dB bandwidth and the total energy of the pulses. This last parameter allows the optical wave breaking phenomenon, characterized by the appearance of side lobes at the edges of the pulse spectrum, to be quantified. It is desirable to avoid this phenomenon in order to restrict the energy spreading towards the wings of the spectrum. The results, obtained for the three different pulse forms, are summarized in Fig. 7.3.a and Fig. 7.3.b. The initial 2 ps sech pulses (red traces) undergo the greatest spectral broadening (∼33 nm for the highest energy level of 100 pJ). However, as soon as the energy levels increase, wave-breaking effects become severe, resulting in only half of the energy remaining in the central part of the spectrum. The 10 ps sech pulses (green traces) do not exhibit such an energy transfer to the spectral wings; more than 90% of the energy remains within the 3 dB bandwidth. Their spectra broaden almost linearly with increasing pulse energy, reaching ∼17 nm for the highest pulse energy considered (100 pJ). By contrast the 10 ps parabolic pulses (blue traces) broaden up to ∼29 nm for 100 pJ pulse energy (similar to the 2 ps sech case). However, in this case most of the energy (∼90%) is confined within the central 3 dB bandwidth of the spectrum, as in the case of 10 ps sech pulses.

In order to confirm the numerical analysis, spectral broadening experiments were performed. The results (diamonds and open circles) are plotted together with the simulated ones (Fig. 7.3.a and Fig. 7.3.b), exhibiting a good agreement between them. They also confirmed that the parabolic pulse shape shows the best performance in terms of spectral broadening and proportion of energy within the central part of the spectrum. Fig. 7.4.a shows the experimental spectra for the three cases, when the pulses were launched into the fibre with the maximum energy level of ∼100 pJ. The spectra are normalized to their total energy. This normalization was chosen to qualitatively demonstrate the energy spreading across the spectrum. Note that the slight peaks at the central wavelengths in the power spectra of the output signals are caused by the finite extinction ratio of the data modulator used to gate down the pulse repetition rate, resulting in the existence of ghost pulses in the zero-slots (see Appendix for further details). While the spectral shapes of both cases of sech pulses show high relative ripple, the spectral shape of the parabolic pulses is smoother and flatter.
Despite the fairly good performance achieved, a slight asymmetry and also fast ripples on the top of the measured spectrum can be observed, especially at shorter wavelengths

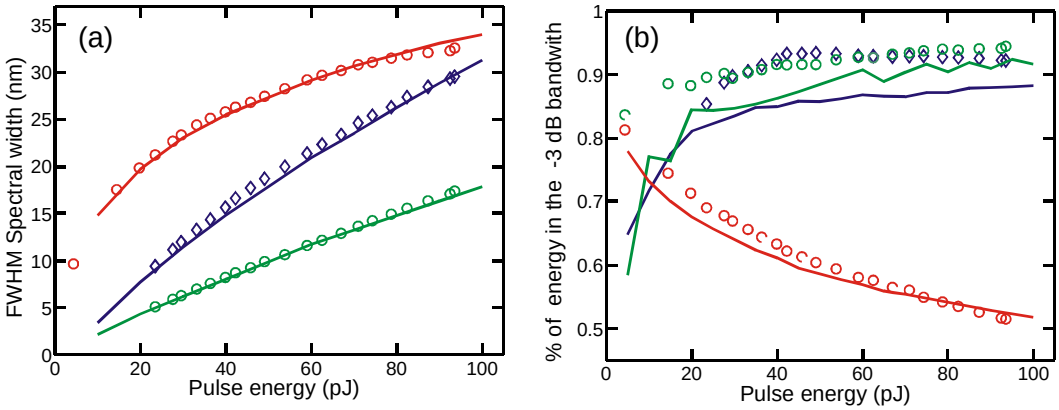

FIGURE 7.3: a) Numerical and experimental FWHM spectral width versus energy level for parabolic pulses (blue line and diamonds), 10 ps sech (green line and circles), and 2 ps sech (red line and circles). b) Numerical and experimental energy percentage stored in the central part of the spectra (3 dB bandwidth), versus energy level. The same conventions hold for all these figures.

for the parabolic case. Indeed, Fig. 7.4.b shows a comparison between this measured spectrum and the simulated one, when an ideally designed parabolic shape is considered, plotted on a logarithmic scale. It is clear that a smoother spectrum should have been achieved and the falling leading and trailing edges, typical of the parabolic form when plotted on a logarithmic scale, are limited by the wavebreaking phenomenon, which still occurs. The discrepancy from the ideal case is mainly due to the initial parabolic pulse form that presents a slight asymmetry and relative pedestal (see Fig. 6.8.d) compared to the designed case. Indeed, in the previous Chapter, a comment on some differences between the designed and measured grating reflectivity have already been reported (see Section 6.3). The main consequence is that the corresponding shaped pulse is still fairly parabolic, but with some pedestal. This pedestal did not cause any particular problem in the retiming system, where the pulse to be retimed sits mainly about the centre of

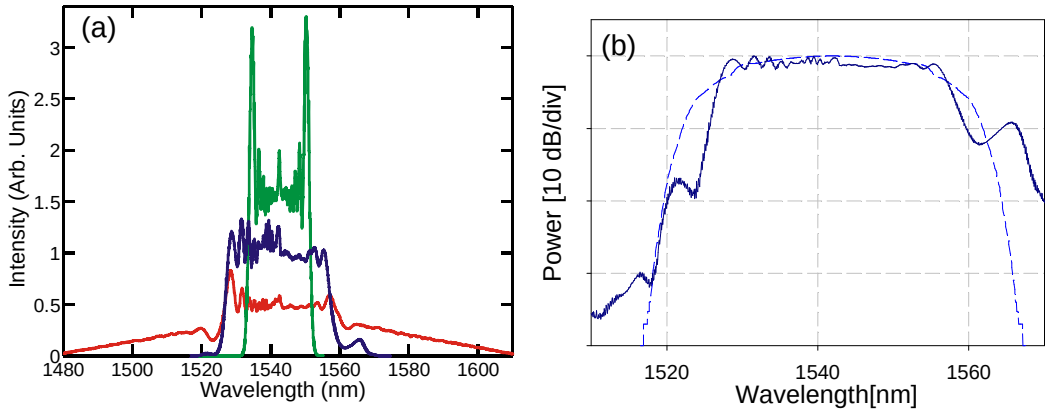

FIGURE 7.4: a) Experimental spectral traces after the HNLF for 10 ps parabolic (blue trace), 10 ps- (green trace) and 2 ps- (red trace) sech pulses. Spectral traces are normalized with respect to their total energy (linear scale). b) Experimental (solid line) and simulated (dashed line) spectra of the parabolic pulses.

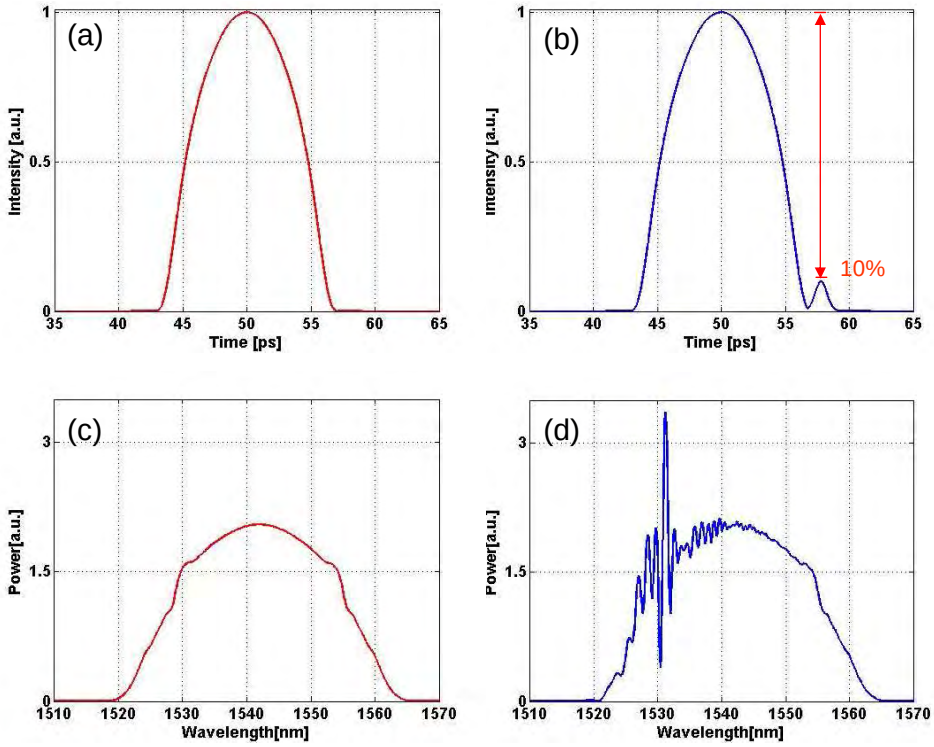

FIGURE 7.5: Ideal designed parabolic pulses considered in the simulations with (b) and without (a) a 10% pedestal. Corresponding numerical spectra at the output of the HNLF with (d) and without (c) a 10% pedestal.

the shaped pulse. On the contrary, in this experiment, this pedestal induces, a nonlinear chirp at the edges of the pulse, causing a fast ringing structure on the spectral profile. This is demonstrated in Fig 7.5.b, where the simulated spectra at the output of the HNLF are shown for an ideal apodized parabolic pulse with (blue solid trace) and without (red dotted trace) a 10% pedestal (Fig 7.5.a).

It is obvious that this pedestal on the temporal pulse shape and consequently these relatively high and fast ripples on the spectrum are not desired and could compromise the quality of the processed signal, for example, in terms of unequal WDM channel amplitudes after slicing of the SC spectrum or in terms of precise linear chirp across the whole signal, if compression of the pulse needs to be carried out.

The SSFBG used to shape the initial pulse was further analysed to identify the origins of the problem and try to solve them. The transmission of the grating was measured and is reported in Fig. 7.6. As can be seen, it appears that the grating is very strong (transmission loss of ∼5 dB), while the model implemented to design this kind of gratings is valid in the weak grating limit (loss in transmission of at most 1 dB). If this weak limit is not observed, the signal does not penetrate completely through all the grating structure and so it will not be properly shaped by it.

In general, one way of controlling the strength of a grating, after fabrication, is to anneal it. So the grating was partially erased using a heating process to reduce the transmissivity down to 1 dB and the quality of the new shaped pulses was assessed

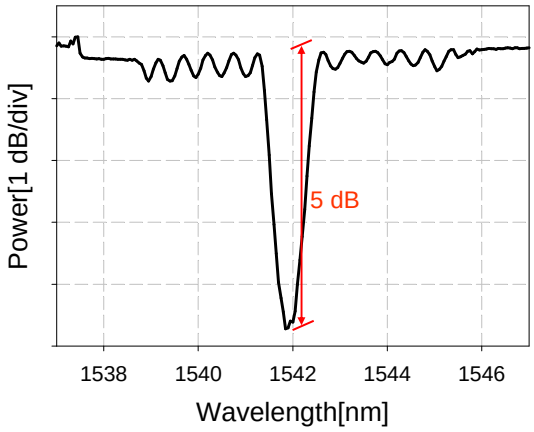

FIGURE 7.6: Grating transmissivity before annealing.

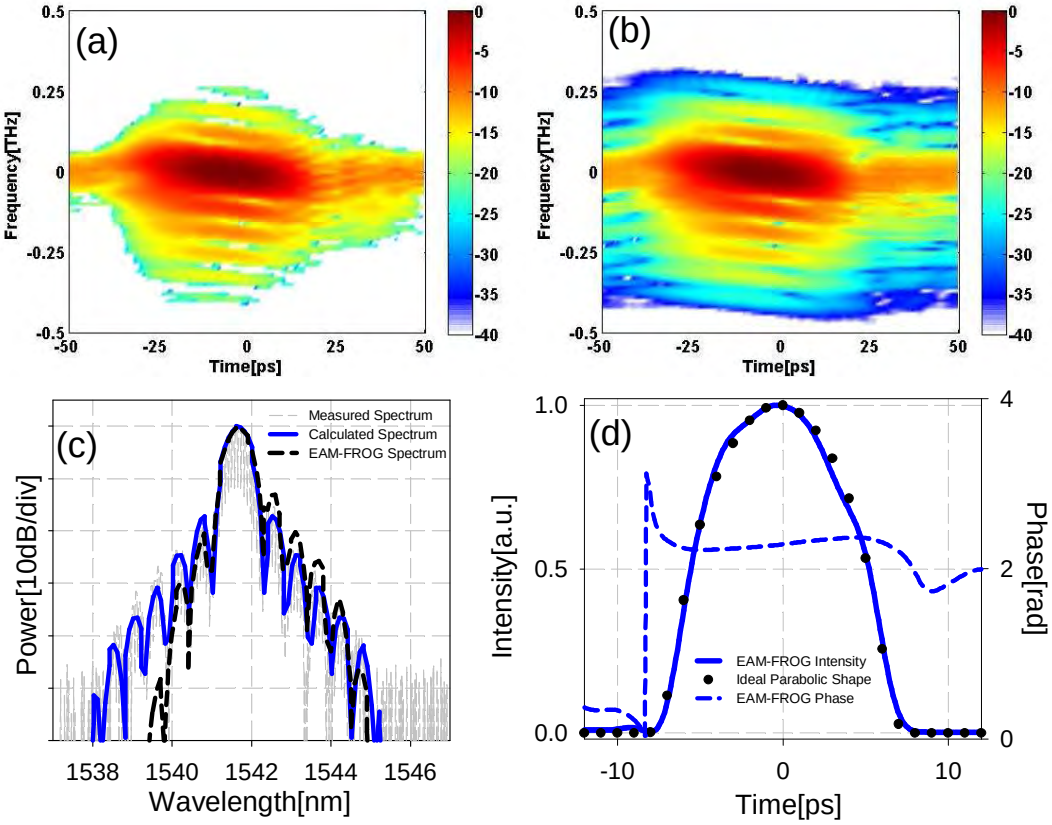

FIGURE 7.7: a) Experimental (gray dashed line), calculated (solid blue line) and EAM-FROG retrieved (black dashed line) spectra of the parabolic pulses. b) Intensity and phase of the parabolic pulses measured using EAM-FROG; the measured intensity profile is fitted to an ideal parabolic pulse (circles).

again using spectral measurements and the EAM-FROG technique (Fig. 7.7). Fig. 7.7.a and Fig. 7.7.b show the measured and retrieved spectrograms of the parabolic pulse in a logarithmic scale. Fig. 7.7.c compares the measured optical spectrum (gray dashed trace) of the pulses reflected off the SSFBG with the designed spectrum of a single parabolic pulse (blue solid trace) and the retrieved spectrum from the EAM-FROG measurement.

As can be seen, the profile of the shaped spectrum is in very good agreement with the required spectral form. Good agreement between the retrieved spectrum (dashed black trace) and the direct spectral measurement is also achieved in this case. However, as can be seen from Fig. 7.7.c, the agreement is slightly worse at shorter wavelengths due to the wavelength dependent insertion loss of this particular sampling EAM. The rms error between the two plots is ∼0.24%. Fig. 7.7.d shows the temporal profile of the measured shaped pulses (solid blue trace), which is fitted with an ideal apodized parabolic pulse (circles), illustrating excellent agreement between the two. No pedestal is visible on the temporal pulse shape, implying that better results in terms of SPM-spectral broadening are expected. Fig. 7.7.d also shows that the phase is nearly constant across the full width of the pulse.

The same studies regarding spectral broadening as those presented in Fig. 7.3 and Fig. 7.4 were then repeated for this new parabolic pulse shape and the results (see red rectangular points) are presented in Fig. 7.8.a and Fig 7.8.b, where they are compared to the results obtained before annealing the SSFBG (white diamond points) and to the numerical simulations (solid trace). As can be noted, the annealing has only slightly affected the amount of spectral broadening of the parabolic pulse shape as well as the percentage of the energy stored in the 3 dB bandwidth, while it has drastically changed the actual shape of the spectrum (Fig. 7.9).

The deviation between the experimental and theoretical results in Fig 7.8.b is only ∼10 % and it is mainly linked to the small discrepancy between the parabolic pulse shape experimentally generated using the particular SSFBG used in the experiment and the ideal apodized one (see Fig. 7.7.d). It is quite well known that the wings of the optical spectrum are quite sensitive to any deviation from a perfectly parabolic pulse, so

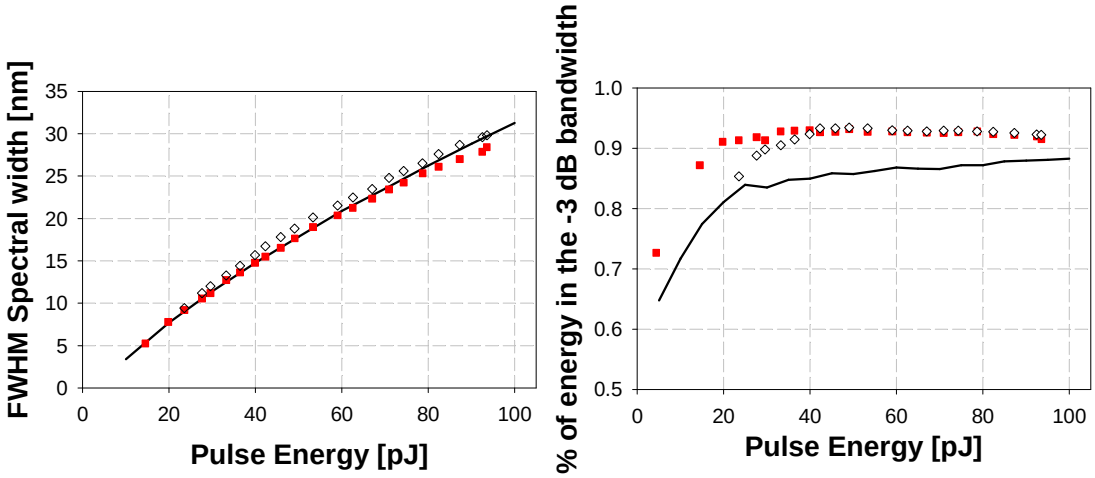

FIGURE 7.8: a) Numerical (solid black trace) and experimental FWHM spectral width before (white diamond) and after (red rectangular) annealing versus energy level for parabolic pulses. b) Numerical and experimental energy percentage stored in the central part of the spectra (3 dB bandwidth), versus energy level for the same pulse shape. The same conventions hold for all these figures.

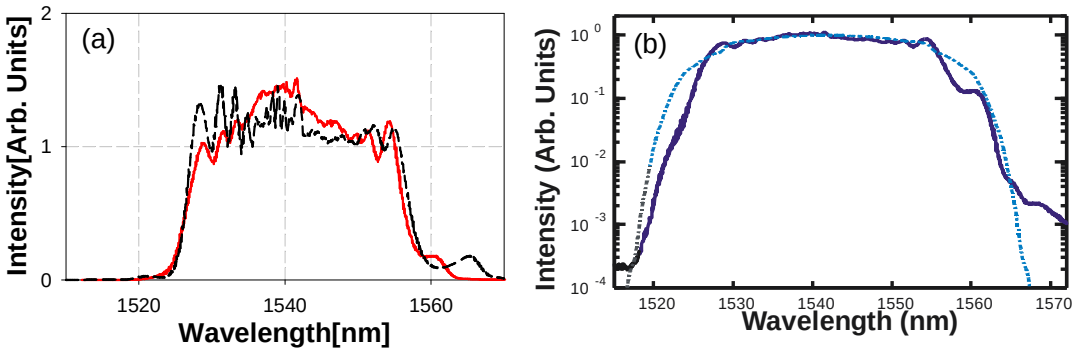

FIGURE 7.9: a) Experimental spectral traces after the HNLF for 10 ps parabolic before (black trace) and after (red trace) the annealing process. Spectral traces are normalized with respect to their total energy (linear scale). b) Experimental (solid line) and simulated (dashed line) spectra of the parabolic pulses after annealing.

it is to be expected that there might be some variations between the experimental and theoretical spectra in the calculation of the portion of energy within the 3 dB bandwidth (see for example [105]).

Fig. 7.9.a shows the experimental spectra before (black dashed curve) and after (red curve) annealing, after the HNLF, for a pulse energy level of ∼100 pJ. The spectral traces are normalized with respect to total energy and plotted on a linear scale. Note that the annealing has significantly reduced the ripples on the broadened spectrum, obtaining a flatter and more uniform spectrum, which will provide optimal conditions for further applications of the signal, implying that the annealing of the grating has truly helped to obtain a better initial pulse shape.

This is also emphasized in Fig. 7.9.b, where it is shown the improved agreement between the spectrum of the measured and ideal parabolic, plotted on a logarithmic scale. The flat top spectrum and some more rapidly falling edges, which are characteristics of the parabolic pulse form with a linear chirp, are now visible on the experimental trace as well and can offer significant benefits in terms of maximising the total throughput in spectral slicing applications, as will be shown below.

7.4 Applications

As discussed above, the flat spectrum and optimised spectral density are attractive for spectrally sliced source applications since the shape of the generated flat spectrum can be tailored to match the full bandwidth of the AWG filter minimising the overall loss and thereby maximising the spectral density per channel. To show this, the broadband spectrum was filtered out using an AWG available in the lab. The AWG consists of 38 channels with a channel spacing of ∼0.8 nm from 1528 nm to 1565.7 nm. Note that an attenuator before the AWG was employed to reduce the nonlinear effects in the AWG and in the patchcords used to go to the diagnostics (Fig. 7.1). However, an attenuator of only 10 dB was chosen so that no further amplifiers need to be added for subsequent

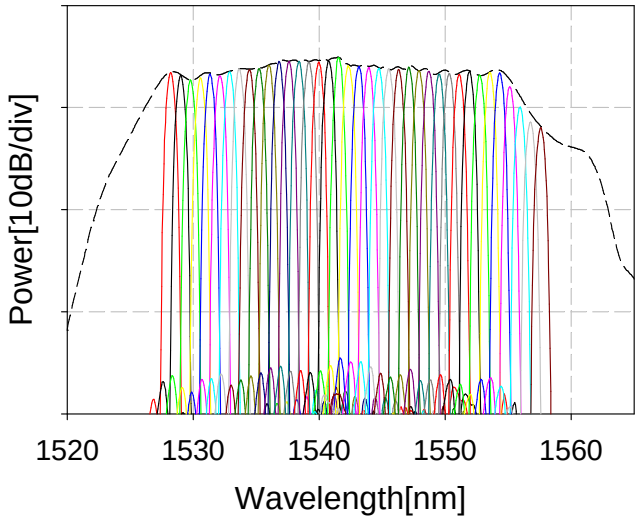

FIGURE 7.10: Superposition of the measured sliced spectra together with the complete spectrum of the parabolic pulse plotted on the logarithmic scale (Res=0.5 nm).

pulse characterization. Fig. 7.10 shows a superposition of the spectra of 38 channels after the AWG. The channels are generated in the 1528-1558 nm-wavelength range. Unfortunately, shorter wavelengths on the spectrum could not be considered due to the operating bandwidth of the particular AWG used. The SNR for each channel was better than 30 dB. The pulse width of each individual channel together with the time bandwidth were also characterized as a function of wavelength, demonstrating the homogeneous pulse quality across the full operating bandwidth (Fig. 7.11). The pulse duration and time bandwidth product are almost constant at ∼7.2 ps and 0.58 respectively, across all channels, as determined mainly by the AWG filter characteristics. Examples of three pulse shapes and chirp profiles associated with the filtered channels, (channel 6, 19 and 29 respectively), measured using SHG-FROG, are shown in Fig. 7.12.a-c. As can be

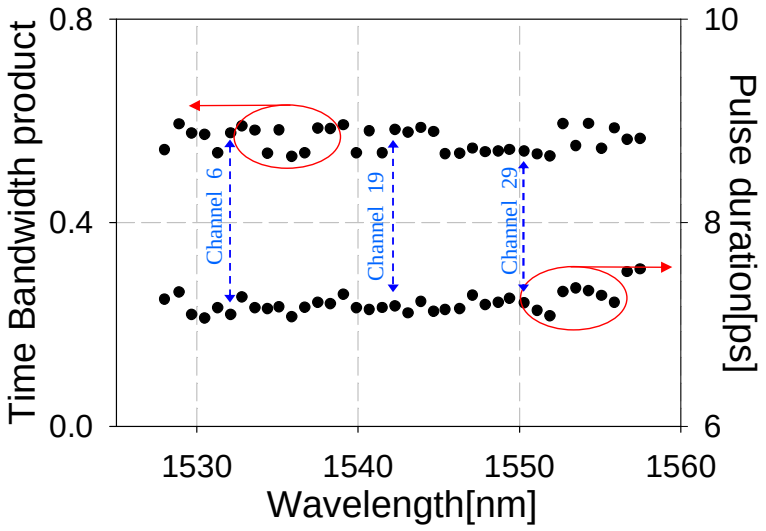

FIGURE 7.11: Measured pulsewidths and time-bandwidth product values for the filtered channels.

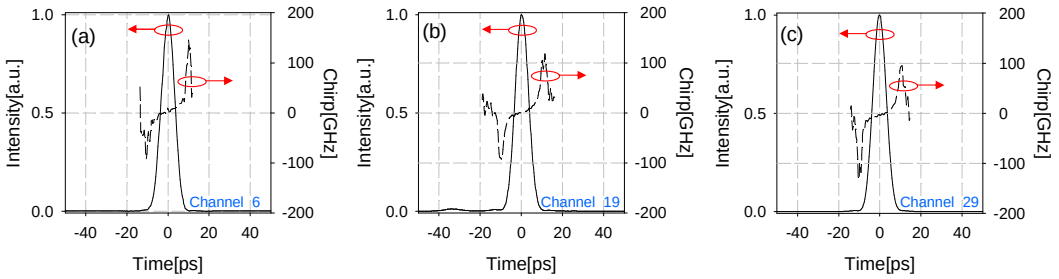

FIGURE 7.12: Examples of three FROG retrieved pulse shapes and chirps of the filtered output channels (Channel 6 (a), 19 (b) and 29 (c)).

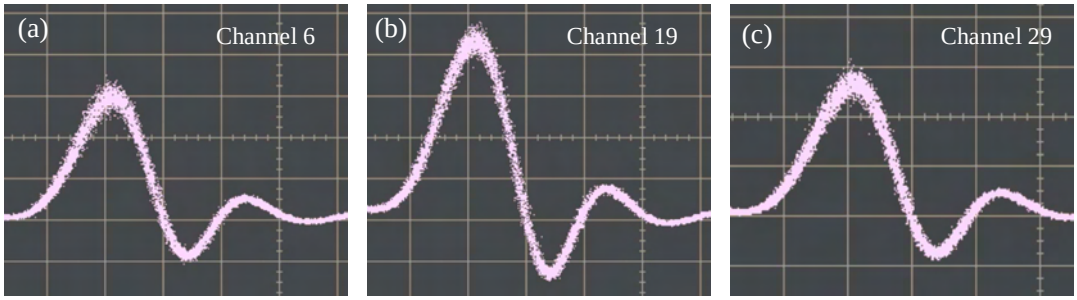

FIGURE 7.13: Oscilloscope traces of three sampled channels (Channel 6 (a), 19 (b) and 29 (c)) taken at the same scale. Time Scale: 10 ps/div. Scope bandwidth: 20 GHz.

seen, Channel 19, which is the closest to the central wavelength of the initial signal, has a slight pedestal. This is probably caused by the nonlinear effects of the highly chirped pulses, which still have relatively high peak powers at the input of the AWG. This pedestal could be avoided by using a higher attenuation before the AWG, with the consequence that an amplifier would have to be introduced before some of the diagnostic devices. For the other channels, this pedestal is not present, because the AWG acts as an off-set filter after the SPM- broadening, so it rejects the noise for low energy levels [44]. Oscilloscope traces of three randomly chosen channels are shown in Fig. 7.13.a-c and confirm the good noise performance of the system. Note that the three traces are shown on the same scale.

Pulses of such a broad spectral bandwidth are potentially useful for other applications such as linear pulse compression, provided of course that coherence is preserved across the pulse. To test this, the spectrally broadened parabolic pulses were launched into ∼30 m of SMF (Fig. 7.1). This particular length was chosen to minimize the duration of the compressed pulses. An attenuator of 20 dB was placed before the SMF to allow the power levels to be set so as to avoid nonlinear effects in the compression fibre, as already discussed. The broad spectrum of the compressed pulse (∼29 nm) meant that it was not possible to use either of the FROG techniques available in the lab, to assess the signal directly in the time domain. Indeed, Fig. 7.14.a shows the pulse characterization attempts using the SHG-FROG straight after the HNLF for the maximum power level of ∼27 dBm at 5 GHz. As can be seen, the retrieved spectrum (blue trace) is narrower

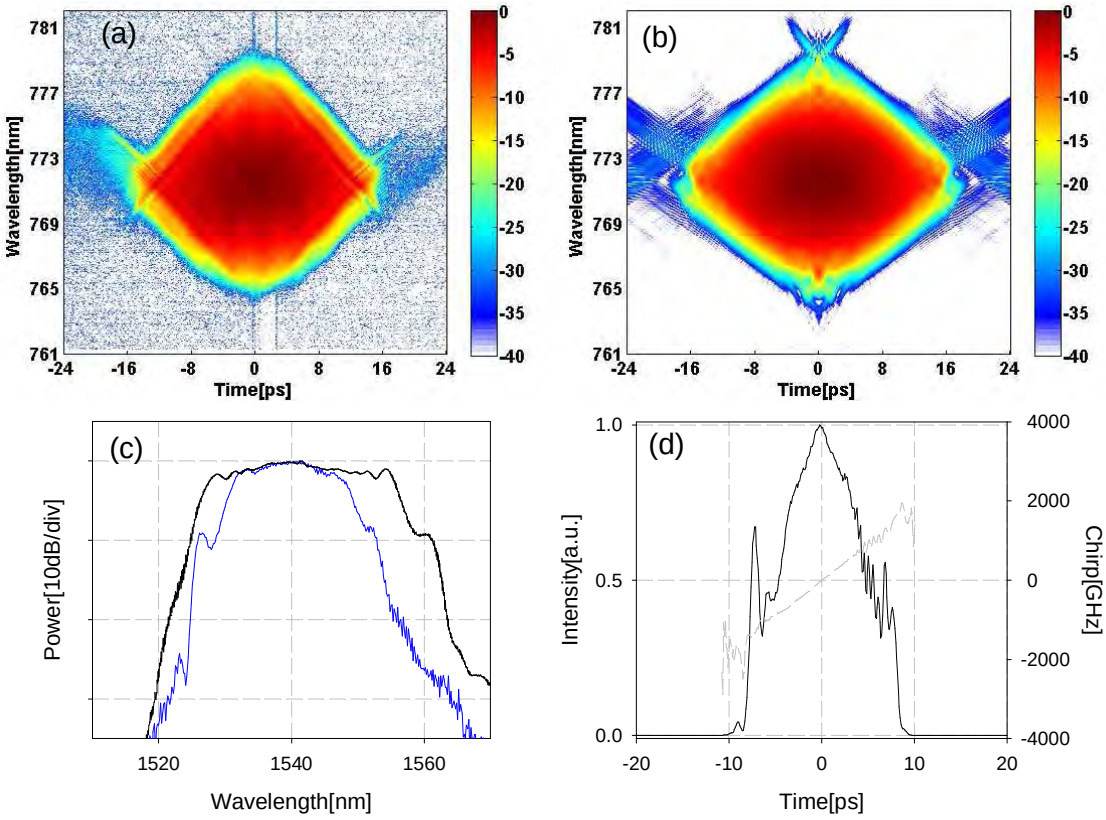

FIGURE 7.14: Attempt to characterize the spectrally broadened parabolic pulses before compression using SHG-FROG technique. Measured (a) and retrieved (b) spectrogram. (c) Measured with an optical spectrum analyser (black trace) and SHG-FROG retrieved (blue trace) spectra of the broadened parabolic pulses. (d) Corresponding retrieved intensity (black trace) and chirp (gray trace).

than the spectrum measured with the OSA (gray trace). This is due to the fact that the information far away from the central wavelength of the signal is lost, due to the high losses of the particular SHG-FROG used. Even though the information retrieved from the spectrogram is bound to be incorrect, due to the missing spectral information, it is interesting to note that the retrieved temporal shape shows a fairly parabolic envelope with a highly linear chirp, as expected.

An EAM-FROG measurement was also attempted. The EAM-FROG characterization results are shown in Fig. 7.15. As a starting point for this characterization, a 10 GHz pulse train was considered rather than 5 GHz, for the maximum power level of ∼27 dBm. (In this way, the available characterization set-up at 10 GHz did not need to be changed). The spectrum measured at the output of the HNLF has a 3 dB bandwidth of ∼17 nm (black trace in Fig. 7.15.c). Already from the measured spectrogram (Fig. 7.15.a), it is possible to see that it is missing information towards the higher frequency side (shorter wavelengths). This is due to the steep increase in insertion loss for wavelengths below 1540 nm for the particular EAM used, as already discussed when characterizing the parabolic pulse (see Fig 7.7.c). The loss is so high that the signal completely disappears into the noise floor of the spectrogram measurement. For this reason, it is impossible

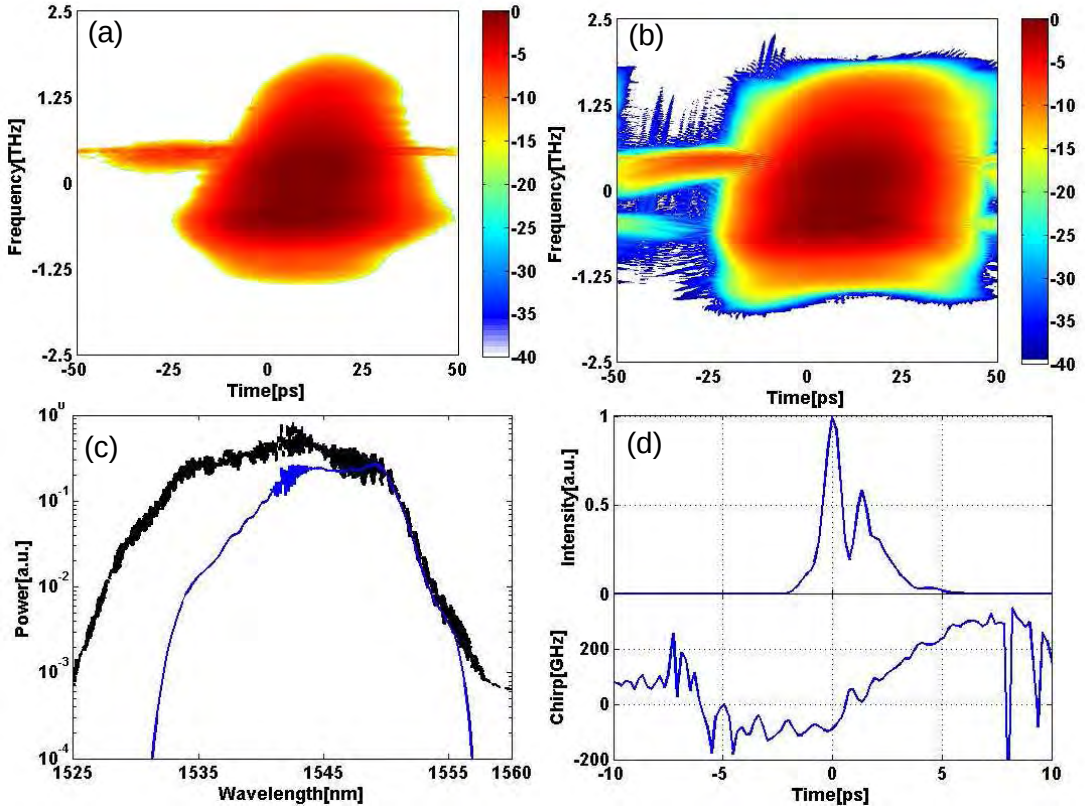

FIGURE 7.15: Attempt to characterize the spectrally broadened parabolic pulses before compression using EAM-FROG technique. Measured (a) and retrieved (b) spectrogram. (c) Measured with an optical spectrum analyser (black trace) and EAM-FROG retrieved (blue trace) spectra of the broadened parabolic pulses. (d) Corresponding retrieved intensity and chirp.

to try to correct mathematically for this loss before deconvolution, so the corresponding retrieved shapes in time and wavelength domains (Fig. 7.15.c and Fig. 7.15.d) are incorrect.

Because it was not possible to use the FROG techniques, only simple autocorrelation measurements were performed. Fig. 7.16.a shows the numerically compressed pulse intensity profile corresponding to the experimental set-up reported in Fig. 7.1. It exhibits a predicted FWHM of ∼190 fs. The formation of such a large pedestal (∼7 %) is due to the third order dispersion effect in the SMF. To confirm this observation, I simulated the propagation of the ideally apodized parabolic pulses after the HNLF through a pure dispersive medium (no third order dispersion contribution effects considered in the SMF). A pedestal as low as ∼2 % is now obtained (see Fig. 7.16.b) implying that the experimental results achieved could be further improved considering very low third order dispersive media. Note that the slight asymmetry on the compressed pulse in Fig. 7.16.b is due to the third order dispersion of the HNLF before the compression stage.

Fig. 7.17 shows the corresponding calculated autocorrelation trace (red trace) of Fig. 7.16.a, which has a predicted FWHM of ∼260 fs. In the same graph the measured autocorrelation trace (Average=8) was also plotted. If we assume the same conversion factor, from

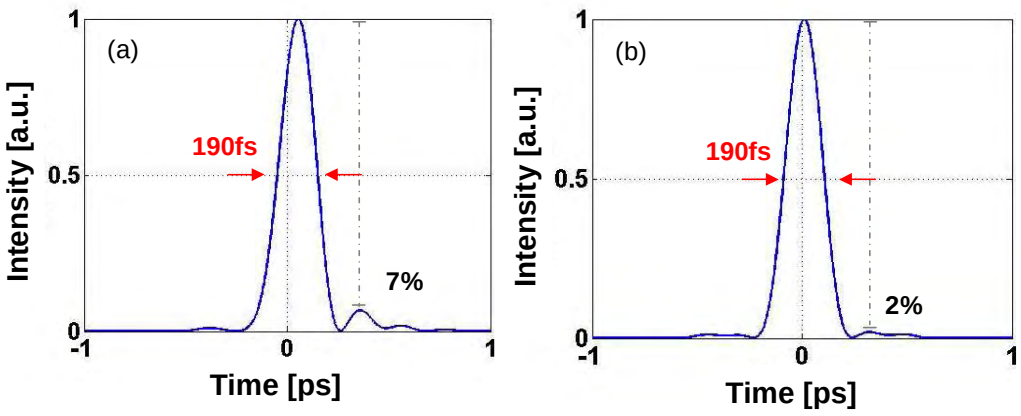

FIGURE 7.16: Numerical compressed pulse shape when the SMF is considered with (a) and without (b) a third order dispersion component. A 20 dB attenuator is considered before the dispersive medium.

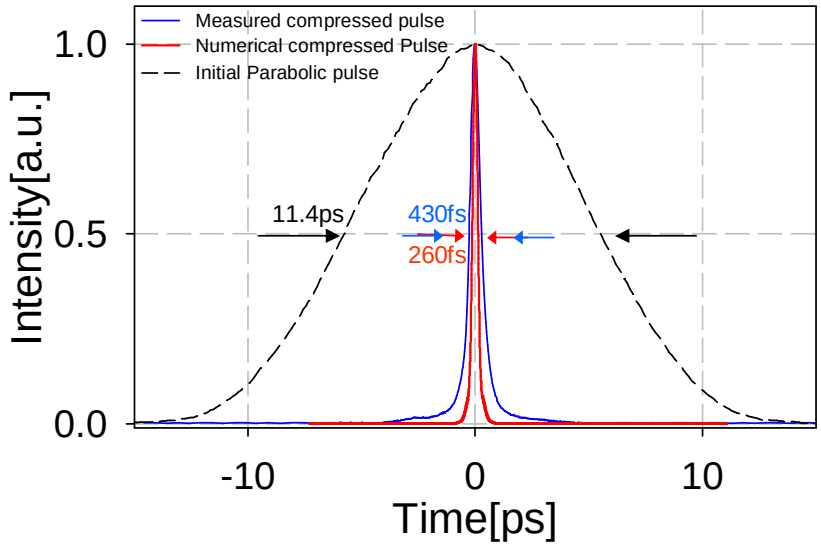

FIGURE 7.17: Measured autocorrelation traces of the initial parabolic pulse (black dash line) and the pulse after fibre compression (blue trace), along with the corresponding calculated autocorrelation profile (red trace).

autocorrelation to real pulse duration as derived from the simulations (1.365), the autocorrelation width corresponds to a de-convolved pulse width of 310 fs (i.e. ∼40% more than the theoretical minimum). This represents a compression factor of more than 30, relative to the initial 10 ps parabolic pulses, highlighting the quality of the linear chirp generated in the HNLF. The difference between the numerical and the experimental predictions can be attributed to deviations of the starting pulse from the ideal parabolic pulse shape. Finally, Fig. 7.18 shows the measured spectrum before (black trace) and after (red trace) the compression stage; the two shapes are very similar, implying that no nonlinear effects occured in the SMF.

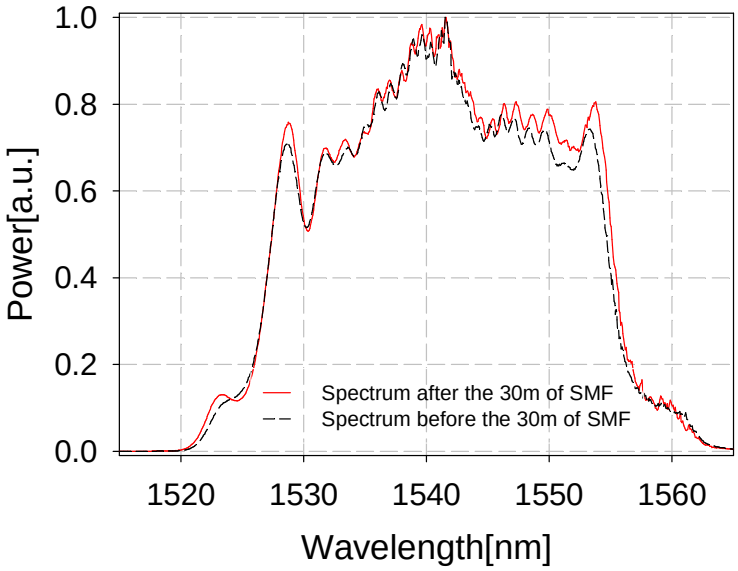

FIGURE 7.18: Measured spectrum before and after 30 m of SMF.

7.5 Conclusion

In conclusion, the application of SSFBG-based linear pulse shaping into parabolic pulses, for the generation of ultra-flat broadened spectra in a normal dispersion HNLF, is numerically and experimentally demonstrated. These parabolic pulses provide optimum performance in terms of spectral broadening, flatness and density as compared to sech pulses of various pulse widths. However, it is very important to start with a good parabolic shape with no pedestal to obtain optimum performance. For this reason, the parabolic pulse shaping SSFBG was annealed, and thereby its shaping performance was improved relatively to what was presented in the previous Chapter. Potential applications, including spectrally sliced pulse source generation and efficient pulse compression, are also discussed and demonstrated. In particular 38 spectrally sliced sources with a spacing of ∼0.8 nm from 1528 nm to 1565.7 nm, a pulse duration of ∼7.2 ps and a TBP of ∼0.58 are demonstrated. A linear pulse compression with a compression factor of more than 30 relative to the initial 10 ps parabolic pulses is demonstrated as well.

Chapter 8

2R Regeneration in Bismuth fibre

8.1 Introduction

As widely discussed in Chapter 5, in-line all-optical signal regenerators are likely to play an important role in future large-scale photonic networks, offering considerable increases in the transmission distances that can be achieved and additional flexibility in the network design. In their simplest form, signal regeneration devices cancel the effects of amplitude noise accumulation in transmitted signals (2R regeneration), and they typically employ a fast nonlinear element with a step-like power transfer characteristic [106]. Such elements can be implemented in optical fibres by making use of the ultrafast Kerr nonlinearity. Fibre-based nonlinear devices offer the advantages of being transparent to the bit rate (to rates that exceed several 100's of Gb/s), and of not degrading the signal-to-noise ratio or the extinction ratio of the signal [107]. However, because of the relatively low nonlinearity of silica, fibre based regenerator devices usually have to be quite long - typically of order >100 m in length. For example, Her et al. [108] have shown an optimization of a regenerator based on spectral filtering of self-phase modulation in fibre, where the length of the HNLF used was 2.5 km.
The implementation of more compact nonlinear devices represents a challenge, and is currently a hot topic in fibre technology research. Recently, promising new highly nonlinear glasses have been developed, such as Bi-Oxide [9], lead silicate [10] and chalcogenide glasses [11]. Fibres drawn from these compound glasses have been shown to exhibit effective nonlinearities per unit length which are some orders of magnitude higher than standard single mode fibres. This allows for a drastic reduction in the length requirements of fibre-based nonlinear devices [109], and enables the implementation of meter-long nonlinear switches with improved performance in terms of stability and input power requirements.

There have been several demonstrations of fibre-based 2R regenerators that make use of either SPM [44], XPM [110], FWM [111], or even SRS [112]. Amongst these, SPM-

based schemes have the advantage that no additional laser source is required, making the regenerator structure simpler [113]. In this Chapter, the performance of a 2-m long all-optical regenerator, based on a bismuth-oxide-based nonlinear fibre with an effective nonlinear coefficient γ of $\sim$1100 $W^{-1}km^{-1}$, is demonstrated at 10 Gb/s and 40 Gb/s. The 2R regeneration scheme used is based on spectral broadening of the signal due to SPM in the Bi-NLF followed by narrow-band offset filtering. The normal dispersion of the Bi-NLF at telecommunication wavelengths favored the generation of a smooth SPM spectrum [114], free from any noise arising from modulation instability, which would be observed in anomalously dispersive fibres [115].

This Chapter opens by explaining the basic principle of the technique and how the amplitude noise was induced in the system. The main characteristics of the highly nonlinear bismuth oxide fibre used are described and a comparison with different kinds of nonlinear fibre is presented. Finally, two slightly modified systems are described at 10 Gb/s and at 40 Gb/s. For each repetition rate, the experimental set-up and a complete characterization of the system, supported both by experimental data and numerical analysis, are presented.

8.2 Reshaping technique: basic principle

The detailed operation principle of the SPM-based 2R regenerator is explained in Section 2.4.1. However, in this Section, some key points of the technique are summarized. For the implementation of the SPM-based 2R regenerator, the amplified data signal propagates through the nonlinear fibre, and the spectrally broadened signal is then passed through a filter, which is centered at a wavelength slightly offset from the original signal [44]. At low powers (i.e. when the transmitted symbol is nominally a "zero"), the signal does not experience any spectral broadening during its propagation through the fibre, such that the signal is rejected by the filter (i.e. suppression of the "zero" bits). However, if the signal power is high enough (i.e. when the transmitted signal is nominally a "one"), then a portion of the SPM-broadened spectrum passes through the filter. Furthermore, since the spectral density of the broadened spectrum at the filter pass-band can be made to be relatively insensitive to the peak power of the input pulse, any amplitude fluctuations on the "one" bits are reduced in the process (i.e. equalization of the "one" bits).
Clearly, this behaviour depends strongly on the launched power, filter offset and fibre characteristics. The aim of this investigation is to achieve the optimum performance of the 2R regenerator; no attempt is made to minimize the input power-fibre length product. For this reason relatively high power levels and wavelength detunings will be considered. However, as will be discussed later, the power-fibre length product of this kind of fibre is more than one order of magnitude lower than conventional silica based fibres, highlighting the potential of these kinds of fibre for compact practical nonlinear

optical processing devices.

8.3 Characteristics of the highly nonlinear bismuth oxide fibre

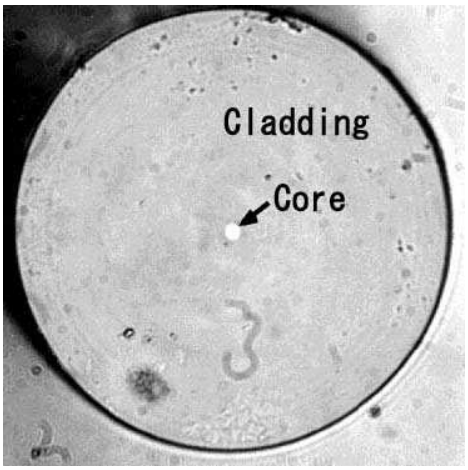

FIGURE 8.1: Example of a cross-sectional image of the highly nonlinear bismuth oxide fibre.

The fibre sample used for the demonstration of the 2R regeneration was fabricated by the Asahi Glass Company. A photograph of the cross-sectional image of the bismuth fibre is shown in Fig. 8.1.

Tab. 8.1 summarizes the characteristics of the fibre, as measured at 1550 nm.

In general, optical fibres with a high Kerr nonlinearity can be fabricated by using novel

Core diameter (μm)	Core refractive index	Cladding refractive index	Effective Mode Area [μm^2]
1.97	2.219	2.13	3.04

Dispersion ($ps\ nm^{-1}km^{-1}$)	Dispersion Slope ($ps\ nm^{-2}km^{-1}$)	Length (m)	Loss ($dB\ m^{-1}$)	Effective Nonlinearity ($W^{-1}km^{-1}$)
-278	0.947	2	0.9	1000 ± 100

TABLE 8.1: Characteristics of the fibre used in the 2R regeneration scheme. The results were provided by the Asahi Glass Company.

glass materials with high nonlinear refractive index, n_2, and/or tightly confining light within the core of the fibre, since the nonlinear coefficient, γ, is defined as follows [29]:

$$\gamma = \frac{2\pi n_2}{\lambda A_{eff}}, \tag{8.1}$$

where λ is the signal wavelength and A_{eff} represents the effective area, which is related to the core size and the numerical aperture of the optical fibre. The nonlinear refractive

index of the core glass in Bismuth oxide fibre is over 40 times greater than the nonlinear refractive index of silica, and the small $A_{eff} \sim 3\mu m^2$ of the Bi-NLF contributes to the achievement of the high γ. On the other hand, the small core causes some difficulties in splicing to conventional silica fibres, leading to large splicing losses. At the moment, the typical splicing loss value from SMF to this kind of fibre is 3 dB. However, in principle this value could be reduced further using tapered waveguide structure [116].
Fig. 8.2 shows the spliced fibre sample used in the experiment.

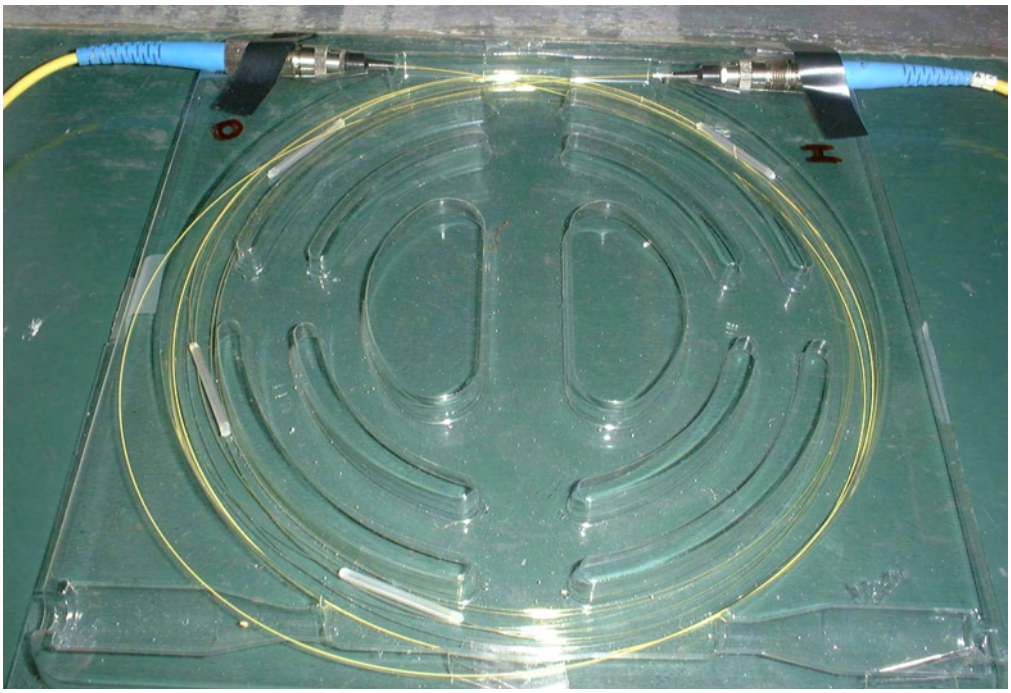

FIGURE 8.2: Photograph of the spliced highly nonlinear bismuth oxide fibre used.

Moreover, as far as the fibre itself is concerned, it is interesting to compare the performance of this kind of fibre with other types of nonlinear fibres. A commonly used figure of merit (FOM) for the nonlinear efficiency evaluation is the $\gamma \times L_{eff}$ product expressed in W^{-1}, where L_{eff} is the effective length, defined in Eq. 2.2 [117]. The $\gamma \times L_{eff}$ product provides the quantitative information of the nonlinear phase shift achievable in an optical fibre at an input peak pump power of 1 W. This FOM depends on both the effective nonlinear coefficient and the propagation loss (indeed L_{eff} depends on the actual length of the fibre as well as the attenuation loss α, see Eq. 2.2). For optimum performance, i. e. large phase shift and/or small input power, both L_{eff} and and γ should be as large as possible. The maximum effective fibre length is the reciprocal of the propagation loss, $L_{eff,max} = 1/\alpha$, and thus the term γ/α describes the FOM when using long fibre lengths. However, short fibre lengths are desirable to allow the realization of compact devices. In this way, this last FOM is not an appropriate value for such devices. A better parameter could be one where the real fibre length is fixed to a reasonable value for compact devices and to use the corresponding effective length. 1 m seems an appropriate fibre length for

fibre	Length (m)	$\gamma \times L_{eff}$ (W_{-1})	$\gamma \times L_{eff,1m}$ ($10^{-3}W^{-1}$)
Bi-NLF	2	1.8	993.5
HNLF	220	4.3	20

TABLE 8.2: FOMs for 2 m bismuth fibre and 220 m HNLF.

compact nonlinear devices, thus the term $\gamma \times L_{eff,1m}$ serves as a reasonable FOM [118]. Taking into account these FOMs, it is interesting to compare the values obtained for the 2 m of bismuth fibre with the ones obtained with the HNLF, previously used in this thesis (see Tab. 3.1). These results are reported in Tab. 8.2. While the low loss values of the HNLF still makes this technology beneficial, Bi-NLF yields better results when compactness is the primary requirement. Obviously, these FOMs alone do not give a complete characterization picture. Dispersion and other nonlinear effects (such as two photon absorption (TPA)) also need to be taken in account.
Finally, the normal dispersion of the bismuth-oxide based step-index fibre at the telecom wavelengths enables its use in 2R regeneration schemes based on SPM and offset filtering, free from modulation instability induced noise, as described in this Chapter.

8.4 Artificial introduction of amplitude noise

It is fair to say that the ultimate test of any signal regenerator is performed through transmission experiments. However, making such measurements is a major undertaking and in this Chapter, I have chosen to add intensity noise in an artificial manner in common with many other researchers reporting regenerator elements in the literature. Compared to the experimental set-up described in Chapter 5, a second modulator driven by a 15 MHz sinusoidal signal is included to add amplitude jitter. The amount of induced amplitude jitter can be varied both by varying the amplitude of the frequency modulation as well as by degrading the extinction ratio between marks and spaces of the data, facilitated by choosing a non-optimum bias voltage for the modulator. The main reason for this choice, rather than considering ASE noise added to the initial signal, is to have increased control over the amount of noise introduced in the system. It has also allowed us to have increased flexibility over the exact amount of noise added on the two levels, allowing us to assess the performance of the regenerator individually both in terms of elimination of ghost pulses and amplitude noise. There are indeed applications where it is more important to be able to compensate for one of the two levels. For example, in Chapter 5, the non-flat top of the rectangular pulse adds further amplitude noise to the "one" level, resulting in an uneven noise on the two levels.
Note that several previous papers have demonstrated the robustness of similar 2R-regenerator based on different HNLFs schemes against possible phase noise on the initial signal, see for example [108, 119]. In particular in [119], a similar 2R regenerator exper-

iment based on 1 m of Bi-NLF was implemented and demonstrated employing an ASE as a noise source to impact the signal degradation.

8.5 Experimental Set-up for the 10 Gb/s experiments

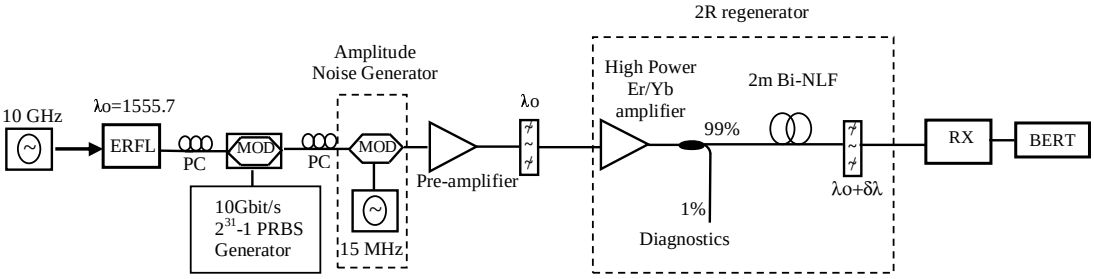

FIGURE 8.3: Experimental Set-up. MOD: modulator. RX: Receiver. BERT: Bit error rate tester.

The experimental set-up is shown in Fig. 8.3. The 10 GHz, actively mode-locked, EFRL was used as the data source to generate ∼2 ps sech pulses at the operation wavelength of 1555.7 nm. The pulses were modulated to provide a $2^{31} - 1$ PRBS and noise was artificially induced via the amplitude noise generator described in Section 8.4. The pulses were then intentionally broadened by a ∼ 0.7 nm bandpass filter to 5 ps and subsequently amplified by a high power Er/Yb amplifier before being launched into the 2-m-long Bi-NLF. Finally, a tunable 0.6 nm bandpass grating filter was used to filter the output of the regenerator. This filter bandwidth was the closest to that of the signal entering the 2R regenerator, available in the laboratory. Note that the power levels quoted herein correspond to the powers at the input of the Bi-NLF patchcord, and not to the input of the Bi-NLF itself (∼3 dB less due to the splicing losses).

8.6 Results and discussion for the 10 Gb/s experiments

In order to assess the performance of the nonlinear thresholder, the SPM-broadened spectra of the pulses for various input signal powers were experimentally studied, see Fig. 8.4.a. It can be seen that the combined effects of SPM and normal dispersion result in a smooth, almost flat-topped spectrum, which is desirable for 2R regeneration since it leads to a flatter power transfer function. It is worth noting, though, that the asymmetric broadening behavior between the longer and shorter wavelengths is indicative that the input pulses are not symmetric transform-limited input pulses since such pulses would give symmetric SPM-induced spectral broadening. To understand this behaviour the non-linear Schrödinger equation was numerically solved, by using the standard split-step Fourier method. Effects included in the simulation were attenuation, group-velocity dispersion, cubic dispersion and Kerr nonlinearity, see Section 2.5.1 for

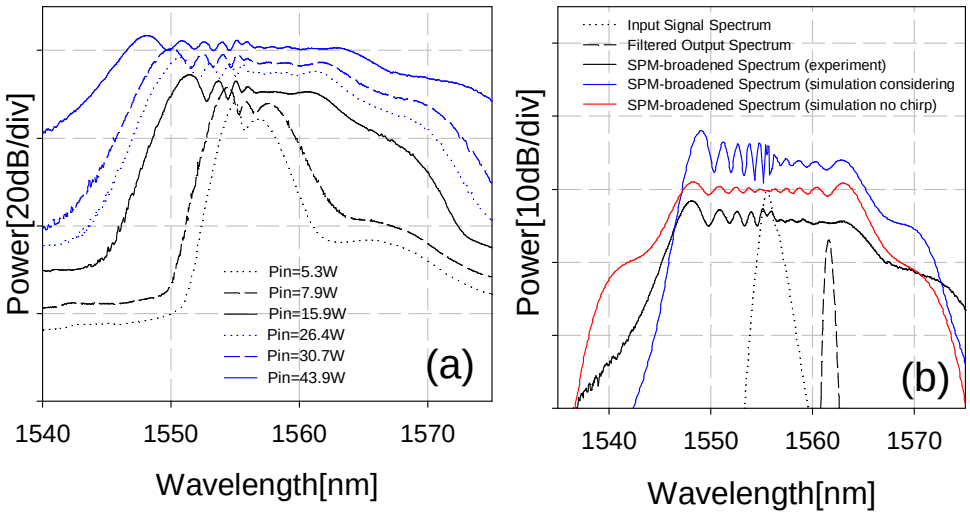

FIGURE 8.4: a) Experimental SPM-induced spectral broadening for various input peak power levels. Resolution: 0.5 nm. b) Optical spectra at the input of the Bi-NLF, after propagation in the fibre (experimental and simulated traces) and at the output of the 0.6 nm filter for an input power Pin∼31 dBm. In both Figures the spectra are vertically offset for ease of reading.

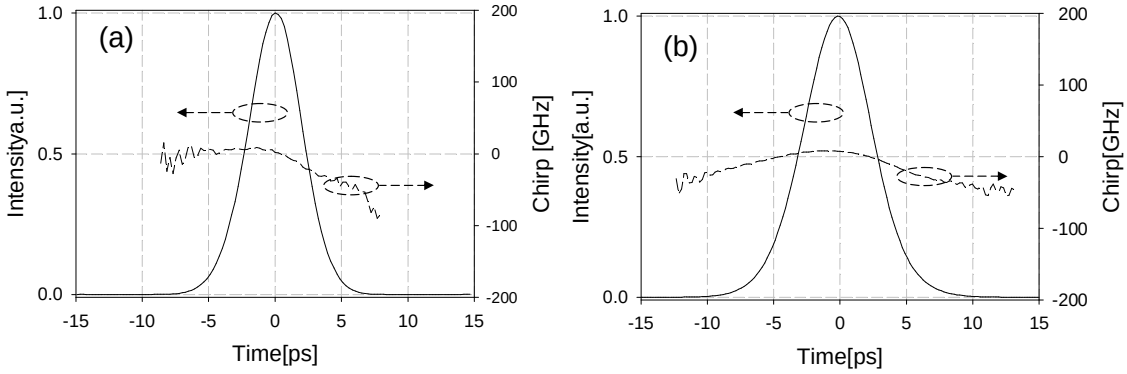

FIGURE 8.5: Intensity and chirp profile of the pulses at (a) the input and (b) output of the regenerator using SHG-FROG.

further details. Considering an ideal 2 ps sech pulse, a symmetric spectrum (red curve in Fig. 8.4.b) was predicted. Consequently, the pulses entering the regenerator system in the experiment were characterized using SHG-FROG. As can be seen in Fig. 8.5.a, the chirp of these pulses exhibits higher order components, which are induced by the filter used to broaden the pulse to ∼5 ps. To understand this observation, the corresponding intensity profile and group delay of the filter used were characterized and the results are shown in Fig. 8.6, where a small local peak in the phase response at the central wavelength of the filter is visible. The slope (chirp) of this central peak is opposite to the overall slope of the grating phase, implying that the filter induces a nonlinear chirp on the pulses. By including this filter characteristic contribution within the numerical Split Step Fourier technique based nonlinear pulse propagation calculations it was possible to accurately account for the observed experimental behaviour. To demonstrate

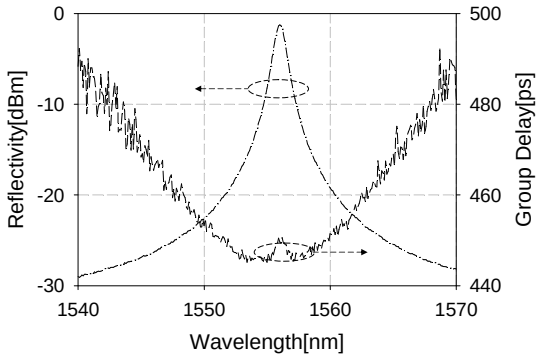

FIGURE 8.6: Reflectivity and group delay profiles of the filter used to broaden up the data signal.

this numerical SPM-induced spectral broadening (blue curve in Fig. 8.4.b) is plotted together with the experimental one (black curve) for similar input power.
In order to make use of this flat spectral region during the implementation of the 2R regenerator, the filter was tuned towards longer wavelengths relative to the original signal wavelength. To optimise the regeneration performance further numerical simulations were carried out, since the filter offset has been shown to be a key parameter for obtaining the best performance. Fig. 8.7.a shows numerical transfer characteristics at different offset filterings. As well known, the higher the offset, the flatter the transfer curve becomes at the "zero" level, although the power requirements to reach the curve peak increases and becomes more challenging experimentally. Fig. 8.7.a also shows that regeneration could be achieved in the instance that the filter was tuned towards shorter wavelengths relative to the original signal wavelength for the same amount of detuning, see grey dashed curve. Because of the asymmetry of the spectral broadening, the transfer functions observed either side of the central wavelength show different behaviour. In particular, for the same amount of peak power, the side of the spectrum towards shorter wavelengths broadens less and exhibits more pronounced ripple compared to longer wavelength operation. For these reasons, the corresponding curve is flatter for lower power levels, while the curve peak, reached at higher power levels, is sharper.
In the experiment, the maximum average input power level available was used ($\sim$31 dBm). Fig. 8.7.b shows a measurement of the transfer characteristic of the regenerator (circles) together with the numerical one (black curve) at a filter offset of 6.1 nm. The corresponding filtered spectrum is shown in Fig. 8.4.b (dashed curve). The relatively large offset wavelength, combined with the very flat SPM spectrum, ensures a clear two-level response between low and high powers. Despite the very good agreement, the reasons for the slight difference between the two curves could be linked to the high power amplifier used. Indeed, in the simulation the ASE noise induced by the amplifier and possible nonlinear effects with the amplifier were not accounted for. These effects are evident in the experimental spectral traces in Fig. 8.4 (for example see the visible ASE noise contribution at longer wavelengths for the lower power levels).
For completeness, the pulses at the output of the regenerator were also characterized

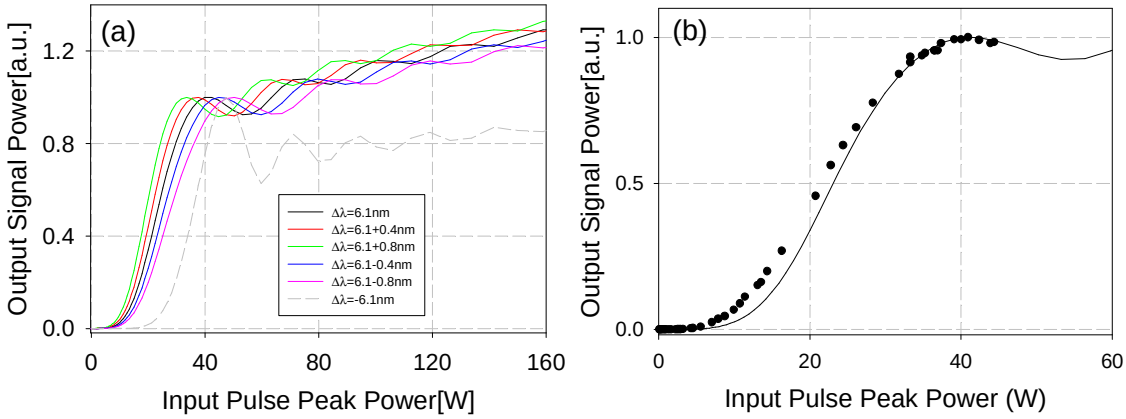

FIGURE 8.7: a) Numerical nonlinear transfer functions at various filter detunings b) Numerical and measured transfer function of the regenerator at 6.1 nm offset filtering. Note that the power levels correspond to the powers at the input of the Bi-NLF patch cord, and not to the input of the Bi-NLF itself.

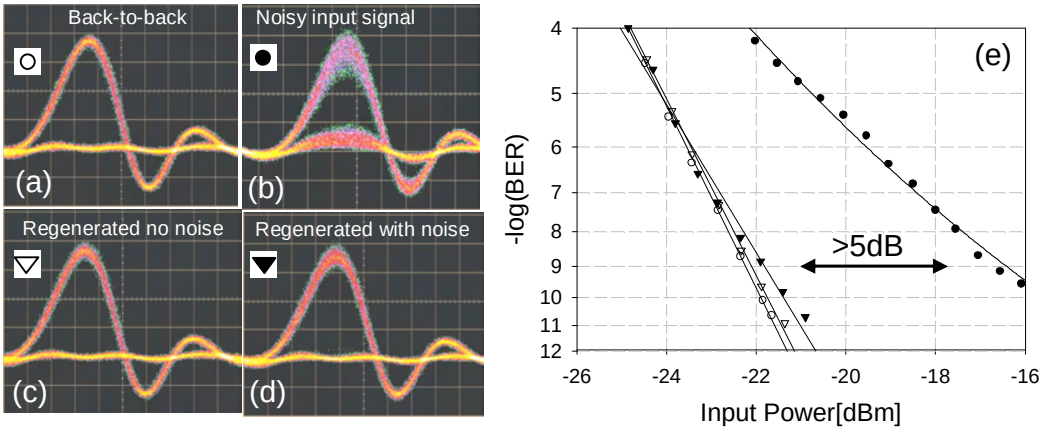

FIGURE 8.8: Eye diagrams of the input and output of the system for no added noise ((a) and (c)) and some induced noise ((b) and (d)). Scale: 10ps/div. Scope bandwidth: 20 GHz. e) Corresponding BER measurements.

using the SHG-FROG technique, (see Fig. 8.5.b), and good quality, fairly unchirped pulses with a FWHM of ∼6.0 ps (as mainly determined by the bandwidth of the offset filter) were demonstrated.

Finally, the noise-rejection properties of the system were examined. Fig. 8.8.a and Fig. 8.8.c show the data signal at the input and output of the system when no amplitude noise is added to the pulses, and demonstrate that the reshaping system does not in itself introduce any additional noise to the signal. Next, some additional noise was induced on the input signal. Defining ρ as the relative power variation (rms standard deviation) around the mean of the pulse for the zero and one levels, then the noise variations introduced on the marks and spaces were 11% and 7% respectively, see Fig. 8.8.b. Note that due to noise restrictions in the DCA-based measuring system used, a 2% standard deviation in amplitude is measured for a nominally noise-free signal. Fig. 8.8.d shows the eye diagram of the received signal at the output of the bandpass filter, which shows that the noise at the spaces has been suppressed, while amplitude equalization

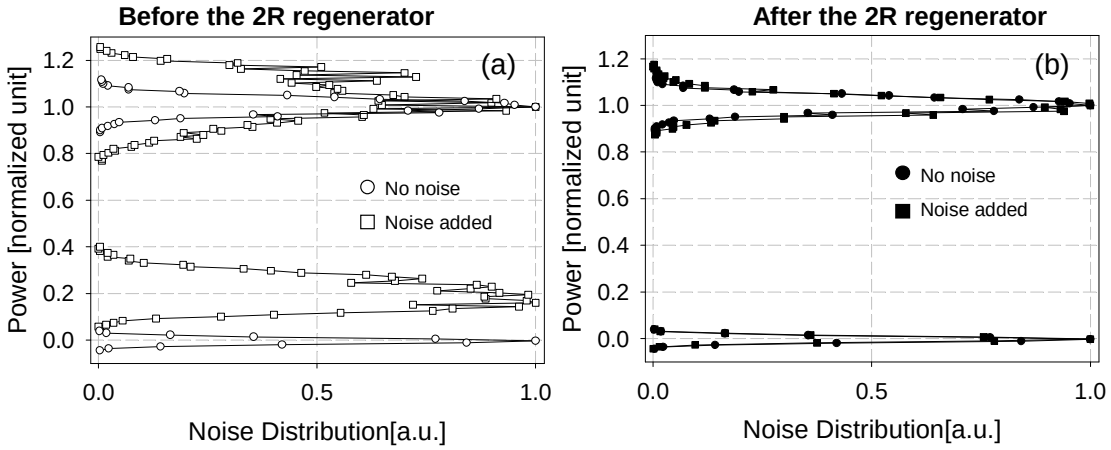

FIGURE 8.9: Distribution of amplitude jitter before (a) and after (b) the reshaping system, when no noise (circle points) and some noise (rectangular points) was applied.

has been performed at the marks. The normal dispersion of the Bi-NLF at the wavelengths of operation ensures suppression of particularly detrimental nonlinear effects, such as modulation instability, that can give rise to additional amplitude noise on the signal. The measured BERs as a function of the launched optical average power into the receiver are presented in Fig. 8.8.e. Penalty-free operation of the regenerator for a noiseless input signal is confirmed, while an improvement in the receiver sensitivity by more than ∼5 dB is achieved for the case when amplitude noise is deliberately applied to the incident data pulses. This significant improvement is due to the flat-topped spectrum achieved in the Bi-NLF. Q-factor measurements of the system before and after the regenerator were carried out also, see Fig. 8.9. The amplitude noise intensity histograms of Fig. 8.9.b demonstrate that amplitude noise associated with the zero and one levels is drastically reduced compared to Fig. 8.9.a and approaches the "no noise" case, as already confirmed by the BER measurements and the nonlinear characteristic function. In particular, when the Q-factor of the initial signal was degraded from 22 down to 5.6, by adding the noise to the system the Q-factor of the final signal remained fairly constant at around 20.

Since fibre based devices have issues such as stability and polarization dependence, a comment related to the stability of the system is required. In this particular experiment, the short length of fibre used and the weak polarization dependence of the SPM-broadening ensured the overall system was insensitive relative to environmental instability. Furthermore, since no additional sources need to be synchronized to the data signal the system configuration is quite simple.

Finally, a comment related to the energy efficiency of this regenerator is required. As already discussed in Section 2.4, the SPM-based 2R regenerator is known to exhibit poor efficiency, and the higher the filter offset, the lower this efficiency becomes. In the experiment described herein, the average optical input power at the optimum point is ∼31 dBm, while the corresponding average power at the output of the filter is ∼7 dBm, resulting in a loss for the overall system of ∼24 dB. In this investigation, I targeted

the achievement of the optimum performance of the 2R regenerator without trying to minimize the input power levels and wavelength detunings. However, the peak power x length product of the device at this optimum operating point is ∼0.09 W km, as opposed to a value of >3.6 W km reported in [44] or 2.5-2.7 W km reported in [108], showing more that one order of improvement due to the fibre used. A further improvement could be obtained by reducing the splicing losses of the fibre.

8.7 Experimental Set-up for the 40 Gb/s experiments

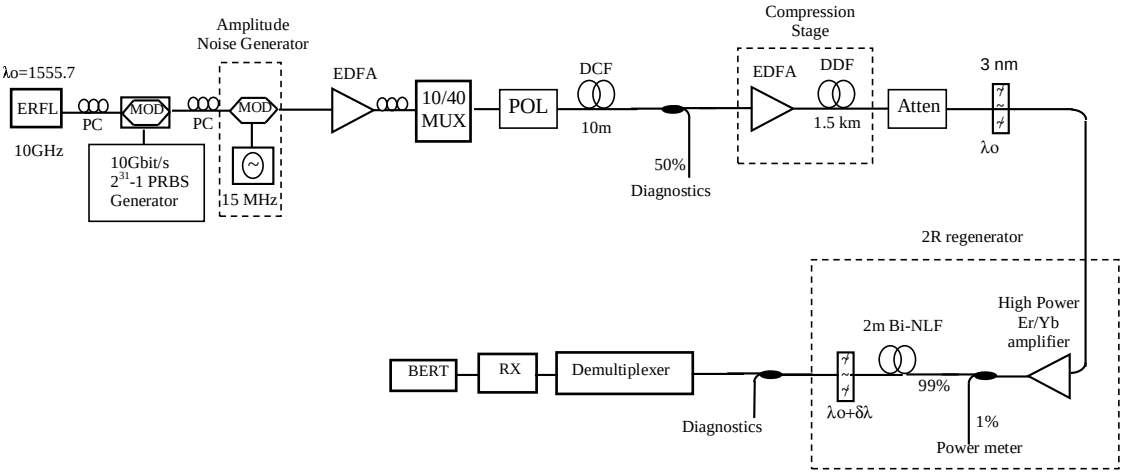

FIGURE 8.10: Experimental Set-up. MOD: modulator. POL: Polarizer. RX: Receiver. BERT: Bit error rate tester.

The performance of the Bi-NLF 2R regenerator was also assessed at 40 Gb/s. The experimental set-up is shown in Fig. 8.10. Compared to Fig. 8.3, the set-up is slightly modified, in order to maintain a similar duty cycle and hence achieve similar peak power levels at the Bi-NLF. In more detail, the 2 ps data pulses were passively multiplexed through a 1:4 multiplexer to a rate of 40 Gb/s and then launched into 10 m of DCF to compensate for the chirp induced by the few hundreds of meters of SMF of the multiplexer. The signal was then amplified and fed onto 1.5 km of Dispersion Decreasing fibre (DDF) and the pulses compressed down to 1.4 ps. The SHG-FROG characterization of these pulses is shown in Fig. 8.11.a, indicating a pedestal at a level of ∼12 dB below the pulse peak, as well as a fairly linear chirp due to the pulse evolution within the DDF. The signal was then amplified by a high power Er/Yb amplifier before being launched into the 2-m-long Bi-NLF. A 0.6 nm tunable bandpass grating filter was used to filter the output of the regenerator. The signal was finally demultiplexed into four 10 Gb/s constituent channels using an EAM and measured.

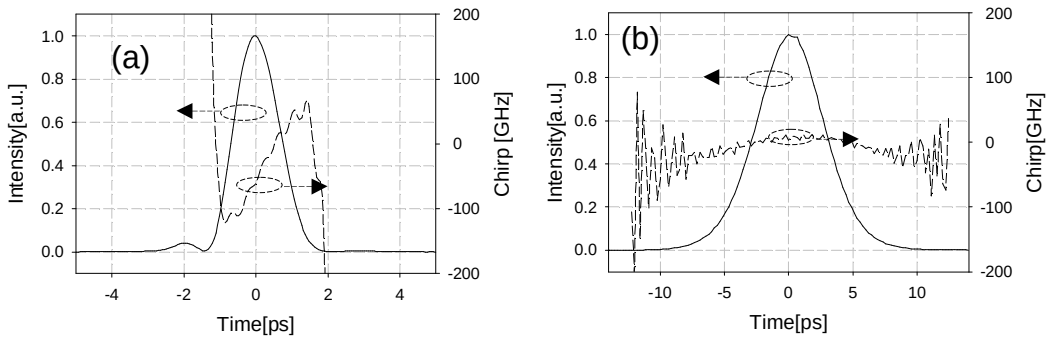

FIGURE 8.11: Intensity and chirp profile of the pulses at (a) the input and (b) output of the regenerator using SHG-FROG.

8.8 Results and discussion for the 40 Gb/s experiments

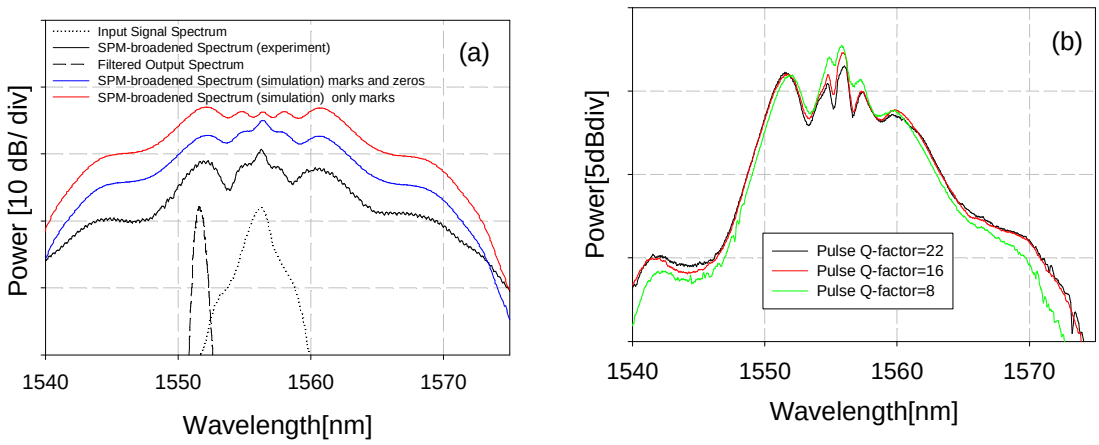

FIGURE 8.12: a) Optical spectra at the input of the Bi-NLF (black dotted trace), after the propagation in the fibre (experimental (black solid trace) and simulated traces (blue and red traces)) and at the output of the 0.6 nm filter (black dashed trace) for an input power Pin∼31 dBm. The spectra are vertically offset for ease of reading. b) Optical spectra after propagation in the bismuth fibre for different extinction ratios between marks and spaces of the data signal.

Due to the difference in the characteristics of the starting pulses relative to the 10 Gb/s case, see Fig. 8.11.a and Fig. 8.5.a, similar measurements to those previously made at 10 Gb/s were carried out. First, an assessment of the performance of the nonlinear thresholder was performed. Again, optimum regeneration performance was achieved for a relatively high power level (∼31 dBm) and wavelength detuning of ∼3.9 nm, (see dashed curve in Fig. 8.12.a for the filtered spectrum). Note again that the power levels quoted herein, correspond to the powers at the input of the Bi-NLF patch-cord, and not to the input of the Bi-NLF itself (∼3 dB less). The measured transfer function of the 2R regenerator is presented in Fig. 8.13. The flat top of the curve is reached at a lower peak power than in the 10 Gb/s case, due to the smaller filter offset chosen in this case. As expected from the FROG characterization in Fig. 8.11.a, the obtained spectrum (see black solid curve in Fig. 8.12.a) is symmetric about the central wavelength,

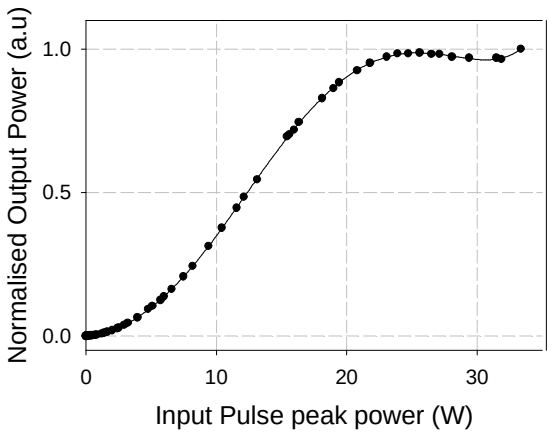

FIGURE 8.13: Measured nonlinear characteristic function of the 2R regenerator.

so similar performance is expected for both positive and negative filter offsets compared to the input signal wavelength. In this case, the offset filter was chosen to be placed at wavelengths shorter than the original data wavelength in order to reduce the ASE noise levels introduced by the EDFA, which peak towards longer wavelengths. However, a comparison of the experimentally obtained spectrum with simulations, (see red curve in Fig. 8.12.a) shows an unexpected peak of ∼2 dB at the central wavelength. This contribution is caused by the finite extinction ratio of the data modulator, and hence the existence of ghost pulses in the zero-slots. This is discussed in the Appendix for a "1 0" sequence and here it is demonstrated for completeness for a PRBS sequence. The SPM broadening of the data signal was numerically investigated, when a modulator with a finite extinction of ∼16 dB was considered, blue curve in Fig. 8.12.a, which shows a good agreement with the experimental trace previously obtained. An evaluation of this contribution was also carried out experimentally. In particular, Fig. 8.12.b shows different spectra at the output of the bismuth fibre at different extinction ratios between marks and spaces of the data signal, when 2 ps sech pulses were considered as the input pulses of the Bismuth fibre. As can be seen, decreasing the extinction ratio of the modulator, i.e. increasing the intensity of the ghost pulses at the input, the central peak on the spectrum increases.

The pulses at the output of the regenerator were characterized using the SHG-FROG technique, (Fig. 8.11.b), and a very similar behavior was obtained to the previous case shown in Fig. 8.5.b. This implies that the features of the output pulses were mainly determined by the optical filter used. Note that no pedestal is observed on the output pulses.

Finally, in order to evaluate the noise-rejection of the system similar measurements to those made for the 10 Gb/s case were repeated. The system is first assessed for the case when no amplitude noise is added onto the data, demonstrating that the technique does not in itself introduce any additional noise to the signal, (see Fig. 8.14.a and Fig. 8.14.c). Amplitude noise was next introduced to the input signal. In this case it was more difficult to evaluate the amplitude noise introduced to the 40 Gb/s signal. The receiver

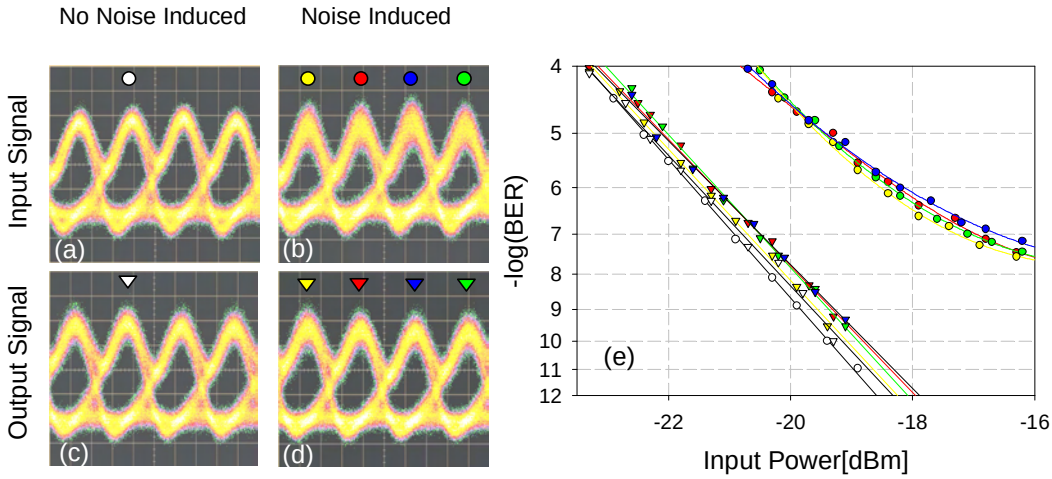

FIGURE 8.14: Eye diagrams of the input and output of the system for no added noise ((a) and (c)) and some induced noise ((b) and (d)). Scale: 10 ps/div. Scope bandwidth: 20 GHz. e) Corresponding BER measurements.

bandwidth of 20 GHz, which was available at the time of the measurements, was not fast enough to repeat similar measurements as those performed in the previous case. Indeed, in Fig. 8.14.a-d it is possible to see the ringing of the photodetector, very difficult to discern it from the noise on the zero level. Direct measurements of amplitude histograms from the eye diagrams would not be the proper way to assess the data signal. For this reason, the noise introduced on the pulse was assessed before multiplexing the signal. Even if this underestimates the real noise before the regenerator, since some noise will be introduced by the propagation in the multiplexer and the DDF themselves, it does however give an idea of the value. From histogram measurements of the 10 Gb/s signal, noise with a ∼11 % and ∼4 % standard deviation in the amplitude of the marks and spaces respectively was introduced, see Fig. 8.14.b for the corresponding eye diagram at 40Gb/s. The eye diagrams of the received signal at the output of the bandpass filter were assessed (see Fig. 8.14.d). The eye opening was clearly improved during the regenerative process. The signal was next demultiplexed into four 10 Gb/s constituents using an EAM, and BER measurements were performed on the four demultiplexed signals, (see Fig. 8.14.e). For power levels <-16 dBm, the noise-degraded signals did not allow error-free operation of the receiver. However, error- and penalty-free operation was achieved after the 2R regenerator, with a receiver sensitivity improvement which exceeds 2 dB in all cases.

8.9 Conclusion

In this Chapter, the use of a 2-m-long highly nonlinear bismuth-oxide-based fibre in a simple 2R regeneration scheme based on spectral broadening due to SPM and offset filtering is reported at repetition rates of 10 Gb/s and 40 Gb/s. The regenerator benefits

from the strong normal dispersion of the Bi-NLF in addition to its high nonlinearity. Indeed, the normal dispersion at the telecommunication wavelengths favours the generation of a smooth SPM spectrum, while the high nonlinearity allows a drastic reduction in the length and input power requirements. For example, the power-length product in this case is ∼0.09 W km, much lower compared to ∼2.5 W km for a silica based highly nonlinear fibre.
The performance of the regenerator was tested with heavily degraded input RZ signals using SHG-FROG characterization, and both eye diagram and BER measurements. Numerical and experimental studies on the spectral broadening of such pulses were carried out as well, to gain a better understanding of the behaviour of the system. Even in such a short piece of fibre, and at power levels which are readily achieved using commercial amplifiers, an improvement in the receiver sensitivity of ∼5 dB at 10 Gb/s and >2 dB at 40 Gb/s was achieved. Because of the compactness and simplicity of the regenerator, the overall system was very stable.
In this work, the use of a high power amplifier was required to achieve optimum performance, although already underlined in this Chapter, lower power levels could have been used to obtain 2R regeneration albeit with reduced regeneration performance. Higher power levels were chosen to obtain maximum improvement. This explains the very low energy efficiency of the regenerator: the higher the filter offset is, the lower the efficiency becomes. Furthermore, the high splicing losses of the bismuth fibre can be reduced using better splicing technologies, meaning that conventional EDFAs might be sufficient to provide the signal power required for device operation in the future.

This experiment highlights the potential of compound glass fibre technology for future compact and robust all-optical signal processing applications. Note again that this scheme is capable of operating at far higher bit rates, due to the fs response of the Kerr effect in optical fibres. However, going to higher repetition rates, the pulsewidth of the signal should be scaled down as well to keep the same duty cycle and so similar performance for identical average power levels. Increasing the initial repetition rate, other issues such as filters bandwidths will also have to be taken into account.

Chapter 9

Conclusion and Future work

In this thesis, I investigate new all-optical techniques for the amplitude and time regeneration of high bit-rate signals. Fibre technology has an important role to play within all-optical processing techniques, both in terms of pulse shape control using SSFBGs and in terms of ultrafast nonlinear optical processing. In my work I have combined both of these types of linear and nonlinear processing, thereby achieving a higher level of control over the properties of the signals under question.

As a first step, I have presented different techniques to measure the shaped pulses. Indeed, direct diagnostic tools with picosecond to femtosecond time resolution are needed to accurately assess the exact pulse shapes. I have discussed the development of an optical sampling oscilloscope and variations on the frequency resolved optical gating technique, both of which I used for the assessment of the fine features of shaped pulses. In my experiments, these techniques are compared to each other confirming the overall good agreement between them.

Subsequently, pulses with a rectangular shape were generated and used in a proof of principle experiment to achieve retiming of a data signal. The amount of jitter that can be compensated for is determined by the width of the reshaped pulses, which can be readily adjusted to fit the specific jitter characteristics of a given transmission system. The upper limit on the compensated timing jitter is obviously determined by the repetition rate of the system.

In a second step, I extended this work and obtained pulse reshaping/amplitude noise reduction as well as retiming of the data pulses in a single switch using the regenerative properties of a NOLM. The S-shaped switching characteristic of the NOLM together with the square switching window provide the pulse reshaping and amplitude noise reduction.

A second application based on pulse re-shaping into 10 ps parabolic pulses was numerically and experimentally investigated for the retiming of short optical pulses. The technique relies on frequency-chirping mistimed pulses using XPM in a HNLF pumped by parabolic clock pulses. The profile of these pulses ensures that the chirp on the

switched pulses is linear over a wide range, so that it can be removed by linear propagation in an SMF.
These linearly shaped parabolic pulses have also been employed for the generation of ultra-flat broadened spectra in a normal dispersion HNLF. They provide optimum performance in terms of spectral broadening, flatness and spectral density as compared to more conventional pulse shapes. Potential applications, including spectrally sliced pulse generation and efficient pulse compression, are also discussed and demonstrated.
Finally, the use of a fibre with higher nonlinear coefficient than standard silica based fibre is shown to allow a drastic reduction in the length and input power requirements of nonlinear switches, so that compact and simple devices can be implemented. As an example, a 2-m-long highly nonlinear bismuth-oxide-based fibre in a simple 2R regeneration scheme based on spectral broadening due to SPM and offset filtering is reported at repetition rates of 10 Gb/s and 40 Gb/s.

Future work

Rectangular pulses

Rectangular pulses are implemented in Chapter 4 and 5, where the developed systems account for re-timing and re-shaping of the data signals. The technique is reported at a repetition rate of 10 Gb/s, however in principle application at far higher repetition rates should be achievable. It is clear thought that the particular 20 ps rectangular-pulse grating used in this demonstration would already introduce a large amount of cross-talk between adjacent shaped pulses at a repetition rate of 40 Gbit/s . To go to even higher repetition rates, therefore, shorter square windows have to be used. A grating that can shape the pulses into 10 ps square pulses has been already fabricated and characterized (see Chapter 3) and can be developed further in order to reduce the desired timing jitter at a higher repetition rate. Furthermore, long period gratings that can shape pulses into square pulses as narrow as 1 ps have been already demonstrated [120].

The true test for a 3R regenerator is the characterization of its performance under transmission (this would thus require a clock recovery module to recover the clock from the data sequence). In the laboratory, a recirculating loop can be used in order to simulate the transmission performance and test regenerators in the regime of a multi-thousand kilometer long transmission system.
Finally, alternative architectures of the non-linear gate and new materials should also be investigated for the implementation of shorter devices at lower operating powers (see for example the discussion on 2R regeneration in Bismuth fibre below).

Parabolic pulses

Parabolic pulses, also formed in a pulse shaping SSFBG, are developed to demonstrate a different re-timing technique. However, in the experiments I described in Chapter 6 the final pulsewidth of the retimed pulses was broader than the initial one due to the dispersive medium used after the HNLF. This broadening can in principle be avoided if the pulses are pre-chirped before entering the retiming system or by carefully choosing the peak power of the control pulse (and consequently the length of the SMF used).

In a similar scheme, these parabolic pulses or more explicitly the XPM induced by them in a HNLF could be used as the basis for an all-optical element that provides quadratic phase modulation in time. Such an element is required in applications that perform OFT. For example this scheme could be then used for mitigating any kind of linear distortions (namely high order dispersion) after transmission, thus improving the overall BER performance of the system. In an analogous way, the scheme could also have potential applications for pulse characterization by mapping the spectral profile of the waveform in the time domain, and vice versa.
Finally, by preceding and following the quadratic phase modulation (XPM in a HNLF) with suitable dispersive elements, the demonstration of scaling in the time domain the waveform under test could be possible, while maintaining the overall shape of the envelope (imaging system).

The sharp tails of parabolic pulses and the fast Kerr response of fibres facilitate scalability of the scheme to far higher repetition rates. For the case examined in this thesis, data signals up to 80 Gb/s could be considered. Operation at higher repetition rates would require the generation of even shorter parabolic pulses to form the control signal. This would obviously present a greater challenge in terms of grating fabrication and higher pump power levels to obtain similar XPM-effects when the same HNLF is used. This last issue could be tackled using different kinds of fibres with higher nonlinearities. On the other hand, considering the experimental set-up described in Chapter 6, the parabolic pulses could be temporally broadened to adapt themselves better to even more extreme cases of system impairment. This could be easily achieved if they propagate in normally dispersive HNLFs (see Chapter 7) before being coupled with the data signal under test. Note again, that the use of different N-HNLF with higher nonlinearities could be used to decrease the power requirements to achieve a given pulse width.

Finally, this technique is directly applicable to the simultaneous retiming of several synchronized WDM channels to increase the data transmission capacity. The dispersion slopes of state of the art HNLFs can be as low as 0.001 ps/nm^2/km, implying good XPM efficiency across all the WDM channels.

2R Regeneration in Bismuth fibre

A 2-m-long compact device based on spectral broadening due to SPM and offset filtering is reported at repetition rates of 10 Gb/s and 40 Gb/s in a highly nonlinear bismuth-oxide-based fibre. In this work, the use of a high power amplifier was required to achieve optimum performance. The high splicing losses (∼3 dB per slice) of the bismuth fibre is one of the reasons for such high power levels and can be reduced significantly using better splicing technologies [116], meaning that conventional EDFAs would be sufficient to provide signal power for the device operation in the future. In this case, this scheme can be demonstrated at even higher bit rates.
If the issue of splicing losses is properly tackled, such fibres could be used as well in interferometric schemes, namely NOLMs, to improve the compactness and stability of such switches.
It would be interesting to consider different materials, which are made of glasses with greater intrinsic material nonlinearity coefficients than silica (chalcogenide, lead-silicate glasses...).
Furthermore, if the intrinsic properties of the corresponding waveguide, and especially the waveguide dispersion, have to be chosen properly, Holey Fibres (HFs) with suitable manipulation of their microstructure design can be considered. HFs based on various nonlinear materials have been already designed and fabricated to tackle this issue [121–123]. Unfortunately, the main drawback of such technologies relates to the possibility of splicing them to conventional SMF.

Appendix A

Alternative method to optimize the extinction ratio of an optical modulator

In this appendix, two new simple methods to optimize the performance of an optical modulator, and thus to obtain the best extinction ratio of the data signal, are demonstrated exploiting the SPM-induced spectral broadening of the pulses at different energy levels in HNLF. These simple but extremely significant and sensitive methods display the signal at the output of the HNLF on an optical spectrum analyzer or an oscilloscope.

A.1 Introduction

For transmission systems employing signals at 10 Gbit/s and higher, external optical modulation is commonly applied for intensity and/or phase modulation of the optical carrier. In this way, the modulator, which carries the data information, modifies the intensity (or phase) of a generic continuous wave or pulse train. To obtain the best performance during transmission, it is then important that the extinction ratio between the ones (presence of an optical pulse) and zeros (absence of an optical pulse) is maximised at the transmitter. In the case of a $LiNbO_3$ intensity modulator, this extinction ratio can be varied by adjusting the polarization of the signal, the temperature of the modulator, the bias voltage and so on. Indeed, even if the V_π of the modulator can be measured easily using a CW source, the optimum bias voltage is a function of the temperature on the device, and hence is difficult to be monitor. This optimization is usually carried out while displaying the data signal on an oscilloscope straight after the modulator (linear method), before transmitting it. However, using this method, it is hard to distinguish between extinction ratios higher than 10 dB, due to the limited dynamic range of the oscilloscope. It is consequently interesting to have a more sensitive technique to be able

to measure higher extinction ratios. In this appendix, it is shown how the SPM-induced phase modulation in a HNLF ans subsequent display either on an OSA or on an oscilloscope after a proper optical filter, can effectively be used to assess directly the quality of the modulated signal for extinction ratios (higher than 10 dB). After a brief explanation of the basic principle and the corresponding set-up, some experimental results will be presented, showing the higher sensitivity of the method compared to the linear method.

A.2 Basic principle and Experimental set-up

The basic principle of this technique is described in Fig. A.1. A generic modulated signal can always be seen to consist of two types of pulses, pulse A and pulse B, of identical forms but different peak power levels ($P_A \gg P_B$) (Fig. A.1.a). Pulse B could for example be seen as a ghost pulse, resulting from the finite extinction ratio of the modulator. In the spectral domain, the resulting spectrum (Fig. A.1.b) is the sum of the spectrum of A, plus the one of B, plus an interference term between the two. If this signal is then injected into a HNLF, where the SPM-induced phase modulation will be the dominant effect, pulse A, which has a higher peak power, will see a strong spectral broadening, while the spectral broadening of pulse B will be almost unaffected [44]. However, if the nonlinearity of the fibre is relatively high, spectral broadening is induced also for relatively low peak power levels, so that any small deviation from the optimum extinction ratio is visible on the spectrum as a beating term (Fig. A.1.c). This beating term can then be directly visualized in the wavelength domain using an OSA (method (a)) or in the time domain after proper optical filtering (method (b)). Indeed, using an optical filter, whose central frequency is identical to that of the initial pulse (case (1) in Fig. A.1.d), the extinction ratio of the signal can be measured on an oscilloscope with a much higher accuracy than before. In more detail, Fig. A.1.d shows that, in the central zone, the spectrum is made up by pulses A and B at the same time. For very high peak powers, the spectral intensity of pulse A in the central zone will have a decreased weight compared that of pulse B. For this reason, even a small change in the peak power of pulse B will translate onto a relatively higher spectral peak, so that the ghost pulse can easily be seen on the oscilloscope, hence increasing the sensitivity of the method.
The experimental set-up, used to validate these new methods, is represented Fig. A.2. Pulses generated by the EFRL at 1550 nm are gated down to a repetition rate of 5 GHz to produce a "0 1" sequence using a lithium niobate modulator. Their quality can be visualized directly on an oscilloscope according to the conventional linear method. Alternatively, after being amplified (high power levels are preferred to facilitate significant spectral broadening in the HNLF), the pulses are launched onto 500 m of normally dispersive HNLF to avoid solitonic type effects and then measured with an OSA (method (a)). Finaly, the pulses can pass through an optical filter, centered at the central frequency of the transmitted signal, and then measured on a suitably oscilloscope (method

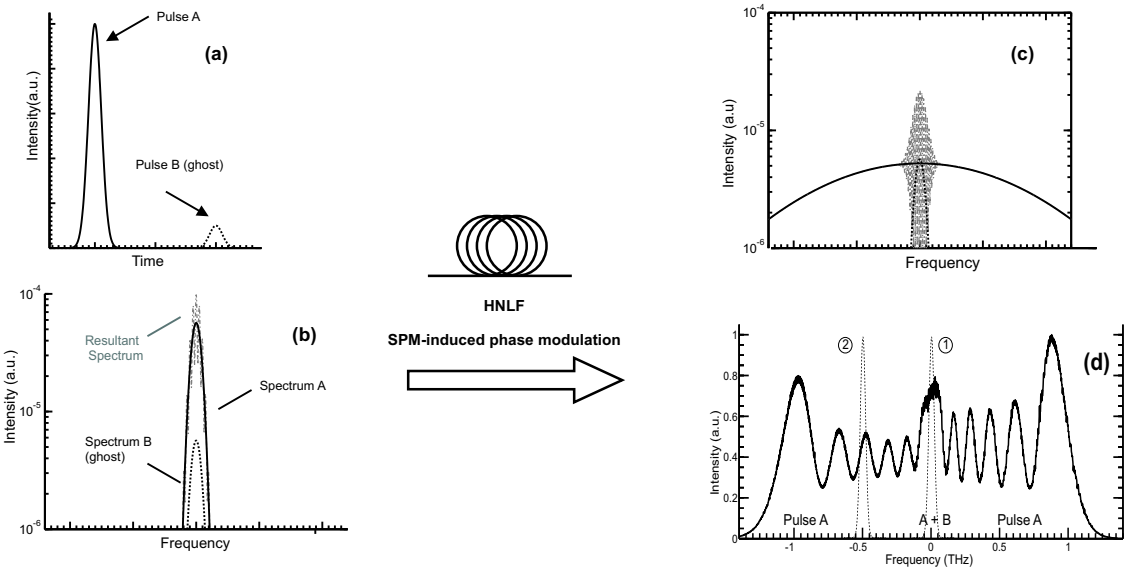

FIGURE A.1: Basic principle of the technique. Generic representation of the modulated signal in the time (a) and frequency (b) domain. c) Zoom of the simulated resultant spectrum at the central frequency of the signal. d) Corresponding measured spectrum.

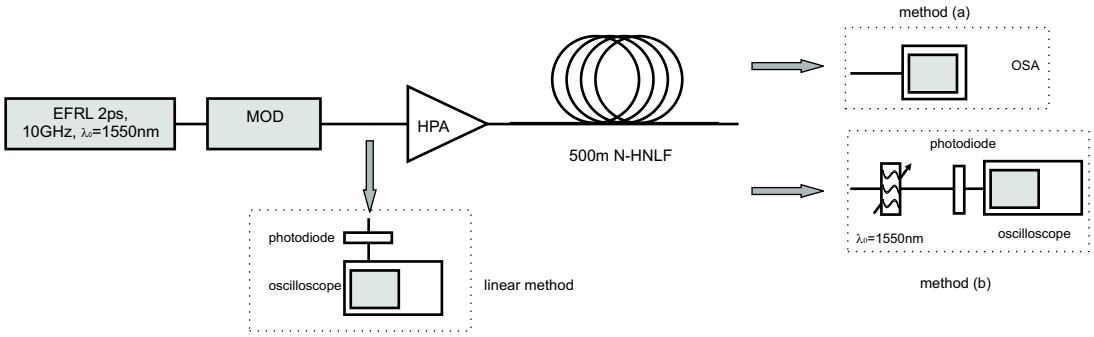

FIGURE A.2: Experimental set-up.

(b)).

A.3 Results and discussion

Fig. A.3 presents various experimental results. First, the optimum extinction ratio of the modulator is considered (top row of Fig. A.3). Fig. A.3.a1 shows the direct measurement of the data signal on a sampling oscilloscope, while Fig. A.3.b1 shows the corresponding spectrum at the output of the HNLF, where the oscillations characteristic of a sech pulse subjected to SPM are visible. No peak is discernible in the central part of the spectrum. The periodicity of the signal is then evaluated calculating the Fourier transform of the measured spectrum. As can be seen from Fig. A.3.c1, it comprises only peaks separated by 200 ps, which correspond to a repetition rate of 5 GHz. A slight change on the modulator bias voltage was then carried out to slightly degradate the extinction ratio of the signal (bottom row of Fig. A.3). The modification is barely visible on the oscilloscope trace, when the signal is detected directly (Fig. A.3.a2). On the other hand, considering method (a), a noticeable central peak appears on the spectrum of Fig. A.3.b2, in accordance with the principle described in Fig. A.1. Trying to minimize the amplitude of this central peak, which is very sensitive to any small changes in the modulator parameters, the optimum extinction ratio for the data signal can be easily and properly found. It is also worth noting that the Fourier transform of the degraded spectrum is marked by the appearance of secondary peaks, circled in Fig. A.3.c2. This different periodicity, which is 100 ps, implies the presence of ghost pulses.

Rather than using an OSA, it is possible to use a photodiode and an oscilloscope to visualize the transmitted signal using method (b). Fig. A.4.a-c represent oscilloscope traces detected using direct detection (green pulses) and the ones obtained using method (b) (blue pulses) for various modulator extinction ratio degrading settings. While no difference is visible from the green scope traces in Fig. A.4, using method (b), it is possible to distinguish among all the different cases from the blue oscilloscope traces, implying more sensitivity to any small changes. On the other hand, if the central wavelength of the optical filter is shifted, compared to the central position of the transmitted signal (case (2) in Fig. A.1.d), the ghost pulse is completely eliminated (Fig. A.5). In the particular case described herein, the -3 dB bandwidth of the filter was $\sim$0.5 nm and the offset filtering was $\sim$1.2 nm. This is a clear and simple illustration of the "Mamyshev" method [44], which is characterized by SPM-induced spectral broadening in HNLF and subsequent off-set filtering, discussed in Section 2.4.1. The "Mamyshev" method is one of the most promising current solutions for all optical regeneration of high-bit rate signals, and an example of application is given in Chapter 8.

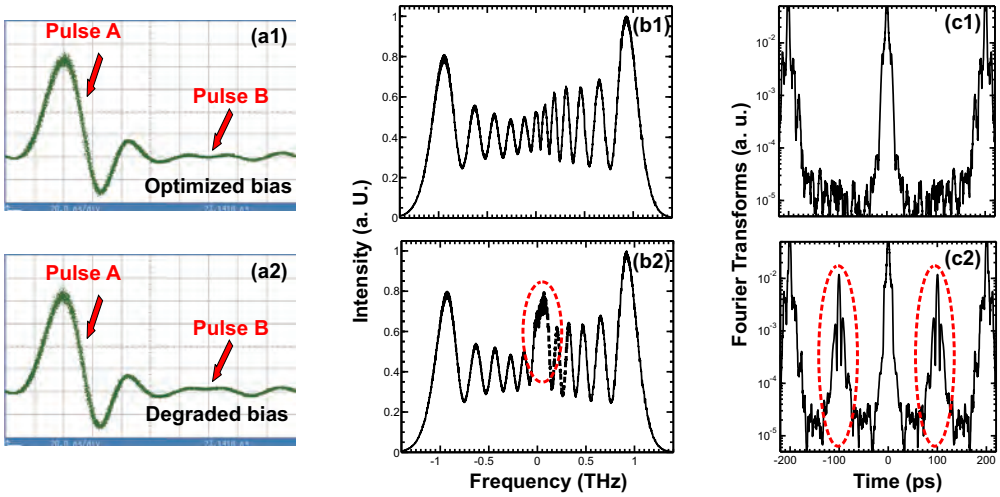

FIGURE A.3: Experimental results obtained for the optimum extinction ratio of the modulator (top row) and for a slightly degraded extinction ratio (bottom row). The modulated signal is visualized directly on an oscilloscope (method (a)) or on a OSA (Res=0.5 nm), after being propagated onto a N-HNLF (method (b)). c) Corresponding Fourier transform of the optical spectra.

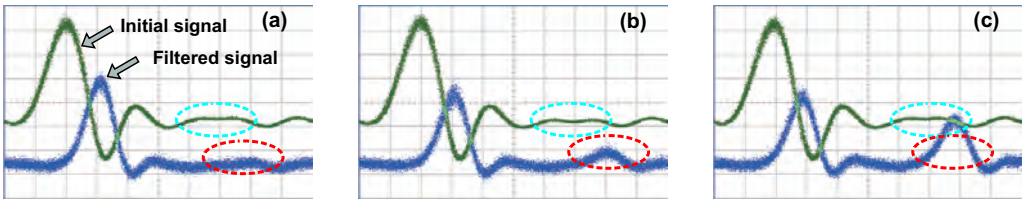

FIGURE A.4: Oscilloscope traces of the initial (green trace) and filtered (blue trace) signals for various levels of extinction ratio degrading, when the optical filter is aligned to the central frequency of the transmitted signal.

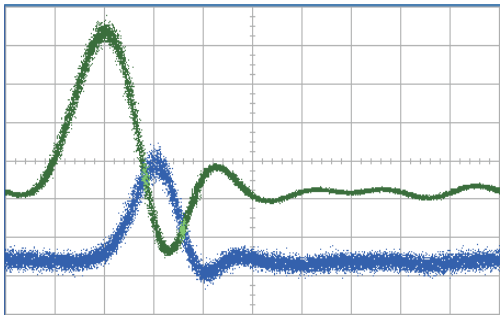

FIGURE A.5: Oscilloscope traces of the initial and filtered signal filtered when the optical filter is offset from the central frequency of the signal.

A.4 Conclusion

Two simple and very sensitive methods to optimize the extinction ratio of an optical modulator to improve the transmission length of a signal are discussed and demonstrated, using either an OSA or an optical filter and an oscilloscope.

List of publications

Journal papers

F. Parmigiani, C. Finot, K. Mukasa, M. Ibsen, M. A. F. Roelens, P. Petropoulos and D. J. Richardson. "Ultra-flat SPM-broadened spectra in a highly nonlinear fiber using parabolic pulses formed in a fiber Bragg grating." *Optics Express*, 14 (17): 7617–7622, 2006.

P. J. Almeida, P. Petropoulos, **F. Parmigiani**, M. Ibsen and D. J. Richardson. "OTDM Add-Drop Multiplexer Based on Time-Frequency Signal Processing." *Journal of Lightwave Technology*, 24 (7): 2720–2732, 2006 (Invited Paper).

F. Parmigiani, S. Asimakis, N. Sugimoto, F. Koizumi, P. Petropoulos and D. J. Richardson. "2R regenerator based on a 2-m-long highly nonlinear bismuth oxide fiber." *Optics Express*, 14 (12): 5038–5044, 2006.

C. Finot, **F. Parmigiani**, P. Petropoulos, and D. J. Richardson. "Parabolic pulse evolution in normally dispersive fiber amplifiers preceding the similariton formation regime." *Optics Express*, 14 (8): 3161–3170, 2006.

F. Parmigiani, P. Petropoulos, M. Ibsen, and D. J. Richardson. "Pulse Retiming Based on XPM using Parabolic Pulses formed in Fiber Bragg Grating." *IEEE Photonics Tech. Lett.*, 18 (7): 829–831, 2006.

F. Parmigiani, P. Petropoulos, M. Ibsen, and D. J. Richardson. "All-optical pulse reshaping and retiming systems incorporating pulse shaping fiber Bragg grating." *Journal of Lightwave Technology*, 24 (1): 357–364, 2006.

J. Prawiharjo, **F. Parmigiani**, K. Gallo, P. Petropoulos, N. G. B. Broderick, and D. J. Richardson. "Cascaded $\chi^{(2)}$ interaction based frequency-resolved optical gating in a periodically poled $LiNbO_3$ waveguide." *Opt. Lett.*, 31 (2): 244–246, 2006.

Conference papers

T. T. Ng, **F. Parmigiani**, Z. Zhang, M. Ibsen, P. Petropoulos, D. J. Richardson "Linear-distortion compensation using XPM with parabolic pulses." OFC, 2006 (accepted).

C. Finot, **F. Parmigiani**, P. Petropoulos, D. J. Richardson. "Methodes simples et sensibles pour optimiser le taux d'extinction d'un modulateur optique." 25th National Conference on Guided Optics (JNOG), Metz 7-9 Nov 2006.

P. Petropoulos, **F. Parmigiani**, T. T. Ng, D. J. Richardson "Linear signal distortion correction using an optical Fourier transform." e-Photon/ONe Workshop, Athens, 6-8 Sep 2006.

F. Parmigiani, C. Finot, K. Mukasa, M. Ibsen, M. A. F. Roelens, P. Petropoulos and D. J. Richardson. "Ultra-flat SPM-Broadened Spectra in a Highly Nonlinear Fiber Using a Fiber Bragg Grating Based Parabolic Pulse Shaper." ECOC, Cannes, 2006.

C. Finot, P. Dupriez, L. Provost, **F. Parmigiani**, P. Petropoulos, D. J. Richardson, C. Billet, J. Dudley, S. Pitois, G. Millot. "Impulsions paraboliques et similaritons dans les fibres optiques (Parabolic pulses and similaritons in optical fibres)." PAMO 2006 - Atomic & Molecular Physics Optics Dijon, 5-7 Jul 2006.

K. Gallo, J. Prawiharjo, **F. Parmigiani**, P. Almeida, P. Petropoulos and D. J. Richardson. "Processing ultrafast optical signals in broadband telecom systems by means of cascaded quadratic nonlinearities." Proc. ICTON 2006, Nottingham, 18-22 Jun 2006 (Invited).

C. Finot, **F. Parmigiani**, P. Petropoulos, and D. J. Richardson. "Parabolic pulse evolution in normally dispersive fiber amplifiers preceding the similariton formation regime." CLEO/QELS, CThR5, 2006.

C. Finot, **F. Parmigiani**, P. Petropoulos, and D. J. Richardson. "Evolution d'impulsions paraboliques dans un amplificateur a fibre optique hors regime asymptotique." 9th Nonlinear Conference 'Whats new in non-linear waves', 2006.

P. J. Almeida, **F. Parmigiani**, M. Ibsen, K. Mukasa, P. Petropoulos, and D. J. Richardson. "35-dB Channel suppression in OTDM add-drop multiplexing based on time-frequency signal processing." OFC, OWW3, 2006.

S. Asimakis, **F. Parmigiani**, N. Sugimoto, F. Koizumi, P. Petropoulos, and D. J. Richardson. "A 2m long reshaping regenerator based on a highly nonlinear bismuth oxide fiber." OFC, OThB5, 2006.

D. J. Richardson, J. Y. Y. Leong, **F. Parmigiani**, P. J. Almeida, M. Ibsen, and P. Petropoulos. "Recent developments in fiber technology and its application within high speed optical communications." IGNOIE-COE05, 2006 (Invited).

H. D. Foreman, **F. Parmigiani**, M. A. F. Roelens, and R. E. Simpson. "The lightwave roadshow." ETOP, 2005.

J. Prawiharjo, **F. Parmigiani**, K. Gallo, P. Petropoulos, N. G. B. Broderick, and D. J. Richardson. "A novel high-resolution and high-sensitivity FROG configuration based on cascaded $\chi^{(2)}$ interactions in a PPLN waveguide." CLEO-Pacific (Postdeadline), 2005.

F. Parmigiani, P. Petropoulos, M. Ibsen, M. A. F. Roelens, and D. J. Richardson. "A novel XPM based pulse retiming system incorporating a fiber grating based parabolic pulse shaper." ECOC, Tu4.6.4, 2005.

F. Parmigiani, P. Petropoulos, P. J. Almeida, M. Ibsen, and D. J. Richardson. "Amplitude and timing jitter reduction using a fiber NOLM incorporating a fiber Bragg grating based pulse shaper." OFC, OME, 2005.

F. Parmigiani, P. Petropoulos, M. Ibsen, B. Thomsen, and D. J. Richardson. "Retiming of short optical pulses using linear pulse reshaping and all-optical switching." OFC, FC7, 2004.

P. J. Almeida, J. H. Lee, M. Ibsen, P. Petropoulos, B. Thomsen, P. C. Teh, **F. Parmigiani**, and D. J. Richardson. "All-optical TDM data demultiplexing based on a highly nonlinear fiber Kerr gate using a linearly chirped rectangular control." CLEO/QELS, 2003.

F. Parmigiani, P. Petropoulos, P. J. Almeida, M. Ibsen, J. H. Lee, and D. J. Richardson. "A direct assessment of the performance of pulse shaping superstructured fiber gratings using an optical sampling oscilloscope." OFC, MF36, 2003.

Bibliography

[1] Y. Chigusa, Y. Yamamoto, T. Yokokawa, T. Sasaki, T. Taru, M. Hirano, M. Kakui, M. Onishi, and E. Sasaoka, "Low-loss pure-silica-core fibers and their possible impact on transmission systems," *J. Lightwave Technol.*, vol. 23, no. 11, pp. 3541–3550, November 2005.

[2] M. Takahashi, R. Sugizaki, J. Hiroishi, M. Tadakuma, Y. Taniguchi, and T. Yagi, "Low-Loss and Low-Dispersion-Slope Highly Nonlinear Fibers," *J. Lightwave Technol.*, vol. 23, no. 11, pp. 3615–3624, November 2005.

[3] R. J. Mears, L. Reekie, L. M. Jauncey, and D. N. Payne, "Low noise erbium doped fibre amplifier operating at 1.54 μm," *Electron. Lett.*, vol. 23, p. 1026, 1987.

[4] E. Desurvire, J. R. Simpson, and P. C. Becker, "High-gain erbium-doped travelling-wave fiber amplifier," *Opt. Lett.*, vol. 12, no. 11, pp. 888–890, 1987.

[5] M. Nawazawa, T. Yamamoto, and K. R. Tamura, "1.28 Tb/s-70 km OTDM transmission using third- and fourth-order simultaneous dispersion compensation with a phase modulator," *Electron. Lett.*, vol. 36, no. 24, pp. 2027–2029, November 2000.

[6] T. Ito, K. Fukuchi, and T. Kasamatsu, "Enabling technologies for 10 Tb/s transmission capacity and beyond," *Eur. Conf. Opt. Comm. (ECOC'01)*, 2001, Th.B.2.3.

[7] H. G. Weber, S. Ferber, M. Kroh, C. Schmidt-Langhorst, R. Ludwig, V. Marembert, C. Boerner, F. Futami, S. Watanabe, and C. Schubert, "Single channel 1.28 Tb/s and 2.56 Tbit/s DQPSK Transmission," *Eur. Conf. Opt. Comm. (ECOC'05)*, 2005, PD Paper Th4.1.2, pp. 3-4.

[8] G. Charlet, E. Corbel, J. Lazaro, A.Klekamp, R. Dischler, P. Tran, W. Idler, H. Mardoyan, A. Konczykowska, F. Jorge, and S. Bigo, "WDM Transmission at 6 Tb/s capacity over transatlantic distance, using 42.7 Gb/s Differential Phase-Shift Keying without pulse carver," *Proc. Optical Fiber Communications Conference (OFC'05)*, 2005, PDP36.

[9] N. Sugimoto, T. Nagashima, T. Hasegawa, S. Ohara, K. Taira, and K. Kikuchi, "Bismuth-based optical fiber with nonlinear coefficient of 1360 $W^{-1}km^{-1}$," *Proc.*

Optical Fiber Communications Conference (OFC'04), vol. PDP26 (Posdeadline paper), 2004.

[10] J. Y. Y. Leong, P. Petropoulos, J. H. V. Price, H. Ebendorff-Heidepriem, S. Asimakis, R. Moore, K. E. Frampton, V. Finazzi, X. Feng, T. M. Monro, and D. J. Richardson, "High-Nonlinearity Dispersion-Shifted Lead-Silicate Holey Fibers for Efficient 1m Pumped Supercontinuum Generation," *J. Lightwave Technol.*, vol. 24, pp. 183–190, 2006.

[11] L. B. Fu, M. Rochette, V. G. Ta'eed, D. J. Moss, and B. J. Eggleton, "Investigation of self-phase modulation based optical regeneration in single mode As_2Se_3 chalcogenide glass fiber," *Opt. Express*, vol. 13, pp. 7637–7644, 2005.

[12] A. M. Weiner, "Femtosecond optical pulse shaping and processing," *Progr. Quantum Electron.*, vol. 19, pp. 161–237, 1995.

[13] A. M. Weiner, J. P. Heritage, and R. N. Thurston, "Synthesis of phase-cogerent, picosecond optical square pulses," *Opt. Lett.*, vol. 11, pp. 153–155, 1986.

[14] T. Kurokawa, H. Tsuda, K. Okamoto, K. Naganuma, H. Takenouchi, Y. Inoue, and M. Ishii, "Time-space optical signal procesing using arrayed-waveguide grating," *Electron. Lett.*, vol. 33, pp. 1890–1891, 1997.

[15] T. Erdogan, "Fiber grating spectra," *J. Lightwave Technol.*, vol. 15, pp. 1277–1294, 1997.

[16] K. Hill and G. Meltz, "Fiber bragg grating technology fundamentals and overview," *J. Lightwave Technol.*, vol. 15, pp. 1263–1276, 1997.

[17] P. Petropoulos, M. Ibsen, A. D. Ellis, and D. J. Richardson, "Rectangular Pulse Generation Based on Pulse reshaping Using Superstructured Fiber Bragg Grating," *J. Lightwave Technol.*, vol. 19, no. 5, pp. 746–752, May 2001.

[18] P. C. Teh, P. Petropoulos, M. Ibsen, and D. J. Richardson, "A comparative study of the performance of seven- and 63-chip optical code-division multiple-access encoders and decoders based on superstructured fiber bragg gratings," *J. Lightwave Technol.*, vol. 19, no. 9, pp. 1352–1365, 2001.

[19] P. Petropoulos, M. Ibsen, M. N. Zervas, and D. J. Richardson, "Generation of a 40 GHz pulse stream by pulse multiplication with a sampled fiber Bragg grating," *Optics Lett.*, vol. 25, no. 8, pp. 521–523, April 2000.

[20] S. Longhi, M. Marano, P. Laporta, and O. Svelto, "Propagation, manipulation, and control of picosecond optical pulses at 1.5μm in fiber bragg gratings," *J. Opt. Soc. Am. B*, vol. 19, no. 11, pp. 2742–2757, 2002.

[21] O. Leclerc, B. Lavigne, E. Balmefrezol, P. Brindel, L. Pierre, D. Rouvillain, and F. Seguineau, "All-optical signal regeneration: from first principles to a 40 Gbit/s system demonstration," *Comptes Rendus Physique*, vol. 4, pp. 163–173, 2003.

[22] J. C. Simon, L. Billes, A. Dupas, B. Kowalski, M. Henry, and B. Landousies, "All-Optical Regeneration," *Proc. Eur. Conf. on Opt. Comm. (ECOC'98)*, Madrid, vol. 1, pp. 467–469, September 1998.

[23] J. P. Gordon and H. A. Haus, "Random walk of coherently amplified solitons in optical fiber transmission," *Optics Lett.*, vol. 11, no. 10, pp. 665–667, October 1986.

[24] A. R. Chraplyvy, "Limitations on lightwave communications imposed by optical-fiber nonlinearities," *J. Lightwave Technol.*, vol. 8, no. 10, pp. 1548–1557, October 1990.

[25] J. Mȧrtensson, A. Berntson, M. Westlund, A. Danielsson, P. Johannisson, D. Anderson, and M. Lisak, "Timing jitter owing to intrachannel pulse interactions in dispersion-managed transmission systems," *Opt. Lett.*, vol. 26, no. 2, pp. 55–57, 2001.

[26] R. J. Essiambre, B. Mikkelsen, and G. Raybon, "Intra-channel cross-phase modulation and four-wave mixing in high-speed TDM systems," *Electron. Lett.*, vol. 35, no. 18, pp. 1576–1578, September 1999.

[27] I. Shake, H. Takara, K. Mori, S. Kawanishi, and Y. Yamabayashi, "Influence of inter-bit four-wave mixing in optical TDM transmission," *Electron. Lett.*, vol. 36, no. 16, pp. 1600–1601, August 1998.

[28] D. Mahgerefteh and C. R. Menyuk, "Effect of First-Order PMD Compensation on the Statistic of Pulse Broadening in a Fiber with Randomly Varying Birifringence," *IEEE Photon. Technol. Lett.*, vol. 11, no. 3, pp. 340–342, March 1999.

[29] G. P. Agrawal, *Nonlinear Fiber Optics*, 3rd ed., A. Press, Ed., 2001.

[30] E. M. Dianov, A. V. Luchnikov, A. N. Pilipetskii, and A. N. Starodumov, "Electrostriction mechanism of soliton interaction in optical fibers," *Optics Lett.*, vol. 15, no. 6, pp. 314–316, March 1990.

[31] M. Eiselt, M. Shtaif, and L. D. Garrett, "Contribution of Timing Jitter and Amplitude Ditortion to XPM System Penalty in WDM Systems," *Opt. Lett.*, vol. 26, no. 2, pp. 55–57, 2001.

[32] M. J. W. Rodwell, M. Urteaga, T. Mathew, D. Scott, D. Mensa, Q. Lee, J. Guthrie, Y. Betser, S. C. Martin, R. P. Smith, S. Jaganathan, S. Krishnan, and S. I. Long, "Submicron Scaling of HBTs," *IEEE Transactions on Electron Devices*, vol. 48, no. 11, pp. 2606–2624, November 2001.

[33] Y. Muramoto, K. Yoshino, S. Kodama, Y. Hirota, H. Ito, and T. Ishibashi, "100 and 160 Gbit/s operation of uni-travelling-carrier photodiode module," *Electron. Lett.*, vol. 40, no. 6, pp. 378–380, March 2004.

[34] M. Yoneyama, Y. Miyamoto, T. Otsuji, H. Toba, Y. Yamane, T. Ishibashi, and H. Miyazawa, "Fully Electrical 40-Gb/s TDM System Prototype Based on InP HEMT Digital IC Technologies," *J. Lightwave Technol.*, vol. 18, no. 1, pp. 34–43, January 2000.

[35] K. Schuh, B. Junginger, E. Lach, A. Klekamp, and E. Schlag, "85.4 Gbit/s ETDM receiver with full rate electronic clock recovery circuit," *Eur. Conf. Opt. Comm. (ECOC'04)*, Stockholm, 2004, PD Paper Th4.1.1, pp. 7-8.

[36] P. J. Winzer, G. Raybon, and M. Duelk, "107- Gb/s optical ETDM transmitter for 100G Ethernet transport," *Eur. Conf. Opt. Comm. (ECOC'05)*, 2005, PD Paper Th4.1.1, pp. 1-2.

[37] R. H. Derksen, G. Lehmann, C. J. Weiske, C. Schubert, R. Ludwig, S. Ferber, C. Schmidt-Langhorst, M. Möller, and J. Lutz, "Integrated 100- Gbit/s ETDM Receiver in a Transmission Experiment over 480 km DMF," *Proc. Optical Fiber Communications Conference (OFC'06)*, 2006, PD Paper PDP37.

[38] I. D. Phillips, A. D. Ellis, T. Widdowson, D. Nesset, and A. E. Kelly, "80 Gbit/s optical clock recovery using an electrical phase locked loop, and commercially available components," *OFC 2000, ThP4-1*, pp. 229–231.

[39] O. Kamatani and S. Kawanishi, "Prescaled timing jitter extraction from 400 Gb/s optical signal using phase lock loop based on four-wave-mixing in laser diode amplifiers," *IEEE Photon. Technol. Lett.*, vol. 8, pp. 1094–1096, 1996.

[40] T. Yamamoto, L. K. Oxenløwe, C. Schmidt, C. Schubert, E. Hilliger, U. Feiste, J. Berger, R. Ludwig, and H. G. Weber, "Clock recovery from 160Gbit/s data signals using phase-locked loop with interferometric optical switch based on semiconductor optical amplifier," *Electron. Lett.*, vol. 37, pp. 509–510, 2001.

[41] D. T. K. Tong, K. L. Deng, B. Mikkelsen, G. Raybon, K. F. Dreyer, and J. E. Johnson, "160 Gbit/s clock recovery using electroabsorption modulator-based phase-locked loop," *Electron. Lett.*, vol. 36, pp. 1951–1952, 2000.

[42] C. Boerner, C. Schubert, C. Schmidt, E. Hilliger, V. Marembert, J. Berger, S. Ferber, E. Dietrich, R. Ludwig, B. Schmauss, and H. G. Weber, "160 Gbit/s clock recovery using electroabsorption modulator-based phase-locked loop," *Electron. Lett.*, vol. 39, pp. 1071–1073, 2003.

[43] C. Boerner, V. Marembert, S. Ferber, C. Schubert, C. Schmidt-Langhrst, R. Ludwig, and H. G. Weber, "320 Gbit/s Clock Recovery with Electro-Optical PLL

using bidirectionally operated Electroabsorption Modulator as Phase Comparator," *Proc. Optical Fiber Communications Conference (OFC'05)*, March 2005.

[44] P. V. Mamyshev, "All-optical data regeneration based on self-phase modulation effect," *Proc. Eur. Conf. on Opt. Comm. (ECOC'98)*, 1998, Madrid, Spain, Sep. 20-24.

[45] S. Taccheo and K. Ennser, "Investigation of amplitude noise and timing jitter of supercontinuum spectrum-sliced pulses," *IEEE Photon. Technol. Lett.*, vol. 14, no. 8, pp. 1100–1102, August 2002.

[46] N. J. Doran and D. Wood, "Nonlinear-optical loop mirror," *Optics Lett.*, vol. 13, no. 1, pp. 56–58, January 1988.

[47] J. H. Lee, P. C. Teh, P. Petropoulos, M. Ibsen, and D. J. Richardson, "A Grating-Based OCDMA Coding-Decoding System Incorporating a Nonlinear Optical Loop Mirror for Improved Code Recognition and Noise Reduction," *J. Lightwave Technol.*, vol. 20, no. 1, pp. 36–46, January 2002.

[48] S. Bigo, O. Leclerc, and E. Desurvire, "All-optical Fiber Signal Processing and Regeneration for Soliton Communications," *IEEE Sel. Topics in Quantum Electron.*, vol. 3, no. 5, pp. 1208–1223, October 1997.

[49] M. Ibsen, M. K. Durkin, M. J. Cole, and R. I. Laming, "Sinc-Sampled Fiber Bragg Gratings for Identical Multiple Wavelength Operation," *IEEE Photon. Technol. Lett.*, vol. 10, no. 6, pp. 842–844, June 1998.

[50] M. Ibsen, M. K. Durkin, and R. I. Laming, "Chirped Moiré fiber gratings operating on two wavelength channels for use as dual-channel dispersion compensators," *IEEE Photon. Technol. Lett.*, vol. 10, pp. 84–86, 1998.

[51] F. Ouellette, P. A. Krug, T. Stephens, G. Dhosi, and B. J. Eggleton, "WDM and broadband dispersion compensation using chirped sampled fiber bragg gratings," *Electron. Lett.*, vol. 31, no. 11, pp. 899–901, 1995.

[52] J. H. Lee, L. K. Oxenløwe, M. Ibsen, K. S. Berg, A. T. Clausen, D. J. Richardson, and P. Jeppesen, "Timing jitter tolerant all-optical TDM data demultiplexing at 80 Gbit/s using fiber Bragg grating based rectangular pulse switching technology," *Proc. Optical Fiber Communications Conference (OFC'03)*, Paper TuH7, March 2003, Atlanta USA.

[53] B. J. Eggleton, P. A. Krug, and L. Poladian, "Long periodic superstructure Bragg gratings in optical fibers," *Electron. Lett.*, vol. 30, pp. 1620–1622, 1994.

[54] R. Feced, M. N. Zervas, and M. A. Muriel, "An efficient inverse scattering algorithm for the design of nonuniform fiber Bragg gratings," *IEEE J. of Quantum Electronics*, vol. 35, no. 8, pp. 1105–1115, 1999.

[55] M. Ibsen, M. Durkin, M. J. Cole, M. N. Zervas, and R. I. Laming, "Recent advances in long dispersion compensating fibre bragg gratings," *IEE Colloquium on Optical Fibre Gratings*, Paper 6, Birmingham, 1999.

[56] B. P. Nelson and N. J. Doran, "Optical sampling oscilloscope using nonlinear fibre loop mirror," *Electron. Lett.*, vol. 27, no. 3, pp. 204–205, January 1991.

[57] P. A. Andrekson, "Picosecond optical sampling using four wave mixing in fiber," *Electron. Lett.*, vol. 27, no. 16, pp. 1440–1441, August 1991.

[58] J. Li, J. Haansryd, P. O. Hedekvist, and P. A. Andrekson, "300-Gb/s Eye-Diagram Measurement by optical sampling Using Fiber-Based Parametric Amplification," *IEEE Photon. Technol. Lett.*, vol. 13, no. 9, pp. 987–989, September 2001.

[59] R. Trebino and D. J. Kane, "Using Phase Retrieval to Measure the Intensity and Phase of Ultrashort Pulses: Frequency-Resolved Optical Gating," *J. Opt. Soc. Amer. A*, vol. 10, no. 5, pp. 1101–1111, 1993.

[60] D. J. Kane and R. Trebino, "Characterization of Arbitrary Femtosecond Pulses Using Frequency-Resolved Optical Gating," *IEEE J. Quantum Electron.*, vol. 29, no. 2, pp. 571–579, 1993.

[61] R. Trebino, K. W. DeLong, D. N. Fittinghoff, J. N. Sweetser, M. A. Krumbügel, and B. A. Richman, "Measuring Ultrashort Laser Pulses in the Time-Frequency Domain Using Frequency-Resolved Optical Gating," *Rev. Sci. Instrum.*, vol. 68, no. 9, pp. 3277–3295, 1997.

[62] D. J. Kane and R. Trebino, "Single-shot measurement of the intensity and phase of an arbitrary ultrashort pulse by using frequency-resolved optical gating," *Optics Lett.*, vol. 18, no. 10, pp. 823–825, May 1993.

[63] J. Prawiharjo, K. Gallo, B. C. Thomsen, M. A. F. Roelens, P. J. Almeida, N. G. B. Broderick, and D. J. Richardson, "Frequency Resolved Optical Gating in a Quasi-Phase-Matched $LiNbO_3$," *IEEE Photon. Technol. Lett.*, vol. 17, no. 4, pp. 849–851, 2005.

[64] J. Prawiharjo, K. Gallo, N. G. B. Broderick, and D. J. Richardson, "Frequency Resolved Optical Gating in the 1.55 μm-Band Via Cascaded χ^2 Processes," *J. Opt. Soc. Amer. B*, vol. 22, no. 9, pp. 1985–1993, 2005.

[65] J. Prawiharjo, F. Parmigiani, K. Gallo, P. Petropoulos, N. G. B. Broderick, and D. J. Richardson, "Cascaded χ^2 Interaction Frequency-Resolved Optical Gating in a Periodically-Poled Lithium Niobate Waveguide," *Opt. Lett.*, vol. 31, no. 2, pp. 244–246, 2005.

[66] C. Dorrer and I. Kang, "Simultaneous temporal characterization of telecommunication optical pulses and modulators by use of spectrograms," *Opt. Lett.*, vol. 27, no. 15, pp. 1315–1317, 2002.

[67] T. Kanada and D. L. Frazen, "Optical waveform measurement by optical sampling with a mode-locked laser diode," *Optics Lett.*, vol. 11, no. 1, pp. 4–6, January 1986.

[68] S. Diez, C. Schmidt, D. Hoffmann, C. Bornholdt, B. Sartorius, and H. G. Weber, "Simultaneous sampling of optical pulse intensities and wavelengths by four-wave mixing in a semiconductor optical amplifier," *Applied Physics Letters*, vol. 73, no. 26, pp. 3821–3823, December 1998.

[69] R. Trebino, *Frequency-Resolved Optical Gating: The Measurement of Ultrashort Laser Pulses*, K. A. Publishers, Ed., 2000.

[70] J. H. Lee, P. C. Teh, P. Petropoulos, M. Ibsen, and D. J. Richardson, "Timing Jitter Tolerant All-optical Modulator and Demultiplexing Systems Incorporating Pulse-Shaping Fiber Bragg Gratings," *Proc. Optical Fiber Communications Conference (OFC'01)*, Postdeadline Paper PD30-1, 2001.

[71] C. Schubert, R. Ludwig, S. Watanabe, F. Futami, S. Ferber, J. Berger, C. Schmidt, and H. G. Weber, "Improved Performance of a 160 Gb/s Fibre based all-optical Switch using Rectangular Gating Pulses," *Proc. Eur. Conf. on Opt. Comm. (ECOC 2002)*, vol. P. 8.3.7, 2002.

[72] K. Uchiyama, T. Morioka, S. Kawanishi, H. Takara, and M. Saruwatari, "Signal-to-Noise Ratio Analysis of 100 Gb/s Demultiplexing Using Nonlinear Optical Loop Mirror," *J. Lightwave Technol.*, vol. 15, pp. 194–201, 1997.

[73] P. C. Teh, M. Ibsen, J. H. Lee, P. Petropoulos, and D. J. Richardson, "Demonstration of a four-channel WDM/OCDMA system using 255-chirp, 320 Gchip/s quaternary phase coding gratings," *IEEE Photon. Technol. Lett.*, vol. 14, no. 2, pp. 227–229, 2002.

[74] D. V. der Linde, "Characterization of the Noise in Continuosly Operating Mode-Locked Lasers," *Appl. Phys. B*, vol. 39, pp. 201–217, 1986.

[75] N. S. Bergano, F. W. Kerfoot, and C. R. Davidson, "Margin measurements in optical amplifier systems," *IEEE Photon. Technol. Lett.*, vol. 5, no. 3, pp. 304–306, March 1993.

[76] J. H. Lee, T. Tanemura, K. Kikuchi, T. Nagashima, T. Hasegawa, S. Ohara, and N. Sugimoto, "Use of 1-m Bi_2O_3 nonlinear fiber for 160-Gbit/s optical time-division demultiplexing based on polarisation rotation and wavelength shift induced by cross-phase modulation," *Opt. Lett.*, vol. 11, pp. 1267–1269, 2005.

[77] G. Gavioli and P. Bayvel, "Amplitude jitter suppression using patterning-tolerant, all-optical 3R regenerator," *Electron. Lett.*, vol. 40, pp. 688–690, 2004.

[78] M. Nakazawa and T. Hirooka, "Distortion-free optical transmission using time-domain optical fourier transformation and transform-limited optical pulses," *J. Opt. Soc. Am. B*, vol. 22, pp. 1842–1855, 2005.

[79] T. Jannson, "Real-time Fourier transformation in dispersive optical fibers," *Opt. Lett.*, vol. 8, no. 4, pp. 232–234, April 1983.

[80] B. H. Kolner, "Space-time duality and the theory of temporal imaging," *IEEE J. Quantum Electron.*, vol. 30, pp. 1951–1963, 1994.

[81] M. A. Muriel, J. Azaña, and A. Carballar, "Real-time Fourier transformer based on finer gratings," *Opt. Lett.*, vol. 24, no. 1, pp. 1–3, January 1999.

[82] M. Romagnoli, P. Franco, R. Corsini, A. Schiffini, and M. Midrio, "Time-domain fourier optics for polarization-mode dispersion," *Opt. Lett.*, vol. 24, pp. 1197–1199, 1999.

[83] L. F. Mollenauer and C. Xu, "Time-lens timing jitter compensator in ultra-long haul dwdm dispersion managed soliton transmissions," *Conference on Lasers and Electro-Optics,* PD CPDB1-1, 2002.

[84] L. A. Jiang, M. E. Grein, H. A. Haus, E. P. Ippen, and H. Yokoyama, "Timing jitter eater for optical pulse trains," *Opt. Lett.*, vol. 28, pp. 78–80, 2003.

[85] M. Nakazawa, T. Hirooka, F. Futami, and S. Watanabe, "Ideal Distortion-Free Transmission Using Optical Fourier Transformation and Fourier Transformation-Limited Optical Pulses," *IEEE Photon. Technol. Lett.*, vol. 16, pp. 1059–1061, 2004.

[86] T. Hirooka, M. Nakazawa, F. Futami, and S. Watanabe, "A New Adaptive Equalization Scheme for a 160-Gb/s Transmitted Signal Using Time-Domain Optical Fourier Transformation," *IEEE Photon. Technol. Lett.*, vol. 16, pp. 2371–2373, 2004.

[87] T. Sakano, K. Uchiyama, I. Shake, T. Morioka, and K. Hagimoto, "Large-dispersion-tolerance optical signal transmission system based on temporal imaging," *Opt. Lett.*, vol. 27, pp. 583–585, 2002.

[88] J. A. Harrison, K. J. Blow, and A. J. Poustie, "All-optical bit-level retiming and jitter suppression," *Opt. Commun.*, vol. 240, pp. 221–226, 2004.

[89] P. J. Almeida, P. Petropoulos, F. Parmigiani, M. Ibsen, and D. J. Richardson, "OTDM Add-Drop Multiplexer Based on Time-Frequency Signal Processing," *J. of Lightwave Technol.*, vol. 24, no. 7, pp. 2720–2732, July 2006.

[90] D. Grischkowsky and A. C. Balant, "Optical pulse compression based on enhanced frequency chirping," *Appl. Phys. Lett.*, vol. 41, pp. 1–3, 1982.

[91] T. Hirooka, K.-I. Hagiuda, T. Kumakura, K. Osawa, and M. Nakasawa, "160 gbit/s-600 km OTDM Transmission using Time-domain Optical fourier transformation," *ECOC, Paper Tu1.5.4.*

[92] B. E. Olsson and D. J. Blumenthal, "All-optical demultiplexing using fiber cross-phase modulation (XPM) and optical filtering," *IEEE Photon. Technol. Lett.*, vol. 13, pp. 875–877, 2001.

[93] J. Li, B. E. Olsson, M. Karlsson, and P. Andrekson, "OTDM Add-Drop Multiplexer Based on XPM-Induced Wavelength Shifting in Highly Nonlinear Fiber," *J. Lightwave Lett.*, vol. 23, pp. 2654–2661, 2005.

[94] K. S. Abedin, "Ultrafast pulse retiming by cross-phase modulation in an anomalous-dispersion polarization-mainaining fiber," *Opt. Lett.*, vol. 30, pp. 2979–2981, 2005.

[95] J. V. Howe and C. Xu, "Ultrafast Optical Signal Processing Based Upon Space-Time Dualities," . *Lightwave Lett.*, vol. 24, no. 7, pp. 2649–2661, July 2006.

[96] M. E. Fermann, V. I. Kruglov, B. C. Thomsen, J. . M. Dudley, and J. D. Harvey, "Self-similar propagation and amplification of parabolic pulses in optical fibers," *Phys. Rev. Lett.*, vol. 84, no. 26, pp. 6010–6013, 2000.

[97] C. Billet, J. M. Dudley, N. Joly, and J. C. Knight, "Intermediate asymptotic evolution and photonic bandgap fiber compression of optical similaritons around 1550 nm," *Opt. Express*, vol. 13, no. 9, pp. 3236–3241, 2005.

[98] C. Finot, G. Millot, C. Billet, and J. M. Dudley, "Experimental generation of parabolic pulses via raman amplification in optical fiber," *Opt. Express*, vol. 11, no. 13, pp. 1547–1552, 2003.

[99] T. Hirooka and M. Nakazawa, "Parabolic pulse generation by use of a dispersion-decreasing fiber with normal group-velocity dispersion," *Opt. Lett.*, vol. 29, no. 5, pp. 498–500, 2004.

[100] I. Hartl, X. D. Li, C. Chudoba, R. K. Ghanta, T. H. Ko, J. G. Fujimoto, J. K. Ranka, and R. S. Windeler, "Ultrahigh-resolution optical coherence tomography using continuum generation in an air-silica microstructure optical fiber," *Opt. Lett.*, vol. 26, no. 9, pp. 608–610, 2001.

[101] S. A. Diddams, D. J. Jones, J. Ye, T. Cundiff, J. L. Hall, J. K. Ranka, R. S. Windeler, R. Holzwarth, T. Udem, and T. W. Hanch, "Direct link between microwave and optical frequencies with a 300 Thz femtosecond laser comb," *Phys. Rev. Lett.*, vol. 84, no. 22, pp. 5102–5105, 2000.

[102] Y. Takushima and K. Kikuchi, "10-GHz, over 20-channel multiwavelength pulse source by slicing super-continuum spectrum generated in normal-dispersion fiber," *IEEE Photon. Technol. Lett.*, vol. 11, pp. 322–324, 1999.

[103] J. W. Nicholson, M. F. Yan, P. Wisk, J. Fleming, F. DiMarcello, E. Monberg, A. Yablon, C. Jorgensen, and T. Veng, "All-fiber, octave-spanning supercontinuum," *Opt. Lett.*, vol. 28, no. 8, pp. 643–645, 2003.

[104] D. Anderson, M. Desaix, M. Karlsson, M. Lisak, and M. L. Quiroga-Teixeiro, "Wave-breaking-free pulses in nonlinear-optical fibers," *J. Opt. Soc. B*, vol. 10, pp. 1185–1190, 1993.

[105] R. H. Stolen and C. Lin, "Self-phase-modulation in silica optical fibers," *Phys. Rev. A*, vol. 17, no. 4, pp. 1448–1453, 1978.

[106] S. Watanabe and S. Takeda, "All-optical noise suppression using two-stage highly-nonlinear fibre loop interferometers," *Electron. Lett.*, vol. 36, pp. 52–53, 2000.

[107] S. J. B. Yoo, "Wavelength Conversion Technologies for WDM Network Applications," *J. Lightwave Technol.*, vol. 14, pp. 955–966, 1996.

[108] T. H. B. Her, G. Raybon, and C. Headley, "Optimization of Pulse Regeneration at 40 Gb/s Based on Spectral Filtering of Self-Phase Modulation in Fiber," *IEEE Photon. Technol. Lett.*, vol. 16, pp. 200–203, 2004.

[109] J. H. Lee, T. Tanemura, K. Kikuchi, T. Nagashima, T. Hasegawa, S. Ohara, and N. Sugimoto, "Use of 1-m Bi_2O_3 nonlinear fiber for 160-Gbit/s optical time-division demultiplexing based on polarization rotation and a wavelength shift induced by cross-phase modulation," *Opt. Lett.*, vol. 11, pp. 1267–1269, 2005.

[110] B. E. Olsson, P. Ohlen, L. Rau, and D. J. Blumenthal, "A simple and robust 40-Gb/s wavelength converter using cross-phase modulation and optical filtering," *IEEE Photon. Technol. Lett.*, vol. 12, pp. 846–848, 2000.

[111] E. Ciaramella and S. Trillo, "All-optical signal reshaping via four-wave mixing in optical fibers," *IEEE Photon. Technol. Lett.*, vol. 12, pp. 849–851, 2000.

[112] D. Dahan, R. Alizon, A. Bilenca, and G. Eisenstein, "Optical noise reduction in inter-band Raman mediated wavelength conversion," *Electron. Lett.*, vol. 39, pp. 307–309, 2003.

[113] M. Matsumoto, "Performance Analysis and Comparison of Optical 3R Regenerators utilizing Self-Phase Modulation in Fibers," *J. Lightwave Technol.*, vol. 22, pp. 1472–1482, 2004.

[114] J. T. Gopinath, H. M. Shen, H. Sotobayashi, E. P. Ippen, T. Hasegawa, T. Nagashima, and N. Sugimoto, "Highly Nonlinear Bismuth-Oxide Fiber for Supercontinuum Generation and Femtosecond Pulse Compression," *J. Lightwave Technol.*, vol. 23, pp. 3591–3596, 2005.

[115] N. Nakazawa, H. Kubota, and K. Tamura, "Random evolution and coherence degradation of a high-order optical soliton train in the presence of noise," *Opt. Lett.*, vol. 24, pp. 318–320, 1999.

[116] T. Hasegawa, T. Nagashima, and N. Sugimoto, "A simple tapered bismuth-based nonlinear optical fiber for low-loss coupling to single-mode silica fibers," *Proc. Optical Fiber Communications Conference (OFC'06), Paper OWI7*, 2006.

[117] A. Boskovic, S. V. Chernikov, J. R. Taylor, L. GrunerNielsen, and O. A. Levring, "Direct continuous-wave measurement of n_2 in various types of telecommunication fiber at 1.55 μm," *Opt. Lett.*, vol. 21, pp. 1966–1968, 1996.

[118] H. Ebendorff-Heidepriem, P. Petropoulos, S. Asimakis, V. Finazzi, R. C. Moore, K. Frampton, F. Koizumo, D. J. Richardson, and T. M. Monro, "Bismuth glass holey fibers with high nonlinearity," *Opt. Express*, vol. 12, no. 21, pp. 5082–5087, 2004.

[119] J. H. Lee, T. Nagashima, T. Hasegawa, S. Ohara, N. Sugimoto, Y.-G. H. andS. B. Lee, and K. Kikuchi, "Output Performance Investigation of Self-Phase-Modulation-Based 2R Regenerator Using Bismuth Oxide Nonlinear Fiber," *IEEE Photon. Technol. Lett.*, vol. 18, no. 12, pp. 1296–1298, 2006.

[120] M. Kulishov, J. Azana, Y. Park, and R. Slavik, "Sub-Picosecond Flat-Top Waveform Generation using a Single Uniform Long-Period Fiber Grating," *ECOC 2006, Cannes, 24-28 September 2006, We2.3.7.*

[121] J. Y. Y. Leong, S. Asimakis, F. Poletti, P. Petropoulos, X. Feng, R. C. Moore, K. E. Frampton, T. M. Monro, H. Ebendorff-Heidepriem, W. H. Loh, and D. J. Richardson, "Nonlinearity and dispersion control in small core lead silicate holey fibers by structured element stacking," *OFC 2006, Anaheim 5-10 Mar 2006 OTuH1.*

[122] S. Asimakis, P. Petropoulos, F. Poletti, J. Y. Y. Leong, H. Ebendorff-Heidepriem, R. C. Moore, K. E. Frampton, X. Feng, W. H. Loh, T. M. Monro, and D. J. Richardson, "Efficient four-wave-mixing at 1.55 microns in a short-length dispersion shifted lead silicate holey fibre," *ECOC 2006, Cannes 24-28 Sept 2006, Th1.3.3.*

[123] F. Poletti, P. Petropoulos, N. G. Broderick, and D. J. Richardson, "Design of highly nonlinear bismuth-oxide holey fibres with zero dispersion and enhanced brillouin suppression," *ECOC 2006, Cannes 24-28 Sept 2006, Tu4.3.2.*